UNIVERSITY of CALIFORNIA
Santa Barbara

Realizing and probing driven quantum systems with ultracold gases

A dissertation submitted in partial satisfaction of the
requirements for the degree of

Doctor of Philosophy

in

Physics

by

Shankari Vani Rajagopal

Committee in charge:

Professor David Weld, Chair

Professor Ania Jayich

Professor Cenke Xu

June 2019

The dissertation of Shankari Vani Rajagopal is approved:

Professor Ania Jayich

Professor Cenke Xu

Professor David Weld, Chair

April 2019

To my parents, and their parents.

Acknowledgements

There is an unbelievably long list of people without whom I could not have gotten through the last 7 years. I cannot hope to name all of them, nor to do justice to what I owe them, but if you are one of them, I hope your crops are flourishing; you have my deepest gratitude.

I first need to thank my advisor, David Weld. At various times through the past 7 years, David has provided experimental guidance, scientific clarity and courage to explore entirely novel ideas, and encouragement to live a well-balanced life. He has taught me of the importance of precise communication (especially when it involves arcane literary references), the value of smelling things in lab, and the sneaky malignance of the word "system." He has approached advising with grounded humility, humanity, and kindness, and I have a deep appreciation and admiration for him as a scientist and as a human.[1]

My committee members have provided scientific and life advice throughout my graduate career. Ania Jayich told me in my first year of grad school, "Remember to work with a sense of urgency, even if the work doesn't seem urgent now. One day you'll graduate and wish you had more time to do more." Despite not fully believing the part about graduating for many years (I do now!), I have kept her advice in mind over the past 7 years and found it to be indispensable to my experimental life. Cenke Xu taught me the course which first piqued my interest in many-body physics, and his work on SU(N) magnetism first piqued my interest in strontium; I thank him for agreeing to be on my committee.

To build a new lab as a group of young graduate students is, to use a rather cliched metaphor, to jump off a cliff with little knowledge of what lies below. Luckily, we were jumping into a large ocean of scientific and experimental AMO knowledge, guided by maps which took the form of Simon Stellmer's and Florian Schreck's excellent theses. We banded together like a raft of fire ants to safely navigate this ocean and avoid inadvertent death; perhaps no part of my graduate experience has shaped me so deeply as the camaraderie shared among us, particularly among the OG5. I have been honored and humbled to learn from my fellow ants, both in and out of the lab. Much like those insects' intelligence, our curiosity as a collective was much more than the sum of its parts and led to learning something new every day, from quadratic Zeeman shifts and lab coat damage thresholds to fire ants' survival abilities and the finer descriptors of ear wax.[2] Thank you, ants.[3]

Zach Geiger, the first Weld student, created a lab culture which valued its members as people, and which allowed for so much fun with each other that scientific productivity no longer seemed like work. No matter how busy he was, even in the thick of writing his thesis, he always had time to be a sounding board for crazy experimental ideas. His ability to check on his labmates' well-being at difficult times was as uncanny as his

[1] Though not as an abiding fan of the New England Patriots, a wholly bizarre and inexplicable affiliation for such a nice person.

[2] Alas!

[3] Thants.

falsetto was annoying[4]; he was always down to take a quick break for sanity-retainment, and he taught me a lot about beer, an important part of my graduate education.

Ruwan Senaratne, my strontian-partner-in-crime, is one of the most perceptive scientists I have had the fortune to work with. He taught me by example how, when presented with a large amount of new information, to focus on and distill the concepts down to the most essential and digestible form. He could find the humour in any dire lab situation, including but not limited to the task of building two machines, and was always willing to talk through solutions (or at least to provide witty commentary, which was oftentimes just as helpful). He was remarkably patient with my nocturnal sleeping habits, and was also a ready Sporcler and fellow fan of British humour, all qualities I greatly appreciated. There is still nobody else I'd rather tighten CF bolts with, nor form a trivia team with, and I use British spellings in this paragraph as tribute.

If I ever have a question or doubt about an AMO idea, I feel confident that after discussion with Cora Fujiwara, I will have a deeper and more correct understanding of the physics. Cora is also a Matlab wizard. The question has often been asked how she got so good at Matlab, and divinity has not yet been precluded since there have been no satisfactory answers; I have benefited from her skills enormously and have had to do less coding as a result, for which I am very grateful. More importantly, Cora has been one of my greatest friends through graduate school, from that fateful Woodstock's meeting to the present. She has lent an empathetic ear to my many, many gripes throughout grad school, and has been my ally in profound ways both in and out of work. The way in which she approaches both her science and her life with a sense of purpose is inspirational, and I am immensely grateful for her presence in my life.

Kevin Singh approaches everything with a remarkable intensity and discipline which is always reflected in his labwork, yet simultaneously manages not to take anything seriously. I've never been sure how he strikes this balance to which I so aspire. His positivity and can-do attitude have been a driving force in this lab, but what I will always appreciate most is the levity and perspective he brought: his ability to poke good-natured fun at science and humans alike, his unbelievable meme-generation rate, and his also-annoying falsetto.[5] He is now tackling cesium (physically, I assume), and I look forward to him soon setting a record for most takedowns of an atom in a single lab.

Our postdoc, Toshi Shimasaki, joined our group in 2017 and immediately became indispensable. His AMO knowledge is as remarkable in breadth as it is in depth, and working with him is a masterclass in considering a problem deeply. He is a consummate experimentalist and has taught me so much about various lab technologies, experimental non-idealities, and tricks that have made my life in optics much easier. He has been a willing sounding board for professional issues and life decisions, and has readily and generously given much of his time to provide excellent advice on those topics. His ability to add an economic perspective to almost every situation is equal parts beneficial and hilarious: I have no doubt that he has surreptitiously trained me to work harder, smarter,

[4]Sorry not sorry

[5]Still sorry not sorry; Mickey Mouse week was the worst.

and more calmly, in some Pavlovian manner of which I will only become fully cognizant years from now when someone hands me a box of Girl Scout cookies and yells "IT'S FINE." I admire his ability to talk to strangers and get along with everyone, as well as his loyalty, curiosity, and compassion.

The youngest strontian, Master Peter "Heimdall" Dotti of BIFROST, brings rigor to everything he does. I am always impressed by his ability to spot inconsistencies in scientific arguments, pinpoint places the experiment could be problematic, and develop the necessary improvements; he has taught this old grad student, set in her ways, to see the value in the occasional experimental upgrade. He keeps immaculate records of experimental data, recording with a level of detail I will strive to replicate in the future. He also has excellent taste in music, which one should have if one can, and a quiet humor which has often disarmed battles of wills. I have no doubt that under the guidance of Peter, Toshi, and their inscrutable relationship with each other, days of glory are ahead for the strontium machine.

Quinn Simmons, despite only being a second year, has taken on an immense amount of responsibility over the past year, and has quickly become a UHV expert in addition to our resident "computer guy." I also really admire how much he cares about being a good colleague and establishing a good environment in the lab. Roshan Sajjad has an ability to onboard AMO physics extremely quickly, a curiosity about a wide berth of physics concepts, and a natural ease and friendliness in working with new colleagues. Both of them have been thrown in the deep end over the past year and are emerging with a good-naturedness that I certainly wouldn't have in their place. I know the lithium machine is being left in the hands of capable and good people, and I am very excited to keep up with their achievements.

Slava Lebedev was our postdoc in the early days of the lab, and I learned a lot of my basic optics knowledge from him: how to efficiently design and set up a laser table, how to fiber-couple, and how to design something quickly to determine if it's a tenable solution worth doing better. I also thank him for sourcing magnets which have found multiple uses in lab, and for the creation of the game Gasket-Post.

Our lab owes much to our army of undergrads, masters students, and postbacs, many of whom have gone on to graduate school themselves. I learned a lot from the process of mentoring and working with them, and wish them the very best of luck in their various pursuits. For their many contributions to the lab, thanks to Erica Mason, Anne Hebert, Erik Anciaux!, Jacob Hines, Krutik Patel, Ted Robinson, Dylan Kennedy, Andrew Ballin, Shura Kotlerman, Robert Salazar, Max Garber, Xiaofei Zhou, Ian Harley, Sean Frazier, Cecile Carcy, Alan Long, Morgan Brubaker, James Chow, Yi Zeng, Shuo Ma, Delia Gratta, Vincent Hirtzel, and Ian Seabury, as well as our two most recent and extremely impressive young'uns, Alec Cao and Max Prichard. In particular, for their friendship, deep kindness, and chats over tea, coffee, and chocolate, I'll always be indebted to Erica, Anne, and Jacob.

The UCSB Physics and CNSI communities have always provided a supportive environment in which to work. I owe particular thanks to Andrew Jayich, with whom I've

enjoyed conversations ranging from laser technology, precision measurements, and future directions of AMO to debates: Star Wars movie rankings, legumes v. drupes, and stouts v. porters. To Mingyu and Craig—I'm rooting for you, you're doing awesome science, and also *whispers* it is okay to take a vacation once in a while. Beth Gwinn and Mark Sherwin have provided advice at critical junctures of grad school, for which I'm very grateful. The Mazin and Martinis groups often lent us their leak checker, and the ABJ, Sherwin, Young, and AMJ groups often lent us optics, electronics, and cleaning supplies when we needed them. Sathya Guruswamy has looked out for great undergraduate candidates to join our lab over the years, and has kindly provided us with much-needed chocolate. Dave Cannell left us an optical table which stands at the heart of the strontium experiment, and advice to sit on the table in event of an earthquake to avoid unpleasant squashing. We wouldn't be able to run anything in lab without the legendary Mike Deal, who fixes building and infrastructure issues for us faster than humanly possible.[6] So many logistics wouldn't be possible without Dan Stack, keeper of keys and ~~grounds at Hogwarts~~ the storeroom at Broida. We wouldn't have anything in lab if we couldn't buy things, and for the angelic work of dealing with companies directly for purchasing, thanks go to Dave Prine, Lynne Leininger, Dan Daniels, and Erin Ferguson, who often go above and beyond to expedite purchases. The department wouldn't function without Jennifer Farrar, who has put up with an absurd number of my lapsed registration deadlines- sorry, Jennifer! Holly Woo, Eva Deloa, Jess Henry, and Shilo Tucker are insanely good at making my life easier by handling all manner of financial reimbursement. We couldn't have build up our technical infrastructure without support from Glenn Schiferl and Rick Barber, and we couldn't have built many parts of our machines without the help of the Physics Machine Shop- thanks to Jeff Dutter, Guy Patterson, Mark Sheckherd, Andy Segale, and Doug Rehn for all of their machining help and expertise.

I've met some incredible people at UCSB. Jack Bradmiller-Feld, Claire McLellan, Alex Walter, Cora Fujiwara, and later, Dave Sutherland have been there for me through the best and worst times, and I could always depend on them for advice, laughs, professional support, running partners, escapes from work, and celebrations of nothing in particular- I look forward to adventuring with them in the future. I have been fortunate to be in graduate school alongside, and to live with, the coolest peeps- Adam Dishaw, Jimmy Chen, Greg Peairs, Matt Weaver, Alex Miller, Andrew Dunsworth, Christina Knapp, Kevin Satzinger, Clyde Dunsword, Cody Knappzinger, Tina Fujiwara, and many other inhabitants of King's Landing, Za City, and Ball Sac Mansion. I always looked forward to hanging out with Netta Engelhardt, Stacy Copp, Curt Nehrkorn, Brayden Ware, Teddy Parker, and Sebastian Fischetti around Santa Barbara. They and the various nucleons and electrons of Kaiser House- Ruwan, Zach, Hunter Banks, Mark Burgers, Amit Rawal, Eric Langman, and Paul Szypryt- were the generators of some epic moments.

The UCSB Women in Physics community are some of the most brilliant people I have ever met. Claire, Netta, Stacy, Christina, Kim Schlesinger, Chantal Nguyen,

[6] Mike's wavefunction is rumored to be distributed around Broida labs; it collapses to your location within mere minutes when you need him.

Takako Hirokawa, Brianna Grado-White, and Isabel Lipartito have made my life in the department better and provided solid advice, support, and levity when I sorely needed it, and I thank them as well as Gabi Abraham, Melissa Quinnan, Sarah Steiger, Molly Wolfson, Samhita Banavar, Lia Yeh, Haley Bowden, and Amalu Shimamura for all of their efforts on behalf of CUWiP, which had an outsize impact on my time here.

My dear swing dancing community consists of the most supportive, musical, wonderful individuals in Santa Barbara. Thanks to Mari Foster, Robbie McConnell, Faye Walker, Melissa Kirby, Robert Moore, Laurie Pfeiffer, Alicia Cortes, Julie and Elliot Lowndes, Karen Little, Malcolm Crum, James Hawkins, Nikka Keivanfar, Kat Chouinard, Lindsey Kasehagen, Mike Nip, and Elliot Simon for the dances, general silliness, board games, and swing dance love- I am not exaggerating when I say I would have moved away from Santa Barbara had I not found you all here.

Depression and anxiety have been companions in grad school. I would be remiss if I did not thank Jocelyn Levitan, Elizabeth May, and Robert Hughes, who compassionately helped me through my darkest days. On a not-unrelated note, I need to thank the Obamas. Yoga with Adriene saw me through ups and downs from early 2013 to present, and Bruce Springsteen, Elton John, Beyonce, Sara Bareilles, Kendrick Lamar, and Fleet Foxes provided the soundtracks to unreasonably-long portions of my Santa Barbara life.

To my pre-California extended family—Lindsey Shi, Lynda Williams, Matt Weaver, Ryker Reed, Tiffany Lin, Victoria Sun, Wei Sun, Johari Frasier, Kyumin Lee, Neil Fitzgerald, Rachel Mills, Rose Chascsa, and Steve Johnson—thank you for visiting me, for believing that I was capable of sticking this out, and for being constants in my life.

And finally, I need to thank my family, who are the best people in the world. My brother Shiva is hardworking and kind and wants to give back to the world through his work; I am proud of everything he has accomplished, and prouder to be related to him. My parents have been my biggest supporters for my entire life, and I cannot fathom how much they have sacrificed to make my life better. They planted the seeds of STEM interest early; I cannot thank them enough for ignoring my requests for Barbies and buying Erector and Lego sets instead, nor for the significant time and effort they dedicated to my education. They have always been there to catch me when the going has gotten tough in grad school, reminding me to have a broad perspective on life, sending me care packages when needed, and making sure I had a fun and relaxing break from work whenever I went home. Most importantly, they are unfailingly good people, examples to which I aspire every day. To paraphrase Paul Simon, "There but for the grace of them, go I."

Curriculum Vitæ

Shankari Vani Rajagopal

Education

2019	Ph.D. Physics (Expected), University of California, Santa Barbara.
2015	M.A. Physics, University of California, Santa Barbara.
2012	B.S. Physics, Massachusetts Institute of Technology

Publications

K. Singh, K.M. Fujiwara, Z.A. Geiger, E.Q. Simmons, M. Lipatov, A. Cao, P.E. Dotti, S.V. Rajagopal, R. Senaratne, T. Shimasaki, M. Heyl, A. Eckardt, and D.M. Weld. *Quantifying and controlling prethermal nonergodicity in interacting Floquet matter.* arXiv:1809.05554 (2019).

R. Senaratne, S.V. Rajagopal, T. Shimasaki, P.E. Dotti, K.M. Fujiwara, K. Singh, Z.A. Geiger, and D.M. Weld. *Cold-Atom Quantum Simulation of Ultrafast Dynamics.* Nat. Comm. **9**, 2065 (2018).

K.M. Fujiwara, K. Singh, Z.A. Geiger, R. Senaratne, S.V. Rajagopal, M. Lipatov, and D.M. Weld. *Transport in Floquet-Bloch bands.* Phys. Rev. Lett. **122**, 010402 (2018).

Z.A. Geiger, K.M. Fujiwara, K. Singh, R. Senaratne, S.V. Rajagopal, M. Lipatov, T. Shimasaki, R. Driben, V.V. Konotop, T. Meier, and D.M. Weld. *Observation and uses of position-space Bloch oscillations in an ultracold gas.* Phys. Rev. Lett. **120**, 213201 (2018).

K.M. Fujiwara, Z.A. Geiger, K. Singh, R. Senaratne, S.V. Rajagopal, M. Lipatov, T. Shimasaki, and D.M. Weld. *Experimental Realization of a Relativistic Harmonic Oscillator.* New J. Phys. **20**, 063027 (2018).

S.V. Rajagopal, K.M. Fujiwara, R. Senaratne, K. Singh, Z.A. Geiger, and D.M. Weld. *Quantum Emulation of Extreme Non-equilibrium Phenomena with Trapped Atoms.* Ann. Phys. **529**, 1700008 (2017).

R. Senaratne, S.V. Rajagopal, Z. Geiger, K.M. Fujiwara, V. Lebedev, and D.M. Weld. *Effusive Atomic Oven Nozzle Design Using an Aligned Microcapillary Array.* Rev. Sci. Instrum. **86**, 023105 (2015).

Abstract

Realizing and probing driven quantum systems with ultracold gases

by

Shankari Vani Rajagopal

Ultracold quantum gases offer a versatile platform to study a wide range of open questions in condensed matter physics and beyond. In particular, their controllability, isolation from noisy thermal environments, and evolution on experimentally-accessible timescales make them a natural choice to probe the effects of driving on time evolution and energy. This thesis details the construction of two cold-atom apparatuses, a lithium machine and a strontium machine, for quantum emulation experiments studying driven systems. Initial numerical simulations along two experimental lines are briefly discussed, and results from the first two experiments on the strontium machine are then presented. In the first, a strontium Bose-Einstein condensate in an optical trap is strongly driven to emulate ultrafast photoionization processes; in a series of proof-of-principle experiments measuring the momenta and energy of particles ejected from the trap, we demonstrate the viability of this technique to study open questions in strong-field physics. The second experiment realizes a tunable quasicrystal, the energy structure for which is described by the multifractal Hofstadter butterfly. Quasiperiodic structures host not only phonons, but also a higher-dimension analogue called phasons. In the experiment, we demonstrate phasonic spectroscopy for the first time by directly driving one of these modes; we characterize the coupling to the resulting excitations, and directly map a slice of the Hofstadter energy spectrum.

Contents

List of Figures

List of Tables

Chapter 1

Introduction

We choose to cool atoms. We choose to cool atoms in this lab and do the other science, not because it is easy, but because it is hard, because that goal will serve to organize and measure their energies...

-John F. Kennedy, probably

Atoms were first predicted to condense into a degenerate state at cold temperatures in the mid 1920s. The technological progress, spectroscopic measurements, and advancement of cooling techniques that followed in the next 7 decades facilitated the experimental observation of that effect: the creation of a Bose-Einstein condensate [1, 2] and then a degenerate Fermi gas [3]. In the following years, a great deal of effort went into studying and understanding the properties of these states of matter on a fundamental level.

The focus of cold atom experiments then saw movement away from studies of the degenerate gases, and towards using them as tools to study more complicated systems in condensed matter physics. To me, that this shift occurred is hardly surprising. A fundamental part of a physics education involves learning to look at a difficult system, ignore many of the more complicated aspects of it, and then write down a toy model to better understand the problem. Invariably, we find throughout this education that these toy models are invaluable; they do not capture all of the physics, but they often capture the

important physics, and we can grasp much of the fundamental behavior of the system by studying them. Cold atoms are great experimental toy models for many-body condensed matter systems: they offer extremely precise control over the fundamental elements of more complicated structures (numbers, densities, spins, and interaction strengths of particles, and dimensionality and tunability of potentials) while conveniently offering respite from the rather gruesome effects of defects, disorder, and coupling to the environment. Additionally, once they are built, cold atom experiments are remarkably versatile, allowing a wide range of experiments to be set up and broken down around them over many years. Using cold atoms in this manner has been dubbed "quantum simulation;" its uses have recently evolved to include noisy intermediate-scale quantum (NISQ) information science, which explores many-body quantum physics without extreme limits on fidelity.

1.1 Quantum Simulation with Neutral Atoms

Quantum simulation has seen much success in several fields of condensed matter. The observation of the superfluid-Mott-insulator transition [4] allowed the study of a quantum phase transition predicted in solids, and the relative ease and low energy densities of cold atoms systems made it relatively straightforward to study Bloch oscillations in an optical lattice [5]. The ability to realize both random and quasiperiodic disorder in optical lattices made it possible to study Anderson localization in a very controllable way [6]. Recently, with the advent of quantum gas microscopy, several groups have been studying magnetic ground states by looking at spin correlations [7, 8, 9, 10, 11]. The advent of degenerate Fermi gases made it possible to observe the BEC-BCS crossover, which paved the way to the study of strongly-correlated Fermi gases and exotic superconducting behavior [12]. Quantum simulation has even expanded into the study of quantum chemistry [13].

1.1.1 Driven systems

One of the most exciting developments of the past few years has been a rising interest in driven systems- what happens to a physical system when it is periodically driven in various regimes. These phenomena are often described by Floquet formalism, and there are a number of general questions that naturally arise: does driving a system give rise to dynamical phases that are otherwise unstable? What does it mean for these driven systems to thermalize, since broken time-translation symmetry leads to lack of energy conservation?

In our lab, we have constructed two cold atom machines over the past several years, a lithium machine and a strontium machine. The lithium machine has been recently focused on using Floquet engineering to study and modify the band structure of optical lattices, and to explore prethermalization: a metastable phenomenon induced by driving prior to thermalization. The strontium experiment, which has been my primary scientific tool during the latter part of my graduate career, has focused on two different experimental lines, both of which try to use driving to answer questions which are difficult for condensed matter physicists to address. The first involves open questions in ultrafast (strong-field) physics, where extremely fast timescales ($\mathcal{O}(10^{-18} - 10^{-15}$ s)) makes it technically challenging to answer questions regarding, for example, the timing of tunneling ionization and the momenta of ionized electrons. The second involves excitations and spectral features of quasicrystals, which are incompletely understood and difficult to study in a solid-state context. It is fitting that the toolbox of cold atoms can be used to spectroscopically probe exotic quantum systems, since the spectroscopic developments of the mid-20th century laid the foundation for the development of that toolbox.

1.2 Dissertation overview

This thesis is divided into 9 chapters and 13 appendices under the following framework:

1.2.1 Chapters

Chapter 2 contains a general overview of some theoretical ideas relevant to atomic cooling and lattice experiments. It is meant to be a quick reference and in no way contains complete descriptions of any topic. **Chapter 3** details specific atomic properties for both lithium and strontium, including level diagrams, scattering properties, and an overview of cooling sequences. **Chapter 4** is split into two main sections. The first details design and construction of the lithium machine, and the second goes into each cooling stage of lithium from the oven to BEC, including experimental parameters. **Chapter 5** is split into two main sections. The first details design and construction of the strontium machine, and the second goes into each cooling stage of strontium from the oven to BEC, including experimental parameters. **Chapter 6** presents some early numerical simulations of the experimental lines we eventually follow. **Chapter 7** details the results of our first strontium-based experiment emulating ultrafast physics, as well as some future directions for that project. **Chapter 8** is essentially a preprint of a forthcoming paper on phasonic spectroscopy of a tunable quantum quasicrystal. It also includes discussion of future directions at the end. **Chapter 9** discusses other future research goals for which we have been laying groundwork on the strontium machine.

1.2.2 Appendices

Many of the appendices will only be useful to members of the Weld Lab. **Appendix A** contains notes on UHV cleanliness and assembly of CF flanges. **Appendix B** is a compilation of best practices for water bakes, which we have learned and assembled over 8 of them. **Appendix C** discusses our lab infrastructure: temperature control, water and electric plumbing, magnet winding, and other things of that ilk. **Appendix D** includes calculations for the atomic polarizability of strontium and magic wavelength calculations. **Appendix E** contains some notes on lattice instability issues we had,

and how we mitigated them. **Appendix F** briefly discusses a couple of techniques to set up an imaging system and align lattices. It also includes images from each of our diagnostic cameras, with labels indicating their direction/rotation. **Appendix G** contains technical drawings for both machine main chambers and all surrounding custom optical breadboards. **Appendix H** shows the AR curves for viewports that are on attached to the machines. **Appendix I** includes technical drawings for several custom parts I designed for the machines. **Appendix J** is the result of a day-long discussion with a scientist at Pacific Laser Equipment, detailing how to operate their waveplate rotators. **Appendix K** discusses what happened when our chiller failed in November 2018, and what we did to diagnose and fix it. **Appendix L** is a visual guide to the machine, intended for an incoming student to help them find their way around. **Appendix M** includes much of the information I have gathered from working with the strontium SHG 461 nm laser over the past seven years, including when to switch out desiccant, how to realign and reoptimize the cavity, and what to do when it's generally making you sad.

1.3 Permissions and Attributions

1. Much of the theory included in this dissertation was adapted from Atomic Physics by Christopher Foot [14], Bose-Einstein Condensation in Dilute Gases by C.J. Pethick and H. Smith [15], Advances in Atomic Physics by Cohen-Tannoudji and Guery-Odelin [16], and course notes from 8.421 at MIT [17].

2. Many of the experimental parameters for the lithium machine came from Zachary Geiger's and Kevin Singh's theses [18, 19].

3. The theses of Florian Schreck [20] and Simon Stellmer [21] were reference guides when we were building the machines, and remained so as I wrote this.

4. The content of Chapter 6 is the result of a collaboration with Cora J. Fujiwara,

Ruwan Senaratne, Kevin Singh, Zachary A. Geiger, and David M. Weld, and has previously appeared in *Annalen der Physik*. It is reproduced here with the permission of http://wileyrights.gms.sg/wiley_content.php.

5. The content of Chapter 7 is the result of a collaboration with Ruwan Senaratne, Toshihiko Shimasaki, Peter E. Dotti, Cora J. Fujiwara, Kevin Singh, Zachary A. Geiger, and David M. Weld, and has previously appeared in *Nature Communications*. It is reproduced here with the permission of SpringerNature: http://nature.com/reprints/permission-requests.html.

6. The content of Chapter 8 is the result of a collaboration with Toshihiko Shimasaki, Peter E. Dotti, Ruwan Senaratne, Mantas Raciunas, André Eckardt, and David M. Weld.

7. The content of Appendix D is the result of a collaboration with Alexandre Cooper-Roy and Ruwan Senaratne.

Chapter 2

Some General and Relevant Theory

This chapter is certainly not meant to replace any number of excellent textbooks; rather, it includes a (very) bare minimum set of ideas I found important to getting started in AMO research. It is meant as a quick reference for the scientific and experimental content of Chapters 3, 4, and 5, chapters in which I try to keep equations to a minimum. It follows content from Atomic Physics by Christopher Foot [14], Bose-Einstein Condensation by Pethick and Smith [15], and notes from my undergraduate AMO course [17], into all of which I highly recommend diving.

2.1 Atoms

In order to cool and manipulate internal and external atomic degrees of freedom, one must first know some things about atoms. These things include, but are not limited to, internal states and level structure, Zeeman shifts, scattering, and properties at degeneracy. This section is intended as a brief and general overview of these topics; any discussion specific to lithium or strontium may be found in Chapter 3.

2.1.1 Internal states and level structure

In order to calculate wavefunctions, we need to solve the Schrodinger equation:

$$\left(-\frac{\hbar^2}{2m}\nabla^2 + V(r) \right)\psi = E\psi \tag{2.1}$$

In undergraduate quantum mechanics, we learn to solve this equation for the hydrogen atom and perhaps the helium atom because the potential $V(r)$ takes rather simple forms. However, it becomes impossible to analytically solve the Schrodinger equation for more complicated atoms due to nuclear screening and more complicated electron-electron interactions. Instead, since we typically work with alkali or alkaline earth atoms in AMO experiments, we use the hydrogenic or helium-like wavefunctions as ansatzes to numerically solve for the eigenenergies of more complicated atoms.

Recall that the hydrogenic wavefunctions, tensor-producted with the electronic spin, take the form

$$\psi = R_{n,l}(r)Y_{l,m_l}(\theta,\phi)|s\ m_s\rangle \tag{2.2}$$

defined by quantum numbers n (the principal/motional state), $\mathbf{l}$ (the orbital angular momentum), $\mathbf{S}$ (the spin angular momentum), and m_l and m_s (the projections of $\mathbf{l}$ and $\mathbf{s}$ along the z-axis). We can consider the approximation that the nucleus and the electronic spin do not interact; this is called the central field approximation, and we can use it to calculate the non-spin part of Ψ, $R_{n,l}Y_{l,m_l}$ without use of any perturbation theory. Under this central-field splitting, states are then identified only by quantum numbers n and $\mathbf{l}$. NB: we typically use $\mathbf{L}^2 = \hbar^2 l(l+1)$ and $\mathbf{S}^2 = \hbar^2 s(s+1)$ in notation instead.

We can then consider the effects of spin-orbit coupling, which arises from the fact that charged particles with angular momentum have a magnetic dipole moment. The proportionality constant between the angular momentum α ($\alpha = \mathbf{L}$, $\mathbf{S}$, ...) and the resulting dipole moment is typically referred to as the Lande g-factor, g_α. The spin-orbit coupling Hamiltonian $H_{so} \propto \mathbf{L}\cdot\mathbf{S}$. In the process of calculating the resulting energy shifts,

it is useful to define quantum number $\mathbf{J} = \mathbf{L}+\mathbf{S}$, the total angular momentum, which may take various values depending on the magnitudes and relative orientations of L and S. The energy splittings between different J-values are called fine-structure splittings. Each J state has $(2J+1)$ possible projections m_J, which are degenerate without a magnetic field. L, S, J, and m_J are good quantum numbers in the LS-coupling scheme, and states may be written in Russell-Saunders notation: $n^{2S+1}L_J$.

It is worth briefly noting that there are some cases where the spin-orbit interaction cannot be treated as a perturbation on the central-field energy; such is the case with many heavier atoms like dysprosium. The energy levels of such atoms must be described using different coupling schemes, such as jj-coupling.

We can go one step further and consider interactions between $\mathbf{J}$ and the nuclear angular momentum, $\mathbf{I}$, for which the Hamiltonian $H_{HFS} = A\mathbf{I}\cdot\mathbf{J}$ where A is the hyperfine constant. In the process of calculating the hyperfine energy shifts, it is useful to define another new quantum number, $\mathbf{F} = \mathbf{I} + \mathbf{J}$; the various values of F represent splitting of the fine structure manifold into hyperfine structure; each F splits further into $(2F+1)$ projections m_F which are degenerate at zero field. Good quantum numbers in the hyperfine coupling scheme include I, J, F, and m_F. We typically only consider one species at a time, so $\mathbf{I}$ is constant. We refer to the $\mathbf{J}$ quantum number (the fine-structure manifold) using Russell-Saunders notation, and simply write states in the basis $|F, m_F\rangle$.

There are a number of other level shifts in atoms: relativistic corrections to the electronic kinetic energy, the Lamb shift (due to interactions with the vacuum energy), the Darwin term (due to an effective potential from the uncertainty in electron position), the quantum defect (due to effective shielding of the nuclear potential from inner-shell electrons), and isotope shifts (due to changes in the nuclear mass and resulting changes of the finite nuclear size). These shifts are discussed in detail in a number of sources far better than this one.

The descriptions of the forest of internal electronic states is very useful to understand

atomic energy splittings from a qualitative perspective. However, since calculations of all of these splittings are based on wavefunctions which become more and more approximate as the atomic number increases, we expect the calculated energies to deviate from the actual energies. For lithium, strontium, and any other atom one might wish to cool, we depend on empirical measurement to ascertain the full energy spectrum.

2.1.2 Zeeman shifts

Many of the splittings above resulted from interactions between the atom and its internal magnetic fields. The Zeeman effect, in contrast, describes energy splittings due to interactions between the atom and an external magnetic field B. Fine structure Zeeman splitting arises from interactions between J and B; in the low-field regime, where the Zeeman splitting is smaller than the fine splitting, the energy shift for a state m_J is given by

$$E_{ZE,FS} = g_J m_J \mu_B B, \tag{2.3}$$

where μ_B is the Bohr magneton and g_J is the Lande g-factor associated with the J manifold:

$$g_J = \frac{3}{2} + \frac{S(S+1) - L(L+1)}{2J(J+1)}. \tag{2.4}$$

We can similarly consider hyperfine structure Zeeman splitting, arising from interactions between F and B; in the low-field regime, where the Zeeman splitting is smaller than the hyperfine splitting, the energy shift for a state m_F is given by

$$E_{ZE,HFS} = g_F m_F \mu_B B, \tag{2.5}$$

where μ_B is the Bohr magneton and g_F is the Lande g-factor associated with the F manifold:

$$g_F = g_J \frac{F(F+1) - I(I+1) + J(J+1)}{2F(F+1)} \quad + g_I \frac{F(F+1) + I(I+1) - J(J+1)}{2F(F+1)}. \quad (2.6)$$

If the coupling between the external field and fine states (hyperfine states) becomes large enough to disrupt coupling between **L** and **S** (**I** and **J**), the splittings become very different. Due to that decoupling, $|J, m_J\rangle$ ($|F, m_F\rangle$) are no longer good quantum numbers, and we instead need to use $|m_L, m_S\rangle$ ($|m_I, m_J\rangle$). This is called the Paschen-Back effect. We will find that this regime becomes relevant for lithium in the presence of magnetic fields which cause Zeeman shifts larger than the hyperfine energy splitting of 800 MHz.

2.1.3 Scattering

Background scattering lengths

Evaporative cooling is driven by elastic collisions between atoms, the rate of which is set by the atomic scattering cross section. Atomic scattering between two colliding particles reduces to a single particle with reduced mass scattering off of the molecular potential of the two atoms. We treat this particle as a scattered wave with incoming and outgoing components:

$$\psi = e^{ikz} + f(\theta)\frac{e^{ikr}}{r} \quad (2.7)$$

where $f(\theta)$ is the scattering amplitude and k is the magnitude of the scattering wave vector.

At long range ($r \to \infty$), the only effect of the potential on the wave is an overall phase shift δ_l relative to a wave scattered off of a point. We can treat the complicated molecular potential, then, as a hard sphere with radius a which induces the same phase

shift as that potential. If the potential is treated isotropically in the radial dimension, we can expand the wavefunction of the scattered particle in terms of axially-symmetric states:

$$\psi = \sum_{l=0}^{\infty} A_l P_l(\cos\theta) u_{kl}(r) \tag{2.8}$$

where l is the partial-wave angular momentum and $u_{kl}(r)$ is some radially-symmetric wavefunction which includes the phase shift. We can plug this ansatz into the radial Schrodinger equation

$$\left(\frac{d^2}{dr^2} + \frac{2}{r}\frac{d}{dr} + k^2 - \frac{l(l+1)}{r^2} - \frac{2m}{\hbar^2}V(r)\right)u_{kl}(r) = 0 \tag{2.9}$$

and solve for $f(\theta)$ to find the scattering cross section.

If $l > 0$, we see that there is an additional centrifugal potential barrier in the Schrodinger equation. This implies that for low-energy collisions, the scattering wavefunction will reflect off of this barrier without any phaseshift. Thus, at the low energies found in cold atom experiments, the only significant cross-section contributions come from s-wave (l=0) scattering.

The effective hard-sphere radius a which gives rise to phaseshift δ_0 is defined as the scattering length

$$a = -\lim_{k\to 0}\frac{\delta_0(K)}{k}, \tag{2.10}$$

and the scattering cross section for indistinguishable particles is calculated to be $\sigma = 8\pi a^2$. A full and excellent treatment of the scattering problem may be found in [15], among other great resources; Ruwan Senaratne also includes a nice treatment of it in his thesis [22].

A positive scattering length denotes repulsive interactions while negative a denotes attractive interactions; note that the scattering rate, dependent only on cross section σ, is the same for attractive and repulsive interactions as long as the magnitude of a is

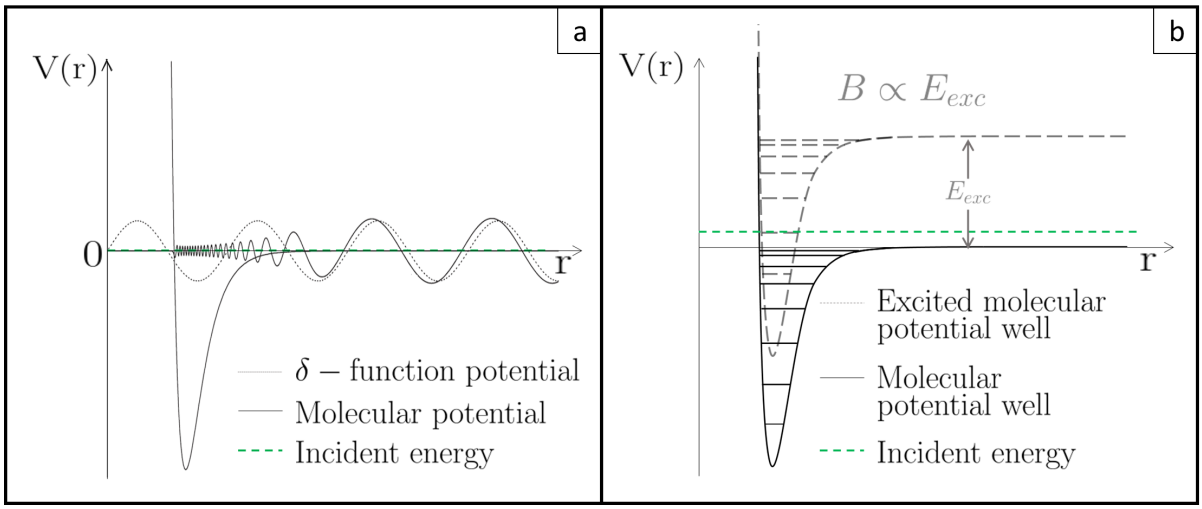

Figure 2.1: **a**: Non-resonant scattering. The incident waves are depicted after scattering off of a δ-function at r=0, compared to scattering off a molecular potential. At large r, the only difference is a phase shift. **b**: Resonant scattering due to a Feshbach resonance. In the drawing, the incident energy of the scattering wave is resonant with a bound state of a higher-lying molecular potential, which can be tuned via a B-field.

the same. Background scattering interactions between particles give rise to an overall effective potential in an atomic cloud. This potential, termed the "mean-field" potential, is dependent on the atomic density n and scattering length a at low energies, and gives rise to an expansion of the cloud size in the case of repulsive interactions:

$$U_{MF} = \frac{8\pi\hbar^2 an}{m} \equiv gn. \tag{2.11}$$

The mean-field interaction can lead to instability of the cloud size or formation of a soliton for attractive interactions [23].

Feshbach resonances

This discussion so far has been relevant to the calculation of background scattering rates, and I noted in the previous section that the molecular potential of the two colliding particles can often be simplified to a hard-sphere potential. There are cases where this is not true; one of the most useful exceptions occurs when an excited-state molecular

potential has a bound state close to the energy of the colliding atoms. The atoms virtually enter the bound state to form an excited molecule before decaying back to free atoms; during this process, the accumulated phaseshift can be very large. The relative energy of that bound state can be tuned through zero by using a magnetic field.

The functional form of a Feshbach resonance is given by

$$a(B) = a_{bg}\left(1 - \frac{\Delta}{B - B_0}\right). \tag{2.12}$$

This means that as a function of B, we can tune a from $-\infty$ to $+\infty$. The functional form is approximate, and describes the scattering length very well near the resonance but less well away from it. For an example of this, please see Fig. 3.3.

2.1.4 Bosonic degeneracy

This subsection contains a brief overview of properties of bosonic quantum gases. It does not touch on degenerate Fermi gases; however, most good AMO texts, as well as the Schreck thesis [20], have excellent discussions about both bosons and fermions.

Non-interacting Bose gases

Bosons can all occupy the same energy state, unlike fermions. This fact may be used to derive the Bose-Einstein distribution, the mean occupation number of a state with energy ε:

$$f_{BE}(\varepsilon) = \frac{1}{e^{(\varepsilon-\mu)/kT} - 1}. \tag{2.13}$$

μ here is the chemical potential, which is determined by the total number of particles N and the temperature T. We can also determine the density of states for an anisotropic 3-d harmonic oscillator with frequencies (ω_x, ω_y, ω_z), which is a good approximation for a crossed optical dipole trap:

$$V = \frac{1}{2}m(\omega_x^2 x^2 + \omega_y^2 y^2 + \omega_z^2 z^2). \tag{2.14}$$

The density of states with energy less than ε is given by

$$g(\varepsilon) = \frac{\varepsilon^2}{2\hbar^2\omega_x\omega_y\omega_z}. \tag{2.15}$$

We can use this to calculate the transition temperature to a Bose-Einstein condensate (BEC), which is the highest temperature at which we should be able to observe macroscopic occupation of the ground state. The transition temperature is the temperature at which all of the particles can be accomodated in excited states. Since we want to be able to add a particle without additional energy cost, we set μ =0 and use

$$N = \int_0^\infty d\varepsilon g(\varepsilon) \frac{1}{e^{\varepsilon/kT_C} - 1} \tag{2.16}$$

to find

$$kT_C = \frac{\hbar(\omega_x\omega_y\omega_z)^{1/3}N^{1/3}}{[\zeta(3)]^{1/3}} \tag{2.17}$$

where ζ is the Riemann zeta function. The critical transition temperature for Bose-condensation of ^{7}Li in our 3D anisotropic harmonic trap, assuming 2×10^5 atoms, is around 700 nK; the critical transition temperature for Bose-condensation of ^{84}Sr in our 3D anisotropic harmonic trap, assuming 8×10^4 atoms, is around 150 nK.

Eq. 2.17 can be usefully recast to write the fraction of total atoms in the ground band:

$$\frac{N_0}{N} = 1 - \left(\frac{T}{T_C}\right)^3. \tag{2.18}$$

It is useful to introduce the de Broglie wavelength $\lambda_D B^3 = (2\pi\hbar/mk_BT)^{3/2}$, which can be thought of as a metric of density in momentum space. This can be combined with the density in real space to give the phase space density n,

$$\rho = n\lambda_{DB}^3, \tag{2.19}$$

which is of order unity at the BEC phase transition.

Interacting Bose gases

It is possible, in some atoms with very low or tunable scattering lengths, to have a BEC which is non-interacting. However, it is much more common for the atoms in a BEC to interact, giving rise to superfluidity. It is simplest to treat the interacton between particles, to 0th order, using a mean-field approach (see Eq. 2.11). That equation describes mean-field interactions in momentum space (as a constant), but may be recast in real space as a contact interaction: $U_{MF}\delta(\vec{r}-\vec{r'})$ for particles at $\vec{r}$ and $\vec{r'}$. This term can be added to the Hamiltonian with the density recast in terms of the wavefunction ($n(\vec{r}) = |\psi(\vec{r})|^2$), and used to write the time-dependent Schrodinger equation. With the proper choice of global phase of the wavefunction, this simplifies to the time-dependent Gross-Pitaevskii equation (GPE):

$$\mu\psi(\vec{r}) = \left(-\frac{\hbar^2}{2m}\nabla^2 + V_{ext}(\vec{r}) + g|\psi(\vec{r})|^2 \right)\psi(\vec{r}) \tag{2.20}$$

where μ is the chemical potential. This equation can be simplified yet further if we make the approximation that the mean field energy is much greater than the kinetic energy; this is known as the Thomas-Fermi approximation, and is valid for sufficiently large, cold clouds. The solution to the GPE is then simply

$$n(\vec{r}) = \frac{\mu - V_{ext}(\vec{r})}{g}, \tag{2.21}$$

which shows that the boundary of the cloud is simply set by $\mu = V_{ext}$. Since our traps can often be approximated by harmonic potentials, this sets a Thomas-Fermi radius: $R^2_{i,TF} = 2\mu/m\omega_i^2$. We can solve for μ using the constraint that the integral of the density over all space is equal to the total number of atoms, finally giving a Thomas-Fermi radius in direction i:

$$R_i^2 = \frac{\hbar\bar{\omega}}{m\omega_i^2}\left(\frac{15Na}{\bar{a}}\right)^{2/5} \tag{2.22}$$

where a is the scattering length and $\bar{a}$ and $\bar{\omega}$ are the geometric means of $a_i = (\hbar/m\omega_i)^{1/2}$ and ω_i along each trap direction. This spatial extent is useful to calculate how interaction rates are affected by various densities and trap geometries.

2.2 Atom-Photon Interactions

Many cooling processes are driven by atom-photon interactions, which allow us to control both internal and external atomic degrees of freedom.[1] The photons relevant to our experimental work are typically monochromatic, but their frequencies range from microwave/RF to optical. Light interacts with neutral atoms in one of two ways. The first is radiative: atoms can absorb and spontaneously emit light if the photon energy is near an optical transition. The first three subsections are dedicated to these dissipative processes which can be used for cooling. The second is a conservative interaction arising from atomic dipole moments induced by external fields; the resulting interactions between the dipoles and the fields themselves can create conservative trapping potentials. The rest of the section will discuss these types of interactions.

The basics of radiation interacting with a two-level system—Fermi's Golden Rule, electric field perturbations, the rotating wave approximation, Einstein A and B coefficients, Rabi oscillations, and the optical Bloch equations—are typically treated in a course at some point during an undergraduate and/or graduate physics education; I leave it to the reader to familiarize themselves with those ideas, as they are the bedrock on which AMO physics stands (and they're fun to learn about!). In this section, I instead will provide a few definitions for experimentally-relevant parameters, and then discuss cooling methods.

[1] Underrated band name.

2.2.1 Optical transitions

Every optical transition between two states has a well-defined natural linewidth which is related to the lifetime of the excited state prior to decay to the ground state. This lifetime, τ, is fundamentally set by spontaneous emission; the coupling of the state to vacuum modes is dependent on the atomic transition frequency as well as the frequency and polarization of the emitted photon. Since the lifetime of the excited state is finite, there is uncertainty of the energy difference between the ground and excited states. This results in natural radiative broadening of the transition frequency into a Lorentzian lineshape. We call the width of this Lorentzian the linewidth, Γ.

It is useful to define a saturation intensity, I_{sat}. It is useful to think about this in a schematic way; imagine a beam of monochromatic radiation impinging on a slab of atoms in a direction z. This light will be attenuated as it permeates through the slab:

$$\frac{dI}{dz} = -\kappa(\omega)I(\omega). \tag{2.23}$$

κ is determined by absorption and emission at rates set by the optical cross section and spontaneous emission. I_{sat} is the impinging intensity (at the atomic resonance frequency) which causes κ to attenuate by a factor of two; it is given by

$$I_{sat} = \frac{\pi hc}{3\tau\lambda^3} \tag{2.24}$$

for resonant transition wavelength λ.

We now know some quantitative properties of the transitions. By standing on the shoulders of spectroscopic giants of decades past, we know the absolute frequency of light needed to drive a given transition. From the linewidth, we know how precise that frequency needs to be to drive the transition, and approximately how much optical power will be necessary to do so efficiently. We can use these tools to buy or build appropriate monochromatic light sources (lasers or RF sources), and begin to laser-cool our atoms.

2.2.2 Radiative trapping and cooling

There are a number of radiative cooling techniques which have made it possible to achieve atomic temperatures in the μK regime. The most ubiquitous of these is Doppler cooling.

Doppler cooling

If an atom in the lab frame is traveling with some velocity v and interacts with radiation at frequency ω_0, in the atomic frame of reference, the light will be Doppler-shifted to $\omega' = \omega_0 - kv$ where k is the radiation wavevector. We can use this fact to our advantage, detuning the light by exactly $\delta = -kv$ (red detuning) such that an atom traveling towards the light will see a resonant frequency.

Radiation carries momentum. It follows from momentum conservation that absorption and emission events involve momentum exchange between the photon and the atom, and this momentum exchange can exert a force on the atoms. The total force which can be exerted depends on the momentum of the photons, $\hbar k$ where k is the wavevector, as well as on the spontaneous scattering rate:

$$F_{scatt} = \hbar k \frac{\Gamma}{2} \frac{I/I_{sat}}{1 + I/I_{sat} + 4\delta^2/\Gamma^2}. \tag{2.25}$$

The maximum force imparted to the atoms by spntaneous scattering events is $F_{max} = \hbar k\Gamma/2$, which defines a maximum radiative acceleration (or deceleration) based on Newton's Second Law,

$$a_{max} = \frac{\hbar k \Gamma}{2m}. \tag{2.26}$$

When an atom spontaneously emits a photon, it does so isotropically in space. However, because we have red-detuned the radiation, we have velocity-selected the atoms which see the light as resonant such that they preferentially recoil against their direction of motion. This effectively slows the atom by the recoil velocity, $v_{rec} = \hbar k/m$, for every scattering event. Because scattering rates scale as Γ, which is typically in the range of

1 MHz for alkali atoms, this cooling can be quite effective.

The spontaneous emission of the photon occurs isotropically, implying that the emission process does not impart any mean velocity to the atom. However, the mean squared velocity is nonzero, and scales with the number of scattering events. This leads to a fundamental limit on Doppler cooling: $T_{Dopp} = \hbar\Gamma/2k_B$.

Doppler cooling can be very effective in optical molasses configuration, shown in Fig. 2.2a, with 3 standing waves of red-detuned light in all the three Cartesian dimensions. The resulting force on the atoms can be written

$$F_{molasses} \approx -2\frac{dF_{scatt}}{d\omega}kv = -\alpha v. \tag{2.27}$$

In this form, it becomes clear that the light is acting as a damping force on the atom.

Since the light is cooling the atoms, the velocity distribution gets shifted to lower velocities. This raises an issue with this cooling technique: once the atoms are slowed, the Doppler shift changes and the atoms are no longer resonant with the light. Two approaches are often used to overcome this. The first is chirped cooling, which requires fast sweeps of the frequency detuning and is only effective on atoms which arrive at the slower at the appropriate time. The second (more common) method is to hold the detuning constant and use a spatially-varying Zeeman shift to compensate the changing Doppler shift. The velocity of the atoms which start at v_{max} at $z = 0$ and end at 0 m/s under constant acceleration a is given by

$$v(z) = v_{max}\left(1 - \frac{2az}{v_{max}^2}\right)^{1/2}. \tag{2.28}$$

However, we do not typically need to slow atoms all the way to 0 m/s, but only to a reasonable capture velocity for a magneto-optical trap (typically around 50 m/s):

$$v(z) = (v_{max} - v_c)\left(1 - \frac{2az}{v_{max}^2 - v_c^2}\right)^{1/2} + v_c. \tag{2.29}$$

We typically assume that the acceleration a is $a_{max}/2$ or $a_{max}/3$ to provide a safety

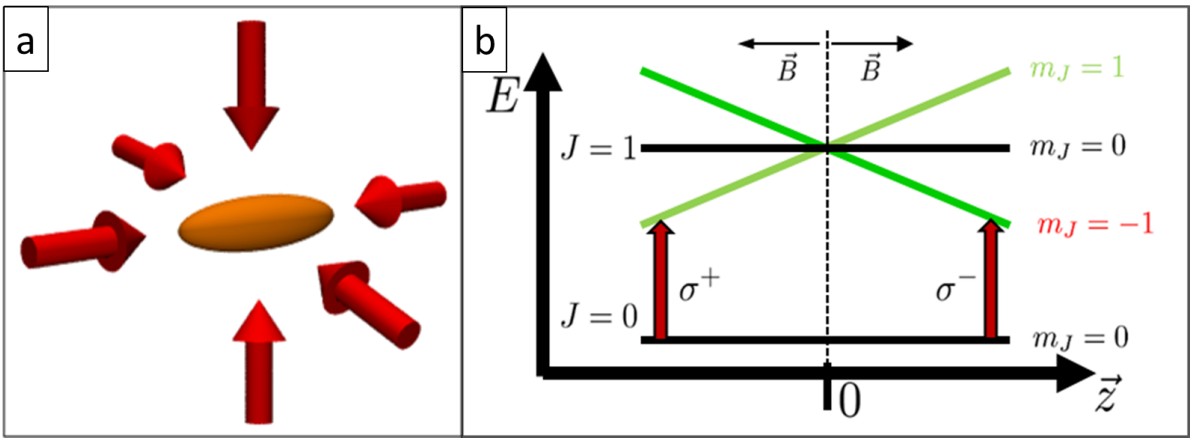

Figure 2.2: **a**: Red-detuned light in three standing waves along Cartesian dimensions creates an optical molasses. **b**: A magneto-optical trap is created by using a linear field gradient (from anti-Helmholtz coils) and optical molasses with red-detuned circularly-polarized light.

factor for the slower length. The functional form of the magnetic field $B(z)$ needed to compensate this shift is

$$\mu_B(g'_J m'_J - g_J m_J)(B(z) - B_{\text{bias}}) = kv(z) \tag{2.30}$$

at which point solenoids can be designed to match this design field as closely as possible.

Magneto-optical traps (MOTs)

Doppler cooling is a very efficient cooling technique, but is not enough by itself to trap atoms. A trap is simply a spatially-varying energy. This is excellent news, because we can use the Zeeman effect to our advantage once more. We need to create a magnetic field gradient, such that B is zero at the trap center and increases linearly outwards in space. This is possible to achieve by using two coils in anti-Helmholtz configuration, where the coil separation z is equal to the coil radius r. This creates a quadrupolar field, with confinement twice as strong along the z-axis as along x or y. Along any direction, the field, and therefore Zeeman energies, change linearly in space (Fig. 2.2b). Now we can preferentially address Zeeman sublevels by using red-detuned circularly-polarized light:

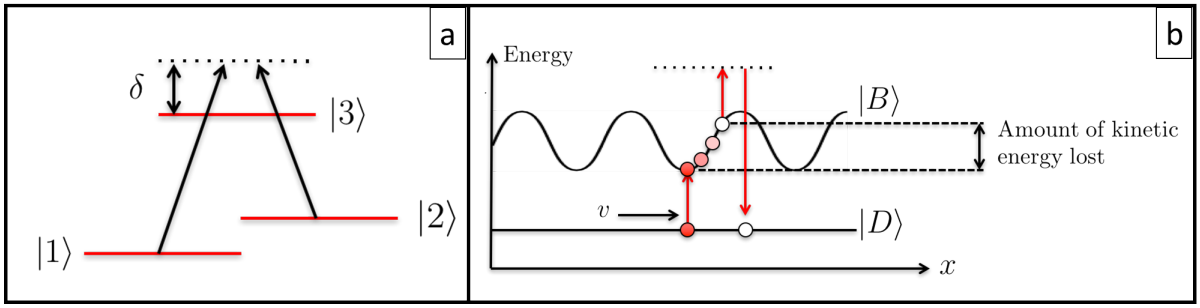

Figure 2.3: **a**: Raman transitions for a λ scheme. **b**: Sisyphus-like cooling in the Raman-dressed atom picture.

the light is only resonant with the atoms at a certain radius from the trap center which are traveling with a certain velocity. Since the force exerted on the atoms is dependent on both position and velocity, the MOT allows simultaneous trapping and cooling of the atoms. Using 6 beams to create an optical molasses in the presence of the anti-Helmholtz field allows us to form a 3d magneto-optical trap, the temperature of which is limited by the Doppler limit.

Sub-Doppler cooling

There are various ways to get around the Doppler cooling limit, including Sisyphus (polarization gradient) cooling. Here I will briefly discuss gray molasses, which works extremely well for alkalis which do not have a well-resolved hyperfine structure. It was first demonstrated for lithium in 2013 [24, 25].

Gray molasses utilizes Raman transitions, two-photon transitions involving simultaneous absorption and stimulated emission by an atom. A Λ scheme is shown in Fig. 2.3a; there are two ground states and an excited state, with allowed optical transitions $1 \rightarrow 3$ and $2 \rightarrow 3$. Intense beams of opposite polarizations form polarization-gradient standing waves in three dimensions. They are set at a blue detuning from the transition frequency which is large compared to the transition linewidth; this light induces a coupling between each ground state and the excited state. We can consider these states in a dressed-atom

picture, accounting for photon coupling. The excited state 3 is unperturbed, but other two states are now orthogonal superpositions of the ground states, once of which couples to the light and one of which does not. We call the former the bright state B, and the latter the dark state D. The bright state sees a pronounced spatially-dependent light shift, while the dark state does not. The energy levels are shown in Fig. 2.3b. This system now behaves very similarly to Sisyphus cooling. Since the bright and dark states are not eigenstates of the kinetic energy operator, they are allowed to weakly couple to each other; this effect is most pronounced at bright state energy minima. Two-photon transitions from the bright state to the dark state are only allowed near bright state energy maxima, due to the polarization gradient. The end result is that the atoms have to climb potential hills, losing kinetic energy in the process.

2.2.3 Magnetic trapping and cooling

Creating a magnetic trap for low-field-seeking states involves making a magnetic field gradient which increases in magnitude away from the trap center. Historically, this has been done using a variety of traps: Ioffe-Pritchard traps, TOP traps, QUIC traps, etc, each with pros and cons. We accomplish this using two coils in anti-Helmholtz configuration, which creates a linear gradient. The spatial distribution of atoms in this trap can be approximated as a Gaussian, but actually deviates slightly; the Fujiwara thesis details the functional form of the atomic distribution. Once the atoms are trapped, it is common to perform forced evaporative cooling from the trap by inducing RF transitions to antitrapped states. However, evaporative cooling depends on atomic thermalization, and there are a number of loss processes with which the elastic scattering rate has to compete.

Atomic momenta and scattering lengths can be used to calculate the scattering cross section σ; the momenta in a magnetic trap typically take the form of a distribution based

Collision type	Dependence on density n_0
Background collisions	1
Majorana spin-flips	n_0
Elastic collisions	n_0^2
Spin-exchange collisions	n_0^2
Dipolar relaxation	n_0^2
Three-body spin exchange	n_0^3

Table 2.1: Collisions in the magnetic trap

on temperature. The elastic scattering rate then follows from the atomic number density N, temperature T, and magnetic field gradient G:

$$\Gamma_{el} = \frac{N}{32\pi}\left(\frac{g_F m_f \mu_B G}{k_B T}\right)^3 \sigma(k)\sqrt{\frac{3k_B T}{m}}. \tag{2.31}$$

This scattering rate needs to compete with inelastic processes: background losses, dipolar relaxation, spin-exchange collisions, and 3-body losses. A comparison of the dependence of each loss rate on density is given in Table 2.1. Background gas collisions are independent of density, and we can work in extremely good vacuum to try to mitigate this. We can minimize spin-exchange collisions by working in a stretched state, and since three-body losses go as n_0^3, we can work at densities at which they are suppressed. Dipolar relaxation is the dominant loss process, but we have found that our evaporation proceeds smoothly at the densities we use.

The other large loss rate comes from Majorana spin flips. One of the negatives of using a quadrupolar field is that the magnitude of the field goes to zero at the trap center. Since there is no well-defined quantization axis, atoms are free to make non-adiabatic transitions to magnetically-untrapped states. We can mitigate these loss processes by shining a blue-detuned "plug" beam to repel atoms from the center of the trap via the AC Stark shift, which will be discussed in Section 2.2.4.

2.2.4 Optical trapping and cooling

This discussion will refer to the excellent treatment in [26] regarding dipole forces in optical traps.

Any monochromatic light field carries with it an oscillating electric field with magnitude E at some frequency ω. We can model the atom as an oscillator; the external field will induce a atomic dipole moment which oscillates at ω with a strength proportional to E:

$$d = \alpha E. \tag{2.32}$$

The proportionality constant, α, is called the complex polarizability of the atom, and in general depends on ω. The real part of alpha is proportional to the potential energy of the atom in the light field, while the imaginary part is proportional to the spontaneous scattering rate of the atoms in the light field. The interaction between **d** and **E** results in a potential proportional to their dot product; this can be rewritten in terms of the light intensity I

$$U_{dip} = \frac{1}{2\epsilon_0 c} Re(\alpha) I. \tag{2.33}$$

The spontaneous scattering rate may be written as

$$\Gamma_{sc} = \frac{1}{\hbar\epsilon_0 c} Im(\alpha) I. \tag{2.34}$$

The polarizability can be calculated by modeling the atom as a two-level quantum system interacting with a classical field, and is dependent on a damping Γ due to spontaneous decay from the excited state:

$$\Gamma = \frac{\omega_0^3}{3\pi\epsilon_0\hbar c^3} |\langle e|\mu|g\rangle|^2. \tag{2.35}$$

Using a damped oscillator ansatz for α and making the rotating wave approximation,

we find approximate analytic forms for the dipole potential and scattering rate:

$$U_{dip} = -\frac{3\pi c^2}{2\omega_0^3}\frac{\Gamma}{\Delta}I \tag{2.36}$$

and

$$\Gamma_{sc} = -\frac{3\pi c^2}{2\omega_0^3}\left(\frac{\Gamma}{\Delta}\right)^2 I. \tag{2.37}$$

We have defined $\Delta \equiv \omega - \omega_0$ as the detuning of the light frequency from the atomic resonance. We see that if Δ is large, the scattering rate falls off more quickly than the dipole potential, which is favorable for trapping. We also see that if the laser is blue-detuned ($\Delta > 0$), the sign of the potential is positive (repulsive), while a red-detuned beam ($\Delta < 0$) results in an attractive potential.

The simplest optical potentials take the form of a TEM_{00} Gaussian mode with a power P and a minimum waist w_0. The intensity profile of this beam is given by the function

$$I(r,z) = \frac{2P}{\pi w^2(z)} e^{-2(r^2/w^2(z))} \tag{2.38}$$

where $w(z) = w_0(1 + (z/z_R)^2)^{1/2})$ and z_R is the Rayleigh range. This yields a potential that looks like

$$U(r,z) = \frac{-U_0}{1 + (z/z_R)^2} exp\left(\frac{-2(r/w_0)^2}{1 + (z/z_R)^2}\right). \tag{2.39}$$

However, at the center of the potential and at nearby low energies, we can expand this up to 2nd order to approximate the gaussians in each direction as parabolas with maximum depth U_0, and solve for trap frequencies $\omega_r = (4U_0/mw_0^2)^{1/2}$ and $\omega_z = (2U_0/mz_R^2)^{1/2}$. For multiple intersecting 1D optical dipole traps, the 1D trap frequencies along each direction may be added in quadrature to get the total trap frequency.

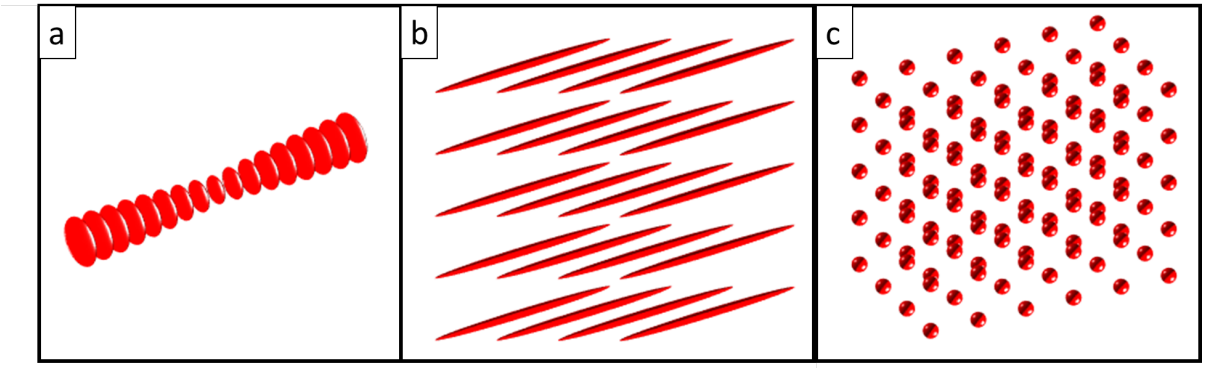

Figure 2.4: Optical lattices formed from interference of light in 1d (**a**), 2d (**b**), and 3d (**c**).

2.2.5 Optical lattices

Two counter-propagating optical dipole traps at the same frequency interfere to form a standing wave of light (this can be easily done using a retroreflecting mirror). In one dimension, the resulting potential looks like a series of stacked pancakes. Lattices may be extended to 2 or 3 dimensions, with resulting potentials of tubes or a 3d lattice. These potentials can be (kind of) visualized in Fig. 2.4. The potential formed from a 1d lattice is

$$U(r,z) = -U_0\, e^{-2(r^2/w_0^2)}\, \sin^2(kz), \tag{2.40}$$

where U_0 is usually expressed in terms of the recoil energy $E_R = \hbar^2 k^2/2m$ (ignoring axial harmonic confinement, which is typically weak). The eigenstates of this potential are called Bloch states; they are the product of a plane wave and a function which has the same periodicity of the lattice:

$$\varphi_q^{(n)}(z) = e^{iqz/\hbar}\, u_q^{(n)}(z) \tag{2.41}$$

where q is the quasimomentum[2] and n is a band index. Using these wavefunctions to solve the Schrodinger equation, we calculate energy eigenstates which are shown in

[2]Just as momentum is conserved in cases of continuous spatial translation symmetry, quasimomentum is conserved in cases of discrete spatial translation symmetry imposed by the lattice.

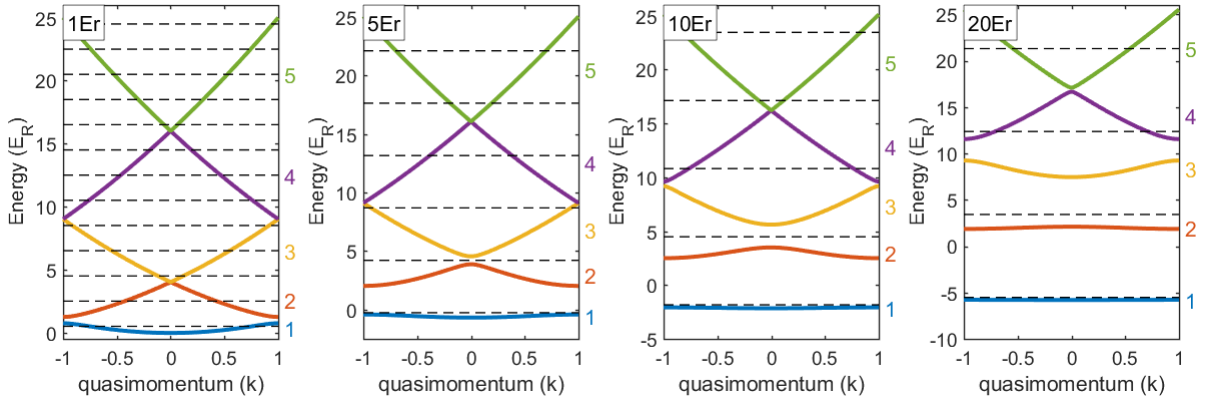

Figure 2.5: Eigenenergies for optical lattices exhibit band structure. The first 5 bands are shown for increasing lattice depths. The lattice well can be approximated as a harmonic oscillator potential; the dashed lines indicate eigenenergies of that approximate potential.

Fig. 2.5 for a full Brillouin zone (set by the reciprocal lattice vectors).

It is worth noting that Bloch states are completely delocalized in lattices. They can be used to construct another set of basis states, Wannier states, which are superpositions of Bloch states that are maximally localized to individual lattice sites. Wannier states are the basis in which many important lattice parameters, such as tunneling rates and local particle interactions, are calculated. There is an excellent MATLAB codebase for calculating Wannier states and lattice parameters, which has been invaluable to us [27].

Periodic lattice modulation

Periodic lattice modulation (amplitude or phase) creates perturbations (with even or odd parity, respectively) near the lattice minima which can allow couplings between different bands. As long as the quasimomentum is conserved, atoms (which often start in the ground band as they are adiabatically-loaded BECs) are allowed to transition to excited bands. Transitions to bands with the same (different) parity as the initial band are much stronger for modulations with even (odd) parity, as long as quasimomentum spread of the BEC does not deviate too far from $k = 0$. This process may be thought of as a two-photon Raman process, in which the modulation puts sidebands on the lattice frequency

and atoms are allowed to absorb a photon from one sideband and emit into the other. The ability to modulate lattices can be highly useful. For example, by modulating the lattice at a range of frequencies and looking at populations of higher bands, one may calibrate the lattice depth.

One of the cleanest ways to extract band populations from data is to use a band-mapping procedure [28]. This process involves ramping down the lattice slowly with respect to the bandgap; this allows energy and quasimomentum in the lattice to map onto free-space momentum. Once the particles are free to expand in time-of-flight, the different momenta will map onto real space.

Kapitza-Dirac diffraction

We typically calibrate our lattice depth using Kapitza-Dirac diffraction, which is the diffraction of our coherent atomic state (a BEC) off of a "grating" made of a standing wave of light. During this process, a standing wave of light is pulsed for a short amount of time, during which momentum is transferred to atoms in a way which is quantitatively dependent on the lattice depth. The atoms expand in time-of-flight, and we extract the populations of each momentum state to calibrate the lattice depth.

Kapitza-Dirac diffraction can be most easily understood in the plane wave basis:

$$\psi(t) = \sum_n \eta_n(t) e^{2\pi i k z} \qquad (n = 0, \pm 1, \pm 2, ...) \tag{2.42}$$

We can write the Hamiltonian (with a potential $U(z) = U_0 \cos^2(kz)$ pulsed for time τ) in this basis and introduce dimensionless parameters

$$\alpha = \frac{2E_R\tau}{\hbar} \tag{2.43}$$

$$\beta = \frac{U_0\tau}{\hbar}; \tag{2.44}$$

note that α is just pulse time in units of the 2-photon recoil time. We can write the

time-dependent Schrodinger equation as

$$i\frac{d\eta_n}{dt} = \frac{\alpha n^2 \eta_n(t)}{\tau} + \frac{\beta}{4\tau}(\eta_{n-1}(t) + 2\eta_n(t) + \eta_{n+1}(t)). \tag{2.45}$$

If τ is much shorter than the harmonic oscillation period $T_{ho} = \hbar/\sqrt{2U_0 E_R}$ (this is called the Raman-Nath regime), we can neglect the first term of the Schrodinger equation, which makes it much easier to solve; the resulting solution gives

$$\eta_n(t) = (-i)^n e^{-i\beta/2\tau} J_n(\beta t/2\tau) \tag{2.46}$$

where J_n are Bessel functions of the first kind. The population of the nth diffracted order is then proportional to J_n^2, and fitting this analytical form to our data allows us to extract β and thus U_0. It is worth mentioning that for very light atoms, it is experimentally difficult to operate in the Raman-Nath regime; for a lithium atom with a pulsed $10E_R$ lattice, the pulse needs to be less than 1.5μs. In this case, Kapitza-Dirac diffraction can still be used, but the full time-dependent Schrodinger equation must be solved to obtain solutions for $\eta_n(t)$.

Bichromatic lattices

One of the nice things about cold atom experiments is that it is almost as easy to generate a nontrivial lattice geometry as it is to create a trivial one. One of the potentials we consider in our experiments is the bichromatic lattice, which is very simply two lattices, each of a different color, superposed with each other. If the period ratio is rational, the unit cell of the lattice is finite. If the lattice vector corresponding to the new unit cell gets smaller, so does the Brillouin zone; the band structure gets more complicated due to new foldings in quasimomentum-space and the resulting avoided crossings. If the period ratio is irrational, two interesting things occur:

1. Since the potential never repeats, it displays quasiperiodic structure, which can be treated as a type of (not truly random) disorder. This means that we can study

physics related to Anderson localization.

2. The unit cell gets infinitely large, and it is impossible to define a band in the traditional condensed-matter sense.

In the tight-binding limit, the Hamiltonian for a bichromatic lattice may be written as

$$H = J\sum_{i=1}^{N} c_i c_{i+1}^{\dagger} + h.c. + \Delta\sum_{i=1}^{N} \cos(2\pi\alpha i + \varphi) c_i^{\dagger} c_i \tag{2.47}$$

where J is the tunneling matrix element, Δ is the disorder strength, α is the period ratio, and φ is the phase between the two lattices. Plotting the energy eigenstructure of this lattice as a function of α famously maps out the Hofstadter butterfly, and with open boundary conditions, edge states may be observed in the calculation, traversing between bands.

For an irrational α, this Hamiltonian exhibits an Aubry-André transition from delocalization to localization at $\Delta/J = 2$. In our experiment, we happen to use a 1064 nm lattice as our primary lattice, and a 915 nm secondary lattice as a perturbation. Fig. 2.6 shows contour lines for Δ/J for the ground band at various lattice depths.

One of the results of an infinite Brillouin zone is that the Hamiltonian can no longer be diagonalized in momentum space. We can calculate the resulting band structure in real space, however. The calculations presented here use a 200 site lattice sampling around 1000 points per site, and the potential is modeled as a superposition of a 1064 nm lattice, a 915 nm lattice, and a weak harmonic confinement. Fig. 2.7a shows the calculated energies for the first 600 eigenstates (eigenstate number is plotted on the x-axis) for an $8E_R$ 1064 nm lattice with varying 915 nm lattice depth. We see the effects of the perturbing lattice, as minigaps start to open in the 1064 nm band structure.

Fig. 2.7 shows the inverse participation ratio (IPR), a measure of localization, for each eigenstate at different 915 nm lattice depths; higher IPR indicates a greater degree

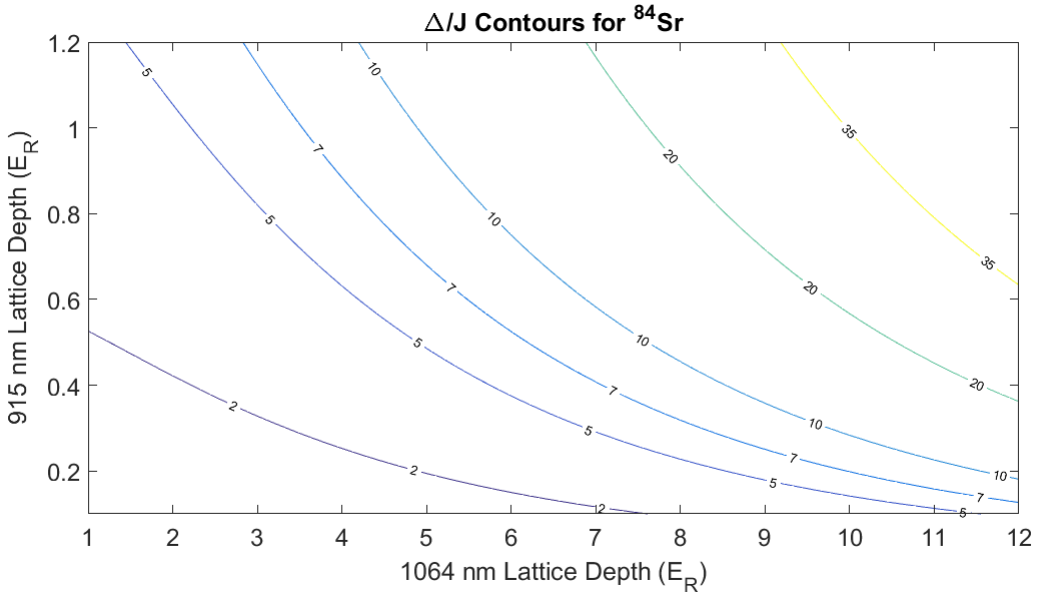

Figure 2.6: Contours show lines of constant Δ/J for varying 1064 nm and 915 nm lattice depths. By fitting

of localization. At $8E_R$, the ground band should localize for a very low 915 nm depth, which we see in the data. Interestingly, at intermediate secondary lattice depths, we see discrete steps in the second band IPR which correspond to the locations of the minigaps. This indicates the presence of a single-particle mobility edge (SPME), where a subset of states in a band are delocalized up to some critical energy, and then localized [29]. Experimental evidence has been found for SPMEs in bichromatic lattices, though they have never been spectroscopically detected [30].

Finally, the ability to realize quasiperiodic structures in an optical lattice system immediately allows access not only to phonon-like (dipolar) excitations via commensurate phase-modulation of both lattices, but also to phason-like excitations via phase modulation of just one lattice. More will be said on this subject in Chapter 8.

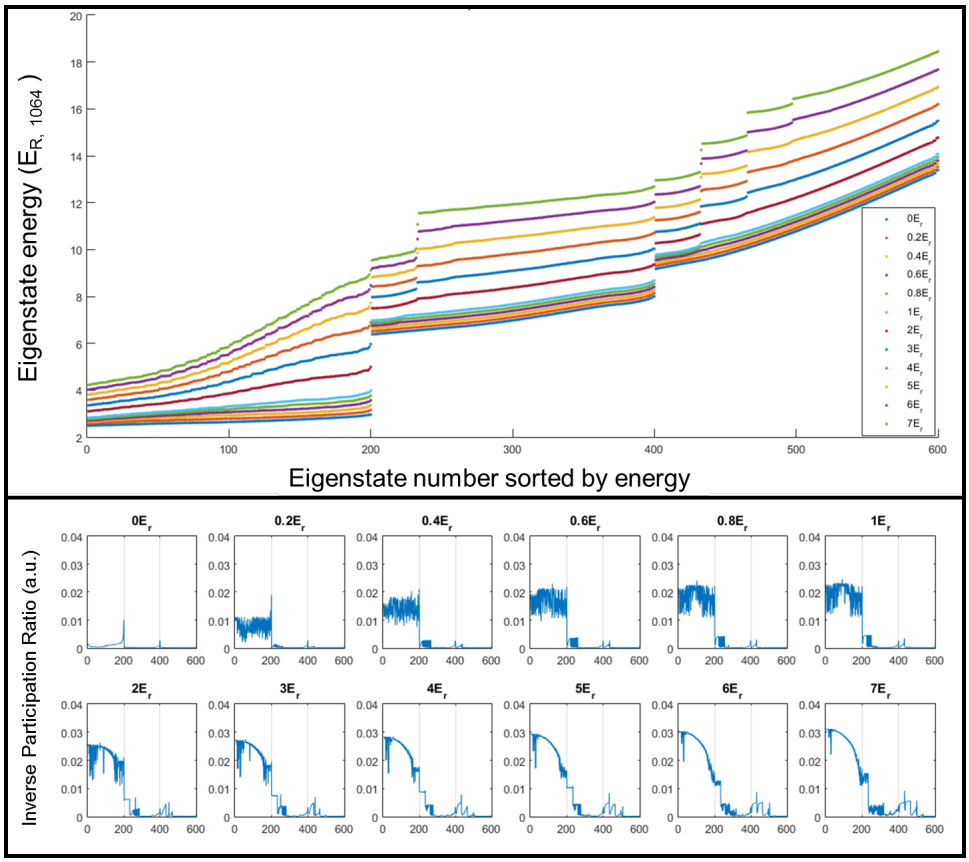

Figure 2.7: **a**: Real-space calculation of bichromatic energy structure over 200 lattice sites for an $8E_R$ 1064 nm lattice and varying 915 nm lattice depth. **b**: Calculation of quantity proportional to inverse participation ratio for each eigenstate at various 915 nm depths. Higher values indicate a greater degree of localization.

Chapter 3

Atomic Properties of Lithium and Strontium

Having covered some basic general theory in Chapter 2, I will now dive into particular properties and parameters of the elements we currently use in our lab, lithium and strontium.

3.1 Lithium

Lithium metal is a light silver, and has the texture of bubble gum tape. It is the lightest of the metals. It is an alkali and, like many of the alkalis, reacts violently with water. Lithium is commonly used in AMO experiments due to its relatively simple electronic structure, and stable isotopes exist in both bosonic and fermionic flavors; because the mass is so low, it can also tunnel through potential barriers very quickly. It shares many properties with other alkalis, including the existence of D1 and D2 cooling lines; however, a number of annoyances make it more difficult to work with experimentally. In this subsection, I will give an overview of the atomic properties of lithium; for more information, the Gehm thesis is very useful [31]. This discussion will gloss over many

Property	Value	Ref.
Atomic Number	3	
Atomic Mass	7.016004 amu 1.1650347712× 10^{-26} kg	[32]
Total Spin (Electronic)	$S = 1/2$	
Total Spin (Nuclear)	$I = 3/2$	

Table 3.1: Lithium atomic properties

properties specific to ^{6}Li, the fermionic isotope, since we have thus far focused our efforts on ^{7}Li.

3.1.1 General atomic properties

There are two stable isotopes of lithium, ^{6}Li (fermionic, with 3 neutrons and natural abundance of 7.59%) and ^{7}Li (bosonic, with 4 neutrons and natural abundance of 92.41%). Some basic properties of ^{7}Li are listed in Table 3.1.

Both the D1 and D2 transitions lie at approximately 670.9 nm (separated by only ∼10 GHz), which is very convenient for the following two reasons:

- Only one master laser is needed to cool on both lines, given enough AOMs and EOMs, and
- 670.9 nm is a relatively convenient wavelength at which to get direct diodes. It is also a bright visible red, which makes alignment easy.

We can calculate many basic properties of this optical transition simply by knowing the precise frequency [33] and lifetime [34, 35]. These are given for ^{7}Li in Table 3.2.

3.1.2 Level structure

We designate the state of the valence electron, at least in an $L - S$ coupling scheme, using Russell-Saunders notation: $n^{2S+1}L_J$, where N is the principal (motional) quantum

	Symbol	D1 line	D2 line
Frequency	f	446.8002 THz	446.8102 THz
Wavelength (vacuum)	λ	670.9766 nm	670.9615 nm
Lifetime	τ	27.102 ns	27.102 ns
Natural Linewidth	Γ	$2\pi\times$ 5.8724 MHz	$2\pi\times$ 5.8724 MHz
Recoil velocity	v_{rec}	0.08477 m/s	0.08477 m/s
Recoil temperature	T_{rec}	3.033 μK	3.033 μK
Saturation intensity	I_{sat}		2.54 mW/cm^2
Doppler temperature limit	T_{Dopp}	140.98 μK	140.98 μK
Doppler velocity limit	v_{Dopp}	0.4009 m/s	0.4009 m/s

Table 3.2: ^{7}Li D line optical properties

number, S is total electronic spin, L is total orbital angular momentum, and J is total angular momentum.

The electronic structure of lithium may be considered at three levels of complexity, at least for experimental purposes (we will not consider quantum defects in this discussion). The first is under the central field approximation, which considers no coupling between the nucleus and the valence electron. In this approximation, the ground state of lithium is 2^2S, and the excited state 2^2P.

We can then account for spin-orbit coupling, which gives rise to fine structure. Since the ground state has no orbital angular momentum, there is only one possible value of J, so we label the state $2^2S_{1/2}$. Alignment or anti-alignment of the spin and orbital angular momenta in the excited state, 2^2P, causes splitting into $2^2P_{1/2}$ and $2^2P_{3/2}$: transitions from the ground state to the former are labeled D1, and to the latter, D2. The splitting between these lines is 10.053 GHz. The isotopic shift between the ^{6}Li and ^{7}Li D2 lines is also around 10 GHz, resulting in a "double-feature" on our spectroscopy signal which hampers us from using it as a lock.

The fine structure lines are further split due to interactions between the electron and the nucleus. ^{7}Li has a nuclear spin $I = 3/2$; we can label the hyperfine states using a new total angular momentum $F = J + I$. The ground state $2^2S_{1/2}$ splits into $F = 1$

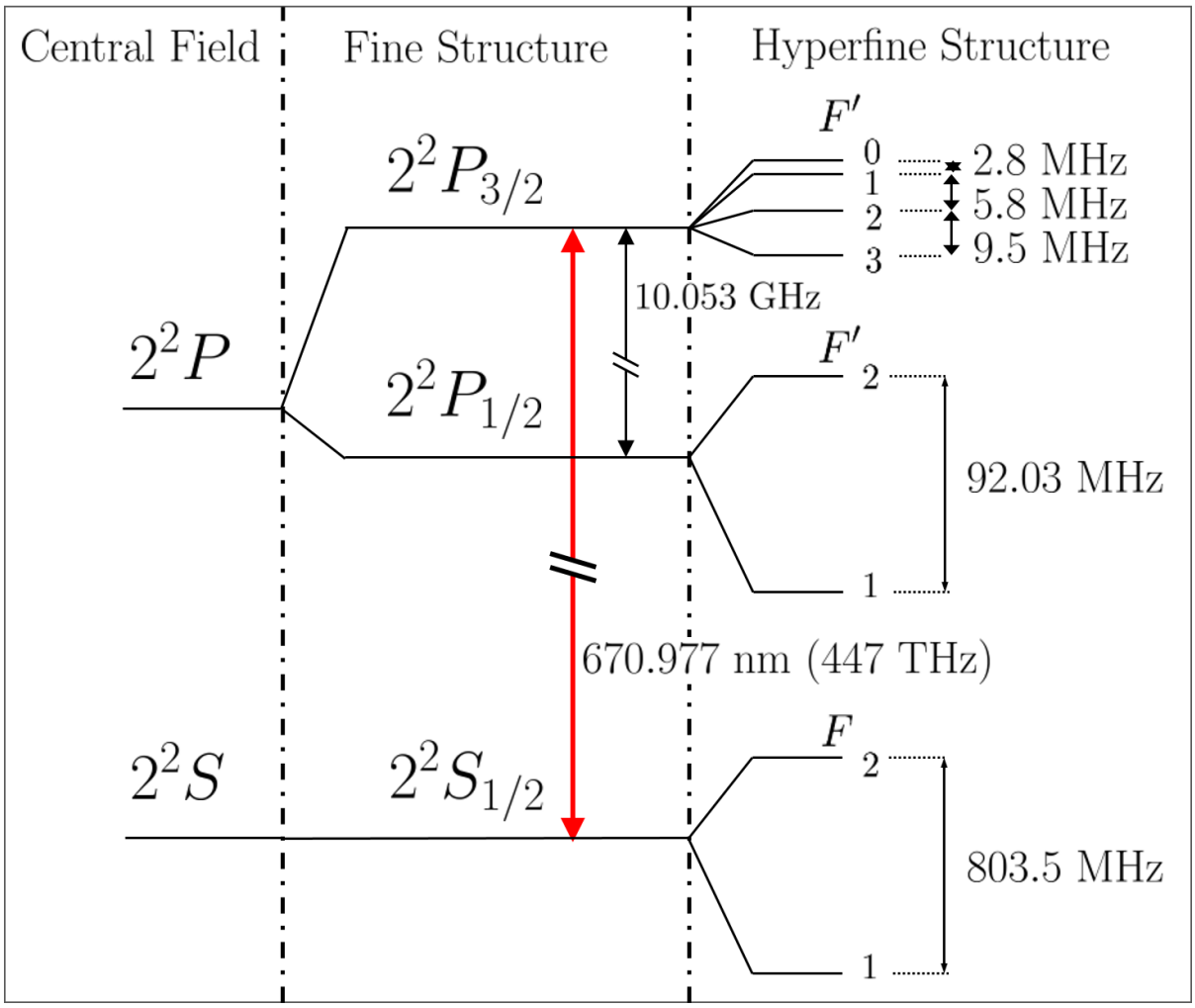

Figure 3.1: Schematic Grotrian diagram for ^7Li D-line transitions, showing central field, fine, and hyperfine splittings. Frequencies from [35]

and $F = 2$ manifolds, split by 803.5 MHz. The D1 excited state $2^2P_{1/2}$ also splits into $F = 1$ and $F = 2$ manifolds, split by 92 MHz. The D2 excited state $2^2P_{3/2}$ splits into 4 different hyperfine manifolds, $F = 0, 1, 2, 3$, which crucially are unresolved with respect to the 5.9 MHz transition linewidth. All of these splittings are shown in Fig. 3.1. Each of the hyperfine manifolds splits further into $(2F+1)$ m_F states.

Our main cooling transition, the "cycler," is $F = 2 \rightarrow F' = 3$ on the D2 line, which should be a closed cycling transition due to selection rules. However, because the $2^2P_{3/2}$ hyperfine manifolds are unresolved, there is a nonnegligible probability of driving

g-factor	State	Value	Ref.
g_I		-0.000447654	[36]
g_J	$2^2S_{1/2}$	2.002301	[36]
	$2^2P_{1/2}$	0.6668	[36]
	$2^2P_{3/2}$	1.335	[36]
g_F, $2^2S_{1/2}$	$F=1$	-0.5011	
	$F=2$	0.5002	
g_F, $2^2P_{1/2}$	$F=1$	-0.1672	
	$F=2$	0.1664	
g_F, $2^2P_{3/2}$	$F=0$	0	
	$F=1$	0.6673	
	$F=2$	0.6673	
	$F=3$	0.6673	

Table 3.3: Lithium fine and hyperfine g-factors

$F = 2 \rightarrow F' = 2$, which can then decay to $F = 1$ in the ground state and become dark. To address this problem, we use a repumper which is 803.5 MHz detuned from the cycler to drive $F = 1 \rightarrow F' = 2$.

3.1.3 Magnetic field interactions

At low magnetic fields (where the Zeeman shift can be considered a perturbation on the hyperfine splitting), F is still a good quantum number, and the energy levels shifts linearly with B

$$\Delta E = g_F m_F \mu_B B \tag{3.1}$$

due to the anomalous Zeeman effect. The Lande g-factors g_F are calculated based on Eq. 2.6, where the g-factors g_J and g_I have been taken experimentally from [36]. All of these may be found in Table 3.3. From Eq. 3.1, it is easy to see that the energy of a given state will increase with field strength if $g_F \times m_F > 1$. We call states that satisfy this condition "low-field seeking", and they are magnetically-trappable in an inhomogenous field; conversely, states for which $g_F \times m_F < 1$ are "high-field seeking" and are antitrapped

since it is impossible to generate a local field maximum.

The Zeeman effect lifts the degeneracy of the hyperfine manifolds into $(2F+1)$ m_F states. These states, labeled $|F, m_F\rangle$, have different magnetic moments and scattering properties, and during various moments in the cooling process, it becomes favorable to place all of the lithium atoms in a particular m_F state by optical pumping in a small bias field.

At high magnetic fields, the Zeeman shift becomes large compared to the hyperfine splitting, and $|F, m_F\rangle$ become poor quantum numbers; this is called the Paschen-Back regime. Instead, we must work in the $|m_I, m_J\rangle$ basis, since at very large fields, the nuclear and electronic spins become independent. Numerically diagonalizing the Hamiltonian in this basis gives the Zeeman shifts plotted in Fig. 3.2. At intermediate fields, "good" quantum numbers are difficult to define, but since the ordering of the states does not change, we typically still refer to them as $|F, m_F\rangle$ states. We can use these calculations to figure out the laser frequencies needed to image at various high fields; they typically land us within a few tens of MHz of the correct frequency.

We can see that some states (in particular, $|F = 1, m_F = -1\rangle$) are trapped at low fields and antitrapped at high fields. It is important to account for this sign change when considering, for example, states to use for RF evaporation.

3.1.4 Scattering properties

Since the majority of cooling after gray molasses is evaporative, it is important for us to know something about the collisional properties of certain states. Typical atomic densities for gases in these experiments range from 10^8 cm^{-3} to 10^{14} cm^{-3}, which means we can largely consider our collisions to be two-body (with one notable exception). We also only take the lowest order of the partial-wave expansion and assume s-wave scattering; this is a good approximation in most cases, since there is typically not enough thermal

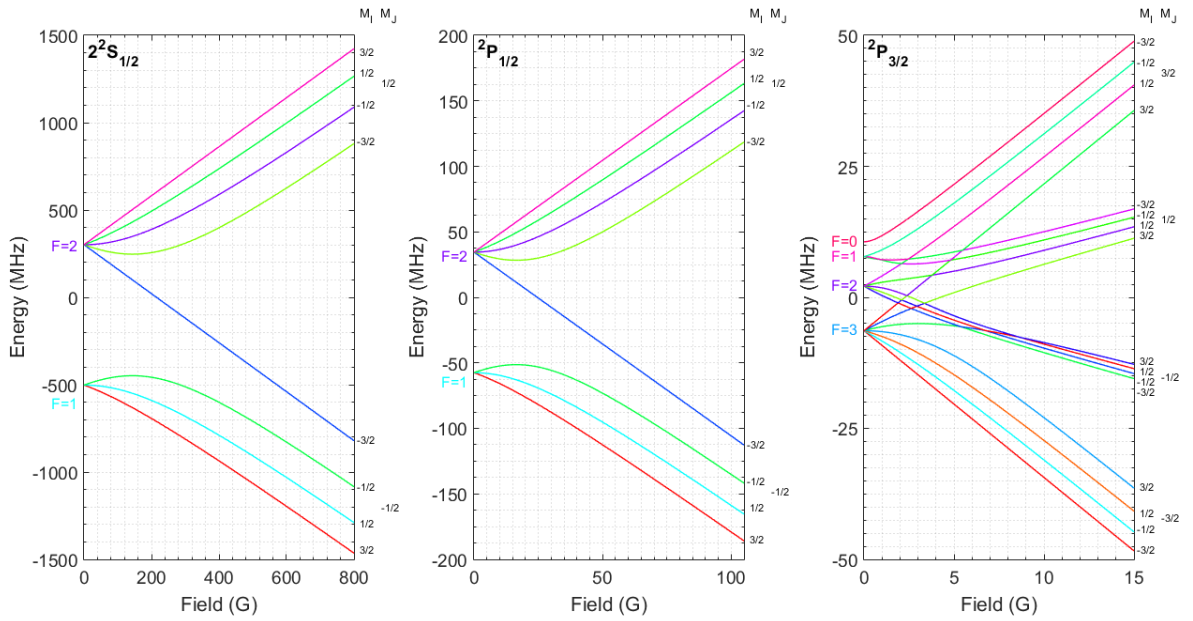

Figure 3.2: Zeeman shifts at low and high fields for $2^2S_{1/2}$, $2^2P_{1/2}$, and $2^2P_{3/2}$.

energy to overcome centrifugal barriers.

During RF evaporation, we use the $|2,2\rangle$ state: it is magnetically trappable, and since it is a stretched state, the rate of (bad) spin-exchange collisions is decreased. The background triplet scattering rate of the $|2,2\rangle$ state was empirically ascertained to be a=-27.4 a_0 [37]. This attractive scattering length is untenable for typical ODT densities, but fine for the densities in the magnetic trap as long as the elastic scattering rate $\Gamma_{el} = 8\pi a^2$ is larger than various inelastic scattering rates. Please see Section 2.2.3.

Before optical evaporation, we use an RF pulse to transfer atoms to the $|1,1\rangle$ state. The background scattering length of this state is a=5.1 a_0 [40] which is too small for optical evaporation to proceed. However, the $|1,1\rangle$ state has a wide Feshbach resonance at B_0=736.8 G, width Δ = 192.3, and background scattering a_{bg}=-24.5 [41] (see Section 2.1.3), which makes it possible to tune the interactions. This Feshbach resonance, along with many other scattering properties of various lithium states, was characterized in detail in the Hulet group [42]; their data, along with the analytical form of the field,

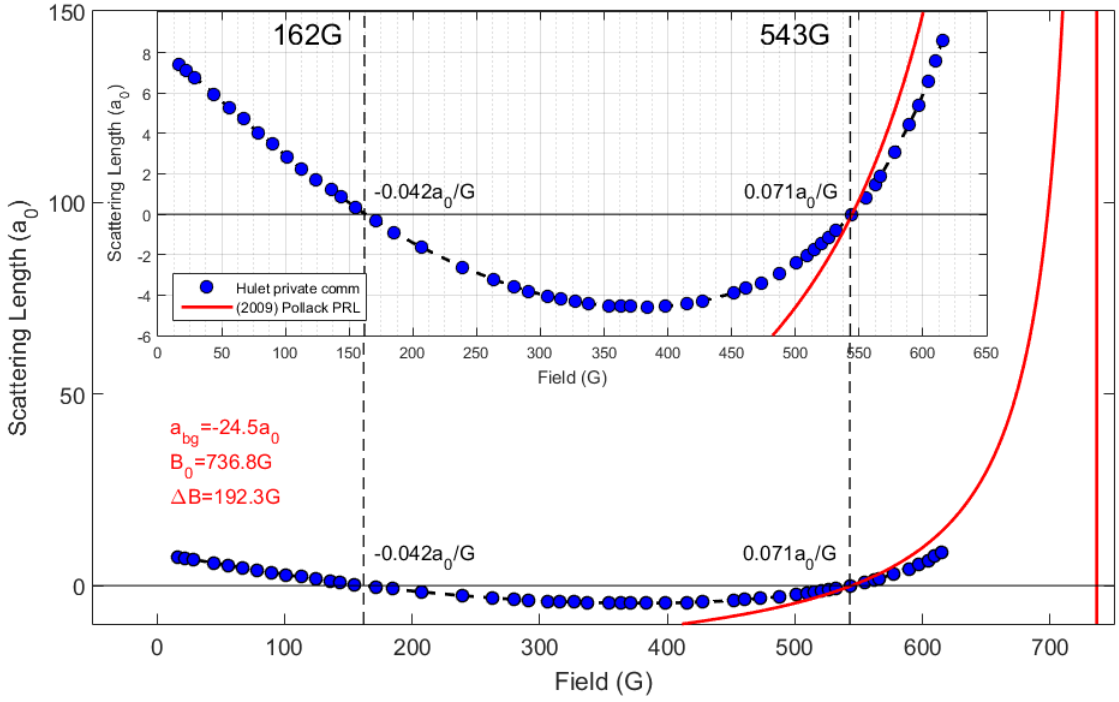

Figure 3.3: Lithium-7 $|1,1\rangle$ Feshbach resonance. Data points from [38], analytic form from [39]. Inset shows zero crossing locations and slopes in detail.

is shown in Fig. 3.3. The scattering length goes to zero at 543.6 G, and the slope of the scattering length at that point is roughly 0.075 a_0/G.

3.2 Cooling stages

Here, at the nexus of the lithium and strontium sections, please enjoy Fig. 3.4, which shows the various cooling stages for the lithium and strontium experiments. While there are some common elements, the different atomic properties of the elements require different cooling strategies.

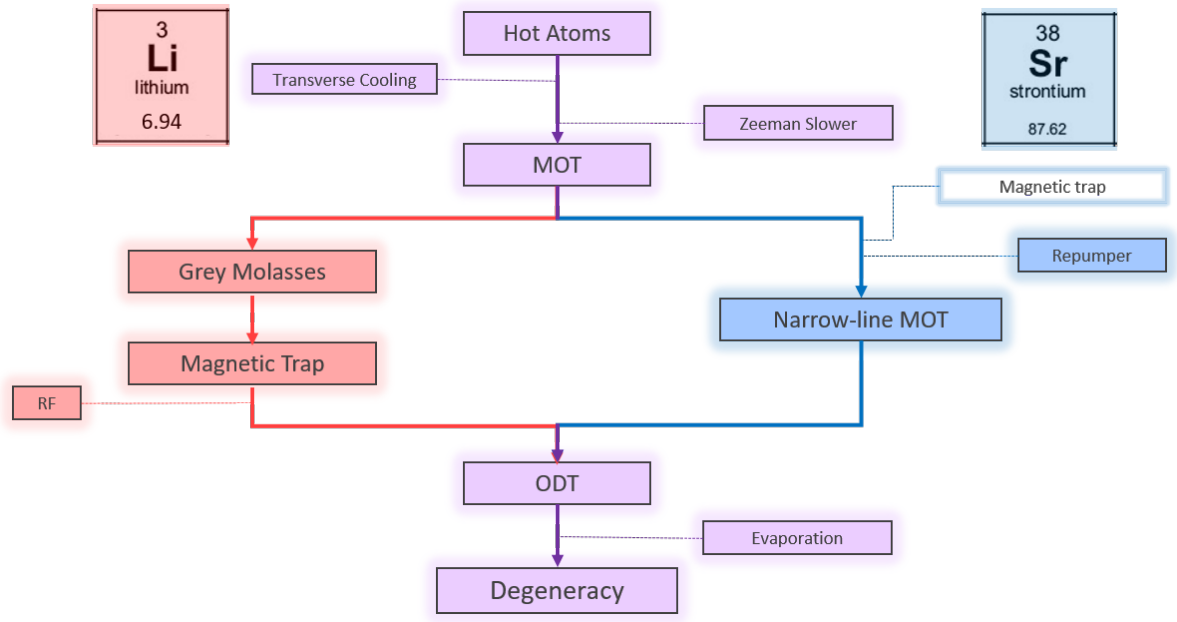

Figure 3.4: Various cooling stages for both lithium and strontium, showing where cooling techniques diverge and converge. For more on each cooling step, please see Sections 4.2 and 5.2.

3.3 Strontium

Strontium metal is a light silver color with a slightly yellow tint. It is an alkaline earth metal and, like many of the alkaline earths, reacts violently with water. Strontium was first brought to degeneracy in 2009 and has become very popular in recent years due to its clock transition and accessible magic wavelengths. It has very narrow intercombination transitions, which provide a natural spectroscopic knife with which to measure energies in experiments. The fermionic isotope, ^{87}Sr, also has a large nuclear spin $I = 9/2$, which makes it an excellent candidate to eventually study SU(N) magnetism.

3.3.1 General atomic properties

There are over 20 unstable isotopes of strontium, but 4 stable ones: bosonic ^{84}Sr, ^{86}Sr, and ^{88}Sr, and fermionic ^{87}Sr. These isotopes and their respective natural abundances

Isotope	Abundance	Type
^{84}Sr	0.56%	Boson
^{86}Sr	9.86%	Boson
^{87}Sr	7.00%	Fermion
^{88}Sr	82.58%	Boson

Table 3.4: Strontium isotopes and abundances. Values taken from [43]

may be found in Table 3.4.

Strontium is an alkaline earth metal, which means its internal states are best described by helium-like wavefunctions: singlet states (S=0) and triplet states (S=1). Singlet to triplet transitions are forbidden by selection rules, but due to spin-orbit coupling, there is some small amount of orbital mixing which gives rise to narrow intercombination lines (one of which is the celebrated clock transition).

The ground state of strontium is $^1S_0$ in the $n = 5$ shell. The two main cooling transitions address the $^1P_1$ state and the $^3P_1$ state. Properties of these transitions are found in Table 3.5 [44]. Unfortunately, the 461 nm transition is not fully closed; there is a decay channel through the $^1D_2$ state to the long-lived $^3P_2$ metastable reservoir, the lifetime of which is on the order of seconds. We have to repump the atoms into a higher state which allows decay back into the $^3P_1$ state. From there, the atoms can decay back to the ground state.

It is worth briefly discussing our choice of repump wavelength. We considered many different repump schemes for this machine, iterating through $|5s6s^3S_1\rangle$ (640 nm/707 nm), $|5s5d^3D_2\rangle$ (497 nm), and finally landing on $|5s6d^3D_2\rangle$ (403.35 nm). Diodes at this wavelength are relatively easy to come by, being close to the 405 nm Blu-ray color. However, because of the higher n quantum number of the associated state, the branching ratios were unknown until 2013, when a reservoir spectroscopy paper[1] [45] showed differences in $|5s5d^3D_2\rangle$ and $|5s6d^3D_2\rangle$ repumping efficiency to be in the single percent range.

[1] This is my favorite paper ever published.

	Symbol	$^1S_0 \rightarrow ^1P_1$	$^1S_0 \rightarrow ^3P_1$
Frequency	f	650.6855 THz	434.8291 THz
Wavelength (vacuum)	λ	460.7331 nm	689.4489 nm
Lifetime	τ	5.219 ns	21.4 μs
Natural Linewidth	Γ	$2\pi\times$ 30.4953 MHz	$2\pi\times$ 7.437 kHz
Recoil velocity	v_{rec}	0.01023 m/s	0.00684 m/s
Recoil temperature	T_{rec}	0.5334 μK	0.2382 μK
Saturation intensity	I_{sat}	40.75 mW/cm^2	3.03 μW/cm^2
Doppler temperature limit	T_{Dopp}	732.1 μK	0.178 μK

Table 3.5: Strontium cooling transition properties

3.3.2 Level structure

The electronic structure of strontium can be found in Fig. 3.5. The clock transition, $^1S_0 \rightarrow ^3P_0$, is shown along with the linewidth for the fermionic isotope only.

Nuclear spin $I = 0$ for all of the bosonic isotopes, so they do not have any hyperfine structure. The fermionic isotope, ^{87}Sr, has nuclear spin $I = 9/2$; however, because $J = 0$ for the ground state, there is still no line splitting. Hyperfine splitting only becomes relevant for the excited states, and vary from around 20 MHz in the $^1P_1$ manifold to around 1.5 GHz in the $^3P_1$ manifold. The full hyperfine structure can be found in Fig. 2.3 of the Stellmer thesis [21].

The other energy shift we have thus far neglected is the isotope shift due to the different nuclear masses. For three relevant transitions, these may be found in Table 3.6, referenced to the ^{88}Sr transition (notation Δ^{88}Sr(isotope)). These are easy to observe by taking fluorescence measurements of a MOT while scanning the laser through all of the isotopic resonance frequencies (Fig. 3.6). Also shown in the same table are the Lande g-factors g_J for each excited state.

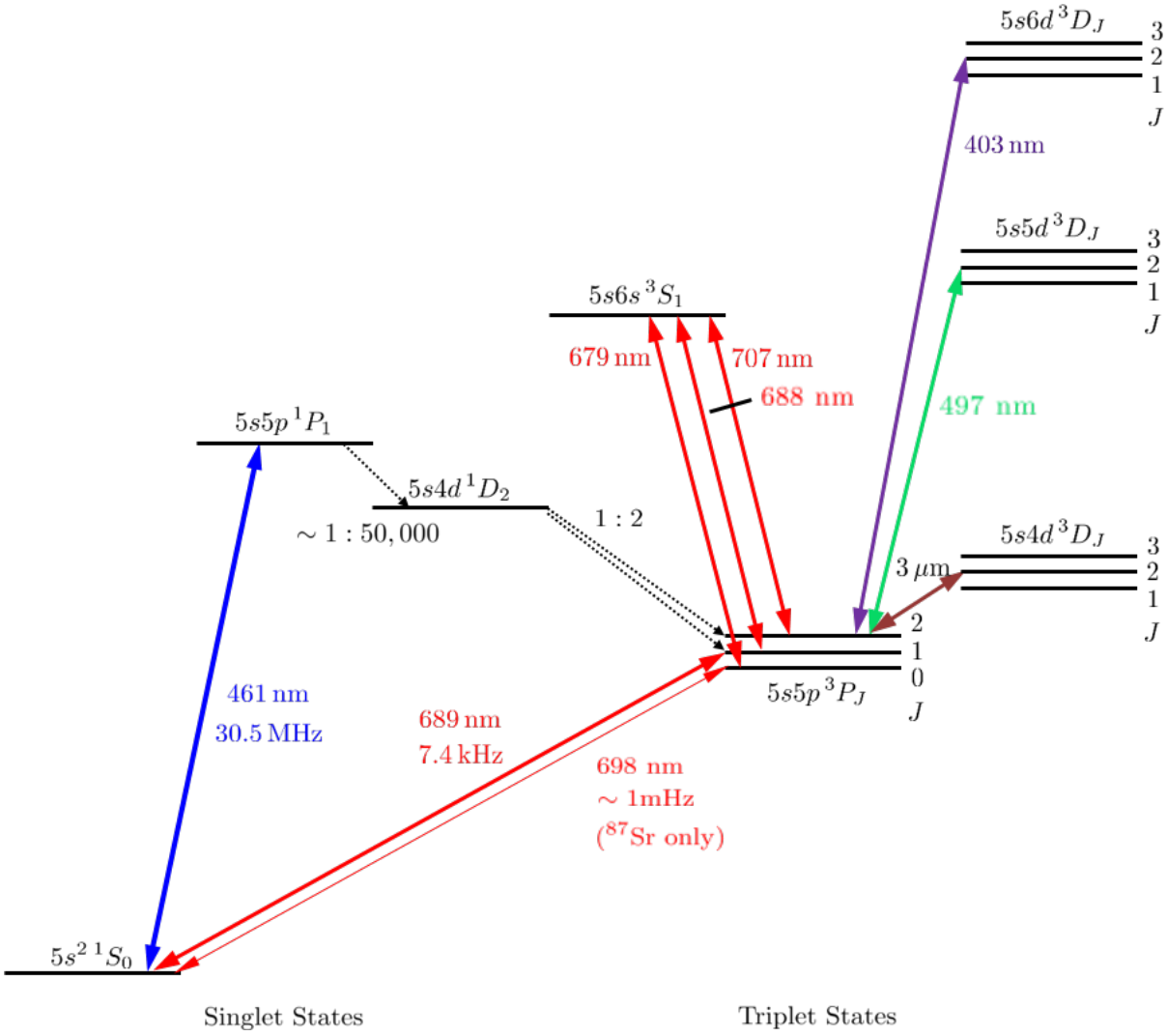

Figure 3.5: Schematic Grotrian diagram for strontium transitions. Hyperfine splitting is not shown.

3.3.3 Scattering properties

Strontium does not have any broad magnetic Feshbach resonances, and has only a few narrow optical Feshbach resonances [46]. We are typically limited to using background scattering rates of the atoms. However, the inter-isotope and intra-isotope scattering lengths vary so widely that by choosing the right species, or mixtures thereof, we can work in different interaction regimes. The scattering rates are given in Table 3.7.

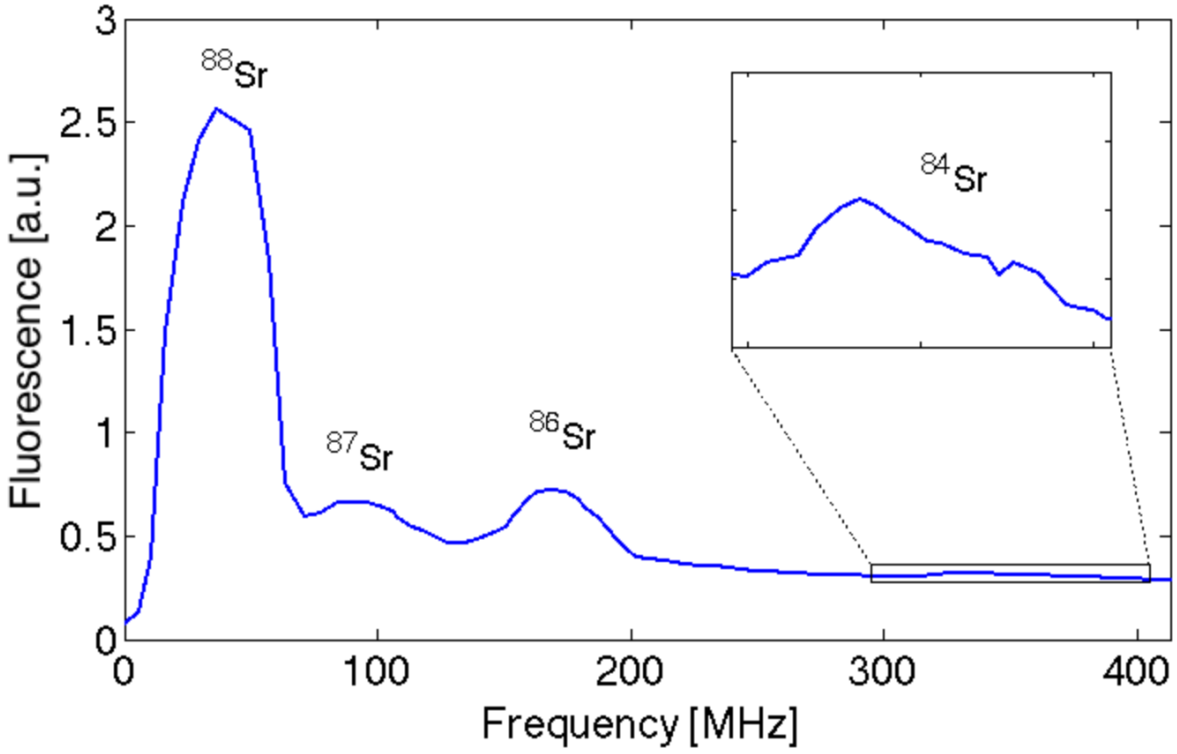

Figure 3.6: Monitoring fluorescence of the blue MOT while scanning the laser shows signals form all four stable isotopes of strontium, which are roughly proportional to their natural abundance.

Transition	g_J	Δ^{88}Sr(^{84}Sr)	Δ^{88}Sr(^{86}Sr)	Δ^{88}Sr(^{87}Sr)
$^1S_0 \rightarrow ^1P_1$	1	-270.8	-124.8	-46.5
$^1S_0 \rightarrow ^3P_1$	3/2	-351.49	-163.81	-62.15
$^3P_2 \rightarrow 5s6d^3D_2$ [45]	7/6	-81	-49	-20

Table 3.6: Strontium isotope shifts and g_J-factors

3.3.4 SU(N) symmetry

It was mentioned in Section 3.3.2 that the ground state of ^{87}Sr does not have any hyperfine structure because $J = 0$. This, in fact, is an extremely interesting scenario, because the nuclear spin is entirely decoupled from the electronic spin even at zero magnetic field; this means that spin-changing collisions are impossible. Atoms in each of the 10 nuclear spins interact extremely similarly with atoms in the 9 other spin states (Pauli exclusion forbids

	^{88}Sr	^{87}Sr	^{86}Sr	^{84}Sr
^{84}Sr	1800	-56	32	124
^{86}Sr	98	164	830	
^{87}Sr	55	97		
^{88}Sr	-1			

Table 3.7: Strontium isotope scattering lengths

interactions with atoms with the same m_F). The symmetry of these interactions is called SU(N) symmetry. Spin models with SU(2) symmetry, such as the Heisenberg model, have ground states which are relatively simple to find in the absence of external fields. It becomes harder to find ground states for systems with SU(3) and SU(4) symmetry; having the ability to study an SU(10) system using strontium as a quantum simulator is extremely powerful.

Chapter 4

Lithium Experimental Design and Setup

This chapter encompasses many experimental details relevant to our lithium machine at UC Santa Barbara, and is divided into 2 sections. Section 4.1 describes the construction of the lithium apparatus, including design details for mechanical and electrical subsystems as well as optical infrastructure and hardware. Section 4.2 discusses the implementation of the cooling sequence for lithium, including experimentally relevant optical parameters.

4.1 Lithium Machine Design

The machine described in this section was constructed to study dilute gases of lithium, largely following the design of the BEC5 machine in the group of Wolfgang Ketterle at MIT; a Solidworks representation may be found in Fig. 4.1. It is one of the few lithium machines which still employ RF evaporation out of a plugged magnetic trap. The basic features of this design are:

- Ability to generate magnetic fields at 800 G to access a Feshbach resonance, and field gradients up to 450 G/cm for magnetic trapping.

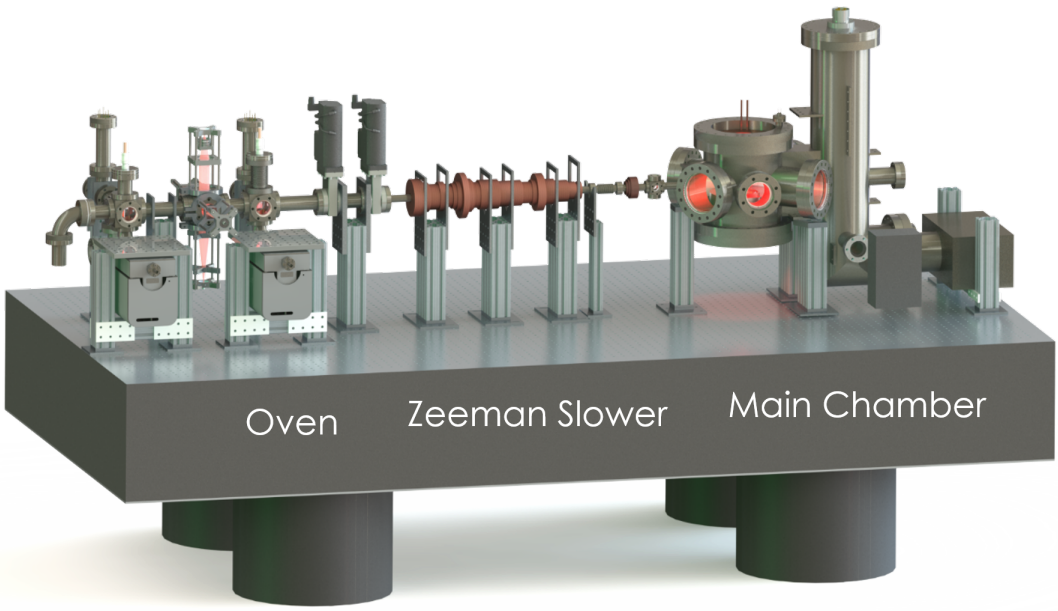

Figure 4.1: Overview of the lithium machine design.

- Good optical access for MOTs, sub-Doppler cooling, optical dipole traps, and optical lattices.
- Ability to switch between isotopes ^{7}Li and ^{6}Li.
- Space for RF antennae for RF evaporation and state transfer
- Ultra-high vacuum to achieve BEC lifetimes longer than 10 s.

As I ceased full-time work on the lithium machine in late 2014, section 4.1.5 is meant as a brief overview which will gloss over many of the experimental challenges and difficulties of implementation; I strongly encourage reading the lithium theses of Zach Geiger [18], Kevin Singh [19], and Cora Fujiwara [47] for more complete descriptions.

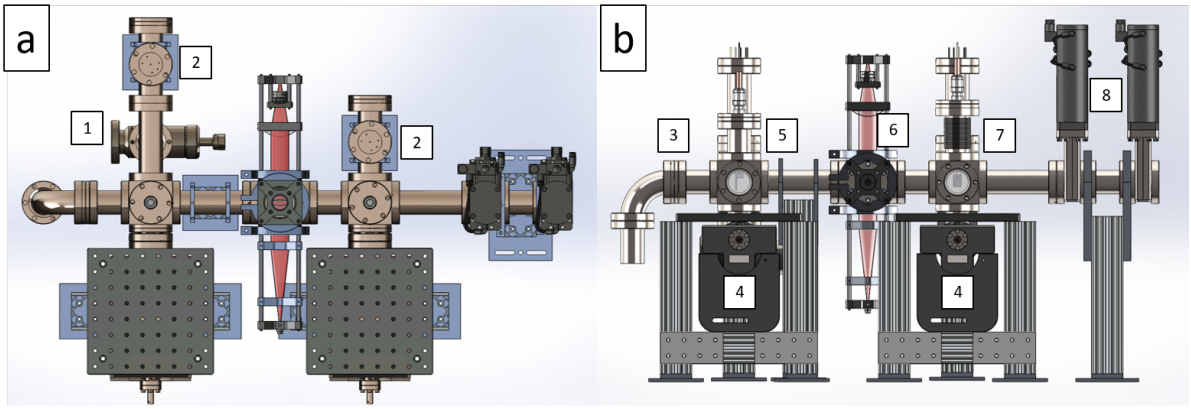

Figure 4.2: **(a)** shows a top-down view of the lithium oven manifold, such that the positions of the angle valve (1) and ion gauges (2) may be noted. **(b)** shows a side view of the same with a clearer view of the (3) the nozzle flange, (4) 45 l/s ion pumps, (5) the coldplate feedthrough, (6) the transverse cooling section, (7) the atomic beam stopper feedthrough, and (8) the gate valves separating the oven manifold from the Zeeman slower. Please see Fig. 4.5 for locations of differential pumping tubes.

4.1.1 Oven

The lithium oven manifold was designed to maximize flux of gaseous lithium into our main chamber, and built from both 316 and 304 stainless steel alloys incorporating off-the-shelf and custom parts. The manifold is shown in Fig. 4.2. It consists of an atomic lithium source, a cold plate to cut off widely-diverging parts of the atomic beam, a first stage of differential pumping, a transverse cooling stage, an atomic beam shutter, and a second differential pumping stage. It also includes two gate valves which separate the oven from the UHV part of the machine and allow it to be baked separately; these gate valves are not all-metal valves, but use Kalrez elastomer which outgasses much less than Viton. The lithium oven was baked in late 2013 and, following a setback described later in this section, baked again in late 2018, according to procedures outlined in Appendix B.

In this section, you will find information about lithium vapor pressure and flux, our atomic beam nozzle, differential pumping, and the atomic beam shutter; discussion of transverse cooling may be found in section 4.2.1. Many of the part numbers for items found in the oven may be found in Table 4.1.

Table 4.1: Lithium oven part numbers

Function	Company/Part Number	Purchased From	Notes
Ion Pumps (2)	Gamma 45S-DI-2H-SC-N-N	Gamma	Fine after 08/2018 vacuum breach
Ion Pump Controllers (2)	Gamma SPC-1-US110-232 Digitel SPC	Gamma	Built-in gauges not so great
Ion Pump Cables(2)	Gamma SCP-SC3-SC 3m SAFE-CONN STANDARD	Gamma	
Ion Gauges	Agilent/Varian UHV-24P B-A	Ideal Vac	Thoria-Iridium filaments replaced 10/2018
Ion Gauge Controller	Agilent XGS-600	Agilent	
Ion Gauge Cables (2)	Agilent R32453010 for XGS-600 Controller	Agilent	
Cup Band Heater	Tempco MI-PLUS MPP02902	Tempco	1.5" × 2"; J-type TC
Flange Band Heater	Tempco MI-PLUS MPP02903	Tempco	2.75" × 1"; J-type TC
Nozzle Band Heater	Tempco MI-PLUS MPP02904	Tempco	2.75" × 1.5"; K-type TC
Oven Heater Controller	TPC-3000	Tempco	Watch the TC types.
Feedthroughs	Lesker EFT0313373	Lesker	Cold plate and beam shutter
Beam shutter solenoid	Uxcell a1405100ux1279	Amazon/eBay	Max current 10A
Angle Valve	MDC AV-150M-11, Kalrez Manual	MDC	Hand-tightened; no torque sealing
Gate Valves (2)	MDC GV-1500M-P-1, Kalrez Pneumatic	MDC	Closed when unpowered

Vapor pressure and flux

The lithium reservoir is a 2.75" CF half-nipple, the cup of which was machined out of a solid piece of stainless steel, currently loaded with around 18-20 g of solid lithium (non-enriched). We required the flux out of the oven to produce around 1×10^{10} atoms/s in the main chamber, as a baseline to achieve our target MOT loading rates. In order to figure out at which temperature we needed to operate the oven to reach this flux, we considered the vapor pressure of lithium. Lithium has a relatively low boiling point of around 454 K; we will only quantitatively consider higher temperatures here. We can use the Antoine equation (a derivation of the Clausius-Clapeyron equation) to estimate the vapor pressure (in bar) as a function of temperature (in K): $\log_{10} P_{\text{vap}} = A - B/(T + C)$, using parameters $A = 4.98831$, $B = 7918.984$, and $C = -9.52$ [48]. However, it is nice to use empirical results when available; P_{vap} is given here in Torr, while T is in Kelvin [31]:

$$\log_{10} P_{\text{vap}} = -10.34540 - \frac{8345.574}{T} - 0.00008840T - 0.68106 \log_{10} T. \tag{4.1}$$

The results are plotted in Fig. 4.3 in units of Torr. We operate the reservoir at 450°C and gradually increase the heat up to the oven exit at 550°C. Assuming a temperature of 500°C for the lithium gives a vapor pressure of 5.8×10^{-4} Torr. Let us assume for a moment that our oven exit is a 1 cm aperture. We can then use the Hertz-Knudsen equation

$$\Phi = \frac{\alpha N_A}{\sqrt{2\pi MRT}}(P_{vap} - P_{vac}) \tag{4.2}$$

to solve for the maximum flux (sticking coefficient α =1) of the gas Φ through the aperture as a function of the difference between the vapor pressure P_{vap}, background pressure $P_{vac} \approx 0$, molar mass M, and temperature T, giving an approximate flux of 1.4 $\times 10^{14}$ atoms/s.

However, there are two issues with this number. The first is that when we operate at

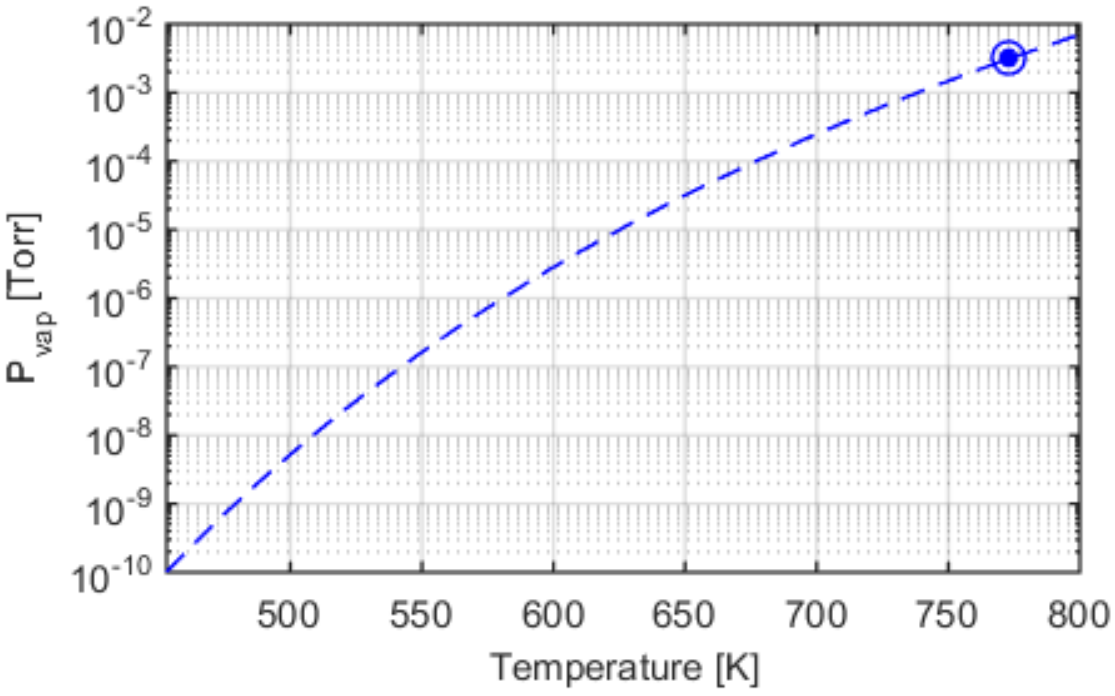

Figure 4.3: Li vapor pressure as a function of temperature. Dot indicates our operating point.

such high temperatures, the average velocity from the Maxwell-Boltzmann distribution will be much higher than any reasonable MOT capture velocity, necessitating a Zeeman slower. For the sake of argument, let's say we build an extremely efficient Zeeman slower which cools 50% of our atoms, providing a flux of 7×10^{13} atoms/s. That number now represents the entire flux out of a 1 cm diameter aperture, over 2π steradians; herein lies the second problem. The number that matters to us is the flux in the center of the main chamber around 2 m away, which results in an effective flux of around 3×10^{9}. Simply increasing the temperature further would result in a shorter oven lifetime, an outcome we wished to avoid.

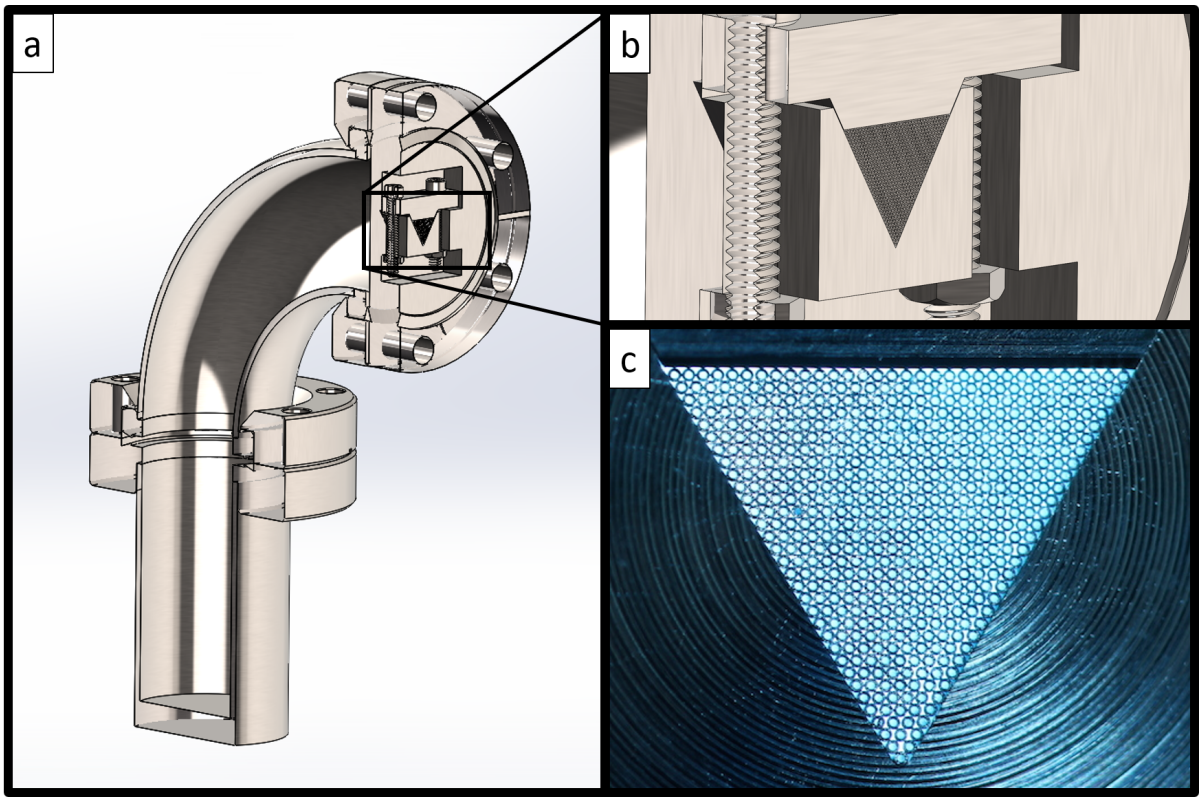

Figure 4.4: **(a)**:A Solidworks schematic of the heated components of the lithium oven: the reservoir cup, flange, elbow, and nozzle. **(b)**: Inset shows microcapillary detail in nozzle design. **(c)**: Image of microcapillary alignment in a constructed nozzle.

Nozzle

Instead of simply using an aperture at the oven exit, we instead used a custom nozzle designed by Ruwan Senaratne which used an array of microcapillary tubes to collimate the beam. Details may be found either in his thesis [22] or in the resulting publication in Review of Scientific Instruments [49], but here are some salient features in brief:

- 304 stainless steel microcapillaries with a large length:diameter aspect ratio of 50 allows atoms with large angular divergence to be "recycled" back into the oven.
- Hexagonal packing into a triangular wire-EDM-cut aperture enforces co-parallelism of the microcapillaries.

- Nozzle provides a measured flux of around 1.4×10^{14} atoms/s in a collimated beam with half-angle divergence of 1.2 degrees.
- Lifetime of a 25 g source should be extended to several decades.

The nozzle is kept at 550°C, sufficiently hotter than the reservoir to ensure that the microcapillaries do not clog. The CF connections for the atomic oven cup, elbow, and nozzle all use nickel gaskets, rather than the traditional copper ones, because lithium quickly corrodes copper gaskets. These nickel gaskets are made from the alloy 201 from Vacs SEV, which is the only company from which we order for a number of reasons: a) the gaskets are slightly thicker than comparable parts from MDC and Lesker, b) 201 is rated to above 600°C, while the more common alloy 200 is only rated to around 350°C. Because 304 stainless steel is not hard enough to cut into nickel gaskets, these few steel parts alone were machined from 316 stainless steel. A schematic showing the nozzle relative to the oven reservoir, as well as an image of the microcapillary packing, may be found in Fig. 4.4.

Setback: At some point during the summer of 2018, someone accidentally changed the thermocouple type setting on the nozzle from J-type to K-type. This resulted in the nozzle being the coldest part of the oven for over a month. We believe that as the lithium was heated and cooled, it clogged and unclogged the microcapillaries and several grams ended up pooled in the chamber on the cold side of the nozzle; we are unsure of the exact mechanism by which this happened. Enough lithium built up that it reached a copper gasket and ate away at it, and when we debugged the problem and turned up the nozzle temperature, the corroded gasket gave way and broke vacuum. That gasket has been changed to nickel, to guard against such human error in the future. **Watch your TC types**.

Differential pumping

Once the atomic beam exits the nozzle, it travels through two stages of differential pumping, which are simply two regions of low conductance between the 3 main oven sections, which are labeled in Fig. 4.5. This two-stage pumping design was based on an early MIT design [50], and is necessary to support pressure differences between our main chamber, where we try to maintain pressures on the order of 10^{-11} Torr, and our atomic beam source production, where pressures can reach into the 10^{-7} Torr regime.

In order to look at this more quantitatively, we consider a region of gas R_1 at high pressure P_1 which is connected via conductance C_{12} to a region R_2. R_2 is at some low pressure P_2 and is being pumped on at speed S_2; both regimes may be considered in the molecular flow regime, where the mean free path of particles is much larger than any characteristic dimension of the chamber. The dominant gas load in R_2 is P_1C, and so the total pressure P_2 is simply P_1C/S_2. We do, however, need to be careful about our definition of pumping speed; an ion pump may have a pumping speed S_{ion}, but if it is connected to the main part of the chamber in series with vacuum part (an elbow or nipple, for example) with conductance C_{ion}, the effective pumping speed is given by $S_{\text{eff}}^{-1} = S_{\text{ion}}^{-1} + C_{\text{ion}}^{-1}$. We can then use the Knudsen formula in the molecular flow regime to calculate the pressure ratios between R_1 and R_2.

In our machine, we have regions R_1 (which includes a 45 l/s ion pump), R_2, (which also includes a 45 l/s pump), and R_3 (the main chamber, which includes a 75 l/s ion pump and a titanium sublimation pump); all regions are marked in Fig 4.5. We can consider the conductance C_{23} to be the conductance of the differential pumping tube in series with the Zeeman slower tube, which is long and narrow. Both pumps are connected to the chamber via 2.75" CF elbows. The differential pumping tubes themselves are narrow 6" long, 0.25" OD, 0.18" ID tubes which are welded to disks in 2.75" CF standard nipples to keep them aligned with the atomic beam path. The Zeeman slower is around 0.5 m

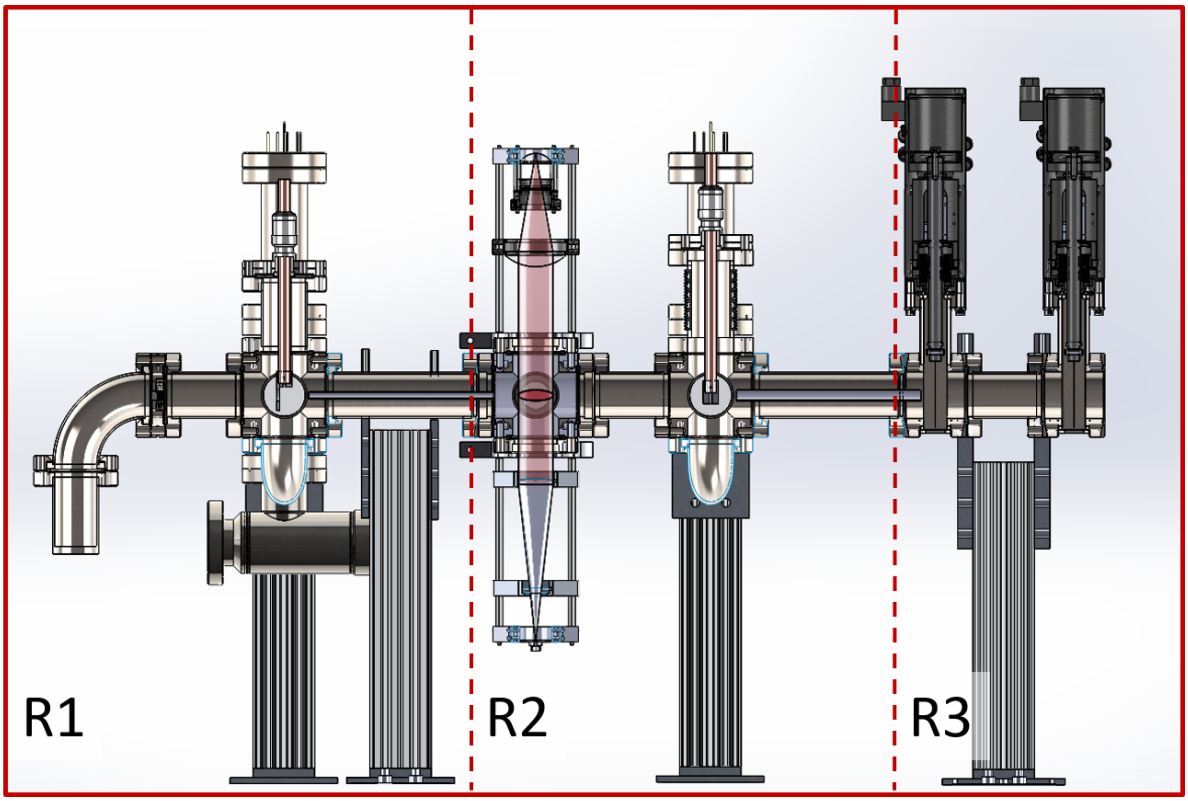

Figure 4.5: Regions of the Li oven manifold under different pressures. Figure shows a section view of the manifold, cut along a plane intersecting the atomic beam; differential pumping tubes may be seen between each section.

long, with OD 0.75" and ID 0.68". We calculate $P_1/P_2 = 100$ and $P_2/P_3 = 800$-1000, depending on estimations of the pumping speed of the titanium sublimation pump and effective conductance of the main chamber.

Atomic beam shutter

The atomic beam shutter is used to mechanically open and close the atomic beam path to the main chamber; it is typically open while the MOT is loading, and closed otherwise. It is constructed from a copper feedthrough and custom stopper, and mounted on a small hydroform bellows. The stopper is actuated by a pull-type solenoid (see Table 4.1) which uses a large spike of current to actuate the shutter and a smaller holding current to keep it open, avoiding any problems with overheating.

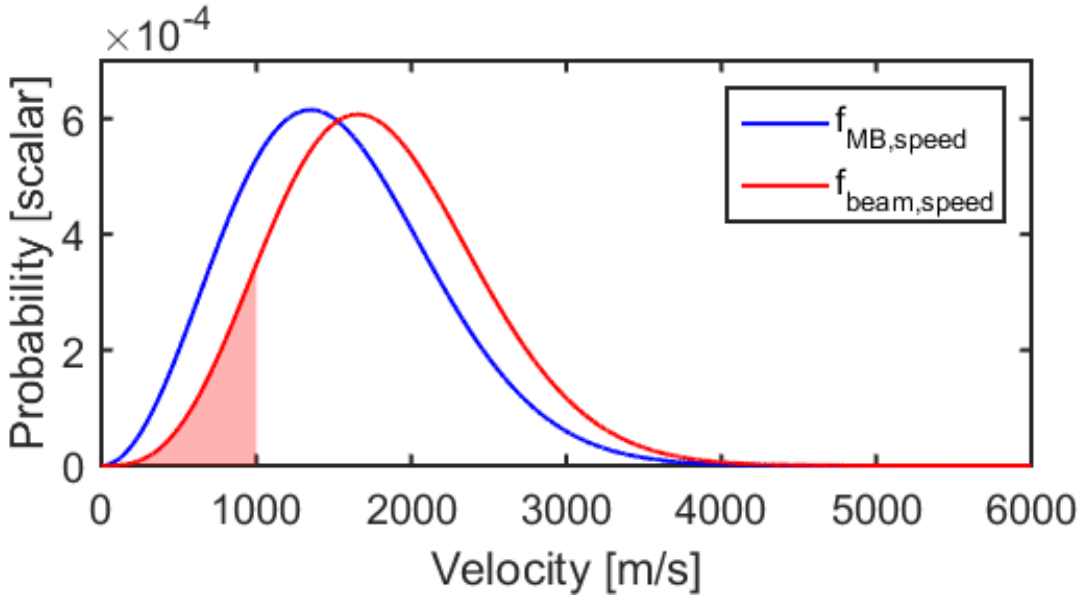

Figure 4.6: Maxwell-Boltzmann distributions for Li

4.1.2 Zeeman slower

At the exit of the oven manifold, we have an atomic beam at a temperature of around 500°C, and we would eventually like these atoms traveling below a reasonable MOT capture velocity v_c of around 50 m/s. Under the assumption that the atoms behave like classical particles, we can simply use a Maxwell-Boltzmann distribution to estimate the fraction of the atomic flux which will be slower than v_c. We recall that the Maxwell-Boltzmann distribution is

$$f_{\mathrm{MB}}(v)d^3v = \left(\frac{m}{2\pi k_B T}\right)^{\frac{3}{2}} \exp\left(-\frac{mv^2}{2k_B T}\right) d^3v \tag{4.3}$$

and we typically assume that the angular distribution is spherically symmetric, allowing us to treat d^3v as $v^2 dv \sin\theta d\theta d\phi$, which we can integrate over solid angle to retrieve the Maxwell-Boltzmann speed distribution:

$$f_{\mathrm{MB,speed}}(v) = \left(\frac{m}{2\pi k_B T}\right)^{\frac{3}{2}} 4\pi v^2 \exp\left(-\frac{mv^2}{2k_B T}\right). \tag{4.4}$$

However, since we are using a nozzle to generate our flux, we cannot assume angular isotropy; the velocity distribution will actually be skewed towards a higher velocity, since there will be a higher flux of faster atoms. Thus, we instead need to write d^3v as $v_z v^2 dv \sin\theta d\theta d\phi$, where $v_z = v\cos\theta$ is the velocity along the direction of the atomic beam.

We can then normalize and rewrite our new speed distribution, which is no longer Maxwellian, to describe an effusive beam:

$$f_{\text{beam,speed}}(v) = \left(\frac{m}{\sqrt{2}k_B T}\right)^2 v^3 \exp\left(-\frac{mv^2}{2k_B T}\right). \tag{4.5}$$

Both of these probability distributions are plotted in Fig. 4.6. Using $m = 7m_p$ and $T = 500°\text{C}$, we integrate both distributions up to v_c to find probabilities $P_{\text{MB,speed}}(v < v_c)$=3.8 $\times$ 10^{-5}, and $P_{\text{beam,speed}}(v < v_c)$=9.4 $\times$ 10^{-7}. From these calculations, we concluded that we needed a Zeeman slower to slow a larger fraction of our atomic beam to below v_c.

Our design target capture velocity for the Zeeman slower was 1000 m/s, allowing us to capture around 10% of the atomic flux from the oven (shown as shaded region in Fig. 4.6). Higher targets would have allowed us to capture more atoms, but were infeasible due to the large magnetic fields and detunings required. We elected to go with an electromagnetic design rather than a permanent magnet design, due to the ability to turn off the field and the relative ease of winding a tapered solenoid.

In the following sections, I discuss details of the field design, solenoid winding and electronics, and water-cooling considerations. The optical details of the Zeeman slower and post-slower transverse cooling may be found in section 4.2.1.

Zeeman field design

Zeeman slowers are typically designed in one of three ways: increasing-field, decreasing-field, or spin-flip. Increasing-field slowers start at low field and end at an extremely high

field, which can cause fringing-field problems at the MOT position; they also require large laser detunings, corresponding to the entire Doppler shift of the fastest atoms. Decreasing field slowers are nice in that they typically end at low fields and require relatively smaller detunings; however, these fields can result in continued slowing of the atoms after the intended end of the slower, resulting in a broadened atomic velocity distribution. Low-detuning slower light also could potentially disrupt MOT loading.

Rather than either of these designs, we chose to build a spin-flip slower. The slower typically starts at some high-magnitude field, pass through zero-field, and end at a moderately high-magnitude field of opposite sign, effectively giving us the best of both decreasing- and increasing-field slowers. Spin-flip slowers are not without their problems; since the field passes through zero, there will no longer be a quantization axis defining atomic spin, leading to possible flips to the non-cycling $F = 1$ manifold. This means we need to address atomic transitions in the slower with our repumping frequency in addition to the cycling frequency. Additionally, because the sign of the magnetic field flips, the polarization of slower light effectively flips from σ^+ to σ^-; because of this, it is advisable to allow the atoms a reasonable amount of time at zero-field to allow them to repolarize.

We can calculate that the Doppler shift of 671 nm light seen by atoms at 1000 m/s is 1.49 GHz, and by atoms at 50 m/s is 74.5 MHz. The Zeeman shift of lithium on the cycling $|F = 2, m_F = 2\rangle$ to $|F' = 3, m'_F = 3\rangle$ transition is 1.4 MHz/G, yielding a required overall ΔB =1.011 $\times$ 10^3 G. However, we can choose an overall detuning of our slower light to shift the maximum and minimum fields such that they are more easily experimentally accessible. We chose a detuning of 400 MHz red of the transition, which allow the maximum field to be 779 G and the minimum to be -232 G.

As discussed in Section 2.2.2, there is a maximum deceleration of the atoms which is constrained by the finite scattering rate of the atomic transition. This imposes a lower limit on the length of the slower. We assume that the maximum acceleration in the

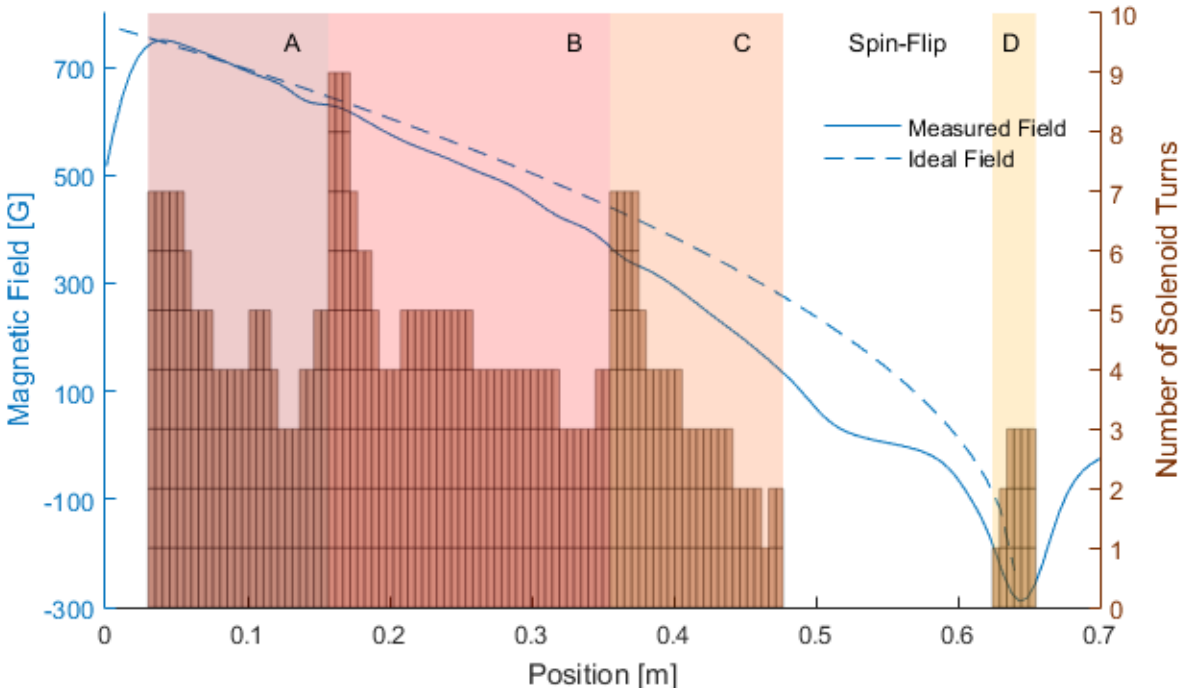

Figure 4.7: Lithium Zeeman slower: designed and measured fields

laboratory is half of the ideal maximum acceleration, due to experimental imperfections, and recover that our slower length should be around 0.62 m. We can then calculate the ideal profile for our slower, plotted as a dashed line in Fig. 4.7, assuming a slower light detuning 400 MHz red of the atomic resonance.

We used the same wire described in Appendix C.5 to wind the solenoids for the slower: alloy 101 OD 0.1875" wire with a wall thickness of 0.032", insulated with Daglass insulation. Some test coils were wound using thermally-conducting electrically-insulating Duralco NM25 epoxy; the resulting effective thickness of each wound layer of wire was 0.2". Using this effective size, Zach Geiger used MATLAB to simulate various tapered solenoid designs to produce the required field profile, allowing the atoms extra time at zero-field to fully repolarize. The resultant expected field profile may be found in his thesis; the wire profile is shown in Fig.4.7.

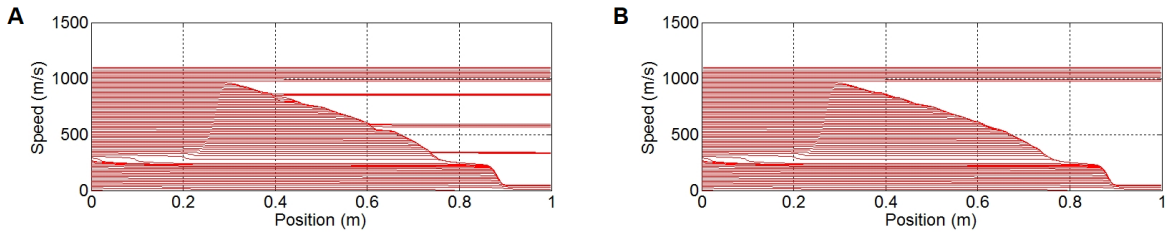

Figure 4.8: Lithium Zeeman slower simulations for an unshimmed slower (left), showing atoms with different velocity classes "escaping" the slower at positions corresponding to field imperfections between coils, vs. a shimmed slower (right).

Slower Coil	Power Supply	Design Current	Actual Current[1]
A	Sorenson DLM8-75	65 A	31.7 A
B	Sorenson DLM8-75	45 A	56.3 A
C	Acopian 0-8 V 40 A	27 A	29.5 A
D	Acopian 0-8 V 64 A	72 A	44.0 A

Table 4.2: Lithium slower currents

Solenoid winding and electronics

The slower was wound in 4 sections, labeled A, B, C, and D; the wire profile in Fig. 4.7 is shaded to show the demarcations. The field was designed to run currents shown in Table 4.2; the field profile of the wound solenoids was measured and is plotted as a solid line in Fig. 4.7. However, eventually the currents were all optimized empirically to maximize our MOT loading rate. The field produced by just the slower coils is unfortunately not perfect, particularly where the different sections abut each other; there are some bumps in the field profile which deviate from the ideal value by around 25 G (35 MHz). At these points, the field no longer compensates the Doppler shift as the atoms are slowed, and the slower "leaks" atoms. Zach Geiger did some simulations to study the velocity classes we would lose if we did not shim out the bumps in our field; Fig. 4.8 shows the velocity classes captured for an unshimmed slower (A) compared to a shimmed slower (B). Based on this, we added small many-turn 22 AWG Kapton-insulated motor-wire shims between each larger slower section and varied the currents using benchtop power supplies. The

only shim that improved MOT load rate, and the only one which remains connected now, is the shim between slower sections A and B (where the measured profile dip is largest).

During machine operation, the slower supplies are switched on and off using solid-state relays from Crydom and high-power diodes from Powerex (part numbers may be found in the Geiger thesis [18]). The power supplies are connected to the coils via custom-made lugs which press onto the stripped square wire leads with set screws, and mate to 10AWG wire also via set-screws. When everything is connected, we get a sizeable flux of atoms into the main chamber at speeds at or lower than MOT capture velocity.

Setback: In the summer of 2014, an alarming smell caught our attention.[a] One of the slower set-screw connections to the wire had come loose; the resultant higher impedance of the connection had led to higher power dissipation and then oxidization of the wire conductor, and the cycle had repeated until a wire was burned and smoking. We keep a close eye on and retighten all of those slower connections, and for any higher currents (e.g. for MOT coils) are careful to use crimp connectors. **Use crimp connections early and often**.

[a] Many impending disasters in our lab have been prevented thanks to keen senses of smell, which have also aided us in the acquisition of free food over the years.

Water-cooling considerations

The water flow rate needed in the turbulent flow regime to dissipate heat from square wire with a given side-length, copper cross-sectional area, hydraulic diameter, length, and pressure differential can be found in various books [51]; this flow rate, along with the power dissipated in the wire and the specific heat capacity of water, can be used to calculate the expected temperature rise. These calculations for our slower sections indicate that only slower section B requires water-cooling (see Geiger and Senaratne theses [18, 22] for more detail on these calculations).

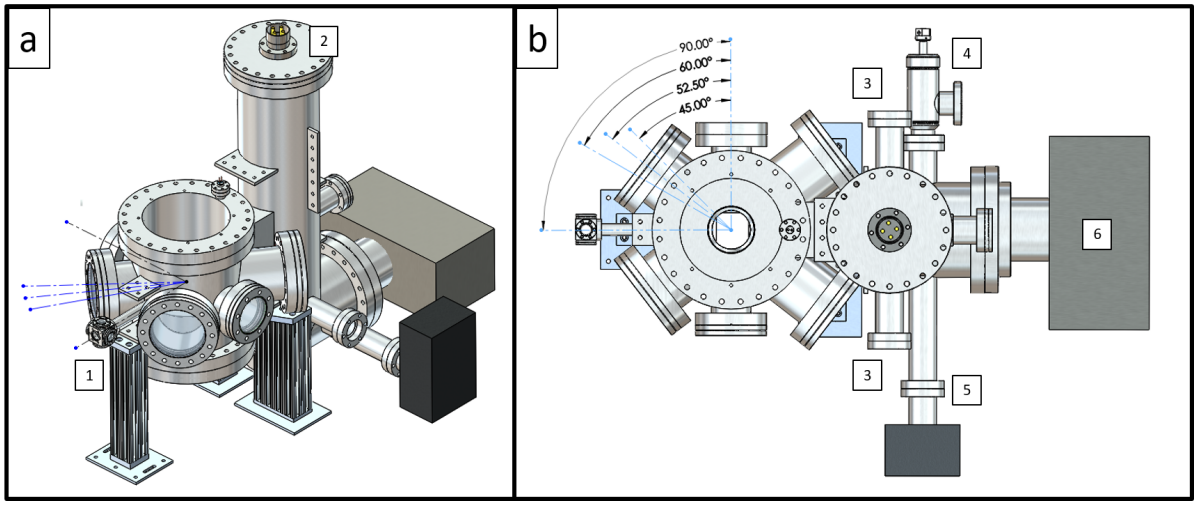

Figure 4.9: **(a)** shows a isometric view of the lithium oven manifold, such that the positions of the post-slower transverse cooling section (1) and titanium sublimation pump (2) may be noted. **(b)** depicts a top view of the same with a clearer view of the (3) ion gauges, (4) angle valve, (5) RGA, and (6) ion pump. It also shows the relative angles of the viewports around the chamber.

4.1.3 Main chamber

Once our atomic beam is slowed, it is captured in a MOT at the center of the main chamber. I will leave details concerning MOT parameters and optimization to section 4.2.2; this section will discuss main chamber design and considerations, MOT magnet construction and mounting, shim coils, and breadboard design.

Main chamber design

The main chamber is the heart of the experiment, where lithium is cooled from a MOT to degeneracy. Technical drawings for the MOT main chamber may be found in Appendix G. The lithium main chamber, shown in Solidworks schematic in Fig. 4.9, was based on the design of the BEC5 main chamber at MIT, custom-machined at the UCSB Physics Machine Shop, and electropolished by local company Electro-Matic. It is made entirely from 316 stainless steel, the magnetic permeability of which is much lower than that of 304 alloy. Generally speaking, it consists of a round stainless steel chamber with

several viewports around the top, bottom, and sides, connected to an L-shaped "chimney" through a wide rectangular tube. At the bottom of the chimney there are ports for two ion gauges, an angle valve, a residual gas analyzer (RGA), and a 75 l/s ion pump, and at the top of the chimney there is a port for a titanium sublimation pump. In the middle of the chimney, at the back of the main chamber, there is a 2.75" CF flange which allows propagation of light down the length of the slower. There are also several tabs welded onto various chamber locations so that it can mated to supports to an optical table; we bought supports such that the center of the machine viewports sit 12.6" above the optical table. This was intended to minimize vibrational instability, and indeed we haven't noticed any great issues from mechanical resonances; however, it does make it extremely difficult to access the bottom viewport of the machine.

Recall from the beginning of Chapter 4 that we need to realize magnetic fields at 800 G to access a Feshbach resonance, and field gradients up to 450 G/cm for magnetic trapping. Practically speaking, the importance of these items, both to cooling atoms and running experiments, means that we need to prioritize magnetic access over optical access. We accommodate this by designing re-entrant ("bucket") windows for the top and bottom of the chamber; the drawings for these may also be found in Appendix G. These 316SS bucket windows mate to 10" CF flanges, with additional tapped holes machined around the top surface to hold the MOT magnets in place. The buckets have an outside diameter of 6.50" and extend 3.82" into the chamber, and a 3.00" viewport sits in the center of the bucket; we can then design our MOT coils to fit inside the bucket very close to the atoms, allowing us to make large fields and gradients. The bucket windows also each have a small 1.33" CF flange welded to the outside to attach RF feedthroughs, as well as 4 small tabs with tapped M4 holes welded to the inside, to allow RF loops intended for state transfer. The viewports themselves are fused silica polished to $\lambda/8$ flatness, and coated for 323 nm, 532 nm, 671 nm, and 1064 nm; the AR curve may be found in Fig. H, also in Appendix H.

In order to maximize optical access as much as possible, rather than arranging a potpourri of small 2.75" and 1.33" viewports at various angles around the sides of the chamber, we decided to place 6 large CF viewports, (2) 4.50" and (4) 6.00", around the chamber. The 4.50" viewports are placed orthogonally to both the atomic beam/slower direction and the direction of gravity; the 6.00" viewports are placed on the same plane normal to gravity, but rather than cutting an angle 45° from both the 4.50" axis and the slower axis, these viewports sit at 52.5° from the 4.50" axis, and 37.5° from the slower axis. This angle was chosen because at the time, in addition to meeting an orthogonality condition for 1"-diameter MOT beams, there was some interest in conducting experiments with triangular and hexagonal lattices, which would have required beams at 120° relative to each other. The angled viewports split the difference, allowing 45° MOT beams as well as 2 mm-waist lattice beams at 60°. These angles may be seen in Fig. 4.9B.

All of the 6.00" viewports as well as the west-facing 4.50" viewport were chosen to be zero-length fused silica viewports from Kurt J. Lesker Company, but custom-made with 316SS flanges and coated for 323 nm, 532 nm, 671 nm, and 1064 nm (see Appendix H for the Lesker-designed AR curve).[2] The last 4.50" viewport was designed as an imaging axis, with a narrow re-entrant window designed for an objective with a fairly short working distance. The objective we ended up purchasing was an Optical Specialties 10X Plan APO OKHNL10 NIR with working distance 35 mm. However, this short focal length resulted in a problem, which was that the minimum bucket length required to place the objective 35 mm from the atoms resulted in cutting off MOT beams placed at 45°; we would either need to compromise on the MOT beam size or the angle. Based on calculations which indicated that MOTs should still function fine even if their beams largely deviate from orthogonality [52], we decided on the latter. This ended up being a poor decision, as we later found that adding a fourth MOT "helper" beam along the

[2]When the viewports actually arrived, Lesker had forgotten the 323 nm coating; rather than wait another few-month lead time for new ones, we forged ahead with what we had. This experience led to 1/4 of the infamous Lesker signs.

4.50" axis significantly boosted the load rate.

The 2.75" CF viewport along the slower axis, called the slower window, is made from 316SS and fused silica and coated for 671 nm only. It is enclosed, to the extent possible, in blue spring steel and thermal insulation, and kept at 140°C to mitigate buildup from the impinging atomic beam. There is also a Thorlabs 405 nm LED which we found helps desorb lithium (via laser-induced acoustic desorption, or LIAD) from the window surface; we have found that turning the diode on leads to a measurable pressure spike in the main chamber, and have successfully used it to clean viewports on our 671 nm spectroscopy cell. We have found this preferable to designs incorporating in-vacuum mirrors for the slower beam.

The chimney on the main chamber was designed to optimize conductance to the main ion pump, a 75 l/s Varian Starcell pump from Agilent. Because we were (maybe overly) concerned with lines-of-sight and numbers of atomic "bounces" between the atomic cloud and the ion pump, the pump was ordered with custom optical baffles. Details of the ion pump as well as other parts in the lithium main chamber may be found in Table 4.3.

Main chamber assembly proceeded smoothly, with one notable exception: the bucket windows needed to be installed on the chamber while simultaneously winding RF loops (33 mm × 111 mm), which we intended to use for spin-flip transitions in experiments. In order to do this, custom (UHV-safe) copper connectors were designed to connect the wire to the RF feedthroughs on the bucket windows. The wire needed to be routed such that it never shorted to the chamber, and the connections to the inside of the bucket windows were made with ceramic screws, nuts, washers, and beads. Figure 4.10 shows all three re-entrant windows through one of the 6.00" ports, as well as the two RF loops wound in place.

The lithium main chamber was baked in late 2013 (see Appendix B for details) and pressure of 1.0×10^{-11} were achieved. However, there was an issue with the side view-

Table 4.3: Lithium main chamber part numbers

Function	Company/Part Number	Purchased From	Notes
Ion Pump	Varian VacionPlus 75 Starcell Pump 9191440m006	Agilent	Optical Baffles
Ion Pump Controller	Varian Minivac Fischer HVConnector 9290191	Agilent	
Ion Pump Cable	HV Bakeable Cable 13' w/interlock 9290705	Agilent	
Ion Gauges	Agilent/Varian UHV-24P B-A	Ideal Vac	
Ion Gauge Controller	Agilent XGS-600	Agilent	
Ion Gauge Cables (2)	Agilent R32453010 for XGS-600 Controller	Agilent	
TiSub Cartridge	Varian Filament TSP 9160050	Agilent	Attached via 2.75" to 6" reducer
TiSub Cable	Agilent 9240730, 3.6m	Agilent	Also used for Sr machine
TiSub Controller	Agilent 9290032 with RS232	Agilent	Also used for Sr machine
Residual Gas Analyzer	ExTorr XT100M	ExTorr	Typically left disconnected
Angle Valve	MDC 314003, All-Metal	MDC	Torque-sealed according to chit

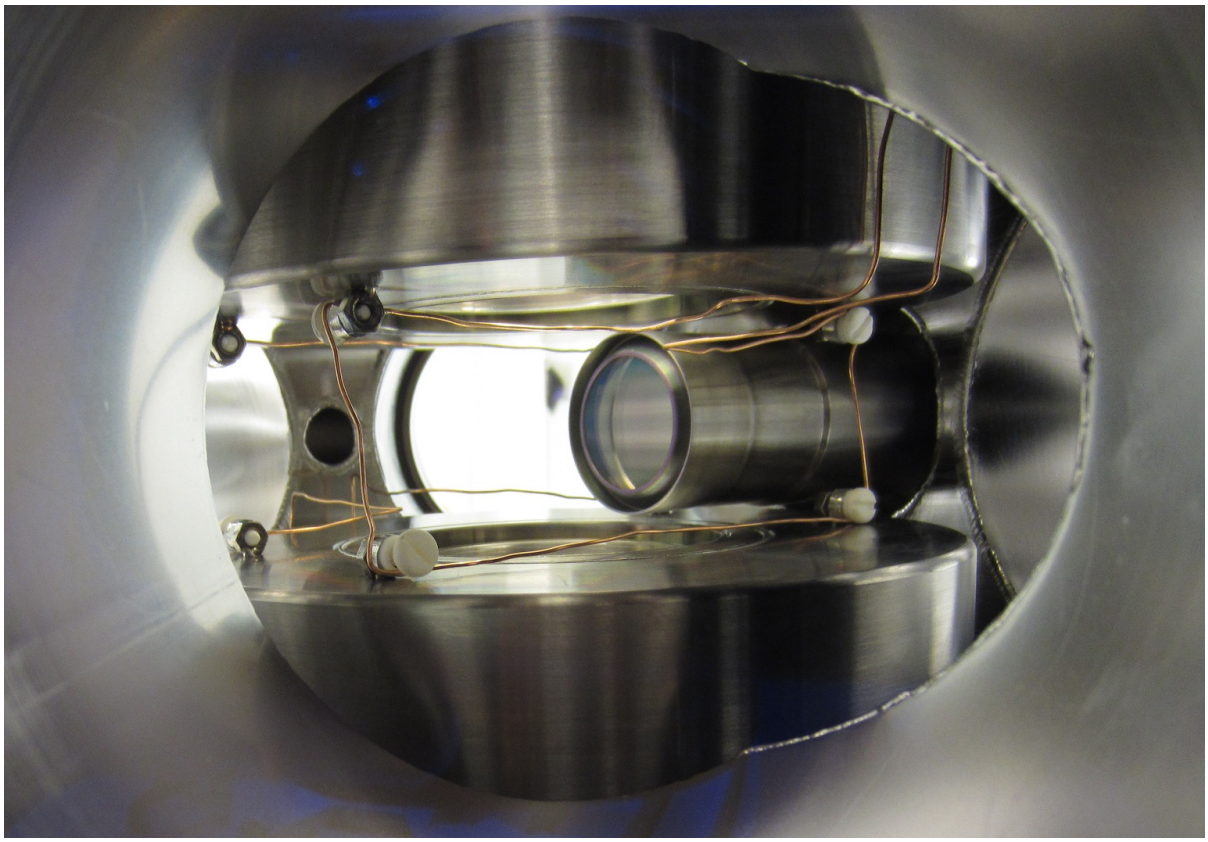

Figure 4.10: Lithium main chamber bucket windows (top, bottom, and side) and now-defunct in-chamber RF loops.

port coatings[3], and we decided to rebake in the summer of 2014 after replacing the affected windows. Unfortunately, after the bakes, the atmosphere-facing side of the RF feedthroughs had become so brittle that they immediately broke when we attempted to attach them to external electronics. Thus, the RF loops languish sadly in the lithium chamber, and all RF is applied from outside the vacuum.

MOT magnet design and construction

The magnets described in this section will be referred to as "MOT coils", but it is important to keep in mind that they serve multiple functions: they create the field gradients necessary to both trap a MOT and magnetically trap the atoms, but they also create

[3]This led to another 1/4 of the infamous Lesker signs

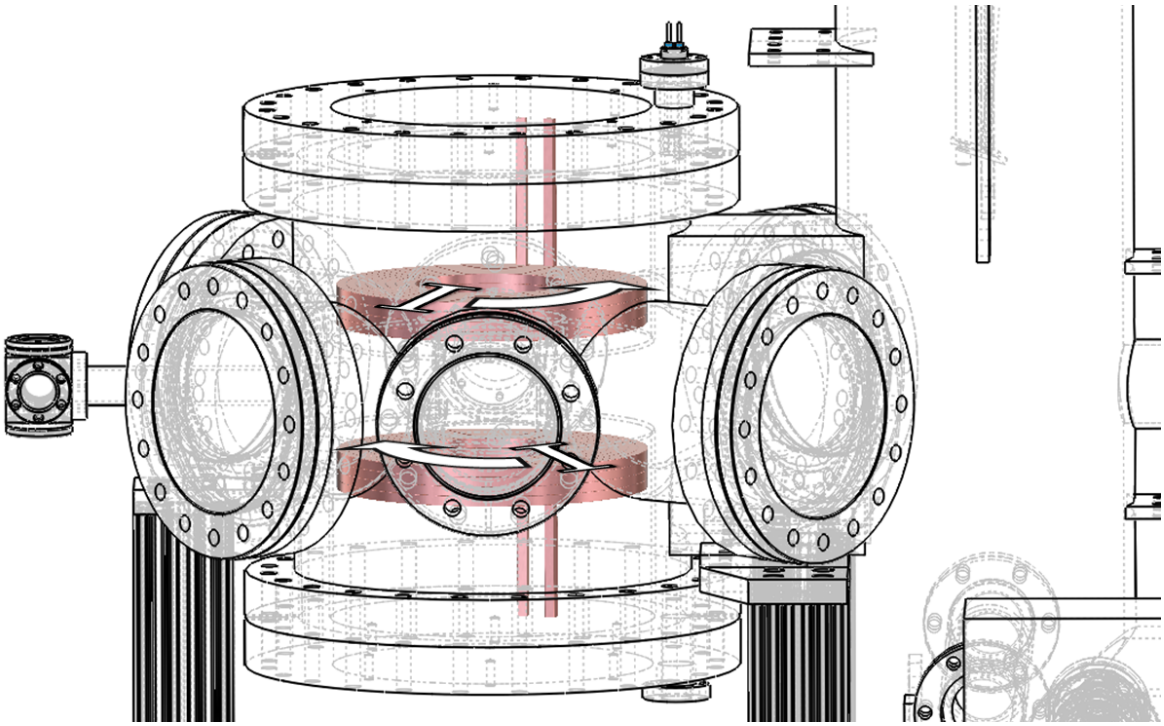

Figure 4.11: Lithium MOT coil directions of current flow (anti-Helmholtz configuration).

Coils	Configuration	Field Produced	Peak Field (500A)
Inner (1-4)	Helmholtz	1.72 G/A	860G
Outer (5-8)	Helmholtz	1.75 G/A	875G
Inner (1-4)	Anti-Helmholtz	0.516 G/cm/A	258 G/cm
Outer (5-8)	Anti-Helmholtz	0.33 G/cm/A	165 G/cm

Table 4.4: Lithium MOT fields

the Feshbach fields necessary to tune scattering length during optical evaporation and experimental sequences. Since they are required to create both flat uniform fields and linear field gradients, we use two coils placed on either side of the atoms with a separation necessary to satisfy the Helmholtz criterion: coil separation z is equal to the coil radius r_0. By flipping the direction of current in one of the coils, we should be able to switch between anti-Helmholtz and Helmholtz conditions.

Strictly speaking, the Helmholtz condition can only be met for infinitesimally small wires; any finite size will result in some part of the current not satisfying the separation

requirement, thus leading to some unwanted curvature of the field. The currents were simulated on Mathematica for varying geometries to give us a sense of the behaviors of the 0th, 1st, 2nd, and 3rd derivatives of the field in both anti-Helmholtz and Helmholtz configurations; these geometries were constrained by the dimensions of the bucket windows, which allowed a maximum OD of 6.4", a minimum OD of 3.1", and a minimum separation of around 1.9". Each coil was eventually designed to have an ID of 3.1", with a cross section of 32 turns: 4 turns in $\hat{z}$ × 8 turns in $\hat{r}$, with every set of 4 turns in $\hat{z}$ × 2 turns in $\hat{r}$ being one continuously-wound solenoid. The inner 4 radial coils are referred to as coils 1-4, and the outer 4 are referred to as coils 5-8; we thus have two leads each (an input and output) for pairs 1 and 2, 3 and 4, etc. These coils were mounted 6.7 cm away from each other to avoid mechanical noise from the magnets affecting the chamber, and measurements were taken *ex-situ* to look at the resultant fields (gradients) in G/A (G/cm/A). A summary of these can be found in Table 4.4, as well as the peak values when the magnets are run at 500 A. Summing the contributions from all 8 coils, we can see that we can readily reach the fields and gradients we need.

The curvature of each coil was also measured around the same time. The outermost coil met the Helmholtz condition with minimal curvature, but the contributions to the curvature from each set of coils all had the same sign, leading to some noticeable field curvature which we can measure in the chamber by looking at atomic behavior. Mitigating it requires some clever wiring and new sets of coils to compensate. In the future, we should try to consider the curvatures of each coil separately and design them to have opposite signs as much as possible, so we can ease the process of curvature cancellation. For better accounts of these ventures and all of the measurements taken, I refer the reader to any of the lithium theses, the Fujiwara thesis in particular, as well as the "Lithium Useful Info" binder in our lab.

The coils were wound in the same way as the Zeeman slower solenoids described in Section 4.1.2, the only difference being that rather than winding the coils around a

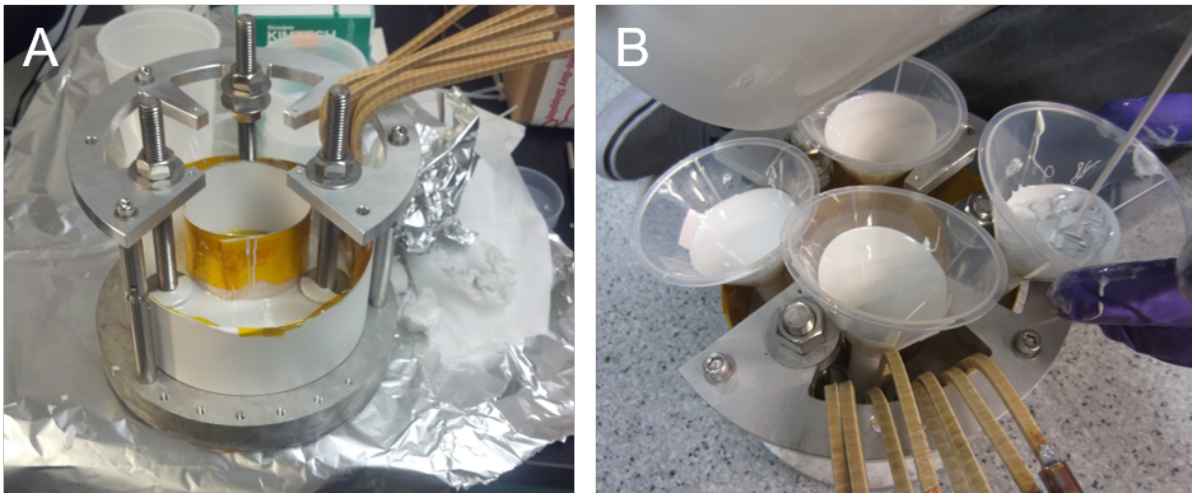

Figure 4.12: Lithium MOT magnet epoxy potting

brass tube, we wound a custom piece of aluminum machined to have the proper OD and covered by Kapton foil for easy removal.[4] We then had to find a way to securely mount each coil in the machine. Our solution, following the advice of others in the community, was to "pot" the magnets in a large pool of epoxy with (3) 1/2"-13 316SS set screws. We designed an adapter plate which could mate these 3 screws to the tapped holes on the top of the bucket window. We wrapped Kapton film and paper around the magnets to contain the epoxy as much as possible, and designed a rig to keep the adapter plate level with the magnet, and the screws as normal as possible to both. We then poured in the same epoxy which we used for the magnet winding, and allowed it to set. During a test run (Fig. 4.12A), we prepared a large batch of epoxy and had difficulty getting it to set properly; we later used many small batches (Fig. 4.12B), to much greater success.

The coils are run at up to 500 A, which presents some difficulties both in terms of thermal management and electrical power. The results of thermal calculations (details of which may be found in the Senaratne thesis) assuming 500 A of current necessitates the use of high-pressure water cooling. The ends of each of the leads was soldered to copper

[4] "Easy removal" ended up being 3 people synchronously beating the magnet off of the aluminum piece with rubber mallets.

Component	Part	Rating
Inner Coil Supply	TDK Lambda ESS 20-500	20 V, 500 A
Outer Coil Supply	TDK Lambda Genesys 20-500	20 V, 500 A
Isolation Amplifiers	AD215BY-ND	
IGBT	Powerex CM600HA-24A	1200 V, 600 A
Ringdown Diode	Vishay Spectrol VS-SD1100C12C	1200 V, 1400 A
Varistor	Littelfuse V661BA60	1050 V, 70 kA
H-Bridge Relay	Kilovac LEV200A4NAA Contactor	900 V, 500 A
Earth Shim Supply	Acopian YL06MC270C6	
Applied DC Shim Supply	GWInstek Benchtop	
Shim MOSFETS	IRL3103PBF	900 V, 64 A
Shim Diodes	VFT1045BP-M3/4W	45 V, 10 A

Table 4.5: Lithium electronics for high currents

tubing for water cooling in the same way as the slower solenoids, and the cooling lines were connected to the water manifolds detailed in Appendix C.2. The current carried in the electrical connections required that we use 3/0 wire, which is difficult to work with. The lugs we initially used were as susceptible to the same set-screw-loosening problems as the slower solenoid lugs, if not more so due to the larger currents running through them. The lugs were redesigned to connect a copper compression lug to a significant length of copper tubing, and all of the water connections were redone to lengthen the copper tubing to at least 2". The copper compression lug then allows mating to 3/0 wire in a mechanically- and electrically-secure way, preventing fires in our lab.

The MOT coils are powered by two 10 kW power supplies, which was effectively the most powerful we could find at 208 V 3-phase power (we do not have 480 V supply in our lab). The outer turns (5-8) on both the top and bottom coils are powered by a TDK Lambda Genesys 20-500, while the inner turns (1-4) on top and bottom are powered by a TDK Lambda ESS 20-500. Both supplies exhibit similar ramping speeds, so we can consider the inner and outer turns effectively as one large coil. The currents are controlled via analog voltage lines, which connect to the power supplies via isolation amplifier circuits to avoid ground loops.

The lithium cooling sequence requires fast manipulation of magnetic fields and field gradients (quantitative values may be found in Section 4.2). In brief, we require high field gradients for a MOT, low uniform fields for gray molasses, very high gradients for magnetic trapping, and then very large uniform fields for thermalization during optical evaporation; successful cooling, therefore, entails a lot of high-current switching in magnets which have extremely large inductance. Using IGBTs and ring-down diodes enable us to turn off our MOT coils in tens of μs. Due to the large amount of power dissipated, both the IGBTs and diodes are water-cooled with Lytron cold plates (aluminum plates with press-fit copper tubing for water). The switching also generates a large induced spike in electromotive force, against which we protect our power supplies by using varistors. The field must then switch back on quickly for magnetic trapping. This is achieved by using a capacitor bank, based off of an MIT design [53]. Charging the capacitor bank for a few seconds allows ramp-up to four times the MOT field gradient in 100 μs. In order to switch our field configuration from anti-Helmholtz to Helmholtz so we can access the Feshbach resonance at 737 G, we switch the polarity of the bottom MOT magnet using a relay circuit, which is effectively an H-bridge. Part numbers for all of the main chamber electronics may be found in Table 4.5; circuit diagrams and discussion of thermal stability concerns may be found in the Geiger and/or Fujiwara theses [18, 47].

RF antenna

Since our in-vacuum antenna feedthroughs broke after two bakes, we needed to design an external antenna to apply all of our RF fields. Many of the antenna design details can be found in the Geiger thesis [18]. We went through many iterations but settled on a spiral loop design, the characteristic inductance and capacitance of which yielded an approximately flat response from a gigahertz roughly down to 800 MHz. It was built with flat copper ribbon cable soldered onto SMA connectors and characterized using a small motor-wire test loop and spectrum analyzer; a custom 3-d printed mount was

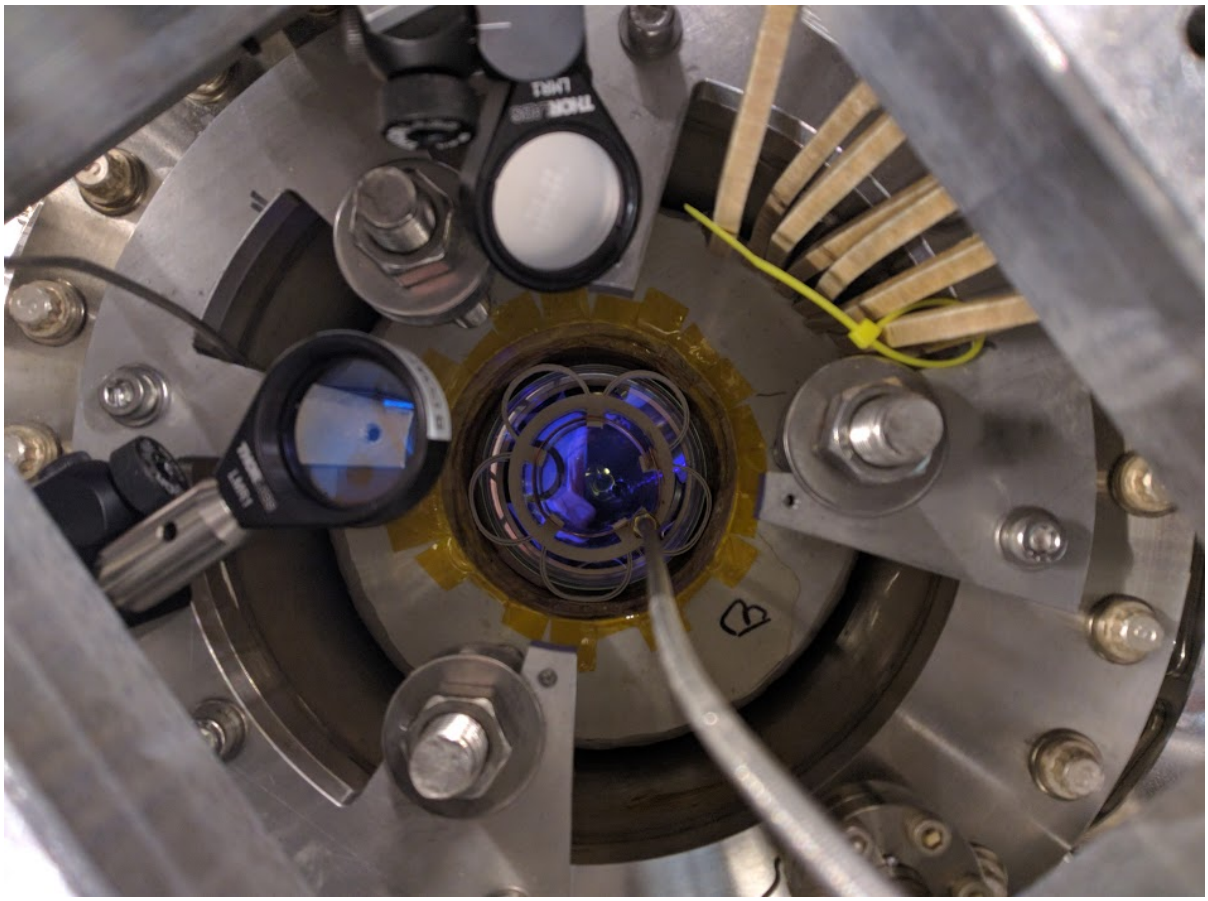

Figure 4.13: Top-down view of main chamber. The RF antenna (connected to the coaxial cable in lower right) is held in place by a custom 3d-printed mount directly above the viewport. The potted MOT coils and MOT coil mounting plate are also visible.

also designed to hold the antenna in place inside the top bucket window. To drive the antenna, we use a Minicircuits VCO and a 200 W Ophir 5020 amplifier; to protect the electronics, we also send the RF through a high-power circulator and terminator, both from Fairview Electronics.

Shim coils

Earth's magnetic field provides a constant background of around half a Gauss underneath any field or gradient we produce in lab. This means that if we are ramping up a field gradient, as we do during magnetic trapping, the location of the field zero will move in

space as a function of the gradient. This is untenable, as we actually need to "plug" our magnetic trap with a 15 μm-waist beam to prevent Majorana spin-flip losses (see Sections 2.2.3 and 4.2.5). To overcome this problem, we need to compensate for the earth field (and any other stray fields from, for example, a neighboring lab) with sets of Helmholtz shim coils. To be able to compensate a field in an arbitrary direction, we need three sets of transverse coils. In practice, we actually wind two sets of coils in each dimension: the first is used to shim out background fields, while the second can be used to apply small DC bias fields for e.g. optical pumping.

These shims are typically wound on supports which are built *in-situ* after the machine is up and running; they are designed from U-channel aluminum which has been sandblasted and coated with Plastidip to prevent wire shorts. It becomes much easier to build supports and wind coils for a square geometry; we can calculate that the Helmholtz condition can still be met for square coils with side length d for separation $z = 0.5445d$. We use the same 22AWG Kapton-insulated motor wire for these earth shims as we do for the slower shims, and wind a few decades of turns around the machine *in-situ*. These coils typically run about 1 A from linear power supplies and are turned on and off with MOSFETs and ring-down diodes, which allows us to switch small fields quickly and with very little noise.

Breadboard design

Every machine needs more breadboards all the time, because extra optical space is always useful. For the lithium machine, we designed four large breadboards which were attached to the optical table and to each other, but were independent from the machine. They are all made from MIC6 aluminum alloy, which is extremely stable compared to other aluminum alloys and retains its flatness when tooled. The three breadboards which attach to the optical table are 1.25" thick with a flatness tolerance of 0.030" and cast with the grain along the longest direction; the top breadboard, which attaches to the

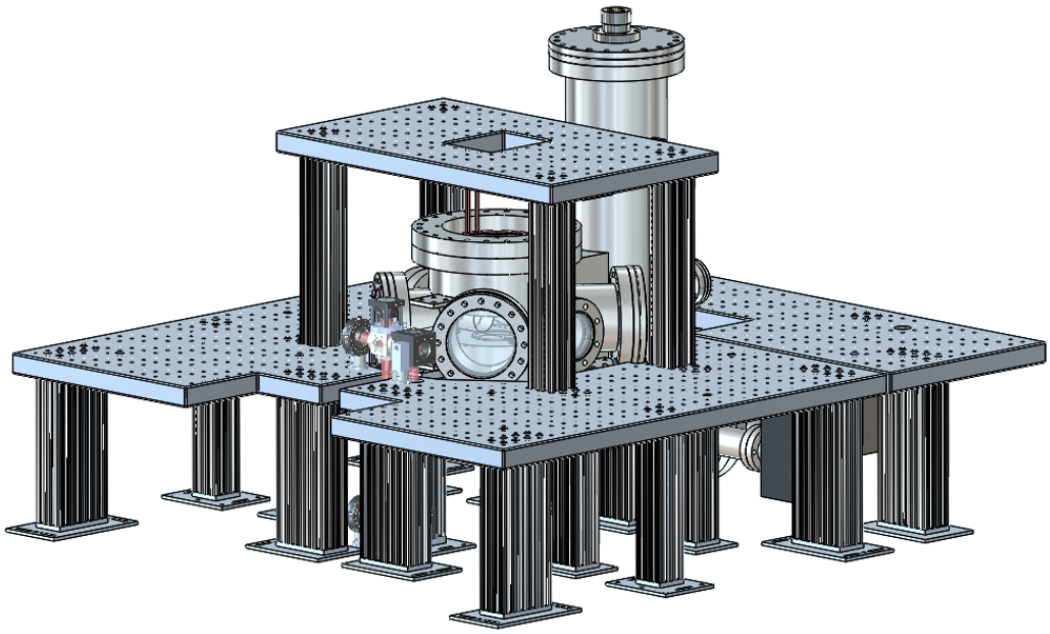

Figure 4.14: Lithium breadboard design

two side breadboards, is 1.00" thick with the same tolerance and grain. The breadboards were ordered from a local Alcoa distributor, and machined according to our specifications by the UCSB Physics Machine Shop. The design includes standard 1/4"-20 holes along a 1" grid, as well as various cutouts to allow beams to pass through. They are mounted on 80/20 and custom-designed optical table mounting feet, such that the center of 2" tall optics on the breadboards aligns roughly with the center of the main chamber. The design was tested for vibrational stability using Solidworks simulations, and was designed such that the majority of mechanical resonances were solidly above 1 kHz. The breadboards are shown in Fig. 4.14. Technical drawings may also be found in Appendix G.

4.1.4 671 nm laser

The 671 nm laser system is the workhorse of the lithium experiment. This section will describe the castle of 671 nm light sources we use to generate the frequencies required to cool lithium atoms. It will not include laser table diagrams; for the full laser table

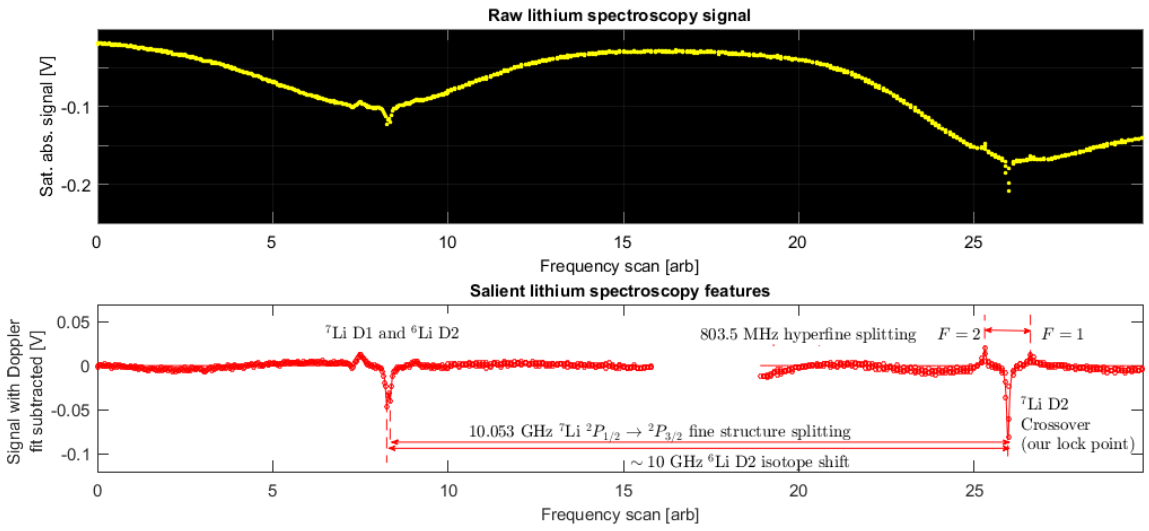

Figure 4.15: Lithium D1 and D2 saturation-absorption spectroscopy

layout, please refer to the Singh thesis [19], and for the subsystem layouts and frequency shifts, please refer to the Geiger thesis [18].

Master laser and spectroscopy

The master laser is a Toptica TA-Pro ECDL+MOPA system which uses an LD-0670-35-AR-2 671 nm diode (the diode and grating assembly were replaced in late 2016; the new diode has a max current of 119 mA). We measured the linewidth to be around 500 kHz by performing a self-heterodyne measurement. The internal mirror which is typically used to shunt a little bit of light to an auxiliary port was replaced almost as soon as we bought the laser with a high-reflectivity mirror, as we found we needed as much TA seed power as possible. The TA-Pro was rated for 500 mW when purchased; the output decayed to 300-320 mW near the diode's maximum current after the first few months of operation, and has held constant over the past few years.

A small fraction of the light produced by the master continues to a spectroscopy cell, which was designed by Zach Geiger. This cell was loaded with a small amount of lithium in an inert buffer gas of argon. The cell was pumped down to 10 mTorr and operated at

350°C, conditions which were eventually chosen to set the mean free path of lithium in the cell small enough so that it would not coat the windows, and large enough so that the atomic density of the accessible lithium cloud gives us a reasonable spectroscopic signal. The saturation absorption spectroscopy signals showing ^{7}Li $F = 1$ and $F = 2$ ground states and crossover signals for the D1 and D2 lines may be seen in Fig. 4.15, on top of the Doppler-broadened absorption profiles. As expected from the level structure, the fine structure splitting is 10 GHz, while the hyperfine splitting is 813.5 MHz. Recall that the isotope shift for lithium is around the same as the fine-structure splitting; we actually see the ^{6}Li D2 line almost overlapped with the ^{7}Li D1 line. We measure the linewidth of the Doppler-free peaks to be around 30 MHz, about 5 times the linewidth of the transition. This broadening comes from unresolved excited-state structure. We use a Toptica Digilock lock-in amplifier module to modulate the probe frequency and lock the master laser frequency to the ^{7}Li D2 crossover.

Tapered amplifiers

We purchased a 500 mW 671 nm BoosTA from Toptica at the same time as the master. The output power has also drifted down to about 300 mW with around 30 mW of seed power. We also developed a home-built TA design which has turned out to be remarkably stable for 671 nm chips, using Eagleyard EYP-0670-00500-2003-CMT02-0000 chips. They were largely developed by Kevin Singh; the designs and drawings may be found in an appendix of his thesis [19].

The master laser is used to seed the BoosTA, the output of which is used for the MOT cycling transition, as well as one of the home-built TAs, the output of which is used for the MOT repumper transition. A small amount of light is chipped off of each of these beam lines and mixed on a cube for tranverse cooling (see Section 4.2.1).

We also use a TA on the machine table to generate light for gray molasses.

Slave lasers

We use 2 slave lasers in the 671 nm setup; both of them are seeded with around 200 μW of power, and produce around 100 mW. We used HL6535MG diodes in Arroyo 224 TEC TO-Can mounts and Thorlabs isolators IO-5-670-VLP. These diodes natively lase at around 660 nm, but we pull their temperatures to make them lase around 10 nm higher. One of the benefits of using slaves is that they are a highly non-linear frequency filter: we can use them after EOMs to select the amplified sidebands. For the gray molasses system, we use a 9.2 GHz EOM to cool on the D1 line, use a slave to filter and amplify the correct sideband, amplify the light further using a TA, and then use another EOM to add a sideband for two-photon transitions (more detail can be found in Section 4.2.3). We also use a slave laser and an EOM on the machine table to generate Zeeman slower light.

4.1.5 532 nm and 1064 nm lasers

Here are brief descriptions of the far-off-resonant laser systems used for the lithium experiment; again, the lithium theses from this group may be consulted for more detail, including full optical setups.

532 nm light

During magnetic trapping and RF evaporation, Majorana spin-flips can lead to significant atomic loss near the field zero. (see theory in Section 2.2.3). To prevent this, we use a 532 nm laser, blue-detuned from the 671 nm transition, to exert a repulsive AC stark force at the field zero, effectively "plugging the leak" in the center of the magnetic trap. This light is produced by a Lighthouse Photonics Sprout-G 10 W laser, which is focused to a 15 μm waist. We found that retention of the Gaussian mode and beam shape was very important to efficient plugging of the trap. Using an AOM changed the mode enough

to make it an untenable solution for fast mode-switching. Instead, we use a Pacific Laser Equipment RSC-103E waveplate rotator to turn the beam power from 10 W to 300 mW in 200 ms, and then use a physical beam shutter to block the beam entirely after optical evaporation. We use Thorlabs fused silica V-coated YAG lenses to focus the beam, since they have better thermal properties at high incident power.

The beam is directed into the chamber using a mirror with picomotor adjustment, and roughly focused onto the atoms using an imaging system and dichroics. Once depletion from the beam can be seen on the atomic cloud, the picomotors are used for fine adjustment.

1064 nm light

Like many other groups, we use 1064 nm light for both optical dipole traps (ODTs) and lattices. We use an Orbits Lightwave 60 mW laser (Ethernal Slow Light model)[5] to seed a 50 W Nufern amplifier (NUA-1064-PD-0050-D0) with 60 dB output isolation; this gives us a maximum of around 35 W at the atoms. The beam path sits on the machine table in a small enclosure made from aluminum, providing an additional layer of protection against IR to the rest of the machine table and to humans in the lab.

The 1064 nm light is shaped and focused by fused silica V-coat YAG lenses to minimize thermal lensing issues. We initially used 1 mm-aperture Intraaction AOMs (ATM-801DA6) to switch some of the 1064 nm beams. However, we found that the thermal properties of this AOM were not good enough for such high powers, which led to a great deal of pointing noise. We switched to solely using the 2 mm-aperture models ATM-802DA6, which helped significantly, but also found that dissipated power trapped in the enclosure still led to some thermal drift. We began to forced-air-cool the 1064 nm enclosure using small computer fans, which helped thermal stability; they can be TTL'd off

[5]We are currently using the strontium NKT seed for the lithium experiment, as the Orbits broke about a year ago (see Section 5.1.7). The Orbits has been repaired and returned to us, but has not yet been replaced on the lithium machine due to activation energy.

during times when we need excellent mechanical stability.

The power directed to the ODTs versus the lattice beams is controlled by two Thorlabs waveplate rotators. One of the ODT beams is directed into the chamber using a mirror with picomotor adjustment, to keep the combined crossed trap as deep as possible.

4.1.6 Cameras

We use several cameras for several different imaging axes. The main camera, used to take the majority of images for experiments, is a PCO.edge 5.5 CMOS camera set up with a magnification of 2.5 (diffraction-limited spot size of 5.5 μm) and looking along the vertical (gravity) direction. In addition to this, we use several auxiliary cameras to monitor fluorescence and aid in beam alignment. These auxiliary cameras are all Basler aCA1920-25um CMOS cameras set up with varying magnification.

4.2 Lithium Cooling

This section will discuss details of each step in the lithium cooling sequence, including detunings and saturation parameters. For details on construction, please see the previous section.

4.2.1 Transverse cooling and zeeman slower

Transverse cooling stage 1

After the nozzle, the atomic beam passes through a coldplate to block any widely-diverging atoms; the beam may be seen fluorescing due to slower light in Fig. 4.16. Immediately after this, we have a section of 2D optical molasses on the D2 line to help collimate the beam further. This transverse cooling section addresses the atoms over a longitudinal spatial extent of 3-4 cm; we can do a back-of-the-envelope calculation to

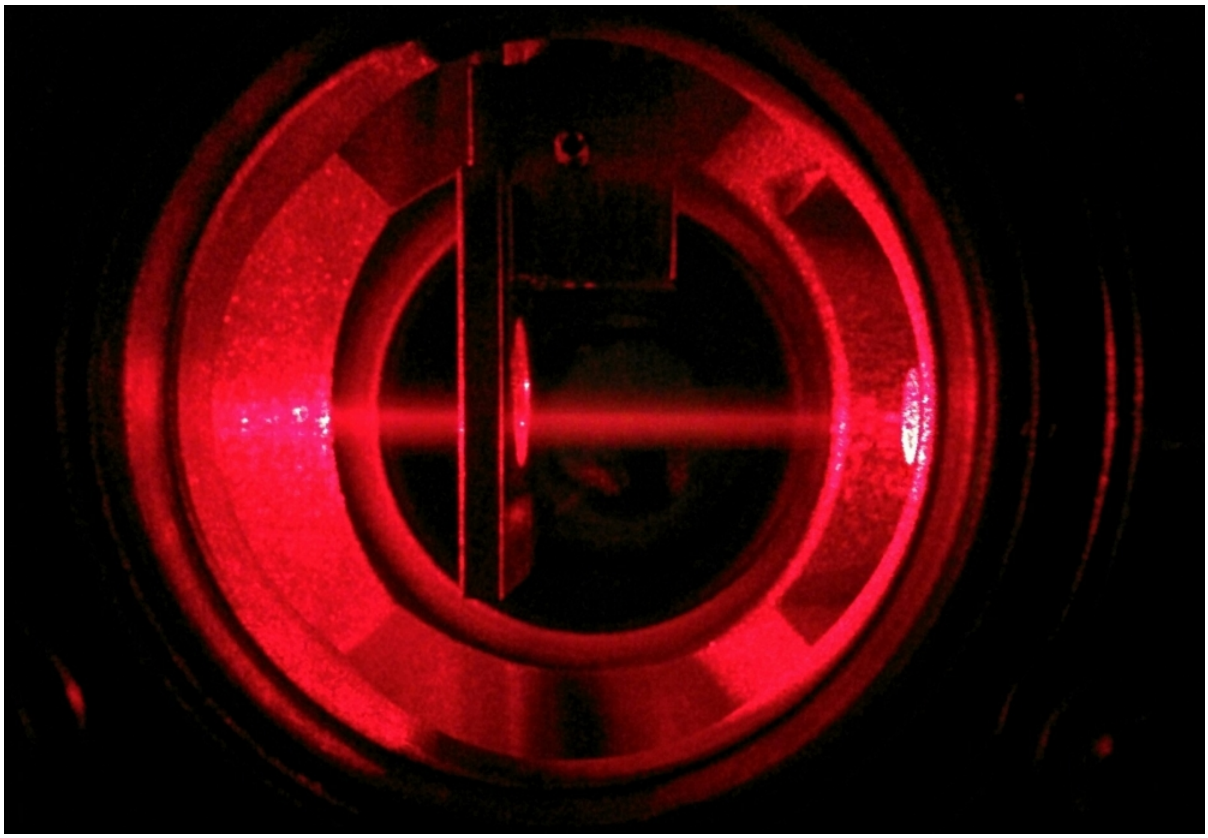

Figure 4.16: The atomic beam fluorescence from slower light is shown in the cold plate section of the oven. This axis provides nice access to take tranverse absorption measurements to characterize the atomic beam.

estimate the number of scattering events which can potentially occur over that distance, and find that it is large enough to necessitate cooling with both cycling and repump light for optimal efficiency. The cycler light operates at a detuning of about 3.7Γ and a saturation parameter $s \approx 0.3$, while the repump light operates at a detuning of 5.4Γ with around a quarter of the power; these parameters were all set empirically with the constraint of the amount of power we have available. When adjusting the balance of the beams, we found that in only one of the four transverse directions did our cooling have any effect (vertical from the top); at its best, we saw improvement in the MOT loading rate by around 30%. We suspected that the direction of the beam was angled slightly opposing gravity, such that only that beam helped cool atoms towards the center of the

chamber. This cooling stage is being reoptimized post-2018 bake.

Zeeman slower parameters

Full details of the Zeeman slower design and magnetic fields may be found in Section 4.1.2. As noted in Section 4.1.4, our slower light is generated by seeding a slave laser with 200 μW of power to generate around 100 mW. Recall from Section 4.1.2 that the slower fields were designed for a detuning of around -400 MHz; we then empirically optimized this detuning to -389 MHz. This light then passes through a home-built EOM to add sidebands at 813.5 MHz, almost equivalent to the hyperfine splitting[6], which effectively introduces some fraction of repumping light to the slower beam. To keep from having problems with blue-detuned sidebands, the 0 order of the EOM was chosen to be -389 MHz from the cycling transition, and the +1 order was chosen to have the same detuning from the repumping transition. The -1 order is then too far red-detuned to affect the atoms. Cubes and waveplates are used to clean up the polarization of the beam. By the time the light enters the chamber, we use around 33-34 mW of cycler power (around $2 \times I_{sat}$ at the slower window) and 8-9 mW of repump power. The beam is weakly focused to about the size of the atomic beam at the nozzle.

Transverse cooling stage 2

After the slower, we have a second section of 2D optical molasses on the D2 line to help collimate the beam further (see information on the first stage in section 4.2.1). This stage helps us address what could otherwise be a concerning "beam explosion;" since slower greatly reduces the mean atomic beam velocity in the longitudinal direction but increases velocity spread in the transverse directions due to spontaneous emission recoil events, the angular divergence of the atomic beam at the slower exit is much larger than it was at the slower entrance. Having a second stage of transverse cooling helps to maximize the

[6]See Section 4.2.7 for why we don't use the hyperfine splitting.

number of atoms which make it to the center of our main chamber and get captured in the MOT. We again have both cycling and repumping light; the cycler light operates at a detuning of about -3.7Γ and a saturation parameter $s \approx 0.15$, while the repump light operates at a detuning of -5.4Γ with around the same amount of power; these parameters were set empirically. Unlike in the first stage of transverse cooling, we find that all four transverse directions have a significant effect on cooling, and any misalignment or lack of power balance in the beams results in harming our atomic flux rather than helping it. When it is fully optimized, we see improvement in the MOT loading rate by a factor of three.

4.2.2 Magneto-optical trap

From this point onwards, all of the cooling is done at the center of the main chamber. Fig. 4.17 shows all of the beams and their relative locations.

As noted in Section 4.1.3, we used coils mounted in re-entrant windows and run in anti-Helmholtz configuration to generate field gradients. We run the power supplies at a relatively low current to create field gradients of around 20 G/cm. As noted in Section 4.1.4, the MOT light is sent from the lithium laser table to the machine table using a 2:6 non-polarization-maintaining single-mode fiber splitter (custom from Oz Optics), which allows us to separately fiber-couple the cycler and repumper light. The repump light is detuned from the transition by -5.4Γ, while the cycler is detuned by -5.8Γ. The four horizontal MOT beams typically have around 8 mW of cycler and 2-3 mW of repumper, while the two vertical beams have around 14 mW cycler and 5-6 mW repumper; the difference in power balance was simply chosen to preserve symmetry as much as possible given imbalance in the 2:6 fiber splitter. Later, we found we needed to add "helper beams" (see Section 4.1.3); these operate at a combined power of around 30 mW, of which around 1/3 is repumper. The total power in the MOT is around 110 mW, of

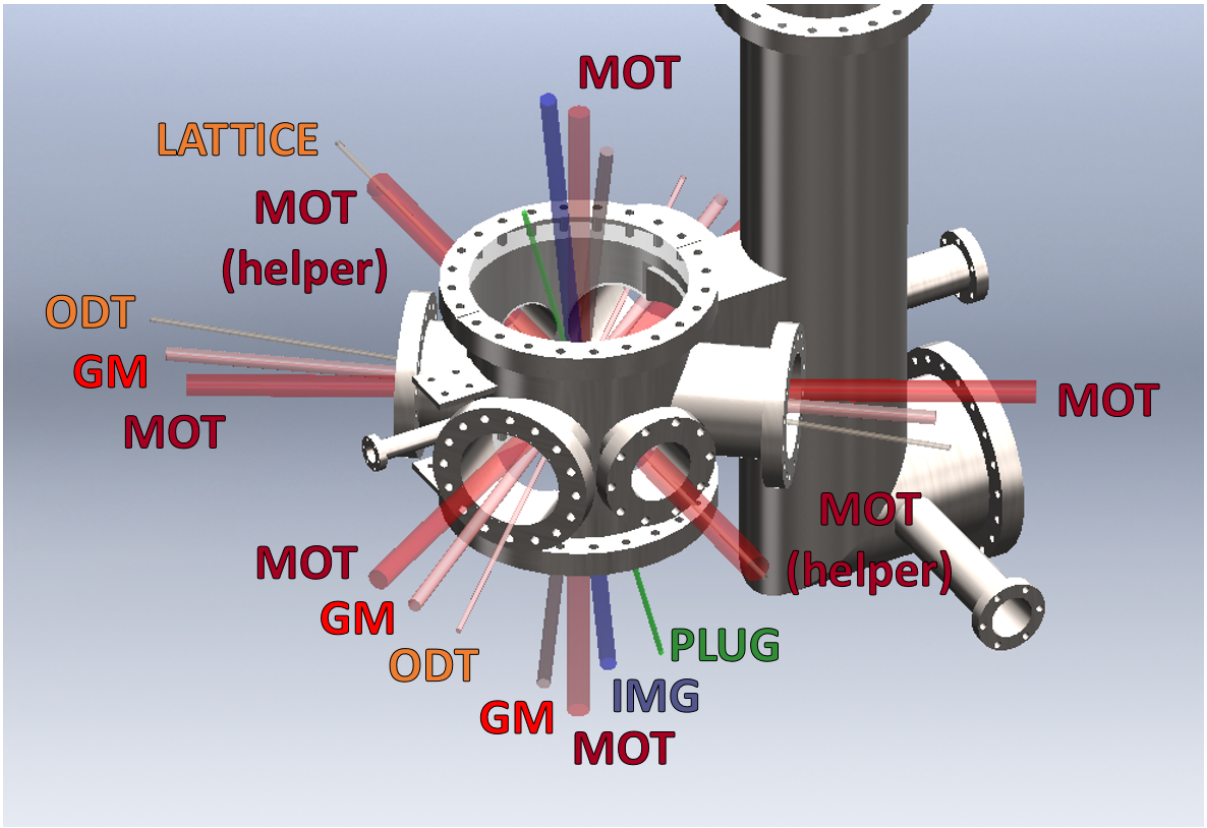

Figure 4.17: MOT, gray molasses (GM), plug, optical dipole trap (ODT), lattice, and vertical imaging beams (IMG) and their relative locations around the main chamber. Each beam is labeled on its respective side of entry into the chamber; retroreflections are neither depicted nor labeled.

which 80 mW ($s \approx 8.5$) is cycler and 30 mW ($s \approx 3.2$) is repumper. The MOT is loaded for about 10 s.

During the last 28 ms of the MOT, the field gradient is ramped from 20 G/cm to 100 G/cm. The cycler detuning is then reduced to -2Γ, the cycler power decreases by a factor of two, and the repumper decreases by a factor of four. In this "compressed MOT" stage (cMOT), atoms are driven towards the center of the MOT before going dark due to lack of repumping light, increasing the spatial density of the cloud. This stage also increases the temperature of the cloud, but the next cooling step—gray molasses—addresses this problem. It is worth noting that the position of the cMOT macroscopically moves

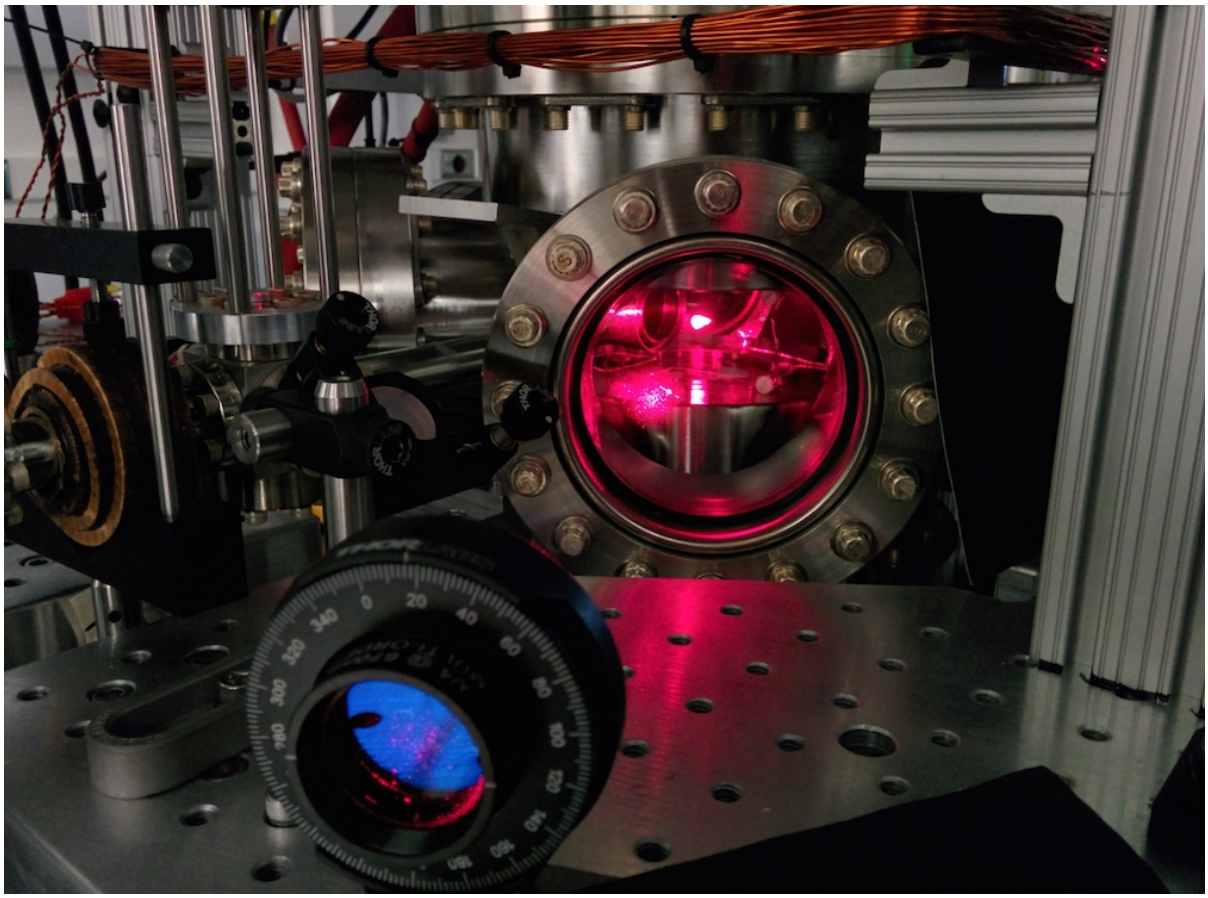

Figure 4.18: ^{7}Li MOT in center of chamber.

as a function of magnetic field gradient if the balance between intensities in the MOT arms is poor, leading to significant loss. Since we cannot tune the power balance using our fiber splitter, we instead compensate the intensity by slightly focusing or defocusing the MOT beams.

4.2.3 Gray molasses

Gray molasses is a type of sub-Doppler cooling technique, some background for which may be found in Section 2.2.2. The technique was first demonstrated for lithium in the Salomon group in 2013 [24, 25]. Recall from that chapter that the gray molasses technique depends upon having a three-level system (we use a Λ scheme, but similar techniques

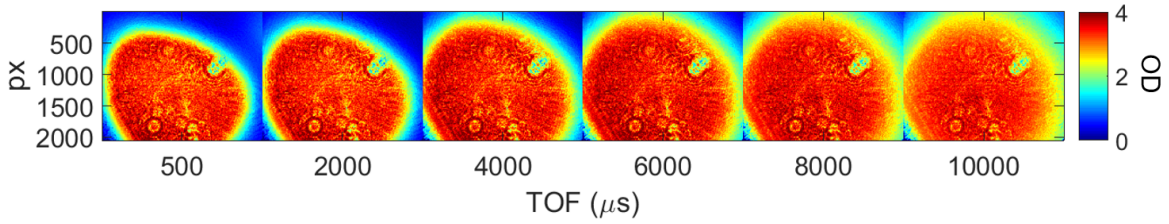

Figure 4.19: Time-of-flight imaging after gray molasses cooling. ODs greater than 4 rail the camera sensor.

may be used for a V scheme). We run our gray molasses on the D1 line (${}^2S_{1/2} \rightarrow {}^2P_{1/2}$); the ground manifold hyperfine splitting $|F = 1\rangle$ and $|F = 2\rangle$ realizes the two low-energy states, and the excited state is $|F' = 2\rangle$. Addressing these two transitions creates coherent superpositions of the ground states: a bright state which couples to the excited state, and a dark state which does not. In order to realize this coupling, it is important that both of the optical beams are sufficiently detuned from the excited state such that single-photon transitions are suppressed. We operate both beams at $+6.5\Gamma$ (blue) detuning from the excited state.[7]

The gray molasses light is produced by a TA, the seed for which has been shifted by 9.2 GHz through an EOM and amplified through a slave laser. The TA light then passes through a second home-built EOM to add 1-2% repumping sidebands at 813.5 MHz. The gray molasses beam in the horizontal plane is in retroreflected bowtie configuration to create standing waves in x and y; the vertical beam is a single retroreflected beam. The beams are aligned to the position of the MOT at the cMOT field gradient, to maximize eventual overlap. Each beam contains 40-45 mW of power, giving $s \approx 20$ for a 0.25" radius beam.[8] Applying the gray molasses beams for around 1ms reduces the cloud temperature to 60 μK. From this point, it is difficult to laser-cool further. Lithium has a narrow-linewidth transition at 323 nm with a low Doppler-cooling limit, which has been

[7] We tried varying their detunings relative to each other, but achieved the best cooling results at 0 relative detuning.

[8] Since we free space-couple the mode out of a TA, the mode is not a perfect Gaussian, so we can only estimate the saturation parameter.

used to create a MOT [54]. As mentioned earlier, an unfortunate snafu with viewport coatings makes this difficult for us, but given enough power, we may still be able to do this with losses on the order of a few %.

4.2.4 Optical pumping

In order to trap the sub-Doppler-cooled atoms magnetically, we need to ensure that they are in the magnetically-trappable $|F = 2, m_F = 2\rangle$ state. The choice of a stretched state significantly reduces the probability of spin-changing collisions to anti-trapped states. We optically pump our atoms on the D1 line, since the excited-state manifold on the D2 line is not well-resolved. We effectively want to address the same transition frequencies as we do for gray molasses, but also want to ensure σ^+ polarization so that we are pumping atoms into higher spin states ($\Delta m_F = 1$). However, if we used the exact same two-photon-transition detunings as the gray molasses beams, we would still be driving a stimulated emission process, conserving angular momentum and resulting in a net $\Delta m_F = -1$. Instead, we add a relative detuning between the beams of about 1Γ, which results in spontaneous emission but still allows us to use effectively the same optical path and setup. The amount of power in the repumping sideband is increased such that we have around 50 mW of cycler power and 25 mW of repumper in the vertical gray molasses arm. The ideal pulse length for the optical pumping light was empirically found to be 450 μs, which allowed nearly 100% transferred to $|2, 2\rangle$ with only minimal heating and cloud expansion to 100 μK and 2 mm radius.

4.2.5 Magnetic trap and RF evaporation

We use a capacitor bank (referred to in 4.1.3 and outlined in detail in lithium theses) to snap on a magnetic field gradient of 422 G/cm, which corresponds to an effective trap depth (across the extent of the optically-pumped cloud) of around 5 mK. Once

the atoms are magnetically trapped, we can proceed with RF evaporation, which is discussed in Section 2.2.3. Our RF evaporation utilizes the Zeeman shift in the magnetic trap as well as the ground state hyperfine splitting transition (803.5 MHz at zero field), resulting in spatially-dependent transitions from the magnetically trapped $|2,2\rangle$ state to the magnetically untrapped $|1,1\rangle$. The RF is applied through the antenna discussed in the RF Antenna section of 4.1.3. Our sweep begins around 1 GHz, higher than any frequency resonant with our cloud, and then sweep down to just above the zero-field resonant frequency, between 805 and 806 MHz, in four stages. As this sweep occurs, the field gradient is lowered to around 42 G/cm, which maintains a density high enough to allow relatively fast thermalization, yet low enough to avoid significant three-body losses.

Since we use a quadrupolar trap design rather than, for example, a Ioffe-Pritchard trap, our magnetic trapping region contains a field zero. As discussed in Section 2.2.3, at low magnetic fields, the Larmor frequency of the atoms approaches the rate of change of the field. The atomic quantization axis becomes poorly defined, and atoms can undergo spin-flips to untrapped states; crucially, this effect is most pronounced in the center of the trap, leading to losses in the coldest, most dense regions of the atomic cloud. The Larmor frequencies can be calculated to define some trap radius below which these spin-flip losses become significant. In our trap, that "region of death" is between 5-10 μm. We use our 532 nm laser, discussed in Section 4.1.5, focused to a 15 μm waist at the center of the trap, to repel atoms from that region. As noted in the shim coil discussion in 4.1.3, we need to properly shim our background fields such that the region of death does not move as the field gradient changes.

By the end of RF evaporation, we typically have around 60 million atoms at about 10 μK in the $|2,2\rangle$ state. However, in order to achieve denser clouds at colder temperatures, the atoms need to thermalize faster. The $|2,2\rangle$ state has an unfavorable (attractive) scattering length of -27 a_0. To cool further, we need to put atoms into the $|1,1\rangle$ state which has an accessible Feshbach resonance. This should allow us not only to switch to

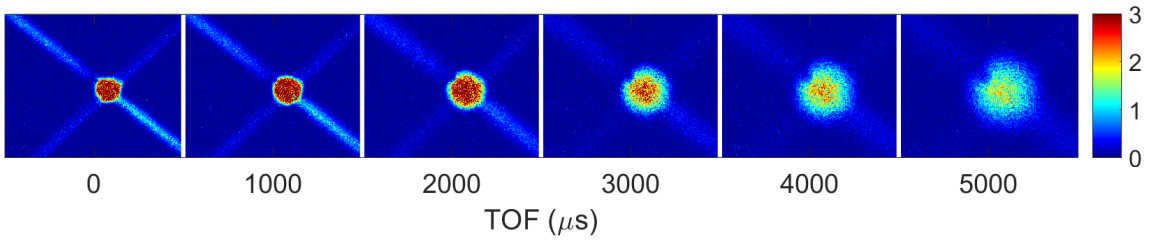

Figure 4.20: Atoms held in a crossed optical dipole trap are allowed to expand for various times of flight. A region of repulsion is visible at longer TOFs; this corresponds to the location of the 532 nm plug beam.

a repulsive scattering length, but also to tune its magnitude, allowing extremely efficient evaporation. Since $|1,1\rangle$ is not magnetically trappable, this evaporation must proceed out of an optical dipole trap.

4.2.6 Optical dipole traps and evaporation

We use a 90° crossed optical dipole trap to capture atoms out of the magnetic trap post-RF evaporation. Each power-stabilized beam contains about 6 W of 1064 nm light focused to a 90 μm waist, such that each ODT has a depth of around 23 μK and the crossed ODT frequencies are $(\omega_x, \omega_y, \omega_z) = 2\pi \times (590, 590, 830)$ Hz.

Once the atoms are trapped, we perform a slow Landau-Zener RF sweep to switch the atomic spin state to $|1,1\rangle$. Since this is the same transition which was being driven for RF evaporation, we can use the same frequency sources and antenna. In the presence of a weak bias DC field, we sweep the frequency from 809.6 MHz to 807.5 MHz over 65 ms, which results in approximately 98% of the atomic population in $|1,1\rangle$. During this sweep, we switch the MOT coils to Helmholtz configuration (see discussion in 4.1.3) and afterwards turn on a strong DC field to access the Feshbach resonance. We do not use any resonant pulses to blow away atoms which were not transferred to the $|1,1\rangle$ state; we do not find that this hurts the atom number.

The scattering lengths of lithium near the Feshbach resonance were characterized

by the Hulet group at Rice [42, 38]; see Fig 3.1.4. Using this information, we initially calibrated the currents for our DC fields by looking for the expected scattering length zero-crossing at 543 G. During the RF sweep, we run our power supplies at around 400 A, yielding a field around 730 G with an associated scattering length just under 300 a_0.

We can then proceed with optical evaporation. We use an exponential ramp over 4.5 s with a time constant of 2.25 s, during which time the power drops to around 2 W in each beam. At the end of the evaporation, we are typically left with around 2×10^5 atoms with a condensate fraction of 95% or greater.

4.2.7 Imaging

There are a number of important considerations to be taken into account when imaging lithium atoms. I will leave it to the lithium theses to go into the gory details on our detunings and optical setups, but will briefly list a few concerns below.

- At low field, we image on $|F = 2, m_F = 2\rangle \rightarrow |F' = 3, m'_F = 3\rangle$. However, calculating detunings based on the ground state splitting of 803.5 MHz does not take into account the unresolved excited state manifolds; using a "center-of-mass" splitting of 813.5 MHz to account for the $F' = 2$ to $F' = 3$ splitting allows us to image much more efficiently.

- Repumper light is also required during imaging to give us a strong absorption signal.

- There are times when we take data and need to image a cloud at high field. As discussed in Section 3.1.3, we can no longer use an LS coupling scheme to define "good" quantum states $|F, m_F\rangle$ at these high fields; instead, we work in the Paschen-Back regime and consider states $|m_I, m_J\rangle$. We find that the energy splitting at high field for the transition $|m_I = 3/2, m_J = -1/2\rangle \rightarrow |m_I = 3/2, m_J = -3/2\rangle$ is equal to the $|F = 2, m_F = 2\rangle \rightarrow |F' = 3, m'_F = 3\rangle$ frequency (within a linewidth or so)

and well enough resolved that we do not need a repumper to image.

Given the above considerations, we set up multiple imaging paths with different frequencies to address transitions at various magnetic fields, while trying to optimize those paths for power. This often involves playing tricks with multiple AOM orders. We plan to eventually upgrade to a separate ECDL so that we can match imaging frequencies continuously over a broad range of interaction strengths.

4.2.8 Final experimental thoughts

The lithium team has spent a long time thinking about solving various thermomechanical problems with MOT coils, designing circuits to work at extremely large currents, figuring out which beams require picomotor alignment precision, generating architectures to modulate AOMs very quickly and precisely, and working with novel lattice setups, among other things, and their scientific results are widely varying and very interesting. Their theses include a lot of technical conclusions which were the result of many months of struggle, and are definitely worth a read for anyone beginning to work with this atom.

Chapter 5

Strontium Experimental Design and Setup

This chapter encompasses many experimental details relevant to our the strontium machine at UC Santa Barbara, and is divided into 2 sections. The first describes the construction of the strontium apparatus, including design details for mechanical and electrical subsystems, while the second discusses the implementation of the cooling sequence for strontium, including experimentally-relevant optical parameters. Each subsection will closely mirror the structure of its counterpart in Chapter 4.

5.1 Strontium Machine Design

The machine described in this section was constructed with an intent to do quantum simulation experiments with degenerate gases of strontium. A Solidworks representation may be found in Fig. 5.1. Some of the features of its design include

- An angled oven and Zeeman slower to preserve optical access through larger viewports.

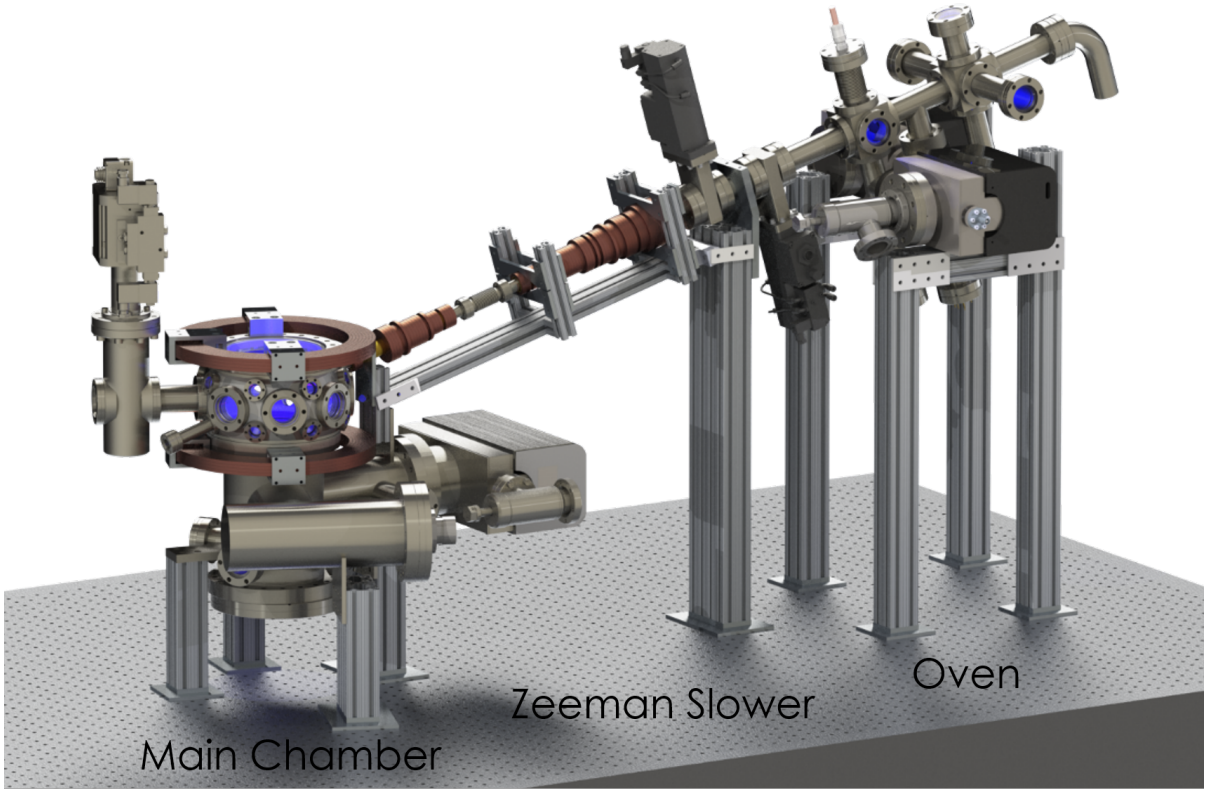

Figure 5.1: Overview of the strontium machine design.

- Cage-mounted MOT optics to preserve breadboard space for experimental setups.
- Flexibility to switch between all (bosonic and fermionic) isotopes ^{84,86,87,88}Sr.
- All-metal gate valve for eventual expansion to science chamber.
- Ultra-high vacuum to achieve BEC lifetimes longer than 10 s.

Much of the work described in this section was done alongside Ruwan Senaratne, whose thesis also includes a lot of useful information about the strontium machine [22].

5.1.1 Oven

The strontium oven manifold was designed much in the image of the lithium oven manifold to maximize flux of gaseous strontium into our main chamber, and built from both 316

Table 5.1: Strontium oven part numbers

Function	Company/Part Number	Purchased From	Notes
Ion Pumps (2)	Gamma 40S-DI-2H-SC-N-N	Gamma	Pump near atomic source baked out late 2016
Ion Pump Controllers (2)	Gamma SPC-1-US110-232 Digitel SPC	Gamma	Built-in gauges not so great, replaced controller for pump near atomic source, late 2016
Ion Pump Cables(2)	Gamma SCP-SC3-SC 3m SAFE-CONN STANDARD	Gamma	Replaced cable for pump near atomic source, late 2016
Ion Gauges	Agilent/Varian UHV-24P B-A	Ideal Vac	
Ion Gauge Controller	Agilent XGS-600	Agilent	
Ion Gauge Cables (2)	Agilent R32453010 for XGS-600 Controller	Agilent	
Cup Band Heater	Tempco MI-PLUS MPP02902	Tempco	1.5" × 2"; J-type TC
Nozzle Band Heater	Tempco MI-PLUS MPP04123	Tempco	2.75" × 1.5"; K-type TC
Oven Heater Controller	TPC-3000	Tempco	Watch the TC types.
Feedthroughs	Lesker EFT0313373	Lesker	Beam shutter
Beam shutter solenoid	Uxcell a1405100ux1279	Amazon/EBay	Max current 10A, replaced Mar 2019
Angle Valve	MDC AV-150M-11, Kalrez Manual	MDC	Hand-tightened; no torque sealing
Gate Valves (2)	MDC GV-1500M-P-1, Kalrez Pneumatic	MDC	Fail closed

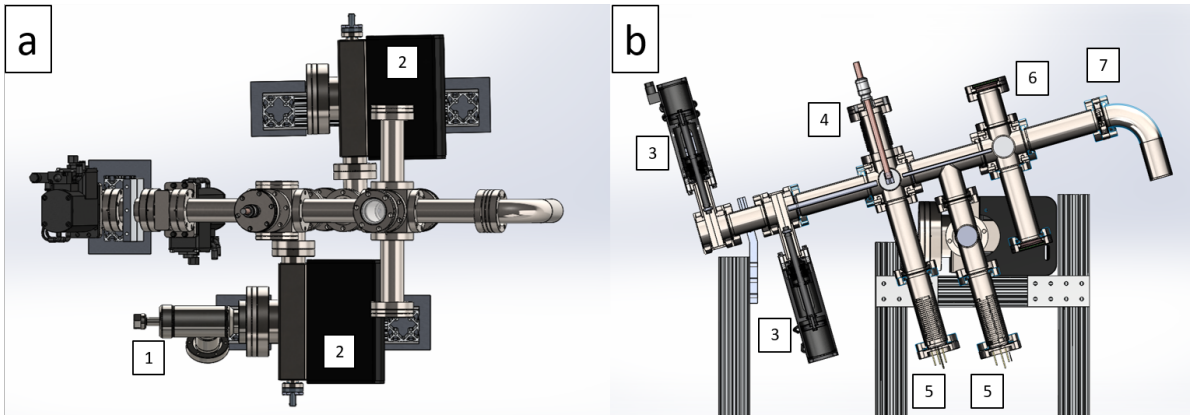

Figure 5.2: **(a)** shows a top-down view of the strontium oven manifold, such that the positions of the angle valve (1) and ion pumps (2) may be noted. **(b)** shows a side section view of the same with a clearer view of the (3) gate valves, (4) atomic beam stopper feedthrough (5) ion gauges, (6) transverse cooling section, and (7) the nozzle flange. Please see Fig. 4.4 for a schematic and image of the nozzle and atomic reservoir.

and 304 stainless steel alloys incorporating off-the-shelf and custom parts. The manifold is shown in Fig. 5.2. It consists of an atomic strontium source, a transverse cooling section, a first stage of differential pumping, an atomic beam shutter which doubles as another transverse cooling section, and a second differential pumping stage. It also includes two gate valves which separate the oven from the UHV part of the machine and allow it to be baked separately; these gate valves are not all-metal valves, but use Kalrez elastomer which outgasses much less than Viton. The strontium oven was baked in late 2014 and, after we ran out of strontium, again in late 2016, at which point we redesigned the transverse cooling section.

As can be seen in Fig. 5.2, the oven sits at a 16° angle to the optical table. The decision to design it this way was based on viewport considerations in the main chamber, and did not significantly affect any considerations in oven design. It did lead to some changes in Zeeman slower design, which will be discussed in subsection 5.1.2.

In this section, I will discuss strontium vapor pressure and flux, as well as differences between our oven and the lithium design. There is a subsection for the atomic beam

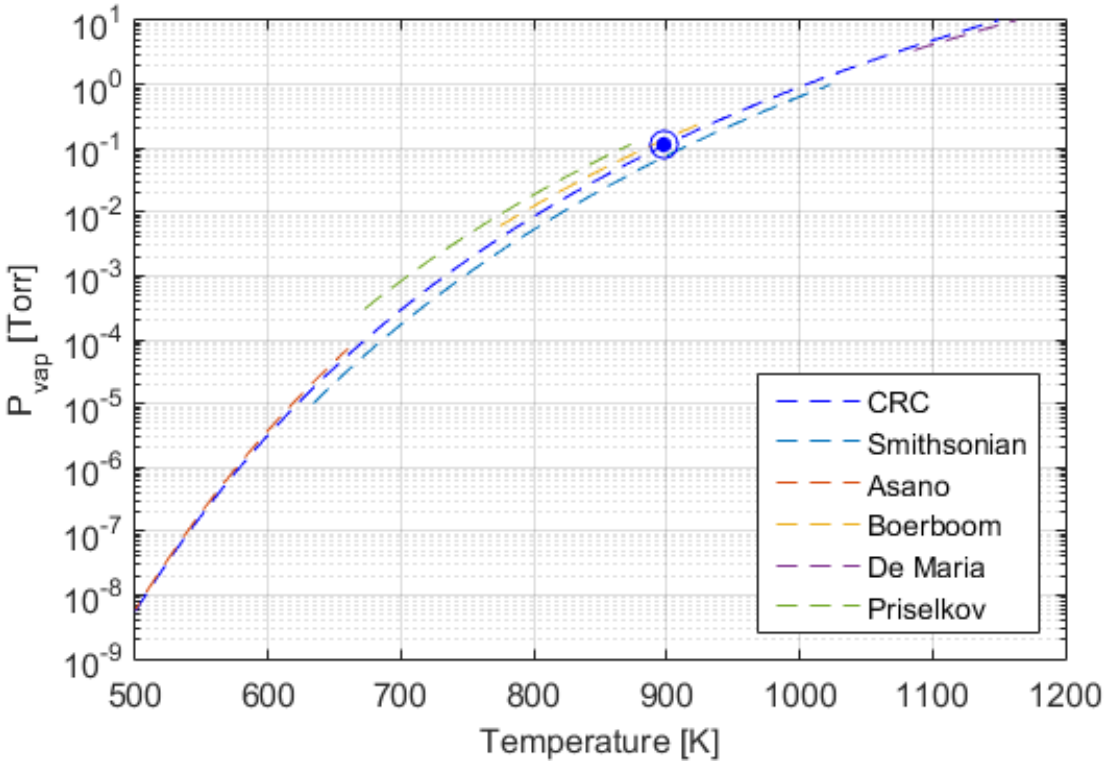

Figure 5.3: Strontium vapor pressure based on a number of different sources: CRC [55], the Smithsonian Physical Tables [56], Asano *et. al* [57], Boerboom *et. al* [58], de Maria *et. al* [59], and Priselkov *et. al* [60]. We use the CRC values, which fits points across temperatures from 298 K to 2500 K to within ±5% error. The dot indicates our approximate operating point.

shutter; though this machine incorporates an atomic beam nozzle and differential pumping, this section will contain pointers to Chapter 4 where they are discussed in more detail, as many of the design considerations were similar. Discussions of our transverse cooling may be found in section 5.2.1. Many of the part numbers for items found in the oven may be found in Table 5.1.

Vapor pressure and flux

The strontium reservoir is a 2.75" CF half-nipple custom-welded onto an elbow to make one continuous 90° part. It was originally loaded with 25 g of strontium, but is now

loaded with 100 g after the initial 25 g ran out after 2 years of running the machine. In order to figure out at which temperature we needed to operate the oven, we considered the vapor pressure of strontium, and later checked the operating temperature of other groups as a guide for what was reasonable. Strontium sublimates into a gas rather than boils. There have been several experimental measurements and corresponding fits for the vapor pressure equation, several of which can be found in Fig. 5.3. We use the CRC equation, which fits points across a large temperature range with less than ±5% error [55]:

$$\log_{10} P_{vap} = 14.232 - \frac{8572}{T} - 1.1926 \log_{10} T, \tag{5.1}$$

where P_{vap} is given in pascals and T is in Kelvin. We operate our reservoir at 600°C using a band heater, a temperature which was empirically set to give us a MOT loadrate of 5×10^6 ^{84}Sr atoms/s, and use a microcapillary array nozzle to collimate the beam at the oven exit (more details of which can be found in Section 4.1.1; a schematic and images may be found in Fig. 4.4). The nozzle is kept at 650°C, also with a band heater, to ensure that the microcapillaries do not clog. Since we have a custom combined reservoir cup and elbow, we do not have a place to attach a third band heater to ensure a monotonic gradient between the cup and nozzle. In its stead, we wrapped a heating tape around the curved section in case we ever needed additional heat, but we have never needed to use it. The CF connection for the atomic oven cup/elbow and nozzle uses nickel gaskets, rather than the traditional copper, out of worry that strontium will corrode copper in a manner similar to lithium. These nickel gaskets are made from the alloy 201 from Vacs SEV, which is the only company from which we order for a number of reasons: a) the gaskets are slightly thicker than comparable parts from MDC and Lesker, b) 201 is rated to above 600°C, while the more common alloy 200 is only rated to around 350°C. Because 304 stainless steel is not hard enough to cut into nickel gaskets, these few steel parts alone were machined from 316 stainless steel.

Taking the equilibrated atomic temperature to be the nozzle temperature of 650°C and using the total nozzle area as our aperture size, we find that the nozzle should be producing around 1.7×10^{15} atoms/s. At first glance, this seems much higher than we should need, and we should be able to run at a lower temperature to preserve oven lifetime. Unfortunately, the fraction of these atoms which are our preferred isotope, ^{84}Sr, is only 0.0056, yielding an effective flux of 9.4×10^{12} atoms/s.

There are two reasons why the ratio of the oven flux to the MOT loadrate is not as efficient for the strontium machine as it is for lithium.

- The nozzle output profile does have a pedestal with broad angular divergence in addition to the collimated beam. We saw the effects of this pedestal firsthand when baking the oven in 2014; during that bake and the following two years, the viewports (intended for transverse cooling) along the beam path immediately after the nozzle got coated with layers of strontium, which eventually took on a mirror-like sheen and prevented us from getting transverse cooling beams into the chamber.[1] When we rebaked the chamber to load more strontium, we added nipples to those viewports so that the parts of the atomic beam with large divergence only hit stainless steel.

- Our transverse cooling is not as optimized as it could be. Between the pedestal mentioned above creating a large flux of uncollimated atoms in the transverse cooling section and the extremely high saturation intensity ($I_s \approx 40\ mW/cm^2$), we have always been power-limited. We cooled in one of the two transverse dimensions after the first differential pumping tube, as this solves the pedestal issue. We recently switched to using multimode fibers, which now allows us enough fiber-coupled power to cool in the other transverse dimension in the intended transverse

[1] LIAD with 2 W of 405 nm light, which we use to clean lithium off of windows, does not work for strontium. Using a much higher intensity, a pulsed laser for example, may work better, but we are unsure.

cooling area. Unfortunately, both of these could still benefit from more power. We would also likely be helped by a transverse cooling stage after our Zeeman slower, but our machine incorporates no such section, and such a section in the strontium machine would be less effective than the for the lithium machine due to the higher mass.

Atomic beam shutter

Recall that the solenoid which drives our atomic beam shutter is a pull-type, which means that it pulls and holds the shutter open upon actuation, but does not actively push the shutter back to its original position. For some reason, the hydroform bellows that constitute part of our atomic beam shutter began to deform soon after our bake, such that the shutter did not entirely block the atomic beam in the closed position. We hung a 400 g counterweight off of the shutter feedthrough and then adjusted the solenoid actuation current to compensate for the extra weight. This has been serving us well for several years. The first solenoid gave way in March 2019 after about 2.5 years of use, and was replaced with the same model.

It is difficult to get a clear sense of our MOT load rate: strontium atoms quickly fall into the magnetically-trapped metastable $^3P_2$ state so MOT fluorescence is not a good guide, and the low abundance of ^{84}Sr makes it difficult to directly image a magnetic trap for that isotope. Our directly-imaged magnetic trap load rate is around 1.2-1.4 $\times$ 10^8 atoms/s for ^{88}Sr atoms, resulting in around 6-7 million ^{84}Sr atoms trapped in 10 s. We have found this to be more than enough to create nicely-sized BECs.

5.1.2 Slower

At the exit of the oven manifold, we have an atomic beam at a temperature of around 650°C, and we would eventually like these atoms traveling at a reasonable MOT capture

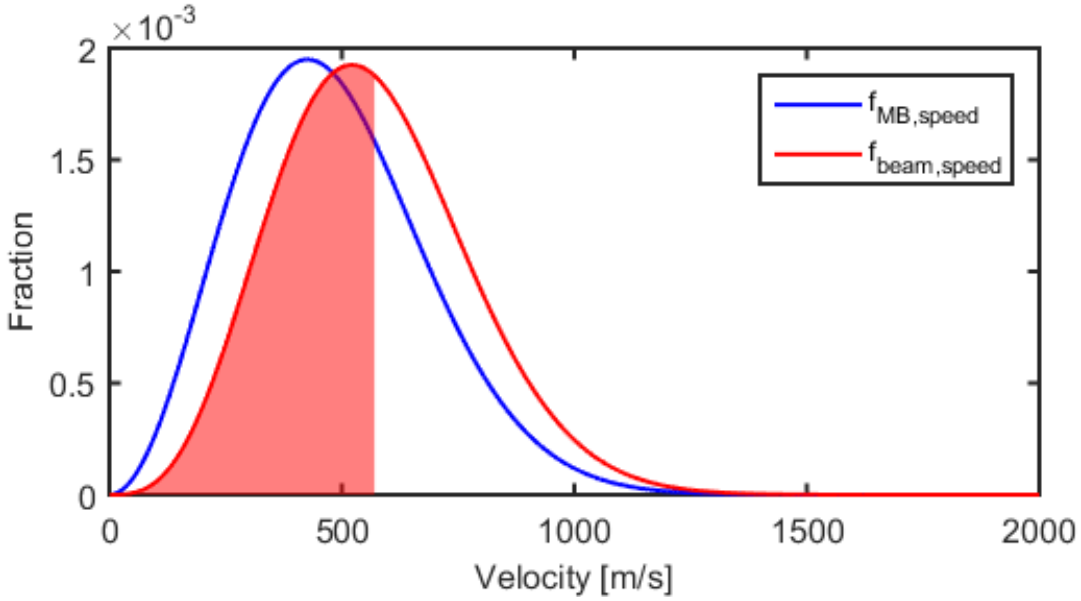

Figure 5.4: Maxwell-Boltzmann and atomic beam speed distributions at 650°C. Shaded region indicates fraction of atoms that designed slower should capture.

velocity v_c of around 50 m/s. Under the assumption that the atoms behave like an ideal gas, we can simply use a Maxwell-Boltzmann distribution to estimate the fraction of the atomic flux which will be slower than v_c. We recall that the Maxwell-Boltzmann distribution is

$$f_{\mathrm{MB}}(v)d^3v = \left(\frac{m}{2\pi k_B T}\right)^{\frac{3}{2}} \exp\left(-\frac{mv^2}{2k_B T}\right) d^3v \tag{5.2}$$

and we typically assume that the angular distribution is spherically symmetric, allowing us to treat d^3v as $v^2 dv \sin\theta d\theta d\phi$ which we can integrate over solid angle to retrieve the Maxwell-Boltzmann speed distribution.

$$f_{\mathrm{MB,speed}}(v) = \left(\frac{m}{2\pi k_B T}\right)^{\frac{3}{2}} 4\pi v^2 \exp\left(-\frac{mv^2}{2k_B T}\right). \tag{5.3}$$

However, since we are using a nozzle to generate our flux, we cannot assume angular isotropy; the velocity distribution will actually be skewed towards a higher velocity, since there will be a higher flux of faster atoms. Thus, we instead need to write d^3v as $v_z v^2 dv \sin\theta d\theta d\phi$, where $v_z = v\cos\theta$ is the velocity along the direction of the atomic

beam.

We can then normalize and rewrite our new speed distribution, which is no longer Maxwellian, to describe an effusive beam:

$$f_{\text{beam,speed}}(v) = \left(\frac{m}{\sqrt{2}k_B T}\right)^2 v^3 \exp\left(-\frac{mv^2}{2k_B T}\right). \tag{5.4}$$

Both of these probability distributions are plotted in Fig. 5.4. Using m =84m_p and T =650°C, we integrate both distributions up to v_c to find probability $\text{P}_{\text{beam,speed}}(v < v_c)$=9.4 $\times$ 10^{-5}. From these calculations, we concluded that we needed a Zeeman slower to slow a larger fraction of our atomic beam to below v_c.

Our design target capture velocity for the Zeeman slower was 570 m/s, allowing us to capture around 53.4% of our atomic flux (shown as shaded region in Fig. 5.4). We elected to go with an electromagnetic design rather than a permanent magnet design, due to the ability to turn off the field and the relative ease of winding a tapered solenoid. At the time we were designing the machine, AO Sense had just come out with their commercial Sr oven using a Zeeman slower and 2D MOT. Other groups had not tested the design yet, and since we had just designed and built a slower for the lithium machine, we decided to do the same for the strontium machine.

In the following sections, I discuss details of field design, solenoid winding and electronics, and water-cooling considerations. The optical details of the Zeeman slower may be found in section 5.2.2.

Zeeman field design

As mentioned at the beginning of this chapter, the oven and Zeeman slower were designed at a 16° angle to the optical table. The largest implication of this decision is that the projection of the MOT fringing fields along the longitudinal slower direction becomes quite large, increasing in magnitude from 0 G to 600 G. Since this field already existed and we knew our MOT currents approximately, we decided to modify that section slightly

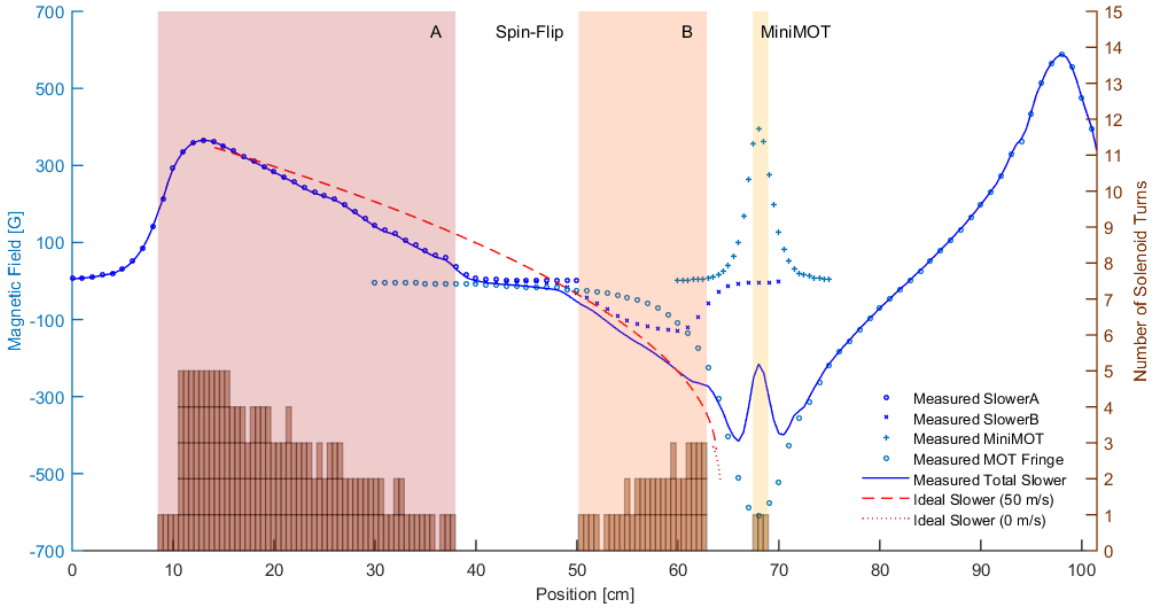

Figure 5.5: Sr Zeeman slower, showing the ideal designed slower field and measured fields for each section of the slower. The profiles of each solenoid are also shown, to scale on the x-axis.

and add a decreasing field section to create a spin-flip slower, designed to begin capturing atoms at 570 m/s and slow them to 50 m/s with a laser detuning of 750 MHz.

One of the problems with cooling atoms is that it is possible to change the velocity of the atomic beam from positive to negative, effectively turning the atoms in the other direction. This is easier to do for heavier atoms within the constraints of reasonable Zeeman slower lengths. The field required to slow the atoms to 50 m/s is shown in dashed red in Fig. 5.5; the dotted extension is the field required to slow the atoms to 0 m/s. By extension, if we did not have a way of stopping the slowing, the atoms would begin traveling with a negative velocity due to the magnitude of the MOT fringe field. We thus decided to wind a small coil with the express purpose of stopping scattering from slower light. We constrained the current of this coil to be equal to the MOT currents so we could use the same power supplies, which earned it the nickname "miniMOT". The performance of the slower is extremely sensitive to the miniMOT position.

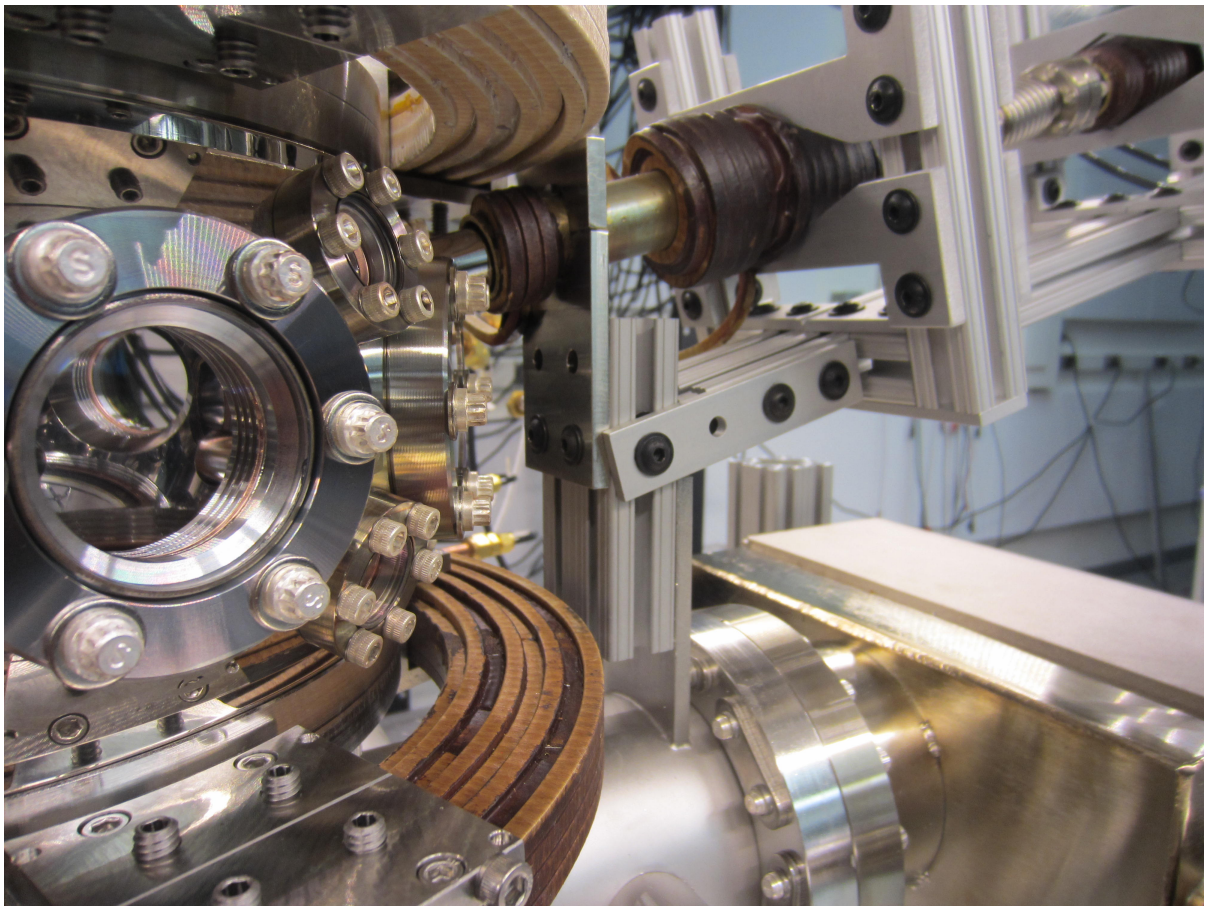

Figure 5.6: Image showing slower B and the miniMOT in relation to the MOT coils.

Fig. 5.5 shows the total measured field along the slower direction from the slower entrance to the main chamber exit, as well as the contributions from various solenoids and their winding profiles. Fig. 5.6 shows an image of Slower B and the miniMOT coils relative to the MOT coils on the chamber.

Solenoid winding and electronics

We used the same wire described in Appendix C to wind the solenoids for the slower: alloy 101 OD 0.1875" wire with a wall thickness of 0.032", insulated with Daglass insulation, epoxied using thermally-conducting electrically-insulating Duralco NM25.

The slower was wound in three sections according to the methods outlined in Ap-

Slower Coil	Power Supply	Design Current	Actual Current
A	Acopian Y08LXU4000	35 A	38.1 A
B	Acopian Y08LXU4000	25 A	28.1 A
MiniMOT	PowerTen P63C-15440	352 A	134 A

Table 5.2: Strontium slower currents

pendix C.5, which we label slower A, slower B, and miniMOT. Table 5.2 shows the power supplies we use, our design currents, and the currents we empirically set to optimize MOT load rate. The miniMOT was originally run in series with the top MOT coil, but we eventually realized that the MOT load rate was optimized running the miniMOT at a much lower current of 134 A, so we moved it to its own power supply and now use an analog input to control the current. The power supplies are electrically connected to the coils via custom-made lugs which press onto the stripped square wire leads with set screws, and mate to 10AWG wire via set-screws as well. The miniMOT is connected to its power supply via the same 3/0 wire we use for the MOT coils. Slower sections A and B are connected to Crydom D1D40 relays and Powerex CS240650 diodes (similar models to those we use to switch the lithium slowers on and off). However, in practice, we do not find that the fringing field makes a large difference, thus we do not switch the currents. The miniMOT section, which runs a much larger current, produces a large fringe field which we initially wanted to switch using an IGBT/relay circuit. However, in practice, the cooling stage during which those magnets turn off lasts around 500 ms, so the analog input rampdown time of 10 ms is more than enough to switch.

Fig. 5.6 shows two of the three wound coils on the Zeeman slower (section B and the miniMOT), as well as the top MOT coil which contributes most significantly to the fringing field. We included a bellows in the spin-flip section to allow for adjustment between the oven and main chamber, as well as to allow for some thermal expansion during bakes. We wound a shim between slower B and the miniMOT, but we have never found it helpful.

Water-cooling considerations

The water flow rate needed in the turbulent flow regime to dissipate heat from square wire with a given side-length, copper cross-sectional area, hydraulic diameter, length, and pressure differential can be found in various books [51]; this flow rate, along with the power dissipated in the wire and the specific heat capacity of water, can be used to calculate the expected temperature rise. These calculations for our slower sections indicate that only the miniMOT requires water-cooling (see Geiger and Senaratne theses for more detail on these calculations). However, we water-cool all three sections. Water connections are described in more detail in Appendix C.6.

5.1.3 Main chamber

Once our atomic beam is slowed, the atoms are captured in a 461 nm MOT at the center of the main chamber. I will leave details concerning any MOT parameters and optimization to section 5.2.3; this section will discuss main chamber design and considerations, MOT magnet construction and mounting, shim coils, and breadboard design. A non-exhaustive list of part numbers for the main chamber may be found in Table 5.3. The strontium main chamber was baked in December 2014, and typically sits at a pressure of around 3 $\times 10^{-11}$ Torr.

Main chamber design

The main chamber is the heart of the experiment, where strontium is cooled from a MOT to degeneracy. Technical drawings for the strontium main chamber may be found in Appendix G. The strontium main chamber, shown in Solidworks schematic in Fig. 5.7, took some inspiration in its "turret"-like design from the Chin group at University of Chicago, and was machined and electropolished by A&N Corporation. It is made entirely from 316 stainless steel, the magnetic permeability of which is much lower than that of 304

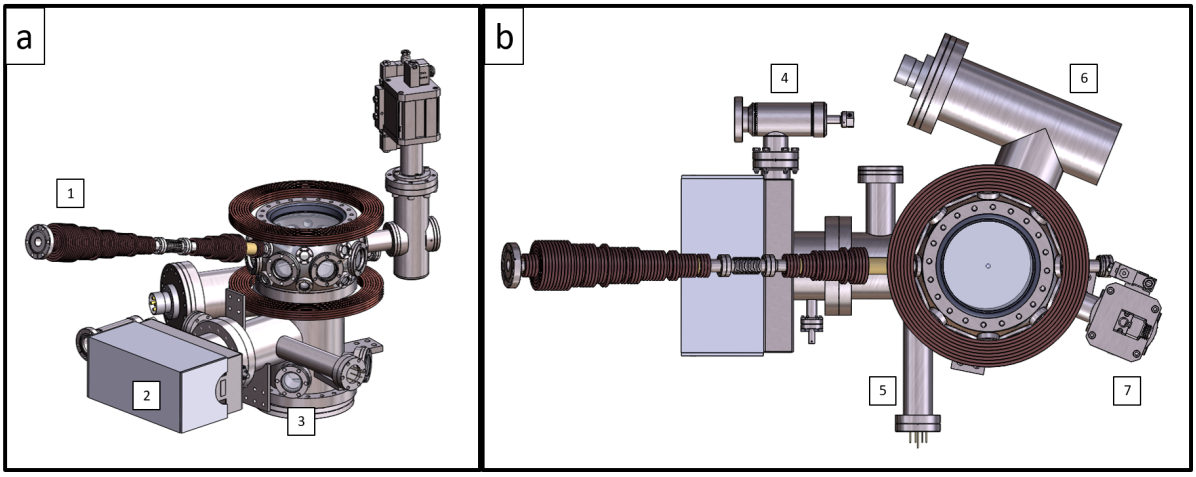

Figure 5.7: **(a)** shows a isometric view of the strontium slower and main chamber, such that the positions of the (1) Zeeman slower, (2) ion pump, and (3) drop ports may be noted. **(b)** depicts a top view of the same with a clearer view of the (4) angle valve, (4) ion gauge, (5) titanium sublimation pump, and (6) all-metal gate valve.

alloy. Generally speaking, it consists of an off-the-shelf Kimball 8.00" spherical octagon with (1) 8.00" CF viewport, (8) 2.75" viewports, and (16) 1.33" viewports around the top and sides. The base of the octagon is connected to a turret chamber which has another large viewport at its base. The turret chamber includes low-conductance ports for an ion gauge, ion pump, and titanium sublimation pump. It also has (4) 2.75" viewports placed at 90° around the bottom of the chamber, for future drop experiments. There are several tabs for supports to attach to an optical table; we bought supports such that the vertical center of the chamber sits 17.72" above the table. This is higher than the lithium machine sits; while it resulted in a tradeoff in mechanical stability (which did affect us later and which we had to fix), we learned our lesson from the lithium machine design and are grateful for the extra space.

Recall from the beginning of Chapter 5 that we need to prioritize optical access over magnetic access. The ground state of strontium $^1S_0$ is nonmagnetic, and the highest field gradients we need are only around 55 G/cm for the initial blue MOT stage of cooling; in contrast, strontium has a number of optical transitions which are scientifically

Table 5.3: Strontium main chamber part numbers

Function	Company/Part Number	Purchased From	Notes
Ion Pump	Gamma 75S TiTan CV 75S-CV-62-SC-N-N	Gamma	Double 6.00" and 2.75" ports
Ion Pump Controllers	Gamma SPC-1-US110-232 Digitel SPC	Gamma	Built-in gauges not great
Ion Pump Cables	Gamma SCP-SC3-SC 3m SAFE-CONN STANDARD	Gamma	
Ion Gauges	Agilent/Varian UHV-24P B-A	Ideal Vac	
Ion Gauge Controller	Agilent XGS-600	Agilent	
Ion Gauge Cable	Agilent R32453010 for XGS-600 Controller	Agilent	
TiSub Cartridge	Varian Filament TSP 9160050	Agilent	Attached via 2.75" to 6" reducer
TiSub Cable	Agilent 9240730, 3.6m	Agilent	Also used for Li machine
TiSub Controller	Agilent 9290032 with RS232	Agilent	Also used for Li machine
Angle Valve	MDC 314003, All-Metal	MDC	Torque-sealed according to chit, attached to ion pump
All-Metal Gate Valve	VAT 48132-CE44-AAM1, DN40	VAT	Pneumatic actuator

interesting for varying reasons. Balancing these considerations, we decided to make our MOT magnets very large to sit away from the spherical octagon, and were very careful about how we assigned usage for each viewport.

Optical viewports

In general, the 1.33" viewports are used for laser cooling (atomic/slower, blue MOT, repump, and red MOT beams), the 2.75" viewports are used for optical dipole traps and lattices, and the 8.00" viewports are used for both.

All of the optical viewports were bought from Kurt J. Lesker company. The vast majority were custom-made from fused silica and 316SS. They were then sent directly to Optical Filter Source (OFS), who designed specialized coating curves for us and coated the windows for 403 nm, 461 nm, 497 nm, 640 nm, 689 nm, 707 nm, and 1064 nm (at the time, we were not sure which repumping line we might use). The AR curve may be found in Appendix H. There is one 1.33" viewport which is extremely difficult to access due to other optics and the Zeeman slower; this viewport and its diametric opposite were purchased from Lesker as uncoated sapphire with custom 316SS flanges, to allow us to address strontium atoms on the $|5s5p^3P_2 \rightarrow 5s4d^3D_2\rangle$ 2920 μm mid-IR transition which is important to some long-term scientific goals.

One of the 2.75" viewports is attached to the main chamber via an intermediate all-metal gate valve, which will eventually be used to isolate the main chamber while a science chamber is added to the machine. The science chamber design will be discussed in more detail in Chapter 9.

The Zeeman slower viewport is offset from the spherical octagon by a 3" long 1.33" CF nipple. To keep strontium from sticking to it, we designed a special cap with an optical-quality window to fit over the viewport (similar to the MOT cagemount caps described in the next subsection) and create a pocket of trapped air. We heat this cap to 140°C, which has largely helped us avoid strontium coating on the window.

Setback: When we were first leak-checking the strontium main chamber, we found that several of the 1.33" CF flanges were leaking.[a] What we eventually found was a manufacturing defect: the edge of the glass-to-metal seal, usually recessed below the bolt/washer plane of the flange, extended just above that plane on some of the viewports. When we eventually tightened the bolts down, the washers overlapped with that seal and very slightly broke them.[b] These issues were compounded by the fact that copper gaskets tend to stick to the 1.33" CF flanges and are very difficult to remove, leading to an irretrievably-destroyed viewport, and that the viewports are very closely-spaced on the spherical octagon, leading to difficulty in isolating problematic viewports. Were we to do this again, we would use silver-plated gaskets. Additionally, we might have immediately used blanks, rather than replacement viewports, to track down leak sources. **Take great care with 1.33" CFs**.

[a] There is still a small leak (or virtual leak) somewhere in the machine, resulting in the pressure increasing from 3×10^{-11} Torr to around 9×10^{-11} Torr over 5-6 months. This is not ideal but when this happens, we simply run our TiSub pump again and recover low pressures immediately.

[b] Thus resulting in the other 1/2 of the infamous Lesker signs.

MOT cage-mount optomechanics

One of the unique aspects of this machine is its cage-mount MOT optomechanical systems. We designed these for in-coupling and retro-reflected blue and red MOT beams, and also use a slightly modified design for the repump; schematics may be found in Fig. 5.8, and a list of parts we used for them is in Table 5.4. The drawings for the cage mount may be found in Appendix I. Some notable features include cutouts to fit over 1.33" CF bolts, and three points of contact with the flange to maintain stability. The in-coupling mounts give us two angular degrees of freedom but not two more typically-desired positional degrees of freedom; we have found that this is still okay, as the center

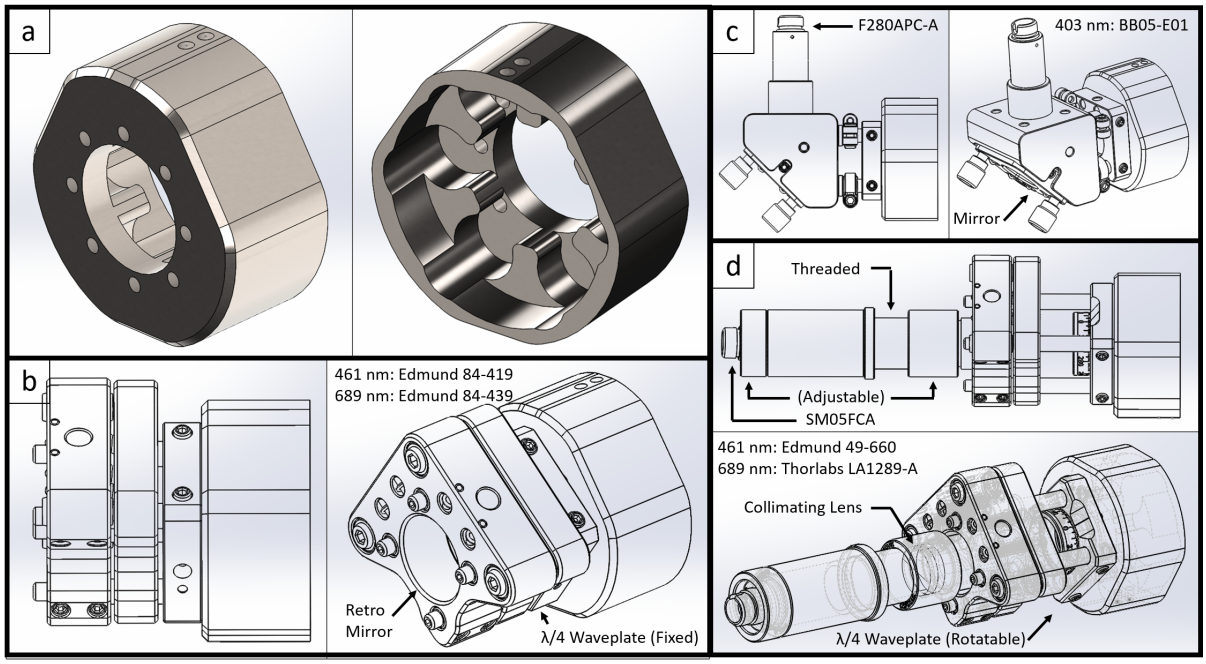

Figure 5.8: **a**: Viewport adapter for MOT and repump cage-mount optomechanics, used in designs **b**, **c**, and **d**. Technical drawing may be found in Appendix I. **b**: MOT retroreflection setup. Part numbers indicated for mirrors. **c**: Repump light input setup; light enters from a low viewport. **d**: MOT light input setup; light enters from a high viewport. Part numbers indicated for collimating lenses.

of our magnetic trap is sufficiently centered within the chamber to ensure a large overlap with the MOT beams. Since each MOT beam is retro-reflected, we also have beam-focusing degrees of freedom so that we can match intensities in case of power losses in the retro path. We only use one (rotatable) $\lambda/4$ waveplate in the in-coupling setup and one (non-rotatable) $\lambda/4$ waveplate in the retro setup; this is all we require since we use polarization-maintaining fibers. We have not seen any major stability issues with these cage mounts, and they save us a great deal of optical breadboard space. The main down-side is that we have to make sure the fibers' polarization-maintaining ability is always good, requiring that we check them every few months.

Setup	Function	Part Number	Purchased from
MOT Retro	Cage Rods	SR1	Thorlabs
	Waveplate Holder	SP02	Thorlabs
	Waveplate	WPC212Q	Foctek
	Kinematic Mirror Mount	KC05-T	Thorlabs
	Mirror	84-419 (461 nm)	Edmund Optics
		84-439 (689 nm)	Edmund Optics
MOT Input	Cage Rods	SR1.5	Thorlabs
	Rot. Waveplate Holder	SRM05	Thorlabs
	Waveplate	WPC212Q	Foctek
	Kinematic Mirror Mount	KC05-T	Thorlabs
	Coll. Lens Holder	SM05V05	Thorlabs
	Coll. Lens	LA1289-A (461 nm)	Thorlabs
		49-660 (689 nm)	Edmund Optics
	Locking Adjustment	SM05T10	Thorlabs
	Spacer	SM05L10	Thorlabs
	Fiber Coupler Adapter	SM05T1	Thorlabs
	APC Coupler	SM05APC	Thorlabs
Repump Input	Cage Rods	SR0.5	Thorlabs
	Cage Rod Mates	SRSCA	Thorlabs
	Waveplate Holder	SP02	Thorlabs
	90° Kinematic Mirror Mount	KCB05	Thorlabs
	Mirror	BB05-E01	Thorlabs
	Fiber Coupler Adapter	AD1109	Thorlabs
	Fiber Coupler	F280APC-A	Thorlabs

Table 5.4: MOT cage mount components

MOT magnet design and construction

The MOT coils for the strontium machine have much less alignment sensitivity than the lithium coils, owing to strontium's non-magnetic ground state. Since the coils are used to create the MOT field gradient and the magnetic trap gradient, we only operate them in anti-Helmholtz configuration and care little about the field curvature. We use two coils placed on either side of the atoms with a separation necessary to satisfy the Helmholtz criterion: coil separation z is equal to the coil radius r_0. (more on theoretical considerations can be found in Section 2.2.3).

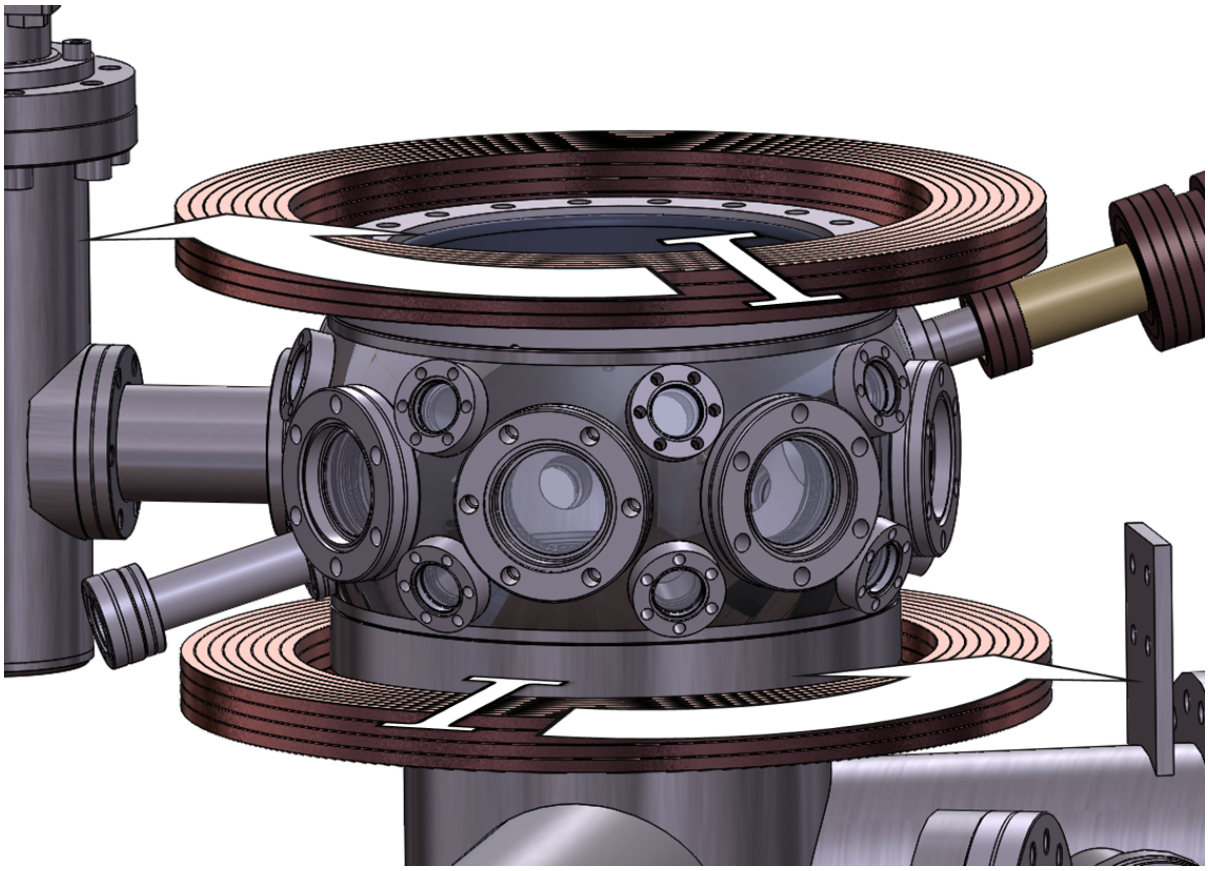

Figure 5.9: Strontium MOT coil directions of current flow

Coils	Field Produced	Peak Field (352A)	Set Current	Voltage Drop
Inner (1-4)	0.081 G/cm/A	28.48 G/cm	288 A	12.9 V
Outer (5-8)	0.062 G/cm/A	21.83 G/cm	289 A	14.1 V

Table 5.5: Strontium MOT fields

The currents were simulated on Mathematica for varying geometries to give us a sense of the behaviors of the 0th, 1st, 2nd, and 3rd derivatives of the field in both anti-Helmholtz configuration; these geometries were constrained by the dimensions of the spherical octagon, which allowed a minimum separation of 5.25". Each coil was eventually designed to have an inner diameter (ID) of 9.1", with a cross section of 32 turns: 4 turns in $\hat{z}$ × 8 turns in $\hat{r}$, with every set of 4 turns in $\hat{z}$ × 2 turns in $\hat{r}$ being one continuously-wound solenoid. The inner 4 radial coils are referred to as coils 1-4, and the

outer 4 are referred to as coils 5-8; we thus have two leads each (an input and output) for pairs 1 and 2, 3 and 4, etc. These coils were mounted 5.25" away from each other, and measurements were taken in-situ to look at the resultant gradients in G/A/cm.[2] A summary of these can be found in Table 5.5; we calculated that we would have to run these coils at 352 A to achieve a field gradient of around 55 G/cm, which is what other groups were using at the time [21]. Winding the coils proceeded in the same way as described in Appendix C.5; we designed and machined new custom mandrels and jigs to accommodate coils with a much larger ID.

Mounting the coils is quite difficult. With a 9.1" ID, the bottom coil is topologically captured; it does not freely move over the spherical octagon, so we needed to wind and place the coil over the turret prior to attaching the octagon on top. To hold the coils in place, we designed special mounts that mate to custom-tapped holes in the top and bottom spherical octagon 8.00" CFs, and hold each coil in place in 4 places. The mounts have tapped holes in the top, bottom, and sides, through which plastic set screws hold the magnets firmly in place. Drawings for the mounts can be found in Appendix I. Because these magnets are externally mounted and we do not have reentrant windows, we did not need to pot these coils in epoxy.

The coils are designed to run up to 350 A, which presents some difficulties both in terms of thermal management and electrical power. The results of thermal calculations (details of which may be found in the Senaratne thesis [22]) assuming 350 A of current necessitates the use of high-pressure water cooling. The ends of each of the leads was soldered to copper tubing for water cooling in the same way as the slower solenoids, and the cooling lines were connected to the water manifolds detailed in Appendix C.2. The electrical connections on these magnets are the same as the old lug designs described for the lithium machine: they have compression-fits secured via set-screw onto stripped square wire leads, and large set-screw attachments for 3/0 wire. These lugs have suffered

[2]These measurements were taken at half of the required current, 176 A, and scaled accordingly.

Component	Part	Rating
Inner Coil Supply	PowerTen P63C-25400	25 V, 400 A
Outer Coil Supply	TDK Lambda 30-500[3]	30 V, 500 A
Isolation Amplifiers	AD215BY-ND	
Earth Shim Supply	GWInstek Benchtop	
Applied DC Shim Supply	Disconnected	

Table 5.6: Strontium MOT electronics

from the same connection problems mentioned as a "setback" in the Chapter 4, and we have had issues with the wire burning due to resistive heating. Additionally, the locations of the power supplies relative to the strontium main chamber result in an extremely large voltage drop over the lengths of 3/0 cable, which typically sit at around 60°C (very close to their maximum rating) when the machine is running. Strontium graduate student Peter Dotti has updated designs using compression lug connections and water-cooled copper tubing instead of long lengths of 3/0 wire, but this will be a future upgrade. In the meantime, we have tightened everything extremely well, switched some connections from set-screw to crimp-type (as they have gone bad), and continued to stay visually and olfactorily aware of them.

The MOT coils are powered by 208 V 3-phase power supplies (we do not have 480 V supply in our lab). The outer turns (5-8) on both the top and bottom coils are powered by a 15 kW TDK Lambda,[4] while the inner turns (1-4) on top and bottom are powered by a PowerTen P63C-25400. Both supplies exhibit similar ramping speeds, so we can consider the inner and outer turns effectively as one large coil. The currents are controlled via analog voltage lines, which connect to the power supplies via isolation amplifier circuits to avoid ground loops.

[4]We initially wanted to use this supply for the miniMOT as well, thus the higher voltage rating

Shim coils

Earth's magnetic field provides a constant background of around half a Gauss underneath any field or gradient we produce in lab. This means that when we decrease our field gradient from the blue MOT to the red MOT (see Section 5.2.5), the position of the magnetic trap center can move, resulting in large atomic losses. To overcome this problem, we need to compensate for the earth field (and any other stray fields from, for example, a neighboring lab) with sets of Helmholtz shim coils. To be able to compensate a field in an arbitrary direction, we need three sets of transverse coils. In practice, we actually wind two sets of coils in each dimension: the first is used to shim out background fields, while the second can be used to apply small DC bias fields if needed.

These shims are typically wound on supports which are built in-situ after the machine is up and running; they are designed from U-channel aluminum which has been sandblasted and coated with Plastidip to prevent wire shorts. It becomes much easier to build supports and wind coils for a square geometry; we can refer to Section 2.2.3 to find that the Helmholtz condition can still be met for square coils with side length d for separation $z = 0.5445d$. We use 22AWG Kapton-insulated motor wire for these earth shims, and wind a few decades of turns around the machine in-situ. Our DC bias field shims are currently disconnected; our earth shims can run up to 3 A, but we typically use currents lower than 1 A to cancel the earth field.

Breadboard design

For the strontium machine, we designed four large breadboards which attached to the optical table and to each other, but were independent from the machine. They are all made from MIC6 aluminum alloy, which is extremely stable and therefore retains its flatness when tooled. The three breadboards which attach to the optical table are 1.25" thick with a flatness tolerance of 0.030", cast with the grain along the longest direction;

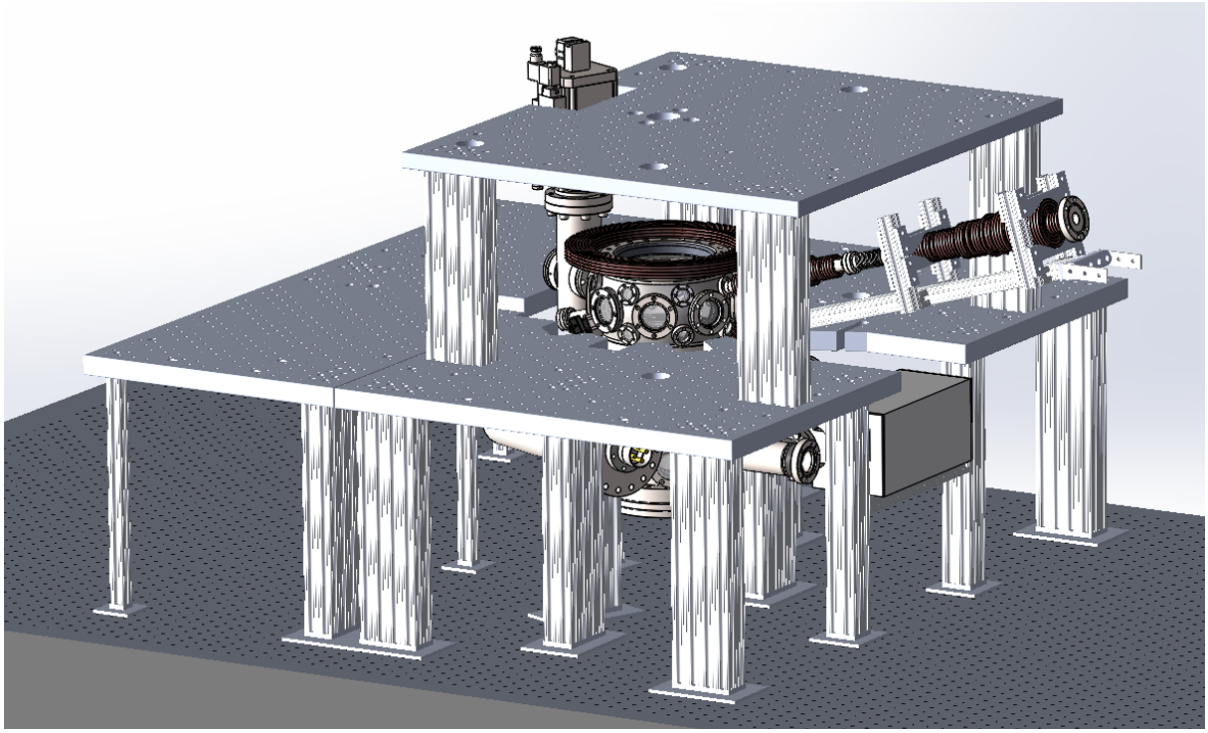

Figure 5.10: Strontium breadboard design

the top breadboard, which attaches to the two side breadboards, is 1.00" thick with the same tolerance and grain. The breadboards were ordered from a local Alcoa distributor, and machined according to our specifications by the UCSB Physics Machine Shop. The design includes standard 1/4"-20 holes along a 1" grid (tapped from the top and bottom), as well as various cutouts to allow beams to pass through. They are mounted on 80/20 and custom-designed optical table mounting feet, such that the center of 1.5" tall optics on the breadboards aligns roughly with the center of the main chamber. Our standard optics height in the lab is 2", but this was not possible for the strontium machine due to the proximity of the bottom MOT coils; we operate at a standard height of 1.5" instead, which often necessitates using 0.5" pedestal pillar posts and machining our own adapter mounts for various optics. This design, unlike that for the lithium breadboards, was not tested for mechanical stability using Solidworks simulation tools. We have actually had some mechanical stability problems, which resulted in needing to add several 45° braces

between the table, 80/20 supports, and breadboards themselves (see Appendix E). The breadboards are shown in Fig. 5.10. Technical drawings may also be found in Appendix G.

5.1.4 461 nm laser

The 461 nm laser provides cooling light for the broad $|^1S_0\rangle \rightarrow |^1P_1\rangle$ 30.5 MHz transition. The master laser is a Toptica SHG-Pro, consisting of a 922 nm ECDL, a tapered amplifier (TA) producing approximately 1 W of 922 nm power, and a frequency-doubling bowtie cavity, as well as many beam shaping optics. The laser was rated to 600 mW when purchased (the TA was producing 1.5 W of 922 nm power at that time), but has been outputting 400 mW of 461 nm light (as measured on a thermal power meter head) fairly stably since 2014. The doubling cavity uses a Pound-Drever-Hall lock to lock to the ECDL; this lock uses both slow feedback (a Toptica PID module) and fast feedback (a Toptica FALC module). For more on the 461 nm internal setup, please see Appendix M.

Unfortunately, the 922 nm light almost exactly coincides with a water absorption line. This means that unless the cavity stays dry, the power attenuation in the cavity will result in much less blue power output and a difficult time locking the cavity. Since our campus is by the ocean, we have to be particularly careful changing the cavity desiccant; it typically needs to be switched out with a frequency between once every couple of days (in rainy weather) and once every few months (typically). We have considered flowing dry nitrogen through the cavity, but it would involve machining the laser lid; the activation energy is too high. Over the years, we have had several adventures with this laser, including dirty cavity mirrors and cavity PZT replacement. For all of the information we've learned over the years pertaining to the usage and alignment of this laser, please see Appendix M.

The 461 nm laser setup is contained on about half of a 4' by 10' optical table, and closely follows the layout described in the Stellmer thesis from the Innsbruck strontium experiment [21]. In particular, we use the trick described by that group of using a

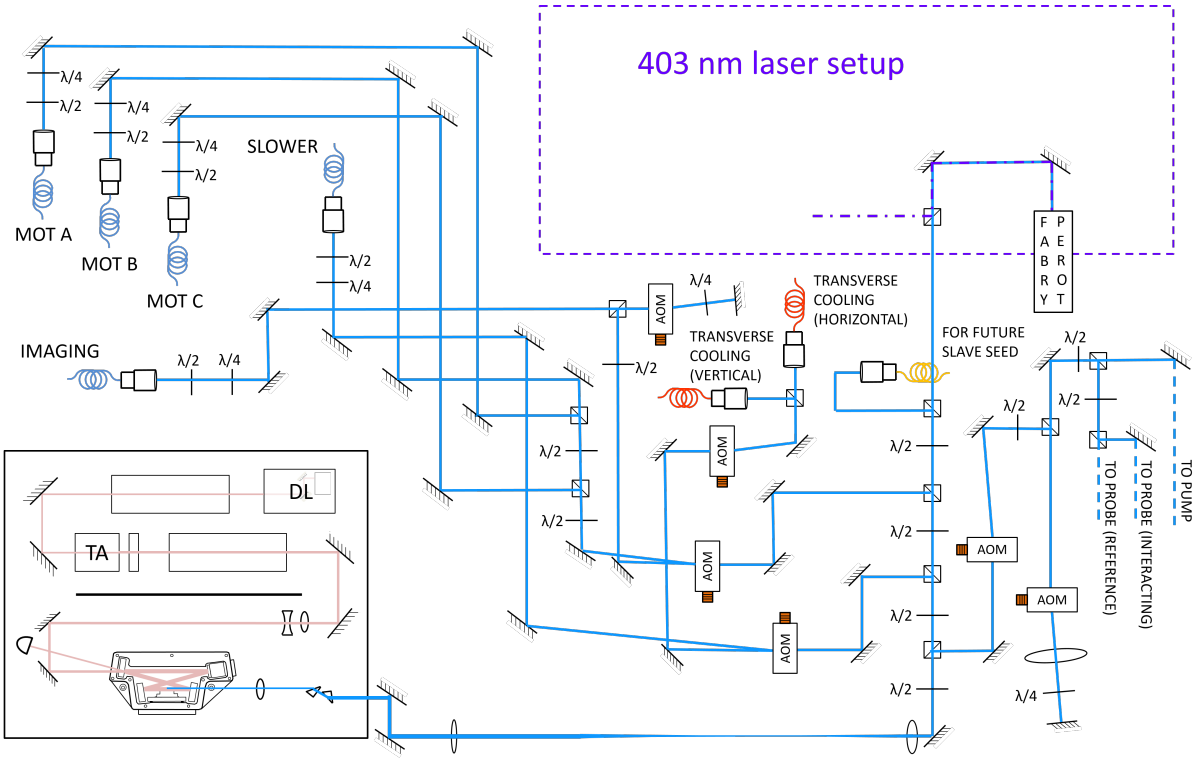

Figure 5.11: 461 nm laser setup, showing 922 nm master and SHG cavity and all main beam paths. Polarization-maintaining single-mode fibers are drawn in blue, non-polarization-maintaining single-mode fibers in yellow, and multimode fibers in orange.

single-pass AOM in series with a double-pass 350 MHz AOM for our spectroscopy setup, the latter of which allows us to quickly tune among all four strontium isotopes. We use polarization-maintaining fibers for the MOT, imaging, and slower light; the former two are from Thorlabs, while the latter is a special glass-capped fiber from Coastal Connections (part no. P-FAnskFAnsk-3.8/125/3-6) to allow us to couple 180 mW of slower light into the fiber without burning the tip. The 461 nm laser setup is detailed in Fig. 5.11. The frequencies for each beam are detailed in Fig. 5.12.

About 20 mW of light is picked off of the main beam path to send to a spectroscopy cell. This cell is loaded with about 20 g of strontium in an inert buffer gas of argon. The cell is pumped down to about 10 mTorr and operated at 430°C, conditions which were eventually chosen to set the mean free path of strontium in the cell small enough

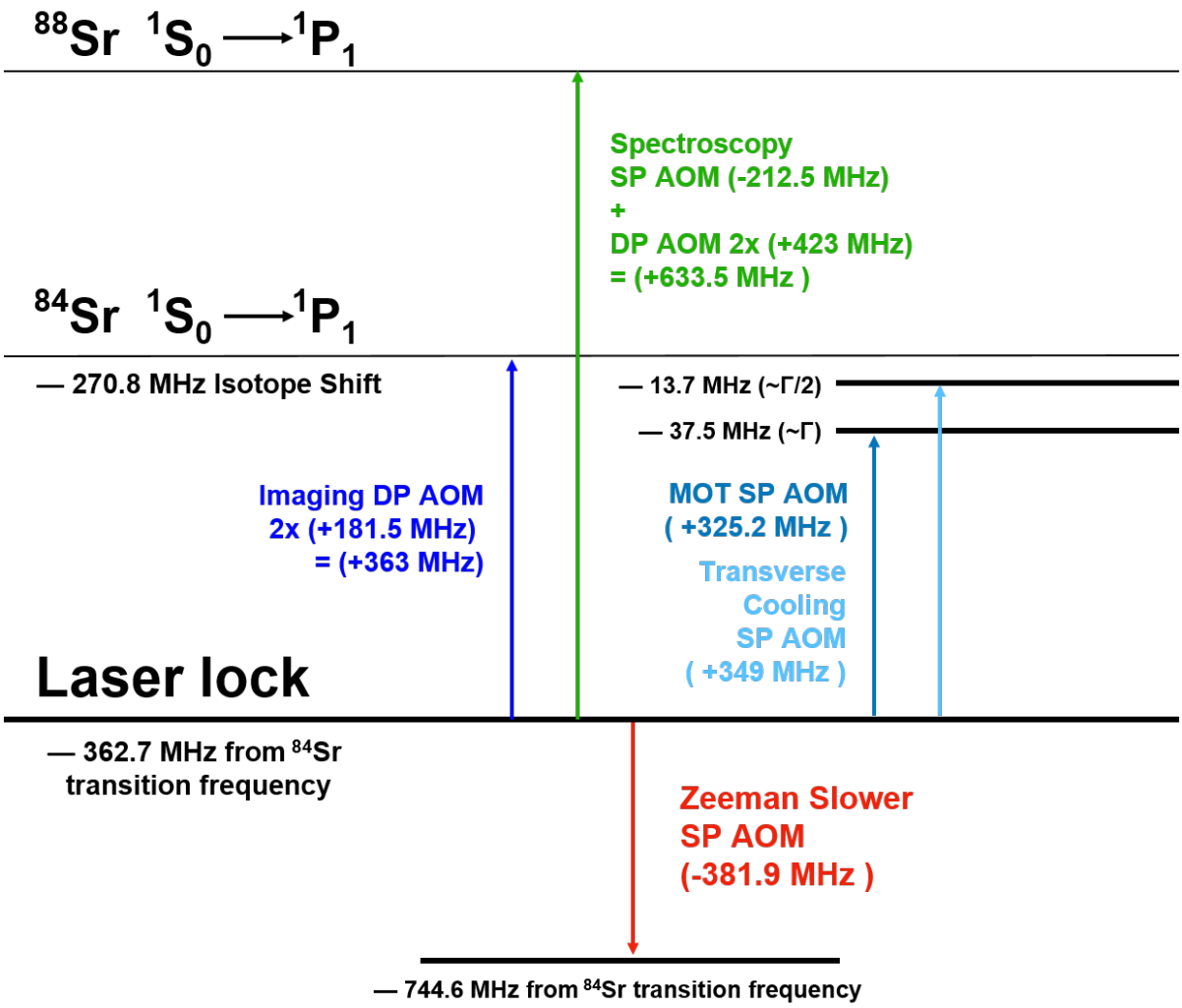

Figure 5.12: 461 nm laser frequency diagram showing detunings of all main 461 nm cooling and imaging beams, and how they are achieved using AOMs in single-pass (SP) or double-pass (DP) configuration. Changing the spectroscopy DP AOM to +287.5 MHz allows us to switch from ^{84}Sr to ^{88}Sr.

that it would not coat the windows, and large enough that the atomic density of the accessible strontium cloud gives us a reasonable spectroscopic signal. We use a Toptica Digilock lock-in amplifier module to modulate the spectroscopy frequency on the double-pass AOM at 11 Hz (the cavity lock has a difficult time following the scan through the full scan range otherwise), and lock to the ^{88}Sr feature as it is by far the most abundant isotope. Because the linewidth of the 461 nm transition is so large, the Doppler signal

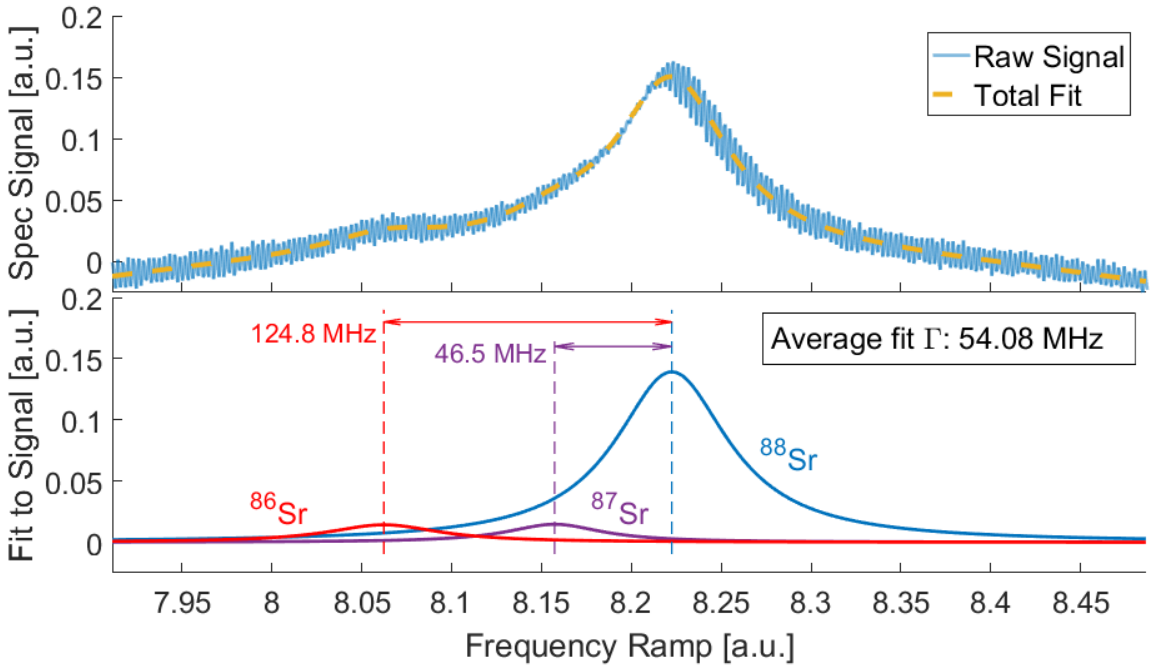

Figure 5.13: 461 nm saturation absorption spectroscopy. We are able to resolve peaks for the more abundant isotopes of Sr.

provides a very large, deep background on the saturation absorption signal, and it is much easier to generate a nice error signal by subtracting a reference probe signal. The saturation absorption spectrum we obtain is plotted and fit in Fig. 5.13; we obtain a fit of around 54 MHz, which is likely the effect of either power or pressure broadening, but could also be the result of fitting with Lorentzians rather than Voigt profiles; it does not hurt our cooling on this line. We used to have a lot of problems locking to this signal when we were mounting mirrors on 8" tall 0.5" diameter Thorlabs posts. We recently changed the optomechanics to include larger, more stable mounts, and became more careful about enclosing the spectroscopy cell to block air currents; this has extended the lifetime of the lock from tens of minutes to a few hours, and made our lives easier.

Setback: For many years, we would see deterioration of the total power on the laser table due to losses on the first couple of cubes in the beam path. At the time, we were using Thorlabs PBS101 cubes for the entire laser table. We discovered that 400 mW of 461 nm light at 1 mm diameter is intense enough to quickly corrode the cement at the interface of the two halves of the cube. One could consider beam-splitting plates, but they are more difficult to work with because unlike cubes, they spatially translate the transmitted portion of the beam in a macroscopic way. We eventually found a company called Casix which makes optically contacted visible broadband PBSs. We are slowly beginning to use them on the table as our old cubes degrade, and they work great. **Be careful with high-intensity short-wavelength light on optics**.

5.1.5 403 nm laser

As mentioned in Section 3.3.2, we choose to repump along the 403 nm transition from ${}^3P_2 \rightarrow 5s6d^3D_2$. Our 403 nm master laser is a Sacher Lynx ECDL, which produces 28 mW of 403 nm power. The necessary laser setup is quite small; it sits in a corner of the 461 nm laser enclosure. It is sent through a double-pass 350 MHz AOM and fiber-coupled to the machine table. We do not strictly need a double-pass AOM for bosonic isotopes of strontium; this setup exists to plan for the future use of ^{87}Sr, for which we will need two repump frequencies to address the large splitting between the $|{}^3P_1, m_F = 11/2\rangle$ and $|{}^3P_1, m_F = 9/2\rangle$ hyperfine states. In the 403 nm laser setup, the first beam splitter in the beam path is a beam-splitting plate (Thorlabs PBSW-405) in lieu of a beam-splitting cube. This is because we see the same degradation of cement at the interface of cubes, even with only 28 mW, due to the short wavelength. Unfortunately, it is extremely difficult to find optically-contacted cubes for 403 nm light.

The 403 nm transition has a linewidth which is alkali-like (a few MHz wide). Because

it is not extremely narrow, we simply use a Fabry-Perot cavity with an FSR of 1.5 GHz to lock the repump frequency. We send both 461 nm light and 403 nm light into the cavity and set the cavity scan parameters to less than 1 FSR such that we see one peak corresponding to each color of light, clearly separated. We then use NI software to digitally stabilize the peak separation, which feeds back to the laser grating piezo voltage. This works as long as the 461 nm laser is locked properly, and the output of the 403 nm laser is single-mode. Unfortunately, the latter condition is often not met; we have had numerous problems getting the laser to operate in single-mode, and often spend a reasonable amount of time every week to find a stable operational mode. The strontium experiment also shares a room with the lithium experiment, and we often find that during lithium RF evaporation, the RF will affect the laser current such that the frequency changes. The cavity lock thankfully mitigates this effect when both machines are running, but we would like to design housing with better shielding for this laser someday.

5.1.6 689 nm laser

Our 689 nm laser addresses the narrow 7 kHz intercombination transition $|^1S_0 \rightarrow ^3 P_1\rangle$. This transition, beyond simply allowing efficient optical cooling, is an attractive feature in strontium experiments because its width provides the ability to probe systems with excellent energy resolution. The following section will discuss the architecture of our 689 nm laser system. It is currently small, but has room to expand to other isotopes, particularly ^{87}Sr. The inspiration for the design and plans for expansion were largely inspired by the omnibus design of the Innsbruck group [21].

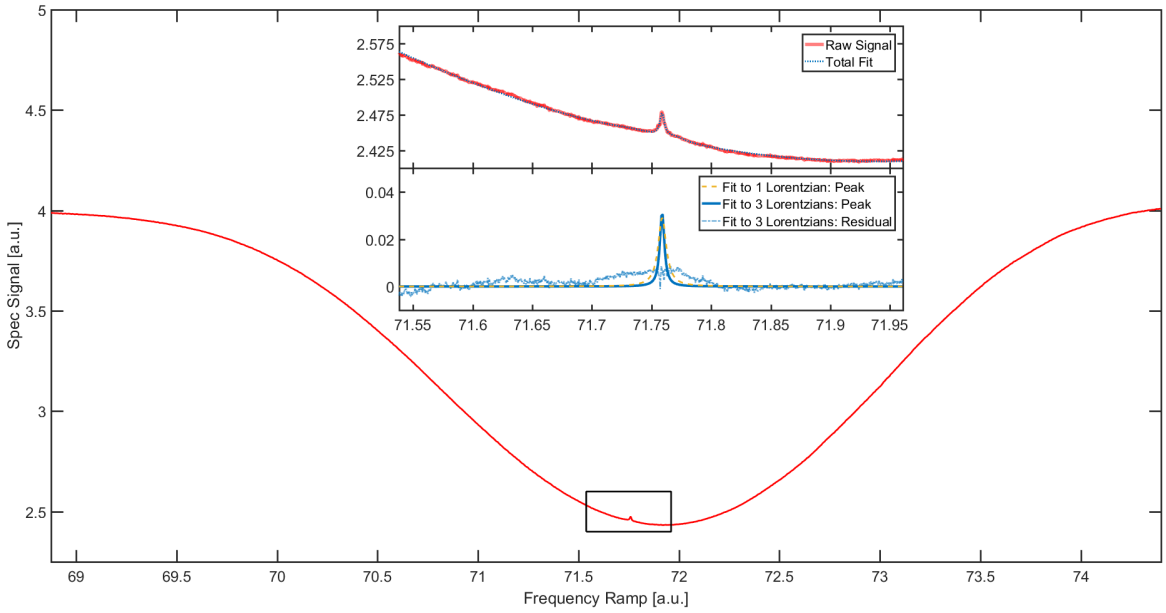

Figure 5.14: 689 nm saturation absorption spectroscopy. The entire Doppler signal is shown as reference for the absorption percentage at 350°C and the relative size of the Doppler-free signal. The top inset shows the same signal zoomed-in, along with a fit to a Gaussian and three Lorentzians. The bottom inset shows the fit Doppler-free peak in yellow, assuming that only one transition with a Lorentzian lineshape contributes to the peak. In practice, the peak is typically broadened due to the presence of other m_J states. By applying a large magnetic field, we can smear out the contributions from those states and obtain a narrower $m_J = 0$ peak. The bottom inset also shows that peak, assuming fits to a sum of three Lorentzians, and the residual smeared-out pedestal.

Master laser and spectroscopy

We use a 30 kHz linewidth 25 mW Toptica DLPro as our master laser. We chose this option for the laser linewidth because while it is still wider than the natural 7 kHz transition, the Doppler cooling limit associated with it is still in the hundreds of nanoKelvin, more than enough to efficiently Doppler cool to high PSD. Because of the abundance of ^{88}Sr, we lock the master to that feature and use a castle of AOMs to achieve the 351.49 MHz frequency splitting necessary to cool ^{84}Sr. Because of the power losses we take on these frequency shifts, we use 689 nm TAs to generate more power.

We chip about 25 mW of power off of a TA output to send to a spectroscopy cell.

Spectroscopy on this transition is extremely difficult; because the transition is so narrow, the optical density of the strontium cloud in the cell needs to be very large. To achieve this, we based our cell design on that outlined in the Stellmer thesis, Appendix B [21]. It is longer and narrower than our other spectroscopy cells, and we blow up the beam to fill the entire diameter of the tubes to maximize interaction with the atomic cloud. The technical drawings for the current cell design, as well as one with improvements for the next iteration of the cell, may be found in Appendix I. We also use a large powerful magnet placed near the cell to split the m_J states, resulting in a narrower signal. The Doppler-free signal can be seen in Fig. 5.14. We went through several iterations of cell operation before we found a configuration that worked. Here is a brief history, for posterity and as warnings to anyone planning to build such a cell:

- We initially loaded about 12 g of strontium into the spectroscopy cell and pumped down to about 0.1 mTorr. We used the DC-current resistive heating wire (SEI 10/50) recommended by the Innsbruck group to heat the atomic reservoir cup. We could initially see a large Doppler-free signal when heating the cell cup to around 400°C, but over a couple of months, we needed to turn the temperature up to 650°C to see any signal. At this time, the windows of the cell also became coated.

- We broke the vacuum, cleaned out the strontium, and baked the cell for a week, operating under the assumption that contaminants in the cell had been reacting with the strontium, thereby necessitating the temperature increase. We also designed copper blocks attached to cooling plates, and attached them to the sides of the cell near the windows to protect them from strontium buildup. We reloaded 12 g of Sr, baked the cell again at 200°C, and pumped down to just under 1 mTorr. This gave us a decent Doppler-free signal with a Doppler signal absorption around 30%.

- We found that over time, we still needed to turn the cell temperature up. We

inevitably would eventually reach operating temperatures near 700°C in attempts to recover sizable saturation absorption signals, at which point the heaters would fail. We damaged all of our heating wire and began to use heating tape powered by variacs, which did not hurt our signal or add any noise compared to the heating wire.

- We finally figured out that mass migration of strontium was a huge problem. Almost the entire 12 g of metal, rather than cooling back to a solid in the bottom reservoir cup, would re-form as a solid in the top of the reservoir cup and in the narrow tube, which had the effect of blocking the light beams. When we saw this start to happen, we would hit the cell with a hammer from the outside to dislodge the metal.[5] We would then start the whole temperature cycle again.

- We finally removed the cooling blocks, which we suspect were encouraging solid formation in the narrow part of the tube. We also attached heating tapes around not only the center of the reservoir, but extending out several inches to both sides. We now heat the cell to around 350°C and get more than 50% Doppler signal absorption. When we suspect that strontium is moving to a particular area in the cell, we preferentially heat that area and cool the others. This has worked extremely well, and we have not needed to increase the cell temperature for the past year. However, there is now still a possibility that the strontium will coat the windows over time.

We offset our pump and probe beam by 160 MHz by putting a double-passed 80 MHz AOM in the pump beam only, such that the laser is offset from the transition by 80 MHz. We then use the lock-in amplifier built into our Toptica DLCPro controller to modulate the frequency of the pump beam ("modulation transfer spectroscopy") to generate an

[5]There were times we also picked up the entire cell and hit it against the optical table. We called this "coaxing the strontium back home."

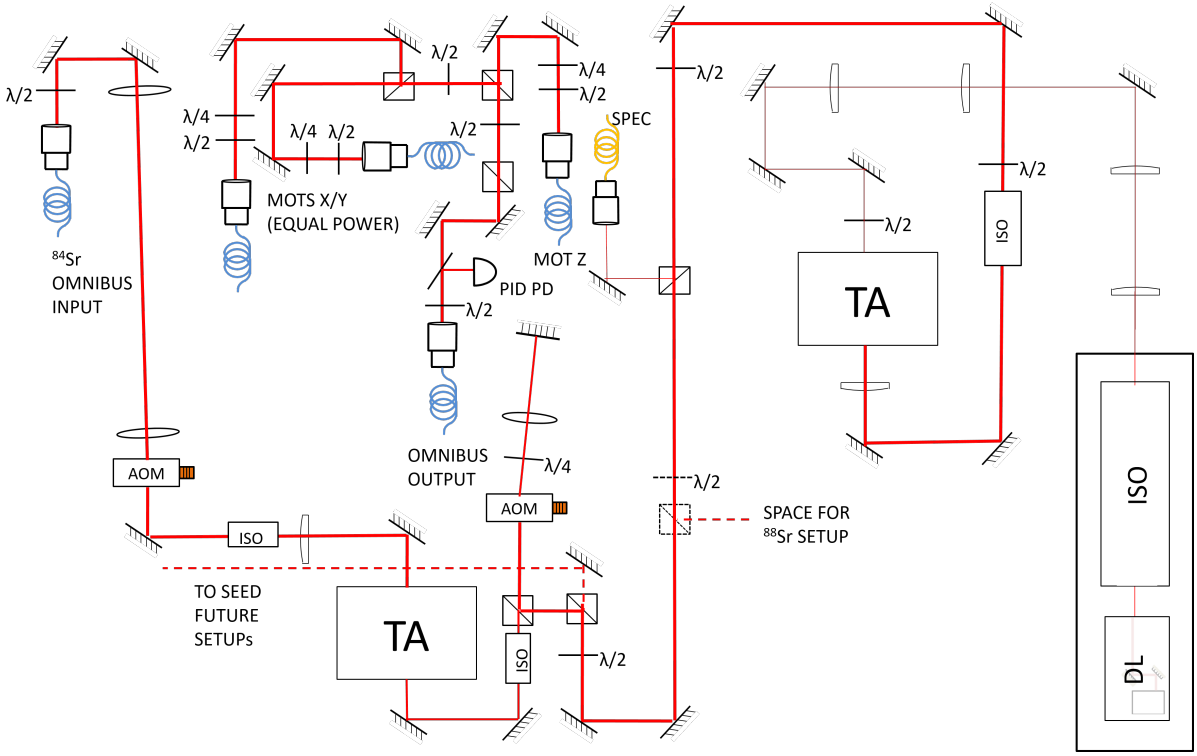

Figure 5.15: 689 nm laser setup, showing 689 nm Toptica DLPro and all main beam paths. Polarization-maintaining single-mode fibers are drawn in blue, and non-polarization-maintaining single-mode fibers in yellow. Spectroscopy setup is not shown.

error signal to which we can lock using the proprietary TOPAS software. We have seen a couple of issues with the DLCPro/TOPAS which are worth mentioning. The first is that the connection between the controller and the computer can be lost. This issue is largely mitigated by using ethernet connection rather than USB. The second is that occasionally, we begin to see digital noise on the spectroscopy signal. This is not caused by ground loops as far as we can tell, but is usually fixed by power cycling the controller.

Tapered amplifiers

We initially set up the 689 nm table with a single homebuilt TA, using an Eagleyard EYP-TPA-0690-00500-2003-CMT02-0000 chip and the design described in the Singh thesis [19]. The TA is seeded directly by 100% of the master laser power, the mode of which is not

great but which we shape to match the TA mode as well as we can. The TA initially output 400 mW, but over a year dropped to 200 mW. At the same time, the spatial output mode deteriorated, which made the setup worse because we fiber-couple the MOT beams. The power stayed stable until mid-2018 when it dropped further to 160 mW, at which point we could not operate the machine anymore. A new TA was built in November 2018 to replace the old one. Like the first, it initially output over 350 mW, but the spatial mode became very poor over just a couple of months, and our power situation again became tenuous. We eventually added the old TA back into the laser setup further down the beam path. This finally gave us enough power overhead to run the machine comfortably. We added PID control to the 689 nm MOT power, which has helped with both machine robustness and troubleshooting. The 689 nm laser table layout may be found in Fig. 5.15.

We are not sure why our TA design seems to be particularly poor for 689 nm chips (the 671 nm versions in the lithium setup seem to be more stable). We have plans to develop a different TA design which will allow fine adjustment of the TA incoupling and outcoupling lenses, which we suspect are drifting.

5.1.7 1064 nm and 915 nm lasers

For our optical dipole traps and optical lattices, we use two different colors of far-off-resonant beams: 1064 nm and 915 nm. Since these setups are ubiquitous among neutral atom AMO groups, I will not include laser setups in this section.

1064 nm setup

We use an NKT Koheras AdjustiK 100 mW seed in conjunction with an NKT BoostiK fiber amplifier to generate 15 W of 1064 nm light. There were two main reasons we decided to purchase from NKT, both of which were motivated by the lithium experiment:

1. We had heard from various groups that running fiber amplifiers (including the Nuferns used by the lithium experiment) without a seed could break the amplifier. By purchasing the seed and amplifier from the same company, we made sure that there was an interlock such that if there was ever a problem with the seed, the amplifier would be protected.

2. The lithium machine seed, a 60 mW Orbits Lightwave, has had issues with power stability since we bought it, and broke about a year ago. The NKT BoostiK only requires a 10 mW seed. By purchasing a 100 mW seed in conjunction with a 75:25 fiber splitter, we ensured that even if the lithium seed broke, we could use the NKT AdjustiK to seed the amplifiers on both machines. This is the configuration in which it is currently being used.

The AdjustiK is controlled via NKT software called GraphiK, which includes useful graphs to monitor output power. The BoostiK is controlled via a simple set of instructions on the Hyperterminal; power output can be changed from 1 W at 0.1 A of current to 15 W at 8 A of current. The BoostiK output is directly coupled to an Oz Optics 30 dB isolator. We add a second (Thorlabs) 30 dB isolator, after which we get around 11 W of usable light out. The entire 1064 nm beam path is enclosed in its own aluminum case on the strontium machine optical table. The light is shaped and focused by fused silica V-coat YAG lenses to minimize thermal lensing issues, and we use zero-order waveplates from Foctek and high-power cubes from Thorlabs. As noted for the lithium machine in Section 4.1.5, we initially used 1 mm-aperture Intraaction AOMs (ATM-801DA6) to switch some of the beams. However, we found that the thermal properties of this AOM were not good enough for such high powers, which led to a great deal of pointing noise. We switched to solely using the 2 mm-aperture models ATM-802DA6, which helped a lot.

The 1064 nm beams, whether optical dipole traps or lattices, all have PID-controlled

intensities.[6] To switch our power between the beams meant for cooling and the beams meant for experiments, we use waveplate rotators from Pacific Laser Equipment. They have a relatively slow rotation rate of 3 to 4 s/rev, but this is still faster than our optical evaporation time, so it doesn't matter to us. For detailed instructions on how to program and control the waveplate rotators, please see Appendix J.

The optical dipole traps for evaporative cooling are free-space coupled on the strontium machine table. We use Polaris double-sprung mirror mounts and custom-designed and machined optomechanics to bounce the light from the optical table up to the breadboard. We also make sure that once the beams leave the aluminum enclosure, they are as protected from air currents and vibrations as possible. The beams for experiments (optical dipole traps and lattices) are fiber-coupled using high-power Thorlabs APC polarization-maintaining fibers. We used to use Oz Optics high-power fibers which we thought were angle-polished but were actually flat-polished; the problems arising from using these fibers for lattices are discussed further in Appendix E, as are various other considerations for optomechanical stability.

915 nm setup

Our 915 nm laser is a Sacher Lynx ECDL, which outputs about 100 mW. We initially bought this laser because 915 nm is the magic wavelength for the 689 nm transition (see Appendix D for Sr polarizability calculations); we eventually want to build two TAs to create a 2d magic lattice for quantum gas microscope experiments. However, in the meantime, we decided to use this laser for our phasonic spectroscopy explorations (see Chapter 8). The ECDL currently seeds one homebuilt TA (using the same design as the 671 nm and 689 nm TAs) with an Eagleyard EYP-TPA-0915-01500-3006-CMT03-0000 chip to generate about 1 W of power. After an isolator and an AOM, this drops to around

[6] We have found that "cleanup" polarizing beam-splitting cubes are necessary at various places in the 1064 nm setup; this is explained in Appendix E.

Axis	Vertical	ODT 1	ODT 2	Phason Expt	Tight Trap Expt
Company	Andor	Blackfly	Blackfly	Blackfly	Blackfly
Model	iXon 897	Type 1	Type 2	Type 1	Type 2
Cicero delay (μs)	60	250	100	600	200
Mag (lenses)	1000/125	500/300	400/200	300/150	35/150
Mag type	Mag	Mag	Mag	Mag	Demag
Pixel size (μm)	16.6	3.75	6	3.75	6
μm/pixel	2.075	2.25	3.00	1.875	25.714
VVA potentiometer	821	720	660	800	700
Cicero exposure (μs)	16	28	28	28	16

Table 5.7: Strontium cameras and corresponding imaging parameters. Blackfly Type 1 refers to model number PGE-12A2M, while Type 2 is PGE-05S2M-CS.

700 mW. We then couple around 300 mW through a Thorlabs polarization-maintaining fiber. The beam power is monitored after the fiber and controlled via PID. All of the optics we use are standard E03 mirrors, B-coated optics from Thorlabs, and achromatic doublets from Edmund Optics.

5.1.8 Cameras

We use several cameras for several different imaging axes. The main camera, used to take the majority of images for experiments, is an Andor iXon 897 EMCCD camera set up with a magnification of 8 looking along the vertical (gravity) direction. This gives us a resolution of about 2 μm/px. The objective lens for this setup, a 125 μm doublet, extends from the top breadboard down towards the top viewport using a lens tube, Z-translation stage for focusing adjustment, and a custom mounting jig. The jig for the camera itself was also custom-designed to mount to the top breadboard. The imaging path along the top breadboard, including an f = 1000 refocusing lens, is all contained in lens tubes to minimize stray light which could result in increased dark counts. Designs for the objective jig and camera mount may be found in Appendix I.

In addition to this main imaging axis, we use several auxiliary cameras to monitor

fluorescence and help with beam alignment. These auxiliary cameras are all PointGrey Blackfly cameras set up with varying magnification. All of our cameras and imaging setup parameters may be found in Table 5.7.

5.2 Strontium Cooling

This section will discuss details of each step in the strontium cooling sequence for ^{84}Sr, including detunings and saturation parameters. It steps through transverse cooling, Zeeman slowing, the blue MOT, repumping, the red MOT stages, optical dipole trapping, and evaporation to BEC. The general techniques discussed here are broadly applicable to the other bosonic isotopes; ^{84}Sr is a nice place to start because despite its low natural abundance, it has a very favorable scattering length for optical evaporation. Cooling ^{87}Sr is a more complicated task. The Stellmer thesis is a nice source for discussion on the experimental quirks associated with the fermion; new SWAP cooling techniques out of JILA have also eased some of the technical difficulty [21, 61, 62].

5.2.1 Transverse cooling

After the nozzle, we have vertical transverse cooling in the cube originally designed for both dimensions, and horizontal cooling in the cube which contains the atomic beam stopper. Both of these beams are detuned from resonance by roughly -$\Gamma/2$ and coupled from the laser table via multimode fibers, so they have strange ring-shaped spatial modes. The vertical beam is roughly a 0.5 cm by 3 cm oval, and contains 5.5 mW of power which is retroreflected (saturation parameter $s \approx 0.2$). The horizontal beam is roughly a 0.5 cm by 2 cm oval, and contains 18.2 mW of power which is also retroreflected ($s \approx 1.1$). The power balance between the two beams is set empirically to optimize fluorescence of the repumped MOT. The two transverse cooling beams together result in a repumped MOT fluorescence increase of roughly 100%. Fluorescence from the slower light and the

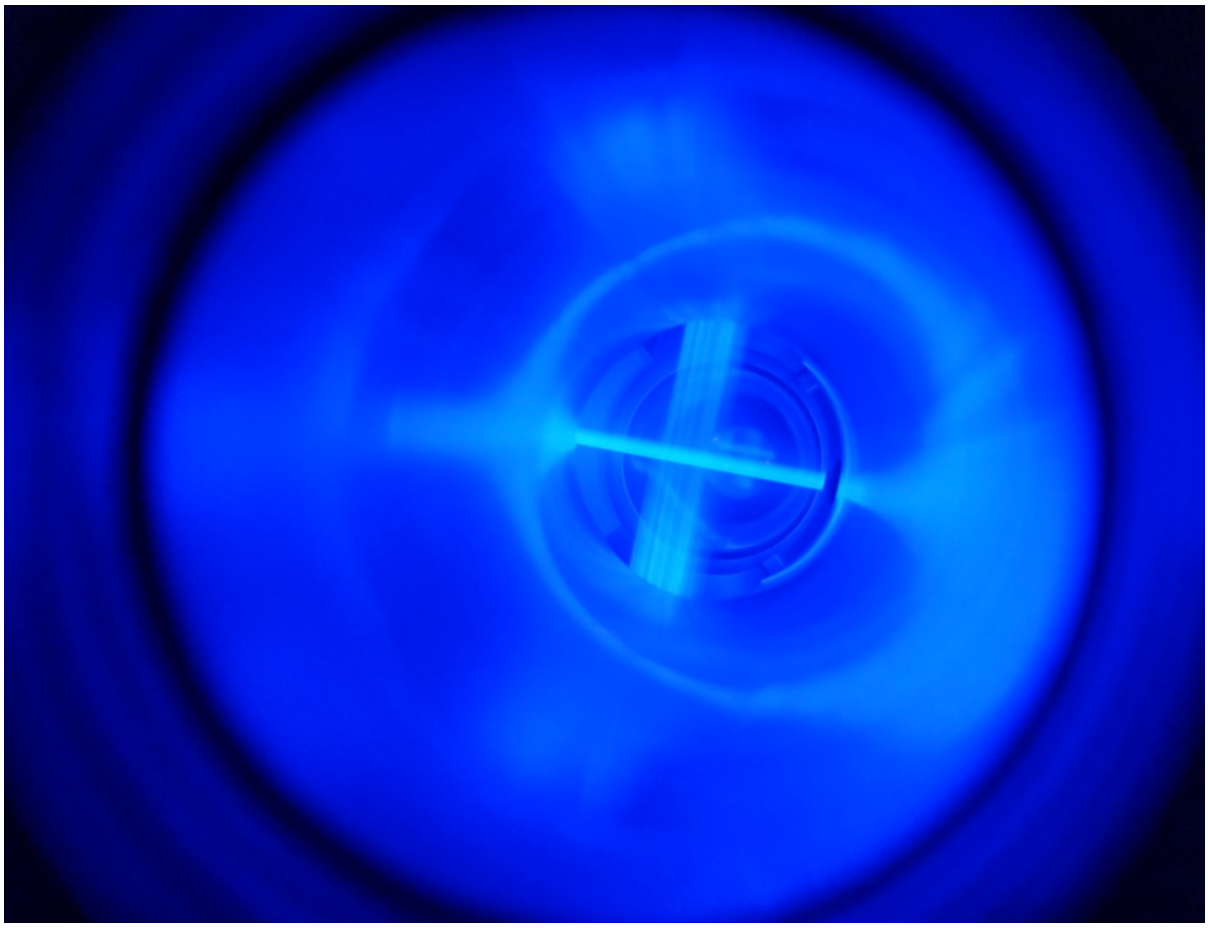

Figure 5.16: The atomic beam and surrounding distribution fluorescence from slower light and vertical tranverse cooling light in the transverse cooling/4-way cross section of the oven.

vertical transverse cooling light can be seen illuminating the atomic beam (and atoms in the "pedestal" of the nozzle distribution) in Fig. 5.16.

5.2.2 Zeeman slower

Full details of the Zeeman slower design and magnetic fields may be found in Section 5.1.2. As noted in Section 5.1.4, our slower light is coupled through a special glass-capped fiber to allow us to couple 180 mW of 461 nm light, and get 130 mW of light out. The beam is set to the proper polarization, and is magnified to fill the slower tube at the

slower exit, and is focused so that it is smaller near the nozzle (the beam convergence is set empirically with a translation stage to optimize the repumped MOT fluorescence). Assuming that the beam fills the slower tube for its entire length, this corresponds to $s \approx 1.1$. Recall from Section 5.1.2 that the slower fields were designed for a detuning of around -750 MHz; we then empirically optimized this detuning to -744 MHz by imaging a ^{88}Sr magnetic trap for various slower detunings and powers.

The transverse cooling light is taken from the 0-order of the slower AOM, while the slower light is taken from the -1-order. The power balance between these orders is set by looking at the unrepumped MOT fluorescence.

5.2.3 Blue MOT

From this point onwards, all cooling is done in the main chamber. Fig. 5.17 shows the locations of all main chamber beams relative to various ports.

We can define a plane parallel to the optical table (normal to gravity) which passes through the atomic cloud; call this the atomic plane. The three MOT beams are labeled A, B, and C, and they are all detuned from resonance by approximately -Γ. A and B are coupled in using MOT cagemount optics discussed in Section 5.1.3; since they are attached to the 1.33" CF viewports, they are orthogonal to each other, but tilted from the atomic plane by 16°. MOT C enters the bottom of the chamber and exits through the top. We try to make this beam orthogonal to both MOT A and MOT B but are limited by the height and radius of the turret; instead of cutting a 16° angle through the chamber, we can only do 11°. This has not seemed to hurt us. We have around 5 mW on the machine table in each beam, and all are retro-reflected. They are all roughly collimated with a 4 mm diameter (any slight deviations from collimation are to compensate for power losses in the retro-reflected beam). Our effective saturation parameter is 6.

The blue MOT requires an approximate field gradient of 42 G/cm, which also forms

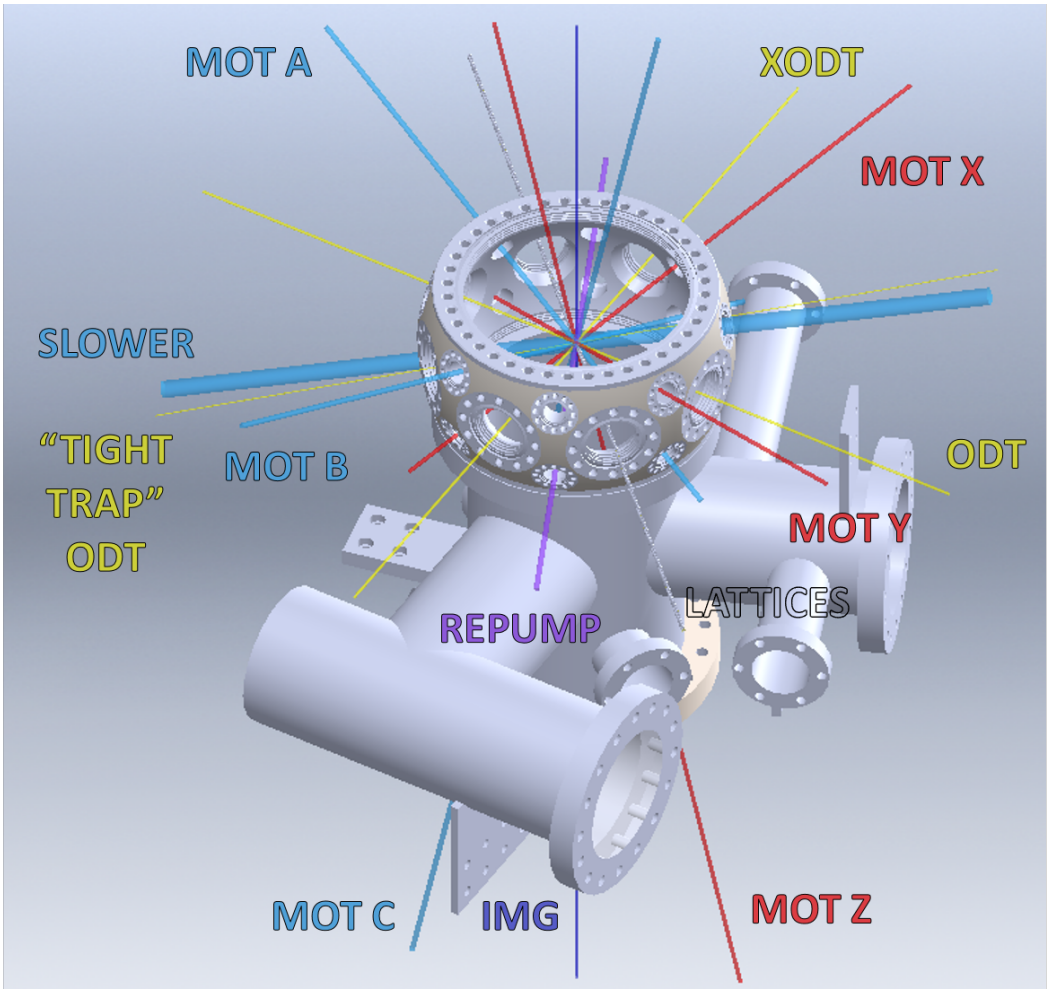

Figure 5.17: Slower, Blue MOT (A, B, and C), Red MOT (X, Y, and Z), repump, optical dipole trap (ODT/XODT), lattice, and vertical imaging beams (IMG) and their relative locations around the main chamber. Each beam is labeled on its respective side of entry into the chamber; retroreflections are neither depicted nor labeled.

a trap for magnetically-trappable states. As the MOT loads, a significant fraction of the atomic cloud becomes dark to the 461 nm light as it falls into the metastable (but magnetically-trapped) $|^3P_2\rangle$ state. This is actually quite convenient, as it allows us to load a reservoir of dark magnetically-trapped atoms, but it means that MOT fluorescence is not a great quantitative metric of the loading rate. It also means that when aligning the MOT beams, we need to make sure that the MOT forms at the location of the magnetic trap to optimize loading efficiency. We found that a good way to do this is to image the

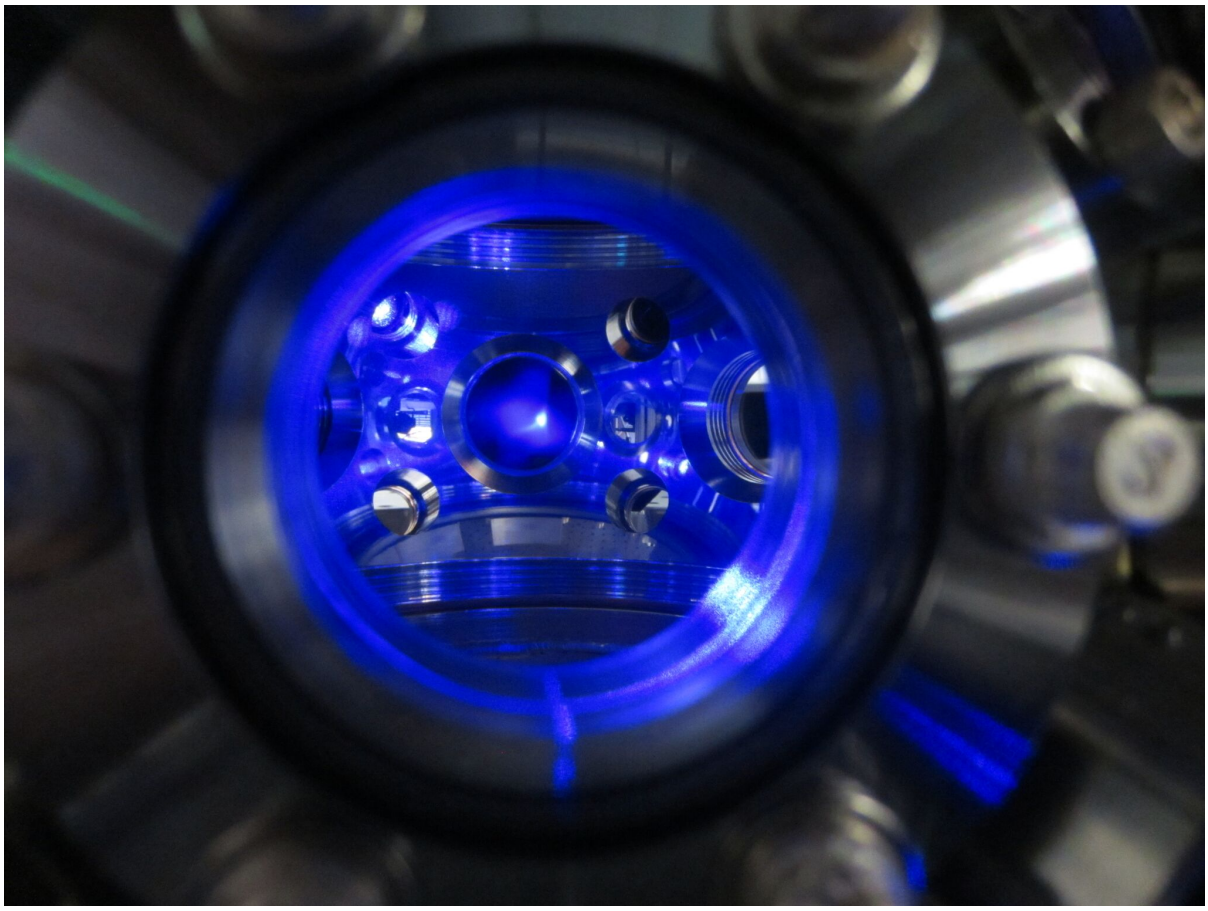

Figure 5.18: Photo of a 461 nm MOT

unrepumped MOT fluorescence using two different cameras (looking along orthogonal axes), and then absorption-image an equilibrated magnetic trap of ^{88}Sr atoms along both of those axes. This process is iterated while walking the MOT beam alignment.

Once the beam alignment is set and the loading rate is optimized, we switch back to ^{84}Sr. As a diagnostic, we look at the ^{84}Sr MOT fluorescence (with and without repump) using the lattice imaging axis just after optimization, and use it as a standard candle at the beginning of every day (this number is around 3.5×10^7 counts with background subtracted). We typically run the MOT for around 10 s to load the magnetic trap (a blue MOT can be seen in Fig. 5.18). We believe this gives us 6-7 million atoms in the magnetic trap, just using natural abundance as a scaling ratio, but we cannot directly measure this.

Once the magnetic trap is loaded, we hold it for 500 ms while ramping down the field gradient to 16 G/cm; this mitigates the experimental difficulty of controllably switching to the much-lower red MOT field gradients. Our temperature at this stage is around 1 mK (effectively set by the Doppler cooling limit of the blue MOT), and our PSD is in the high 10^{-6} s to low 10^{-5} s.

All of the cooling parameters for the next stages—the repump, red MOT 1, and red MOT 2—are summarized in the cooling schematic (Fig. 5.19).

5.2.4 Repumping

Once the atoms are magnetically trapped, we need to repump them back to the $|^3P_1\rangle$ state to cool and trap them on the 689 nm cycling transition. We do this by flashing 1.5 mW of 403 nm light collimated at 4 mm beam waist (saturation parameter $\mathcal{O}(1)$) on the magnetic trap for 3 ms. During this time, we also preemptively turn on the red MOT 1 light to catch any repumped atoms that may escape within those 3 ms.

5.2.5 Red MOT

Strontium's intercombination transition allows us to use Doppler cooling to realize much greater PSDs than are typically achievable without the use of sub-Doppler and evaporative cooling. The 7.4 kHz linewidth corresponds to a Doppler cooling limit of around 180 nK, lower than the critical temperature of the BEC transition! Practically speaking, we cannot cool much further than 1 μK due to experimental inefficiencies, but this is still cold enough to easily trap in a crossed ODT. Since these MOTs are operated on the intercombination line, they are sometimes called intercombination or narrow-line MOTs. We usually just refer to it as a red MOT, referring to the 689 nm transition wavelength.

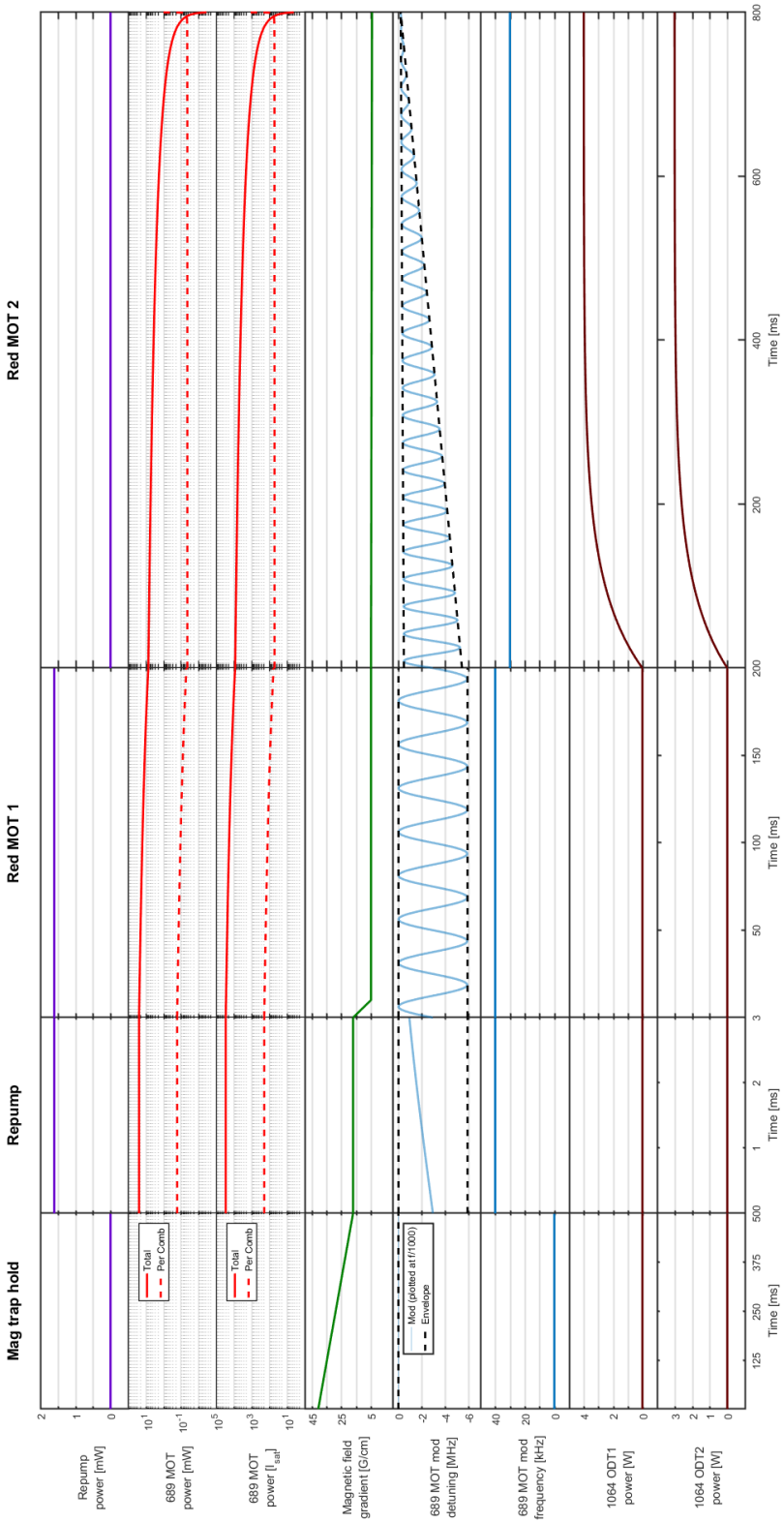

Figure 5.19: Graph of red MOT modulation, currents, and ODT ramps

Red MOT 1

Addressing atoms with any significant velocity requires working in the regime where the light detuning is much larger than the natural linewidth (contrast this with, for example, the blue MOT). We require the detuning of the light to balance the Zeeman shift of the atoms. Using a $\Gamma = 7.4$ kHz linewidth, the Zeeman shift of 1.4 MHz/G, and a 5 G/cm field gradient in $\hat{z}$, we find that regardless of the detuning, this condition is only met for a spatial "shell" of 10 μm which is symmetric about the field zero[7]. The only thing we can affect by varying the detuning is the distance from the field zero at which this shell occurs. For a detuning of 6 MHz, we can address atoms in a 10 μm shell which sits an at $\hat{z}$ radius of 8 mm (the $\hat{x}$ and $\hat{y}$ radii will be roughly twice this, since the field gradient is half as strong). We find that we need to modulate the detuning of the red light from resonance down to -6 MHz, effectively broadening the linewidth of the laser, to create a "comb" of light detunings which are spaced by the frequency of the modulation. Those combs correspond to concentric shells of resonance in space, each at a slightly different radius from the field zero and containing a fraction of the total power. We call this broadly-modulated atom-capturing stage Red MOT 1 (RM1).

At the start of the RM1 stage, we switch our field gradient from 16 G/cm to 4.7 G/cm using analog controls (the effective switching time is around 10 ms, which does not hurt us). Our RM1 detuning ranges from -10 kHz to -5.9 MHz at 40 kHz modulation frequency. We start with 6.9 mW in the vertical MOT beam and 2.5 mW in each horizontal beam, and linearly ramp down to 2.05 mW in the vertical and 0.75 mW horizontal; all three beams are collimated to a 3 mm waist and retroreflected. This corresponds to a total MOT intensity of $28000 I_{sat}$ ($190 I_{sat}$ per comb) at the beginning of capture, and $8300 I_{sat}$ ($50 I_{sat}$ per comb) at the end. This stage lasts for 200 ms, and typically results in 6-7 million atoms captured at around 35 μK (density $\sim 10^{10}$ cm^{-3}, PSD $\sim 10^{-3}$). This is

[7]Note that this 10 μm number assumes an intensity $I/I_{sat} \approx 1$. By working at larger intensities, we can power-broaden the natural linewidth by a factor of $\sqrt{1+s}$ to broaden that region of resonance.

around the number of ^{84}Sr atoms we believe are loaded into the magnetic trap over 10 s.

It is worth noting that the maximum acceleration from photon scattering is inversely proportional to mass; for relatively heavy strontium atoms, the effects of gravity become important during the red MOT. This is the main reason we preferentially divert power to the vertical beam. Images of the RM1 stage along each imaging axis can be found in Appendix F.

Red MOT 2

We would like to achieve as high PSDs as possible by the time we load into the crossed ODT. While modulating the light during RM1 allows us to efficiently capture a large number of atoms, it also effectively increases the Doppler cooling limit by artifically broadening the linewidth. We need to do more if we wish to cool further. The next stage, which is focused on increasing the PSD, is nicknamed Red MOT 2 (RM2).

During RM2, the field gradient is gently weakened from 4.7 G/cm to 4 G/cm over 800 ms. The RM2 detuning is simultaneously ramped down and the modulation narrowed: We start with detuning modulation from -470 kHz to -5.4 MHz, and linearly ramp both the maximum and the minimum detuning to -200 kHz[8] At the end of this detuning ramp, we are left with a single frequency in our comb. We simultaneously linearly ramp down our intensity to just a few μW in the vertical beam, and essentially no power in the horizontal beams ($I/I_{sat} = \mathcal{O}(1)$). The acceleration from photons is no longer able to counterbalance gravity partway through this intensity ramp, so we need to ramp up our crossed ODT beams 1 and 2 to hold onto the atoms. We ramp both up to their maximum powers of 4 W and 3 W, respectively, using an exponential ramp.

[8]If we go to smaller detunings during this stage, we immediately begin to see atomic losses, which makes us suspicious that the laser linewidth is actually on the order of 100 kHz (corroborated by a self-heterodyne measurement). This also limits our achievable final temperatures, which are much higher than the 1 μK achieved by groups at Innsbruck and Rice, among other places [21, 63].

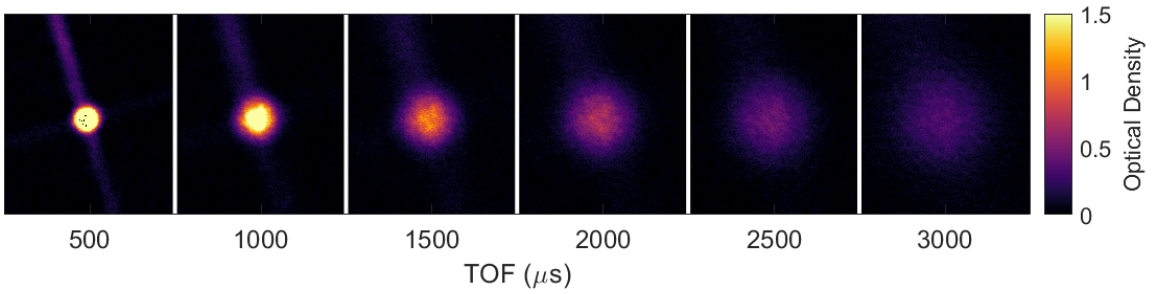

Figure 5.20: A time-of-flight out of a crossed ODT yields a temperature of around 12-13 μK, a temperature we believe is limited by the linewidth of our 689 nm laser. The slight defocusing of the ODT beam is evident at short TOFs.

5.2.6 Crossed ODT and evaporation

We typically refer to our crossed ODT beams as ODT 1 (ODT), which contains more power (4.15 W in the enclosure, 3.8 W at the atoms) at a larger waist (65 μm), and ODT 2 (XODT), which contains less power (3.85 W in the enclosure, 3.5 W at the atoms) at a smaller waist (50 μm). The ODT beam has a peak depth of 31 μK while the XODT has a peak depth of 48 μK. The crossed ODT frequencies at peak depths are $(\omega_x, \omega_y, \omega_z)$ = 2π $\times$ (270, 430, 515) Hz. However, we find that we trap the maximum number of atoms where the ODT is slightly defocused (on the order of 100s μm) to give a larger trap volume, so the actual trap frequencies are slightly weaker.

After the ODT and XODT beams are ramped up during RM2, we allow the trapped atoms to thermalize. The cloud is initially very dense, and we typically see an extremely quick (10 ms) period of atomic loss which may be due to three-body losses, followed by a slower (100 ms) thermalization period. We hold the atoms for 500 ms to allow these processes to equilibrate. At the end of this hold, we are left with around 8×10^5 to 1×10^6 atoms at 13 μK (density $\sim 10^{13}$ cm^{-3}, PSD $\sim 10^{-2}$). The lifetime of clouds in this trap exceeds 30 s.

We can then proceed with optical evaporation. We use an exponential ramp over 8.5 s with a time constant of 2.25 s, during which time the power drops to around 200 mW

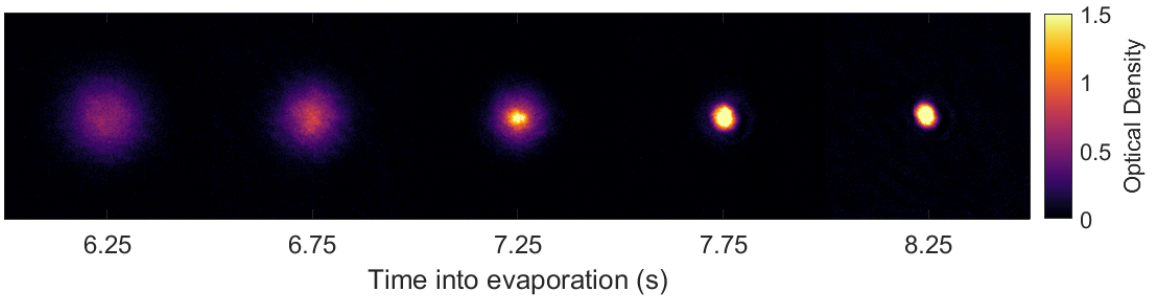

Figure 5.21: We begin optical evaporation and look at condensate formation at different times during that process, allowing the atoms to expand for 7 ms so we can image the momentum distribution. We see a clear transition from a thermal distribution to a bimodal distribution and finally to a cloud with condensate fraction ∼98%.

in each beam. The evaporation is extremely efficient due to a high initial PSD and a favorable ^{84}Sr intra-species scattering length of $124a_0$; at the end of evaporation, we are typically left with around 1×10^5 atoms with a condensate fraction of 95% or greater. Fig. 5.21 shows images of our BEC at various times-of-flight.

Chapter 6

Numerical Investigations of New Directions for Quantum Simulation

We discuss and present initial calculations elucidating two new directions for experimentally exploring extreme non-equilibrium phenomena using ultracold trapped atoms: quantum emulation of ultrafast strong-field physics, and coherent phasonic spectroscopy of tunable optical-lattice quasicrystals. Both directions seek to probe what one might call the "non-equilibrium frontier" by making use of unique features of trapped atoms such as extreme tunability and ability to be placed arbitrarily far from thermal equilibrium. Both are capable of exploring regimes of parameter space that cannot be straightforwardly attained in solid-state experiments. Certainly other related directions of research in this area exist as well; we have focused on these two as an indication of the exciting open possibilities for cold-atom quantum emulation of extreme non-equilibrium phenomena. Much of the content in this chapter is adapted from [64].

6.1 Introduction

Ultracold atoms in optical traps are increasingly being used as tools for the experimental study of many-body quantum systems important in other areas of physics [65, 66, 67]. Such experiments, often called "quantum emulation" or "quantum simulation," are made possible by the exquisite level of quantum control that can be exerted over cold-atom Hamiltonians.

A major emerging area of interest in this field is the direct experimental investigation of non-equilibrium dynamics in tunable quantum systems [68, 69, 70, 71]. Although much has already been done in this area, unexplored frontiers remain. In this chapter we define and discuss a part of this new frontier of quantum simulation experiments: the study of extreme non-equilibrium phenomena.

Since many if not most cold atom experiments have some non-equilibrium component, it is worth specifically defining the scope of this work. In the context of quantum emulation of condensed-matter physics, what we mean by an "extreme" non-equilibrium phenomenon is one which is difficult or impossible to realize in the solid state, for practical or fundamental reasons. Several new directions along these lines are possible. For concreteness, we will focus on two such new directions for extreme non-equilibrium quantum emulation:

1. Quantum emulation of ultrafast processes.

2. Phasonic spectroscopy in tunable quasicrystals.

Each of these directions concerns extreme non-equilibrium phenomena in the sense that cold atom quantum emulation techniques can move beyond what is possible in condensed-matter experiments. In the sections below we define and discuss these new directions and present the results of initial calculations elucidating the advances that are within the reach of current experimental technology.

6.2 Quantum emulation of ultrafast processes

The first experimental direction we discuss is the use of trapped atoms to understand how electrons in atoms and solids respond to ultrafast strong electric fields. Following earlier proposals [68, 69], we examine the possibility of quantitatively measuring the strong-field impulse response of artificial atoms and solids with variable pulse parameters, interactions, and lattice geometry, to advance understanding of the behavior of matter in pulsed-laser fields. Such cold-atom quantum emulation of strong-field solid-state phenomena would probe some of the fastest processes in atomic physics using some of the slowest. This approach, which is complementary to existing experimental techniques, has the potential to address important open questions in strong-field physics and to investigate unexplored regimes of ultrafast-equivalent dynamics. In this section, we will begin by motivating the proposed approach, proceed to a specific discussion of experimentally feasible ultrafast quantum emulation, and then present and discuss numerical models of simple initial experiments.

6.2.1 Scientific motivation: ultrafast phenomena

Revolutionary scientific and technological advances in ultrafast lasers have made strong-field ultrafast physics a vibrant and growing area of research [72, 73]. Some exciting prospects include real-time imaging of valence electron motion, sub-optical-cycle control of solid-state conductivity, petahertz information processing, imaging of charge transfer in biomolecules, and production of Floquet-Bloch states of matter. However, especially in the solid state, our theoretical understanding of non-equilibrium strong-field physics is limited. Important open questions include the precise mechanism and timing of tunneling ionization, the effects of interactions and correlation, and the nature of the quantum-classical crossover. Accurate numerical treatments are infeasible even for moderate-sized single atoms, let alone solids. Simplified models of ultrafast dynamics are widely used

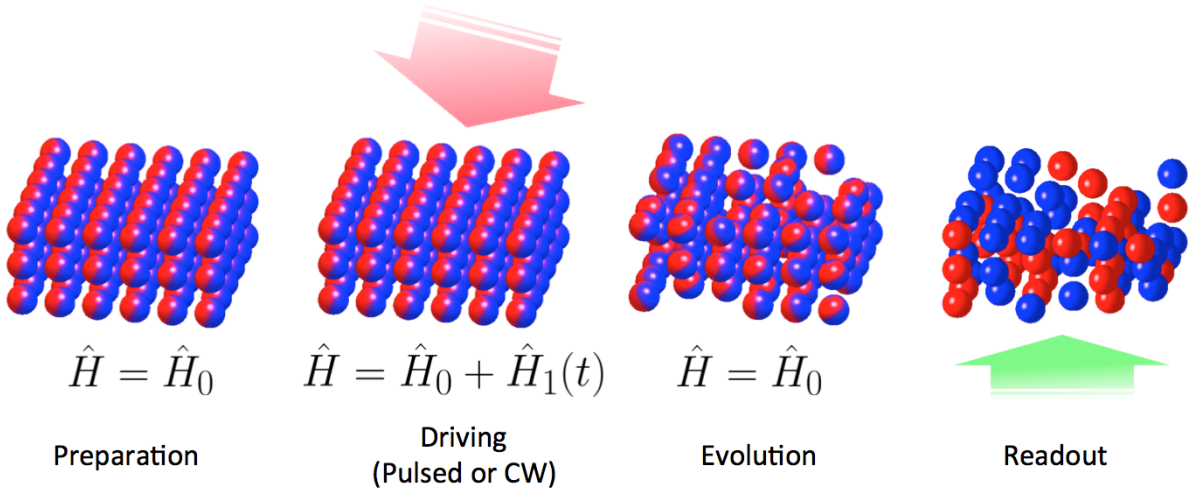

Figure 6.1: General diagram of an experiment performing quantum emulation of ultrafast phenomena. An initial state (e.g. a two-component Mott insulator) is prepared using standard techniques. This system is then subjected to a strong pulsed or continuous drive, using optical or magnetic forces. Subsequent evolution under the original Hamiltonian is followed by readout using absorptive, dispersive, or diffractive imaging.

([74], e.g.), but their range of applicability is unknown and validation is difficult. In addition to these theoretical challenges, physical limitations of pulsed laser experiments (on time resolution, pulse shape, maximum field intensity, net applied force, and readout) restrict the experimental investigation of some of the most exciting prospects in ultrafast physics: many processes occurring inside atoms and solids are still too fast for us to see or control. Many of these limitations can be addressed or circumvented by the complementary technique of cold atom quantum emulation.

Quantum emulation experiments often rely on the analogy between neutral atoms in optical lattices and electrons in crystals. Although these two systems have vastly different energy densities, they can in many cases be described by equivalent Hamiltonians, which give rise to equivalent physics. This analogy has been fruitfully used to explore equilibrium solid-state phenomena from Mott insulators to antiferromagnets [75, 76, e.g.], and dynamical phenomena from quantum quenches to dynamical suppression of tunneling to

integrability [77, 78, 79, 80, e.g.]. In the non-equilibrium context, the difference in energy scales leads to a rescaling of time: the processes underlying ultrafast phenomena like tunnel ionization occur over milliseconds rather than attoseconds, and are thus in a sense observable in ultra-slow-motion [68]. This greatly simplifies experimental access to the dynamics. It is worth noting that the low energy density of cold atom experiments also enables freezing out of all internal degrees of freedom of the constituent atoms: preparation of an atomic sample in a single hyperfine state (or two, to model spin-1/2 particles) is a standard technique. This level of quantum control of internal states is what allows for the emulation of a relatively structureless electron by a much-more-complex quantum object such as an alkali or alkaline-earth atom.

Despite the large temporal magnification factor and the ease of applying arbitrary driving fields to cold atoms with optical or magnetic field gradients, very little of the growing body of quantum emulation research has directly addressed ultrafast phenomena in atoms and solids. Earlier work on accelerated optical lattices (e.g. [81, 82]) can be understood as pioneering this approach. A few trailblazing theoretical proposals have suggested the use of cold atoms to simulate gas-phase attosecond dynamics [68] and multiphoton resonances in solids [69], and recent theoretical work has recommended the use of cold atoms to study femtosecond dynamics in an artificial benzene molecule [70].

A general diagram of an experiment implementing quantum emulation of ultrafast phenomena in a lattice appears in Fig. 6.1. Cold trapped atoms moving and interacting in an optical lattice are often approximately modeled with a modified Bose-Hubbard Hamiltonian:

$$\mathcal{H}_{\text{latt}} = -J \sum_{\langle ij \rangle} (\hat{a}_i^\dagger \hat{a}_j + \hat{a}_j^\dagger \hat{a}_i) + \frac{U}{2} \sum_i \hat{a}_i^\dagger \hat{a}_i^\dagger \hat{a}_i \hat{a}_i + \sum_i \mu_i \hat{a}_i^\dagger \hat{a}_i. \tag{6.1}$$

Here J is the tunneling matrix element, U is the onsite atom-atom interaction energy, μ_i is the site-dependent chemical potential resulting from the trap, $\hat{a}$ and $\hat{a}^\dagger$ are ladder operators, and $\langle ij \rangle$ represents the sum over all nearest-neighbor pairs. This model,

representing a "tunable artificial solid," supports rich physics including a well-studied quantum phase transition between superfluid and Mott insulator [75]. Generalizations of this model, including to the case of multiple bands, Fermi statistics, or long-range or spin-dependent interactions, are experimentally possible. External forces take the form of a space- and time-dependent chemical potential $\mu_i(t)$; these are the forces used to perform quantum emulation of ultrafast processes.

While optical lattices enable access to complex and potentially useful ultrafast solid-state dynamics [69], many ultrafast experiments use individual atoms in the gas phase rather than solid materials. Quantum emulation of single-atom phenomena can be done using a tight optical dipole trap, which plays the role of the Coulomb potential of the atomic nucleus [68]. In this context, the relevant Hamiltonian is

$$\mathcal{H}_{\text{trap}} = \sum_{i=1}^{N} \frac{\mathbf{p}_i^2}{2m} + \sum_{i=1}^{N} V_{\text{trap}}(\mathbf{r}_i) + \mathcal{H}_{\text{int}} + \sum_{i=1}^{N} V_{\text{applied}}(\mathbf{r}_i, t), \tag{6.2}$$

where $\mathbf{p}_i$ and $\mathbf{r}_i$ are the position and momentum of the i^{th} atom, V_{trap} is the trapping potential which emulates the Coulombic nuclear potential, $\mathcal{H}_{\text{int}}$ describes atom-atom interactions, and V_{applied} is the time-dependent applied potential which emulates the effect of the electric field of an ultrafast laser.

We emphasize that the goal of ultrafast quantum emulation experiments is not exclusively the preparation of systems with eigenstates and response functions mapping exactly to those of a particular atom, molecule, or solid (though interesting ideas along these lines are already being pursued, for example in the work on artifical benzene presented in Ref. [70]). A goal of equal or even greater importance is to advance our understanding of general phenomena which are relevant to a broad range of far-from-equilibrium quantum systems. We mention several examples of such general phenomena in the next subsection. Especially with this goal in mind, the cold-atom context offers advantages complementary to those of ultrafast experiments.

Two main features of such quantum emulation experiments will allow them to ex-

plore new regimes of extreme non-equilibrium matter. The first unique feature is the ten-trillion-fold temporal magnification factor resulting from operation in the ultra-low-energy regime. The second feature, enabled by the well-stocked toolbox of ultracold atomic physics, is near-complete spatiotemporal control of the energy landscape. Together, these features may enable a new approach to studies of ultrafast solid-state dynamics. The ability to study dynamics on ultrafast-equivalent timescales has the potential to facilitate fully quantum-mechanical emulation of light-matter interactions in regimes well beyond the limits of existing theories and experiments.

6.2.2 Ultrafast quantum emulation experiments

The first step in an ultrafast quantum emulation experiment is state preparation, in which well-understood cold atom techniques create an initial state of interest, such as a superfluid or Mott insulator, or simply macroscopic occupation of the ground state of a single trap. The atoms in this state serve as quantum-mechanical models of bound electrons. The next step is illumination, in which strong pulsed or continuous drive fields are applied to the sample. These fields serve to emulate the electric field of a pulsed laser. They can either be the result of magnetic field gradients or optical field gradients, and can be strongly spin-dependent. Pump-probe pulse architectures are also straightforwardly implemented, thanks to the easily accessible experimental timescales. In the next step, the fields are turned off and the system is allowed to evolve under its original Hamiltonian. Finally (possibly after an additional probe pulse), the state is read out. The cold atom context enables a set of readout techniques distinct from those possible in solid-state experiments: methods like time-of-flight momentum-space imaging, bandmapping, optical Bragg diffraction, and tomography allow precise projection and measurement of sample parameters at any time during or after a pulse. This opens a path towards quantum emulation of a holy grail of ultrafast science: fully general

attosecond-pulse attosecond-probe spectroscopy of complex correlated systems.

The first and simplest measurements such emulators will enable are studies of ultrafast photoionization (see Chapter 7. In these experiments, bandmapping or simple time-of-flight imaging will be used to determine "ionization yield" (unbinding of atoms from the optical potential) as a function of the parameters of a few-cycle pulse. Even in the gas phase this cannot be considered a solved problem: the dynamics underlying ultrafast impulse response cannot be modeled exactly for atoms with more than two electrons. Quantum emulation of such processes thus has an important role to play in elucidating the underlying physics, a role complementary to that of conventional ultrafast experiments. To give an idea of future possiblities, we suggest a few examples of this complementarity. The effects of nuclear motion can be cleanly separated from the ionization physics, and tunneling ionization studies in the presence of only s-wave contact interactions can serve as a direct test of approximate theories which make use of a zero-range core potential [83]. Measurement of still-bound excited states after a pulse may enable new probes of frustrated tunneling ionization [84]. The high temporal magnification and well-understood microscopic dynamics of the quantum emulator may provide valuable input into the long-running debate regarding tunneling times in field ionization experiments [85, 86, 87], by measuring ionization yield and the momentum of unbound atoms as a function of time at sub-cycle timescales. Studies of strong-field atomic stabilization [88] are an intriguing possibility. Another experiment enabled by ultrafast quantum emulation is the study of nonperturbative multiphoton resonances in driven lattices. While barely accessible with modern pulsed lasers, such resonances can be studied cleanly and directly in strongly driven optical lattices [69]. Other possible targets for quantum emulation of few-cycle pulsed fields include studies of polarization dependence and multifrequency fields, and the effects of defects or inhomogeneities. Polarization and multicolor excitation are straightforwardly implemented using two modulated optical or magnetic field gradients with variable relative phase, while defects and inhomogeneities

can be introduced by additional optical potentials or atoms of different spins or species.

Finally, interactions are a critical ingredient for a quantum emulator of ultrafast solid-state phenomena. Because several options exist for emulation of electron-electron interactions, an array of exciting experiments is feasible. Experiments with multiple spin states or multiple species are a natural possibility. One exciting goal is quantum emulation of the physics of recollision which underlies high-harmonic generation (HHG) in solids [89]. Although HHG itself depends upon the charged nature of the mobile constituents of matter, the recollision dynamics which result in HHG can be probed precisely by time-of-flight measurements of scattering halos (as in Ref. [90]). Studying halo structure as a function of pulse parameters and time should enable recollision studies with strongly-interacting isotopes. Long-range interactions are more difficult to realize than contact interactions, but not impossible. For example, transitions from the metastable triplet state of strontium can be used to engineer tunable long-range interactions via the exchange of mid-IR photons [91]. Quantum emulation of ultrafast laser-solid interactions in the presence of arbitrarily tunable long-range interactions would represent a truly new capability for science.

6.2.3 Calculated performance of ultrafast quantum emulators

To provide specific insight into the operation of cold atom quantum emulators of ultrafast phenomena, we have numerically modeled two simple non-interacting experiments by integration of the time-dependent Schrödinger equation. In these and all calculations presented in this chapter, the time-evolution operator is computed by a finite-difference method with periodic boundary conditions using the midpoint Crank-Nicolson method. Appropriate time steps are chosen adaptively to control numerical error. For periodic drives, long-time numerical integration is achieved by iterative application of the single-period time-evolution operator.

We present the results here mainly in order to elucidate the relationship between ultrafast experiments and cold-atom experiments, and the relevance of the latter for performing quantum emulation of the former. A crucial point underlying the motivation for experiments of the type we discuss is that no ab-initio theoretical calculation is capable of fully modeling the long-time dynamics of an interacting many-body quantum system driven far from equilibrium. Because of this, a close dialogue between theory and experiment is necessary to advance our understanding of any complex quantum phenomenon (as has happened, for example, in recent years with experiments and theories probing the quantum critical point of the superfluid-Mott insulator phase transition). Thus, the interaction-free calculation results we present are intended as a starting point for fruitful theory-experiment dialogue rather than a complete model of an interacting physical system. We emphasize that cold-atom quantum emulation is a technique which can complement ultrafast experiments rather than replace them. For more calculations and discussion of expected performance of ultrafast quantum emulation experiments, see also refs. [68] and [69].

The first experiment we analyze concerns the spectroscopic response of a bound system to a single ultrafast pulse. This can be realized by loading degenerate bosons into the ground state of a tight Gaussian-beam optical dipole trap and observing the response to position-modulation of the trap. Along a direction x transverse to the trapping beam, the potentials in the Hamiltonian of Eq. 6.2 are then given by

$$V(x,t) = V_{\text{trap}} + V_{\text{applied}} = De^{-(x-x_{\text{mod}}(t))^2/2\sigma^2}, \tag{6.3}$$

where D is the optical trap depth, σ is its waist, and

$$x_{\text{mod}} = A_{\text{mod}} \sin(\omega_{\text{mod}} t). \tag{6.4}$$

Here A_{mod} is the modulation amplitude and $f_{\text{mod}} = \omega_{\text{mod}}/2\pi$ is the frequency of the modulation.

The resulting inertial forces play the role of an electric field in an ultrafast experi-

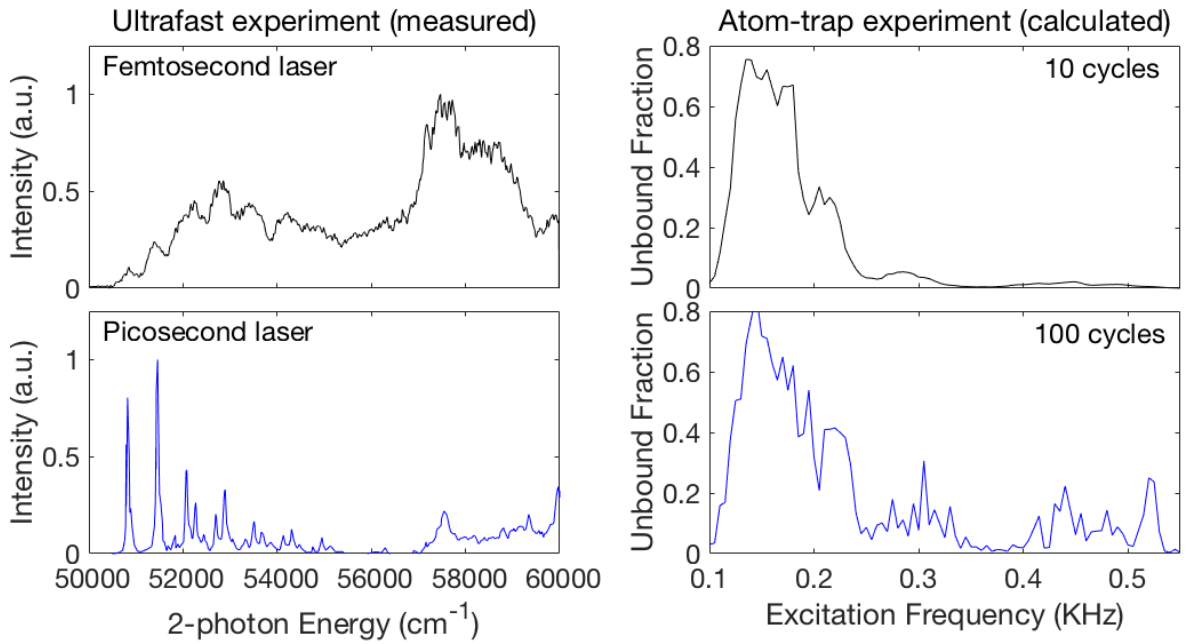

Figure 6.2: Analogy between ultrafast and atom-trap experiments. **Left:** Measured resonance-enhanced multiphoton ionization spectra of pyrazine-H4 at two different pulse times (data from Ref. [92]). **Right:** Calculated results from a strong-field quantum emulator consisting of ^{84}Sr in a shaken optical dipole trap (waist σ is 5 μm, depth D is 100 nK, shaking amplitude A_{mod} is 1064 nm). The unbound fraction (which corresponds to the ionization yield) is plotted as a function of excitation frequency for two different pulse times.

ment. A more exact realization of an effective electric field could be accomplished without substantially increased experimental complexity by using an applied optical intensity gradient or magnetic field gradient to provide the time-varying force. This can be understood as a cold-atom model of an ultrafast resonance-enhanced multiphoton ionization spectrum like those presented in Ref. [92]. Near the Fourier-limited regime, the pulse duration affects the form and sharpness of the resulting spectra; this is demonstrated for femtosecond and picosecond excitation of pyrazine-H4 in the left panels of Fig. 6.2 (data are taken from Ref. [92]). We have modeled a roughly equivalent cold-atom experiment by integrating the time-dependent Schrödinger equation in the time-varying potential of Eq. 6.3. For simplicity we have neglected interactions. The right panels of Fig. 6.2

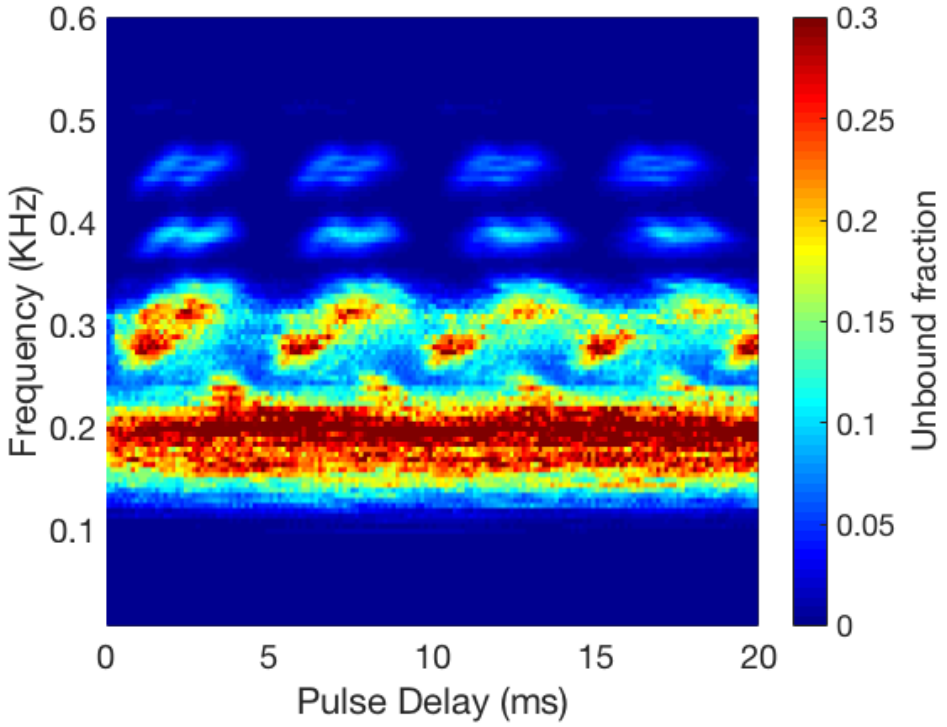

Figure 6.3: Two-pulse ultrafast quantum emulation in an atom trap. Calculated unbound fraction (corresponding to ionization yield) after 2-pulse excitation is plotted versus pulse frequency f_{mod} and inter-pulse delay. Note the interference effects in the dependence on pulse delay. Trapped species is ^{84}Sr, trap waist σ is 5 μm, depth D is 500 nK, and modulation amplitude A_{mod} is 2 μm for both 20-cycle pulses.

show the dependence of unbound fraction (which corresponds to ionization yield) on pulse frequency for two different pulse lengths. The point here is not to make quantitative comparisons between a single atom trap and a pyrazine molecule, but to support the possibility of useful quantum emulation by showing that similar Hamiltonians give rise to similar dynamical phenomena. Experiments along these lines are discussed in Chapter 7.

The second experiment we have modeled is slightly more complex; it concerns the response of a bound system to a pair of ultrafast pulses separated by a variable delay time. This is realized in the cold atom context in exactly the same way as the first experiment, but with a different modulation protocol consisting of two separated identical

pulses. Interference effects of varying the inter-pulse delay are clearly visible in the numerical results shown in Fig. 6.3; even in a non-interacting system, the features of such spectra are not always simple to understand. The two-pulse protocol could easily be extended to model phenomena involved in related ultrafast experiments such as those making use of the so-called RABBIT technique (reconstruction of attosecond beating by interference of two-photon transitions) [93, 94]. Further extensions involving varying polarization, multifrequency fields, partial-cycle pulses, and tunable interactions would be quite straightforward in the cold-atom context and would add substantially to the richness of the phenomena which could be investigated with this technique.

6.3 Phasonic spectroscopy in tunable quasicrystals

The previous section focused on quantum emulation of phenomena which occur when matter is illuminated by intense pulsed fields, and discussed the complementarity of conventional and emulator-based experiments. The extreme tunability of cold-atom experiments also enables the realization of extreme nonequilibrium phenomena that cannot be studied in any other experimental context. In this section we propose and discuss one such class of experiments: coherent phasonic spectroscopy of tunable quasicrystals.

6.3.1 Scientific motivation: quasicrystals and phasons

The formation, stability, excitation, and electronic structure of quasicrystals remain incompletely understood. Open questions include the effects of electron-phason coupling, the nature of electronic conductivity or diffusivity, the spectral statistics, the nature of strongly correlated magnetic states on a quasicrystalline lattice, topological properties of quasicrystals, and even the shape of the electronic wavefunctions [95, 96, 97, 98, 99, 100, 101, 102, 103]. Just as phonon modes arise from discretely broken real-space translation symmetry, phason modes arise from broken translation symmetry in the higher-

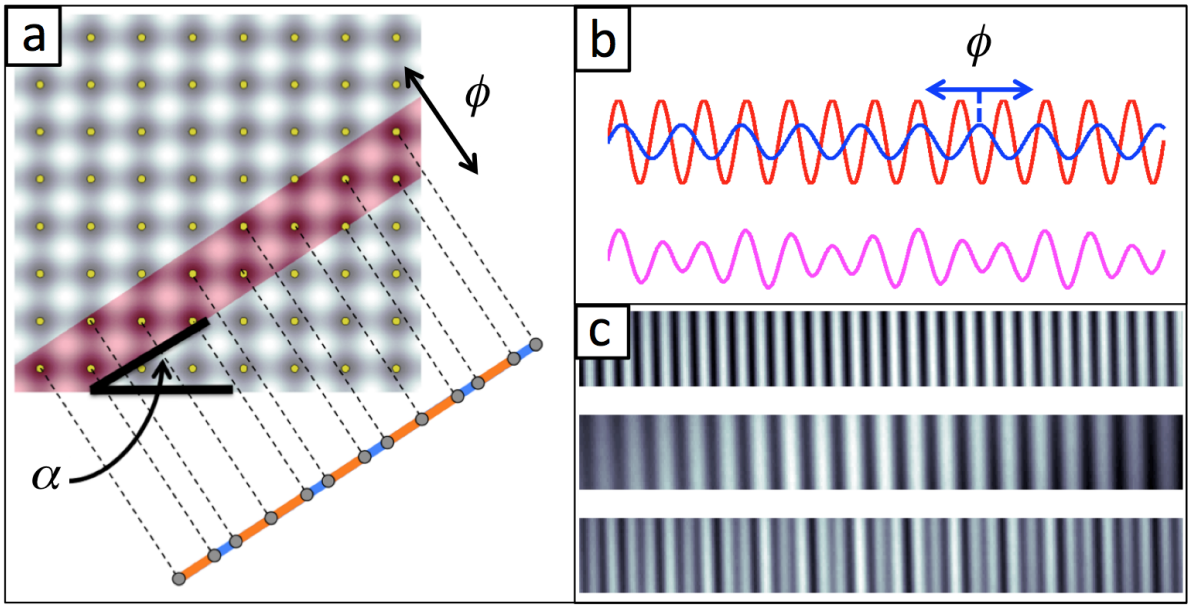

Figure 6.4: Phasons in quasiperiodic optical traps. **a:** Cut-and project construction of optical Fibonacci lattice, as described in Ref. [108]. The cut angle α controls the quasiperiodicity, and translations in the direction labeled ϕ correspond to phasons. **b:** Schematic of bichromatic optical lattice. Here the phason parameter ϕ is the relative phase between the two single-frequency lattices. **c:** CCD images of tunable monochromatic and bichromatic lattices created with angled-beam interference.

dimensional space from which all quasiperiodic lattices are projected [104, 105, 106]. Phasons have important but incompletely understood effects on thermal and electronic transport in real quasicrystals [107]. Because they involve long-range rearrangement of atoms, phasons are typically not dynamical degrees of freedom in solid-state quasicrystals; they are generally pinned to disorder or present as strain. The influence of phasons is not understood in large part because of the experimental difficulty of disentangling the effects of domain walls, crystalline impurities, and disorder from those due to phason modes. This is of interest not only for fundamental reasons, but also because of potential technological applications of quasicrystals' anomalous electrical and thermal transport characteristics.

6.3.2 Coherent phason driving with trapped atoms

The exquisite controllability of cold atoms makes them a natural choice for direct experimental investigation of such questions. Quasiperiodic potentials that have been realized or proposed for cold atoms include bichromatic lattices, well explored in the context of disorder-induced localization [109, 110, e.g.], and the recently described generalized Fibonacci lattices [108]. These two quasiperiodic structures are in fact topologically equivalent [111]. The phason degree of freedom ϕ in Fibonacci lattices and bichromatic lattices is diagrammed in Fig. 6.4.

A key experimental point is that both types of lattice enable driving of phasonic degrees of freedom via phase modulation of lattice beams. This enables a simple procedure which is essentially impossible in a solid-state quasicrystal: measurement of the response of a quasicrystal to driving phasonic modes at variable frequency and amplitude. This would constitute a new form of lattice modulation spectroscopy, in which the modulation effectively occurs in the higher-dimensional space from which the quasiperiodic lattice is projected.

In the simplest such experiment, energy absorption from the phasonic drive could be measured via standard time-of-flight calorimetry. Better characterization of the effect of strong phason driving is possible with experiments that move beyond time-of-flight calorimetry and pursue measurements using Bragg spectroscopy and (in a deep lattice) doublon creation. This new kind of spectroscopy, impossible in other quasiperiodic systems, has the potential to allow clean and precise investigation of electron-phason coupling in quasicrystals.

6.3.3 Modeling phasonic spectra

Because phasonic spectroscopy is a fundamentally new tool, theoretical predictions for the results of such experiments are scarce. In general, one expects significant differences

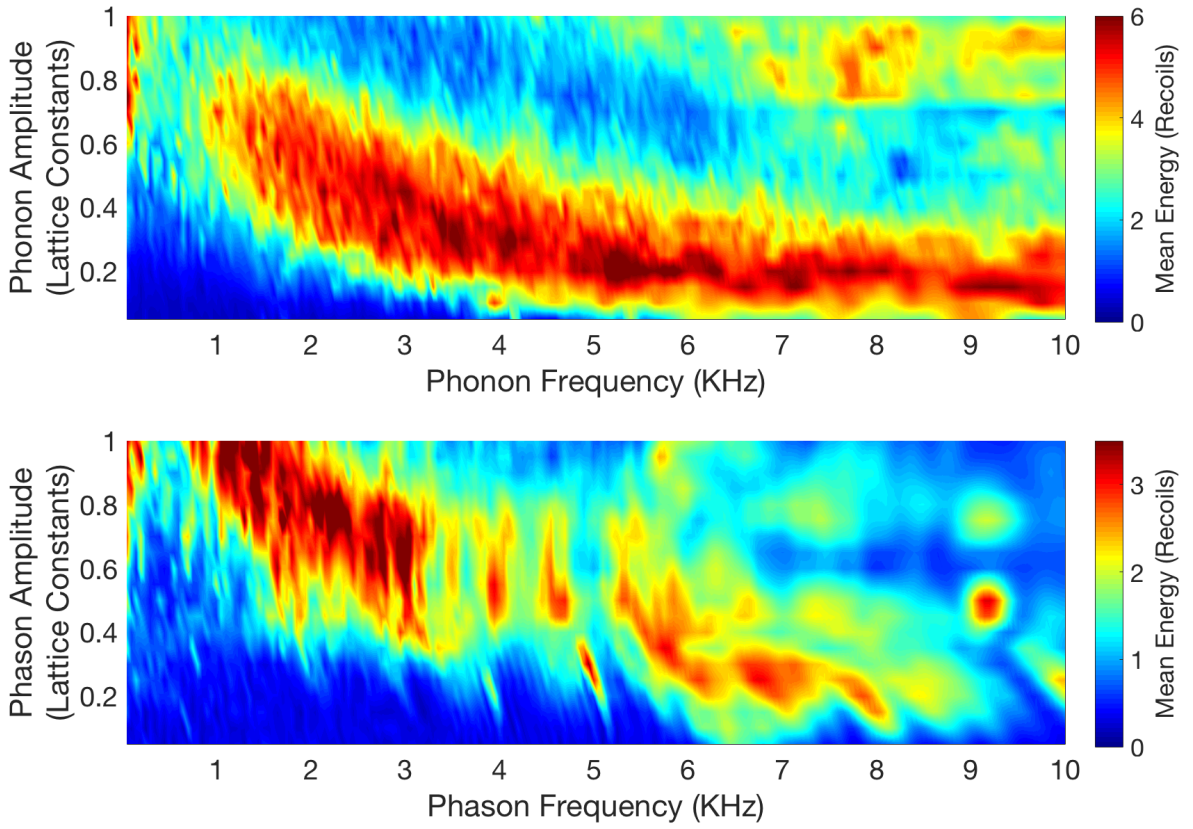

Figure 6.5: Coherent phasonic spectroscopy in quasiperiodic atom traps. Plots show calculated energy absorption as a function of frequency f and amplitude A of phononic (top) and phasonic (bottom) excitation. Calculations were performed for a 30-site bichromatic optical lattice with k_S/k_L equal to the golden ratio $(1+\sqrt{5})/2$. Here $V_L = 1E_R$, $V_S = 5E_R$, and $k_S = 2\pi/\lambda_{\mathrm{YAG}}$, with $\lambda_{\mathrm{YAG}} = 1064\mathrm{nm}$, $E_R = \hbar^2 k_S^2/2m$, and m taken to be the mass of ^{84}Sr. Each modulation was applied for 20 cycles, with the lattice phases varying in time as detailed in Eq. 8.2 (top) and Eq. 8.4 (bottom). All energies are referenced to the energy of the ground state.

from conventional "phononic" excitation as well as significant nonlinearities, particularly in the Fibonacci lattice, as large-amplitude phasonic displacements rearrange the lattice structure of the quasicrystal. To demonstrate the potential of phasonic spectroscopy as a tool for investigating quasiperiodic quantum systems, we have calculated the response of a non-interacting cold-atom quasicrystal to phasonic and phononic excitation, again by integration of the time-dependent Schrödinger equation in a time-varying potential.

The potential of a 1D bichromatic lattice can be written

$$V(x) = V_L \cos(k_L x + \phi_L) + V_S \cos(k_S x + \phi_S), \tag{6.5}$$

where V_L, k_L, and ϕ_L (V_S, k_S and ϕ_S) are the amplitude, wavevector, and phase of the long (short) lattice. Phasonic excitation of this lattice can be achieved for example by making only ϕ_L time-dependent:

$$\begin{aligned} \phi_S(t) &= 0, \\ \phi_L(t) &= 2\pi A_{\text{phason}} \sin(2\pi f_{\text{phason}} t). \end{aligned} \tag{6.6}$$

Here we refer to A_{phason} and f_{phason} as the amplitude and frequency of the phasonic drive; these are the y and x axes of the bottom panel of Fig. 6.5. More conventional "phononic" driving can be achieved by translating the entire potential without changing the phase between the sublattices, for example by applying time-dependent phases as follows:

$$\begin{aligned} \phi_S(t) &= 2\pi A_{\text{phonon}} \frac{k_S}{k_L} \sin(2\pi f_{\text{phonon}} t), \\ \phi_L(t) &= 2\pi A_{\text{phonon}} \sin(2\pi f_{\text{phonon}} t). \end{aligned} \tag{6.7}$$

Here A_{phonon} and f_{phonon} are the amplitude and frequency of the phononic drive, and are the y and x axes of the top panel of Fig. 6.5. The factor of k_S/k_L is used so that all amplitudes are in units of the longer lattice period.

Fig. 6.5 shows the calculated mean energy in a bichromatic lattice with $k_S/k_L = (1+\sqrt{5})/2$ after both phononic excitation (following Eq. 8.2) and phasonic excitation (following Eq. 8.4). The phasonic and phononic spectra display numerous intriguing structures and are qualitatively different from one another. We saw qualitative differences later on, when we realized this experiment in the lab (see Chapter 8). It should be noted, however, that the simulations presented here were done for very different parameters: Our scaled drive amplitude for a $5E_R$ primary lattice decreases in the experimental case, so the results in Fig. 6.5 are expected to be power-broadened.

In keeping with our focus on extreme non-equilibrium phenomena, we have focused here on fast (diabatic) modulation of the phasonic degree of freedom. It is worth noting

that very slow phason modulation is also possible. The resulting dynamics are of interest in part because adiabatic phasonic driving is expected to lead to long-range topological pumping of edge states [108, 112] and bulk states [113]. Both the nature of mass transport at the crossover between the diabatic and adiabatic regimes and the role of (Feshbach-tunable) interactions are further intriguing frontiers for experimental investigation of the proposed extreme non-equilibrium technique of phasonic spectroscopy in finite-size systems.

Chapter 7

Quantum Simulation of Ultrafast Dynamics using Trapped Ultracold Atoms

This chapter includes the contents of our paper, "Quantum Simulation of Ultrafast Dynamics using Trapped Ultracold Atoms" [114] which reports experiments along the lines proposed in Chapter 6.

Electronic dynamics at the shortest timescales are typically studied using ultrafast pulsed lasers. We demonstrate a complementary experimental approach: quantum simulation of ultrafast dynamics using trapped ultracold atoms. This technique counterintuitively emulates some of the fastest processes in atomic physics with some of the slowest, giving rise to a temporal magnification factor of up to twelve orders of magnitude. In these experiments, time-varying forces on neutral atoms in the ground state of a tunable optical trap emulate the electric fields of a pulsed laser acting on charged particles in a binding potential. We demonstrate the correspondence with ultrafast science by a sequence of experiments: nonlinear spectroscopy of a many-body bound state, control

of the excitation spectrum by shaping the potential, observation of sub-cycle unbinding dynamics during strong few-cycle pulses, and direct measurement of carrier-envelope phase dependence of the response to an ultrafast-equivalent pulse.

7.1 Introduction

The study of ultrafast-equivalent electronic and vibrational dynamics is a natural but largely unexplored application of cold-atom quantum simulation techniques [115, 68, 69, 116, 117]. Quantum simulation experiments often rely on an analogy between trapped neutral atoms and electrons in matter [66, 67, 118]. Although these two systems have vastly different energy densities and constituents which differ in mass and charge, they can often be described by equivalent Hamiltonians, which give rise to equivalent physics. This analogy has been used to explore equilibrium solid-state phenomena from Mott insulators to antiferromagnets [75, 119], and dynamical phenomena from Bloch oscillations to many-body localization [120, 110]. Here we extend this analogy to quantum simulation of ultrafast dynamics, with the aim of realizing an alternate experimental approach to open questions in a vibrant and expanding area of science [72, 73, 121], testing approximate theories [122, 123, 124, 74, 125], and pushing into experimentally unexplored regimes.

The quantum simulator we describe consists of an artificial atom or molecule made from a trapped quantum gas. The analogue of the atomic or molecular binding potential is the tunable AC Stark potential of an optical trap, and the analogue of the pulsed laser's electric field is an inertial force arising from rapid trap translation. The time-dependent Gross-Pitaevskii equation describing the evolution of the condensate wavefunction $\Psi(\mathbf{r}, t)$ is [115]

$$\left[-\mathrm{i}\hbar\partial_t - \frac{\hbar^2\nabla^2}{2m} + V(\mathbf{r} + \alpha(t)\hat{\mathbf{x}}) + gN|\Psi|^2\right]\Psi = 0, \tag{7.1}$$

where m is the atomic mass, $g = 4\pi\hbar^2 a_\mathrm{s}/m$ parameterizes interactions among N atoms,

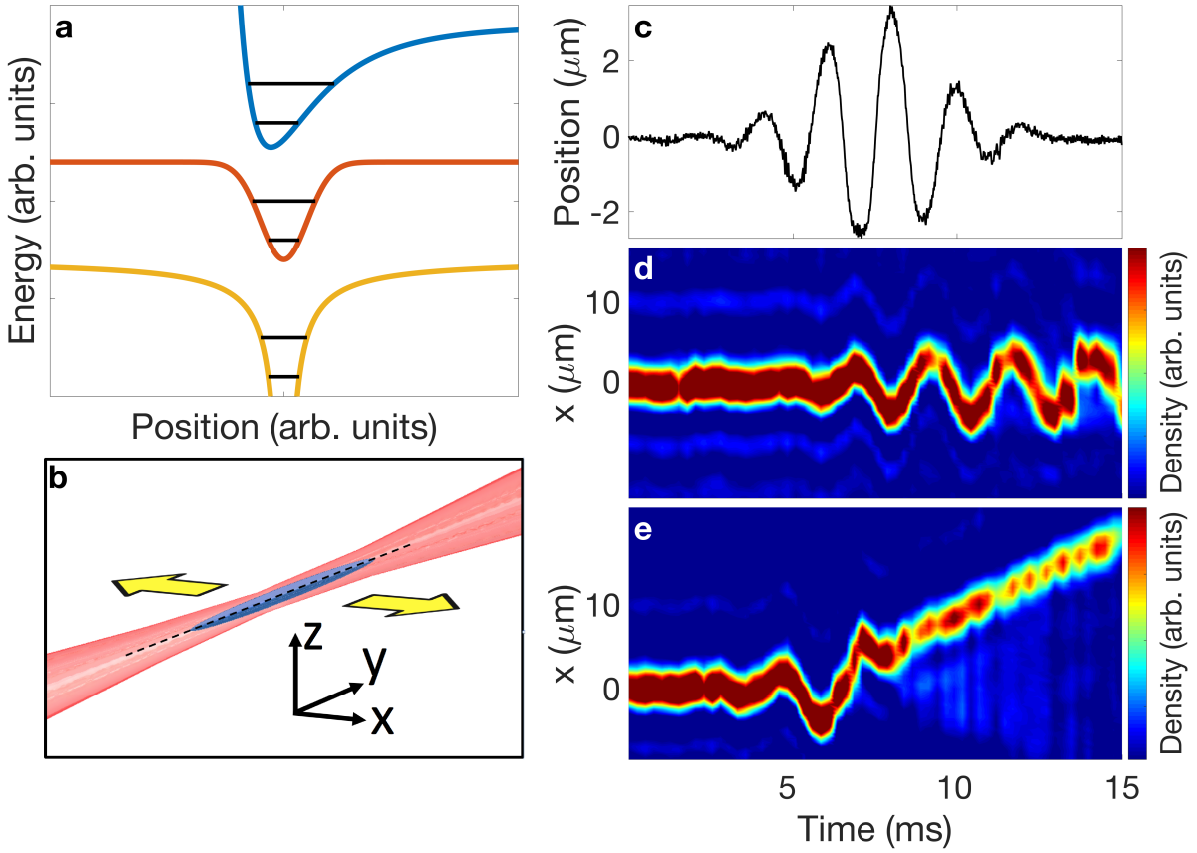

Figure 7.1: **Quantum simulation of ultrafast dynamics. a:** Schematic bound states of Lennard-Jones, Gaussian, and $1/r$ potentials (offset for clarity). **b:** Diagram of optical trap (red), which is shaken in the $\hat{\mathbf{x}}$ direction to generate inertial forces on the condensate (blue). **c:** Measured trap position $\alpha(t)$ during a pulse. **d:** Response to a weak pulse. Colourmap shows density distribution after time-of-flight as a function of time. Pulse carrier frequency is 450 Hz, pulse envelope width is 3.76 ms, pulse amplitude is 0.6 μm, and carrier-envelope phase is 0, as defined in Eq. 7.3. **e:** Response to a stronger pulse. Unbinding occurs near 8 ms, after which the atoms propagate with constant velocity. Pulse amplitude is 2.4 μm. All other pulse parameters are identical to those in **d**.

a_s is the scattering length, and the optical potential $V(\mathbf{r})$ is shaken in the $\hat{\mathbf{x}}$ direction with waveform $\alpha(t)$. Crucially, the same equation also describes the evolution of the wavefunction of an atomic electron interacting with a linearly-polarized laser field in the Kramers-Henneberger frame of reference [115], taking m to be the electron mass, V the nuclear potential including screening effects, and $g \to 0$. For dipolar excitations like those in the experiments we present, the impact of the atoms' nonzero g is minimized due to Kohn's theorem. Very similar dynamics have been theoretically predicted [115] for the cold-atom and ultrafast realizations of Eq. 7.1. A closely related equivalence is described in [68]. This equivalence between the evolution of condensate and electron wavefunctions motivates cold atom quantum simulation of ultrafast dynamics, much as the Bose-Hubbard model motivated early quantum simulation of Mott insulators [75].

Though very little of the growing body of quantum simulation work has addressed ultrafast phenomena, a robust toolkit exists for controlling and measuring excitations in trapped gases. Collective excitations in Bose condensates were a major focus of early experimental and theoretical research [126, 127, 128, 129, 130, 131], and the analogy between degenerate trapped gases and individual atoms was noted at that time [132, 133, 115]. Ultrafast probes have recently been used to study many-body dynamics in Rydberg atoms [134], and recent theoretical proposals have suggested the use of cold atoms to simulate ultrafast dynamics in atoms [68, 117], molecules [116], and solids [69].

Cold gases offer unique capabilities for dynamical quantum simulation. Due to the extremely low energy scales, the dynamics are slowed, or magnified, with respect to atomic or molecular timescales by as much as twelve orders of magnitude, allowing the observation of ultrafast-equivalent processes in ultra-slow-motion [68]. This extreme temporal magnification — quantum gas chronoscopy — enables simple and complete control over all parameters of an applied force pulse, as well as straightforward measurement of the artificial atom's or molecule's response, with time resolution much faster than all relevant dynamics. The excitation spectrum itself can also be controlled by trap shaping.

Using this toolkit of capabilities, we demonstrate experimentally that cold atom quantum simulation can be used to probe complex phenomena of ultrafast science such as the effect of carrier-envelope phase and pulse intensity on unbinding dynamics. These experiments demonstrate a new application for cold-atom quantum simulation and establish a potentially fruitful connection between ultrafast and ultracold atomic physics.

7.2 Results

7.2.1 Ultrafast-equivalent pulse synthesis

The experiments we describe use a Bose condensate of $N \simeq 20,000$ atoms of ^{84}Sr [135], with a scattering length $a_s \simeq 6.5$ nm. Rapid trap translation gives rise to time-dependent inertial forces designed to have the same approximate functional form, and the same effect of driving dipole-allowed transitions, as the electric field of an ultrafast pulsed laser. This is achieved by applying a trap which depends on x and t as

$$V(x,t) = -V_{\text{trap}} \cdot \exp\left[-2(x-\alpha(t))^2/w^2\right], \tag{7.2}$$

where w is the $1/e^2$ trap waist and

$$\alpha(t) = A \,\text{sech}\left[\eta\,(t-t_0)\right] \sin\left[2\pi f\,(t-t_0) + \phi + \pi\right]. \tag{7.3}$$

Control over the pulse is effectively arbitrary; variable parameters include amplitude A, carrier frequency f, pulse full-width at half-maximum $\tau = (2\ln(2+\sqrt{3}))/\eta$, and carrier-envelope phase ϕ. The measured trap centre translation as a function of time during a typical pulse is shown in Fig. 7.1c. All data reported here use pulse amplitudes well below the trap width. The effective Keldysh parameter in such an experiment is $\gamma_K = \sqrt{V_{\text{trap}}/2U_p}$, where the optical trap depth V_{trap} corresponds to the ionization energy and the ponderomotive potential $U_p \simeq m\overline{\dot{\alpha}^2}/2$ is the time-averaged kinetic energy imparted to the atoms by the pulse. The use of inertial forces enables realization of

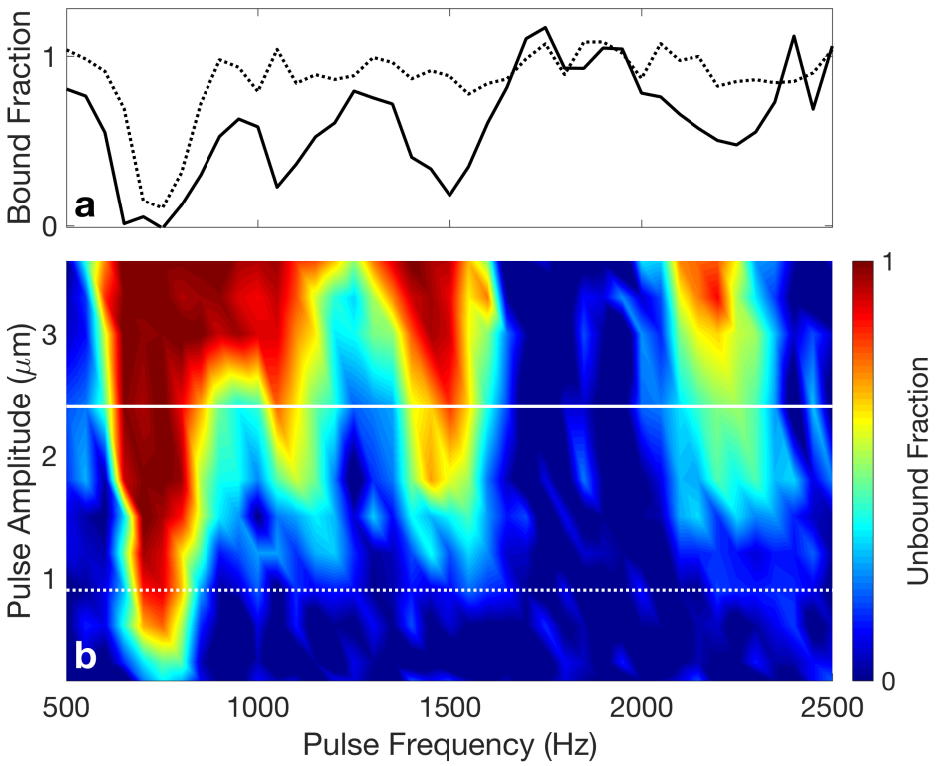

Figure 7.2: **Spectroscopy of the quantum simulator. a:** Remaining bound fraction as a function of carrier frequency for pulses with $\tau = 250$ ms, $\phi = \pi$ and amplitudes of 0.9 μm (dotted) and 2.4 μm (solid). Note the emergence of higher-order peaks and power broadening at larger amplitudes. **b:** Unbound fraction as a function of applied pulse frequency and amplitude, for a 250 ms pulse. Lines indicate cuts plotted in panel **a**.

Keldysh parameters of order unity and greater. Keldysh parameters much less than 1 could be straightforwardly attained by using a time-varying optical potential gradient rather than trap motion to apply the simulated electric field.

7.2.2 Spectroscopy of tunable collective excitations

We performed initial spectroscopic characterization of our quantum simulator by applying pulses of constant length much greater than a drive period and variable carrier frequency f. After each pulse, the atoms that had not been unbound from the trap were counted with absorption imaging. The resulting plots of bound fraction versus pulse frequency

characterize the collective excitation spectra of the trapped condensate. Nonlinear effects are straightforwardly probed by increasing the pulse intensity.

Excitation spectra for one particular trap are shown in the top panel of Fig. 7.2. The resonance at ∼750 Hz corresponds to dipole oscillation in the trap and is at the same frequency as the resonance for a non-interacting gas. As the pulse amplitude is increased, higher modes are excited and power broadening is observed. Since our trap is deeply in the Thomas-Fermi regime, these modes are anharmonic and strongly collective. The bottom panel of Fig. 7.2 shows a 2D amplitude-frequency spectrogram.

The excitation spectrum can be tuned by adjusting the trap shape, enabling the study of ultrafast-equivalent dynamics in systems with specific spectral characteristics such as mode degeneracies. The results of such tuning of the excitation spectrum are presented in Fig. 7.3. We observe good agreement with analytic predictions for dipole-allowed collective resonance positions in the broadened and unbroadened trap [131]. Note that the frequencies of these complex anharmonic modes are not simply rescaled by broadening, but disperse at different rates; this enables tunable creation of mode degeneracies. This tunability of the collective excitation spectra is a key feature of cold-atom based quantum simulation of ultrafast dynamics. Static adjustments like those demonstrated here enable the realization of desired spectral properties, and rapid tuning of mode degeneracies could enable the study of controllably diabatic or adiabatic dynamics. Future experiments could use this ability for quantum simulation of molecular energy relaxation mechanisms in the vicinity of tunable mode degeneracies similar to conical intersections [136].

7.2.3 Momentum-resolved sub-cycle unbinding dynamics

Having demonstrated quasi-CW spectroscopy of bound states with tunable energy spectra, we turn to the use of this tool for quantum simulation of ultrafast dynamics during few-cycle pulses [83]. In ultrafast streaking measurements, the electric field of a

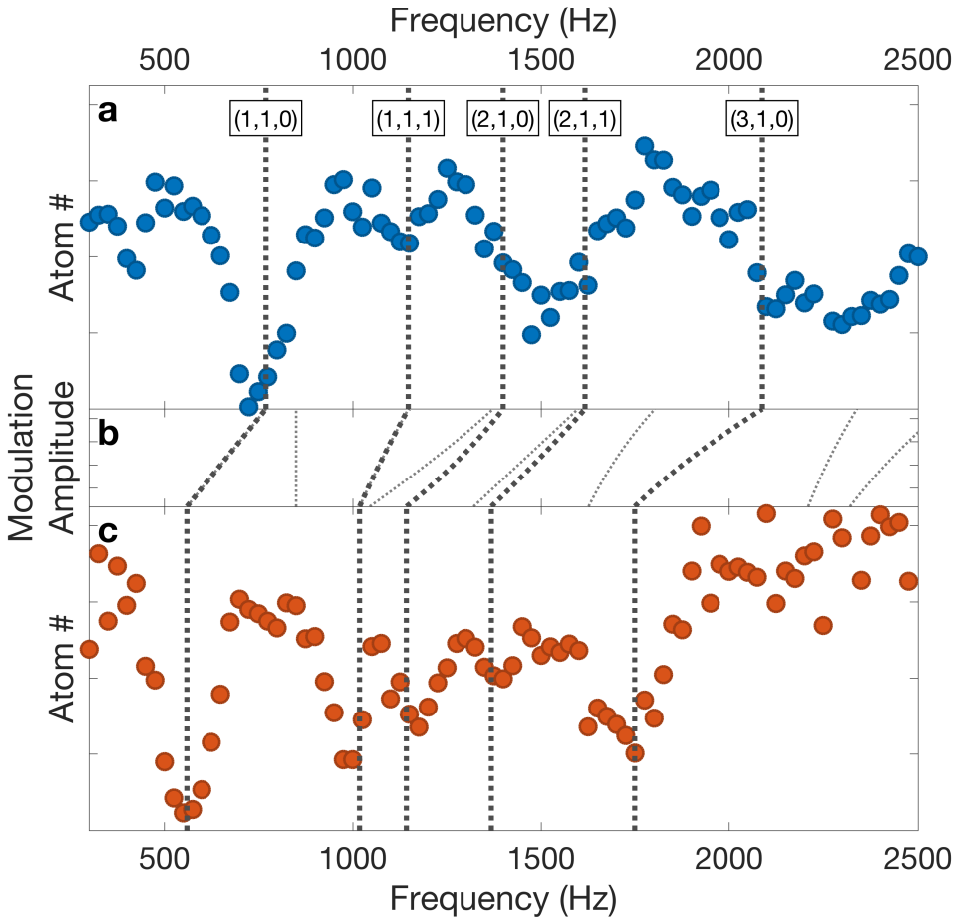

Figure 7.3: **Tunable excitation spectra via trap shaping. a:** Bound fraction after a 1-second pulse as a function of excitation frequency for an unmodified trap. Bold dotted lines are theoretically predicted frequencies of collective resonances expected to couple to our drive. Labels on theory lines indicate the quantum numbers (k, β, γ), using the notation of [131]. β and γ are parity quantum numbers, and k indicates the form of the nodal surface for the excitation. The quantum number m is 1 for all resonances plotted. The only inputs to this theory are the three trap frequencies. The resonance at half the fundamental frequency is believed to be due to parametric excitation of a dipole oscillation in the direction of gravity. Pulse amplitudes were increased from 0.6 μm at low frequency to 3 μm at the highest frequency to maximize peak visibility. **b:** Evolution of predicted resonances under continuously increasing trap broadening. Thinner dotted lines represent resonances which are not dipole-allowed for this drive polarization. **c:** Bound fraction after a 1-second pulse as a function of excitation frequency for a trap broadened in one direction as described in the methods section.

few-cycle femtosecond pulse deflects photoelectrons produced by an attosecond extreme ultraviolet pulse striking an atom, allowing characterization of both the pulses and the atom [137, 138, 139]. In the quantum simulator, qualitatively similar techniques allow high-resolution measurement of sub-cycle quantum dynamics. Here, instead of using photoionization to terminate the dynamics, the experimenter can simply instantaneously turn off the trapping potential at any point before, during or after the pulse. The atoms then propagate freely in space, and their instantaneous momenta at the time of trap removal are mapped onto their positions after some time of flight. Varying the time at which the trap is removed enables measurement of the time evolution of the bound quantum system with time resolution far below a drive period. This experimental technique, while commonplace in ultracold atomic physics, represents a powerful and general tool for the study of ultrafast-equivalent dynamics in our quantum simulator.

Fig. 7.4 presents the results of such measurements for both off-resonant and near-resonant pulses. The Bose-condensed atoms initially occupy mainly a single eigenstate of the transverse trapping potential. Quantum dynamics during and after the pulse can be tracked by direct momentum-space imaging of the atoms. Panels **b** and **d** of Fig. 7.4 show the density distribution after time-of-flight, integrated over the directions transverse to the excitation, as a function of time. For a pulse carrier frequency significantly below the dipole oscillation frequency ν_x in the dimension of driving, the momentum of the BEC evolves coherently during and after the pulse, as shown in Fig. 7.4b. Incoherent heating due to the pulse is observed to be minimal on the few-cycle time scales we probe. The atoms respond to the pulse at ν_x — a higher frequency than the carrier — but remain bound. During a pulse with carrier frequency near ν_x, however, qualitatively different is observed. Fig. 7.4d shows momentum evolution during a near-resonant pulse for an amplitude near the unbinding threshold. In this parameter regime, atoms do not leave the trap all at once, but do not incoherently heat either; instead, ejection starts at the time of the pulse peak, with additional bursts of atoms emitted during each subsequent

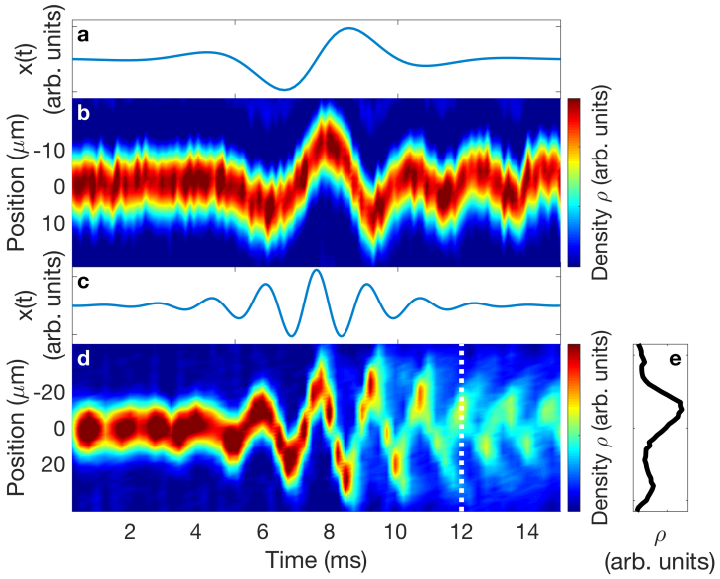

Figure 7.4: **Sub-cycle dynamics during off-resonant and near-resonant pulses.** **a:** Trap minimum position as a function of time for a pulse with $\tau = 3.76$ ms, $f = 200$ Hz, $A = 3$ μm and $\phi = \pi$. **b:** Post-time-of-flight integrated spatial density distribution versus trap turn-off time during the off-resonant pulse depicted in panel **a**. Here $\nu_x = 450$ Hz. **c:** Trap minimum position as a function of time for a pulse with $\tau = 3.76$ ms, $f = 550$ Hz, $A = 1.5$ μm and $\phi = \frac{3\pi}{2}$. **d:** Post-time-of-flight integrated spatial density distribution versus trap turn-off time during the near-resonant pulse depicted in panel **c**. Here $\nu_x = 600$ Hz. **e:** Density distribution at the time indicated by the dashed line in panel **d**. Peaks from bound and ejected atoms are visible.

half-cycle of the pulse. Fig 7.4e shows one such burst. This unbinding process models ionization or molecular disintegration during an ultrafast laser pulse.

7.2.4 Dependence of unbinding dynamics on pulse amplitude and carrier-envelope phase

The ability to precisely measure the population and momenta of unbound states as a function of pulse parameters and time opens up the possibility of flexible quantum simulation of ultrafast unbinding dynamics. As an initial application of the quantum simulator presented herein we have measured the dependence of simulated ionization yield or photodissociation on both pulse amplitude and carrier-envelope phase. This

represents a complementary method of testing the effects of two parameters central to numerous experimental and theoretical studies of ultrafast multiphoton ionization and bond-breaking processes [122, 123, 124, 140, 141, 142].

Both the precise unbinding time during an applied force pulse and the final unbound momentum depend sensitively and non-monotonically on pulse amplitude. In the quantum simulator, the amplitude of the pulse can be straightforwardly varied over a wide range, keeping the carrier-envelope phase, carrier frequency, and total pulse time constant. As the amplitude is increased from that used in Fig. 7.4d, the unbinding dynamics change drastically. Fig. 7.5a shows the momentum distribution of the atoms (measured by detecting the position distribution after 2 ms time of flight) after few-cycle pulses with amplitudes from 0 up to 6 μm. The bottom panels show the full time evolution of the momentum distribution during few-cycle pulses of selected amplitudes. Below a critical amplitude, no atoms are ejected from the trap. For some intermediate amplitudes, the behaviour mirrors that shown in Fig. 7.4d, with bursts of atoms unbinding at different points during the pulse. Above that intermediate regime, all of the atoms unbind at one well-defined time and continue to move with constant momentum after unbinding. Strikingly, as the amplitude is increased further, the momentum of the unbound atoms reverses sign, as they unbind half a drive cycle earlier, in an oppositely-directed simulated electric field.

Even for fixed pulse amplitude, the final state of the initially bound system after the force pulse depends sensitively and non-trivially on the carrier-envelope phase ϕ (CEP). In the pulsed-laser experimental context, the advent of few-cycle pulses with adjustable, stabilized CEP [143] has enabled advances such as probes of the effects of CEP on ultrafast dynamics [144, 145], study of interference patterns in multiparticle ionization signals [146], and control of recollision processes in molecular ions [147, 148]. The nearly arbitrary pulse-shape control available in the cold-atom quantum simulator makes it a flexible tool for probing the dependence of ultrafast-equivalent dynamics on

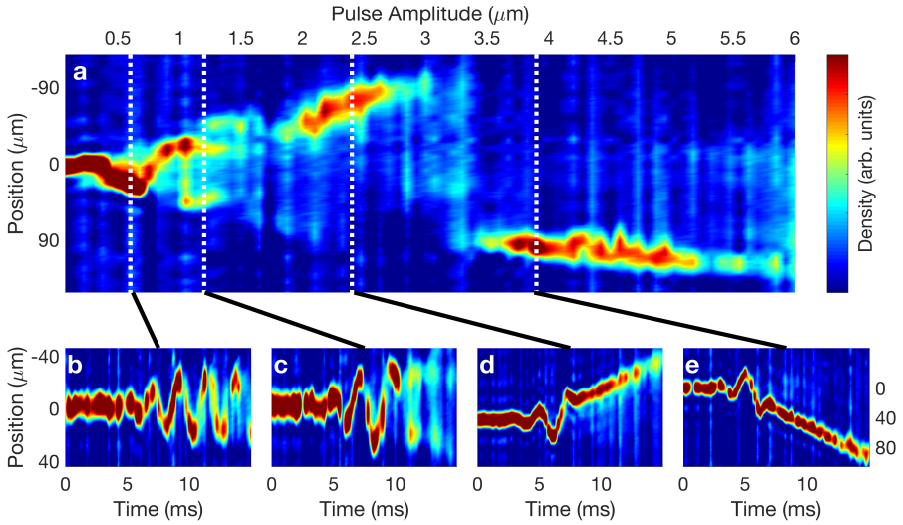

Figure 7.5: **Dependence of unbinding dynamics on pulse amplitude. a:** Integrated spatial density distribution after application of a near-resonant 480 Hz pulse with $\tau = 3.76$ ms and $\phi = 0$ followed by 2 ms time-of-flight, versus pulse amplitude A. **b-e:** Integrated spatial density distribution versus time during pulses with the indicated amplitude. Panels **d** and **e** have an expanded y-axis (indicated at right) to track the unbound atoms. Note the momentum of the unbound atoms changing sign as the pulse amplitude increases.

CEP. Fig. 7.6 shows a measurement of post-pulse momentum distribution (again detected via time of flight) as a function of the carrier-envelope phase of a near-resonant applied pulse. Changing the CEP from 0 to π flips the sign of all forces during the pulse, and results in inversion of the momentum of the unbound atoms. As shown in the bottom panel of Fig. 7.6, the pulses at integer values of ϕ/π have sine-like character, possessing odd symmetry under reflection in time around the pulse centre. Pulses with a CEP of $3\pi/2$ have cosine-like character and give rise to very different unbinding dynamics at this pulse amplitude, populating more than one momentum class of unbound atoms. More complex dynamical phenomena are also visible in Fig. 7.6: the inward slope of the unbound momentum as CEP increases in the neighborhood of $\phi = \pi$ can be understood as the consequence of the force at the first unbinding peak sliding down the pulse envelope, and the observed asymmetry between $\phi = \pi/2$ and $\phi = 3\pi/2$ indicates a violation of inversion symmetry in the potential. The most likely cause of this symmetry-breaking is slight trap aberration; this points the way to future work elucidating the effects of potential shape on unbinding dynamics.

7.3 Discussion

The results presented here open the door to a broad class of quantum simulation experiments investigating ultrafast nonequilibrium phenomena, with numerous possible scientific targets. Emulation of pump-probe experiments, multichromatic light fields, and non-physical (for example, half-cycle) pulse shapes impossible to create with lasers would require no techniques beyond those demonstrated here apart from changing the form of $\alpha(t)$.

Additional possibilities require only modest extensions of the experimental approach reported here. The simplest such extension would be to replace the inertial forces used to emulate electric fields with time-varying Zeeman or Stark potential gradient;e are cur-

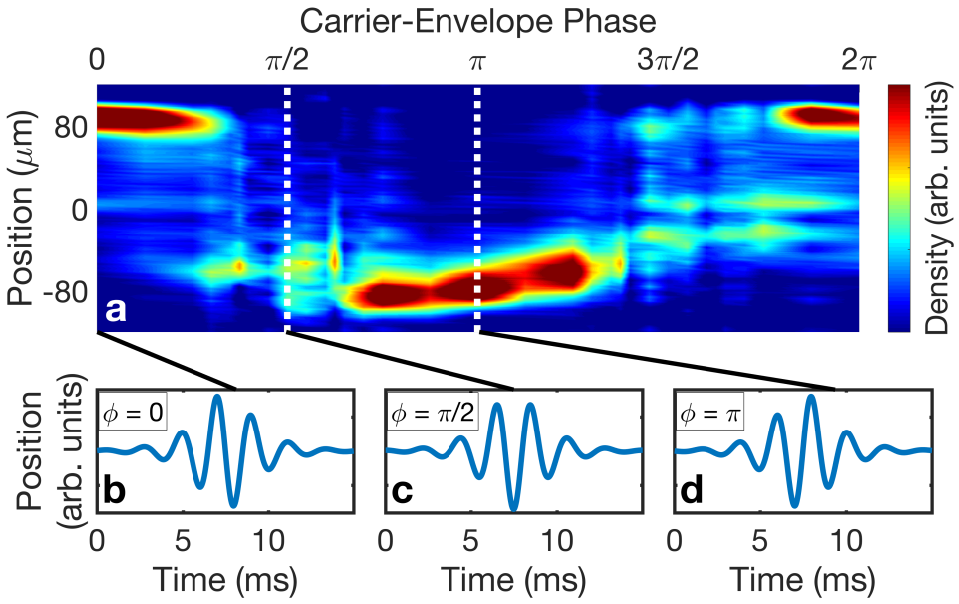

Figure 7.6: **Carrier-envelope phase dependence of final momentum. a:** Integrated spatial density distribution after application of a near-resonant 450 Hz pulse with $\tau = 3.76$ ms and $A = 2.4$ μm followed by 3 ms of time-of-flight, versus CEP. **b-d:** Pulse waveforms (force versus time) for CEP values indicated in the inset.

rently actively pursuing this direction by developing a DMD architecture for use with a 450 nm beam. This would allow ultrafast quantum simulation in the regime of Keldysh parameter γ_K less than one, and enable the direct experimental investigation of open questions of current interest in ultrafast science. Potential scientific targets include the creation of photoelectron vortices with circularly-polarized pulses [149], the demonstration and study of strong-field stabilization, wherein the ionization probability becomes a decreasing function of pulse amplitude [88], and detailed quantitative measurement of sub-cycle tunnel ionization timing effects [85, 86, 87, 150].

Other extensions to the basic technique are also possible. The use of traps with multiple minima could enable modelling of more complex molecular configurations [116]. Ultrafast quantum simulation could also be pursued with small numbers of trapped fermions [151], making a more direct analogue of atomic electrons. However, the use of Bose condensates and the analogy of Eq. 7.1 does greatly magnify the signal, making

experiments feasible with bosons that would be very challenging with fermions. Finally, an expansion of the analogy underlying these quantum simulation experiments beyond atoms and molecules could enable the study of ultrafast-equivalent dynamical phenomena relevant to nuclear excitations [152] and strong-field dynamics in solids [69].

In summary, we present experimental results from a cold-atom quantum simulator of ultrafast phenomena, including nonlinear spectroscopy of collective excitations, control of the energy spectra of the bound states of the simulator, imaging of sub-cycle dynamics during an unbinding process similar to ultrafast ionization, and measurement of the effects on unbinding dynamics of pulse amplitude and carrier-envelope phase. Such cold atom quantum simulation of ultrafast dynamical phenomena has the potential to enable benchmarking of relevant theories and explorations of experimentally challenging regimes, in an approach complementary to both ultrafast theory and pulsed-laser experiments.

7.4 Methods

Preparation of a Bose-Einstein condensate in an optical trap. During the computer-controlled experimental sequence [153], atoms from an effusive source are collimated by a nozzle [49], Zeeman-slowed, trapped and pre-cooled by sequential magneto-optical traps using the 461 nm and 689 nm ground-state transitions, and evaporatively cooled to degeneracy in a crossed-beam 1064 nm optical dipole trap (ODT) [135]. In the emulation stage of the experiment, the resulting condensate of 2×10^4 ^{84}Sr atoms is adiabatically loaded into a single-beam ODT with a waist of 15 μm. The trap depth can be varied across a wide range; a typical value used in the work presented here is 10 μK. The s-wave scattering length of ^{84}Sr is 6.5 nm.

Temporal magnification of the quantum simulator. Varying the power and shape of the trap beam yields transverse trap frequencies ν_x and ν_z between 300 and 1000 Hz, and an axial trap frequency ν_y between 5 and 15 Hz. Drawing the analogy

between the optical trap and a single hydrogen atom, the energy difference $h\nu_x$ between the ground and first relevant excited states (typically $\simeq$500 Hz) is analogous to the 2.47 PHz Ly-α line. Although the detailed energy spectrum of the ODT differs from that of hydrogen due to the different potential shapes, comparison of these two frequency scales indicates an approximate temporal magnification factor of 5×10^{12}. Emulation of molecular vibrational excitations or cluster dynamics leads to a ratio of up to 10^{11} between characteristic timescales of the emulator and emulated system.

Application of time-varying inertial forces. An acousto-optic modulator (AOM) can translate the trap centre in the x-direction (see Fig. 7.1c for axis definitions) at amplitudes up to 6 μm and frequencies from DC up to hundreds of kHz. Because of the direction of translation and the wide separation between transverse and axial frequency scales, the axial degree of freedom is irrelevant to the results we present. Under the assumption that the atoms remain near the centre of the trap during the pulse, which we observe to be true until unbinding, the effective applied force is $m\ddot{x} = F(t) = -dV(x,t)/dx|_{x=0}$. $\ddot{x}$ can be specified as desired; for the particular functional form chosen, $\ddot{x}(t)$ has a similar enveloped-pulse shape to $x(t)$.

Tuning the trap geometry. Shaping of the trap is achieved most simply by periodic translation on much faster time scales than the dynamics of the BEC, so that the atoms experience a time-averaged potential. For this purpose, the trap AOM's RF drive frequency was sinusoidally modulated at 500 kHz, giving rise to a maximum trap translation amplitude of 4.2±0.3 μm.

Chapter 8

Phasonic Spectroscopy of a Tunable Quantum Quasicrystal

In Chapter 6, I introduced ideas regarding quantum simulation of quasicrystals. In this chapter, I present results of experiments along these lines. The contents of this chapter constitute a draft of a paper which is currently in preparation, in collaboration with Mantas Račiūnas and André Eckardt at MPIPKS [154].

Phasonic degrees of freedom are unique to quasiperiodic structures, and play a central role in poorly-understood properties of quasicrystals from excitation spectra to wavefunction statistics to electronic transport. However, phasons are difficult to access dynamically in the solid state due to their complex long-range character and the effects of disorder and strain. In this chapter I discuss phasonic spectroscopy of a tunable quasicrystal, achieved by directly measuring the frequency-dependent response to phasonic driving of a quantum gas in a quasiperiodic optical lattice. Using this technique, we observe that strong phasonic driving excites high-order multiphoton modes more efficiently than standard dipolar driving, that the critical driving amplitude for phasonic multiphoton transitions depends only weakly on transition order, and that sufficiently

strong phasonic driving gives rise to a broad infrared absorption feature in the quasicrystal. Phase modulation enables direct mapping of the quasicrystal's energy spectrum, allowing direct imaging of slices of the Hofstadter butterfly at varying disorder strength.

8.1 Background

Phasons are degrees of freedom unique to quasicrystals which arise from broken translation symmetry in the higher-dimensional space from which the quasiperiodic lattice is projected [104, 105, 106, 155]. The role of phasons in determining quasicrystal properties remains incompletely understood: open questions include the effects of electron-phason coupling, the nature of electronic transport, spectral statistics, topological properties, and even the shape of the electronic wavefunctions [95, 96, 97, 156, 99, 100, 157, 101, 102, 103]. These lacunae are in part due to the theoretical intractability of quasiperiodic condensed matter, and in part due to the experimental difficulty of disentangling the effects of domain walls, crystalline impurities, and disorder from those due to phason modes. Beyond the fundamental interest of such questions, they may point the way to potential technological applications of quasicrystals' anomalous electrical and thermal transport characteristics.

The exquisite controllability of ultracold atoms makes them well-suited to the study of quasicrystal physics: bichromatic lattices have been used to probe quasidisorder-induced localization [158, 109, 159], atomic temperature, density, and diffusion have been studied in fivefold-symmetric quasiperiodic potentials [160, 161], and generalized Fibonacci optical lattices have been proposed [108]. Time evolution of the momentum of a BEC has also been probed using matter-wave diffraction in both 1D and 2D quasicrystals, with the latter demonstrating self-similarity of the momentum structure [162, 163].

Here we report the first realization of phasonic spectroscopy on a quasicrystal, using quantum degenerate ^{84}Sr atoms in a dynamically-tunable bichromatic optical lattice. We

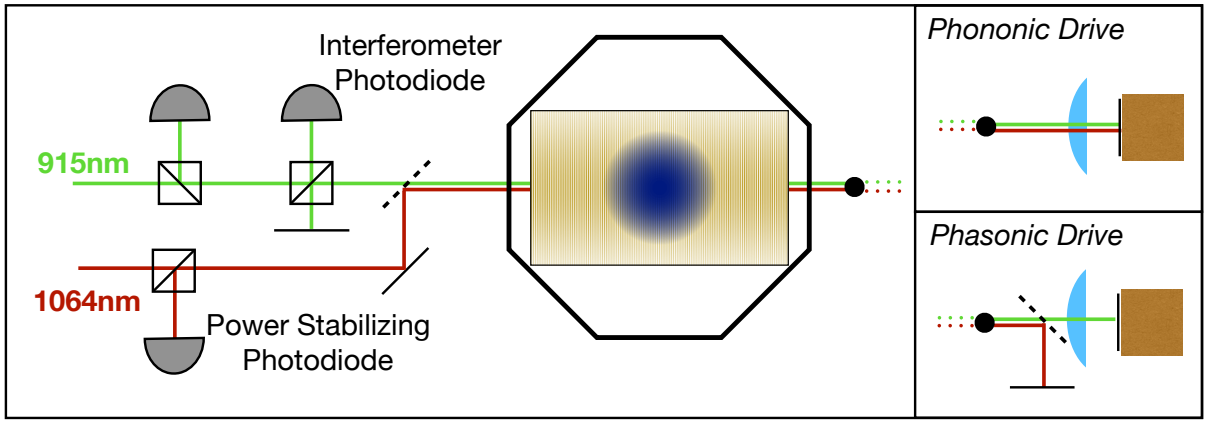

Figure 8.1: Schematic of experimental setup. Chamber inset shows BEC (blue) in a 1D bichromatic lattice potential. Setups for lattice retroreflection are shown on the right; the PZT is shown mounted on a copper block.

drive a long-range phasonic mode via phase modulation; there are expected links between the macroscopic picture of driving this mode and the microscopic picture of phasonic flips in the lattice which are correlated across a macroscopic number of lattice sites [164, 165]. We compare the results of phasonic and standard dipolar driving at a range of frequencies and amplitudes, observing a significant enhancement of multiphoton transition strengths for phasonic drives, and measure the effect on the energy spectrum of of varying the strength of the quasiperiodic component of the potential.

8.2 Experiment

The 1D bichromatic potential we use is a superposition of a primary lattice and secondary lattice formed by standing waves of laser light with wavelengths λ_P =1064 nm and λ_S =915 nm, respectively. Ignoring contact interactions, the Hamiltonian of atoms trapped in this potential is

$$\hat{H} = -\frac{\hbar^2}{2m}\frac{d^2}{dx^2} + V_P \cos(2k_P(x-\delta_P)) + V_S \cos(2k_S(x-\delta_S)) \tag{8.1}$$

where $k_i = 2\pi/\lambda_i$ and V_P and δ_P (V_S and δ_S) are the depth and translation of the primary (secondary) lattice. In the nearest-neighbor tight-binding limit for $V_P \gg V_S$, this Hamiltonian becomes equivalent to the Aubry-André model, which is closely related to the Harper model which famously describes the multifractal energy spectrum of integer quantum Hall systems. Dipolar excitation of this lattice, related to the lowest-energy phononic mode of the system, may be achieved by equal translation of both lattices:

$$\delta_S(t) = \delta_P(t) = A_{\text{dip}} \sin(2\pi f_{\text{dip}} t) \tag{8.2}$$

A_{dip} and f_{dip} are the driving amplitude and frequency of the dipolar drive. Moving into the lattice reference frame, we can write the force applied to the atoms as $F(t) = F_0 \sin(2\pi f_{\text{dip}} t)$ for $F_0 = m(2\pi f_{\text{dip}})^2 A_{\text{dip}}$. We may further define a dimensionless driving parameter

$$K = aF_0/\hbar\omega_{\text{dip}} = am\omega_{\text{dip}} A_{\text{dip}}/\hbar \tag{8.3}$$

where $\omega_{\text{dip}} = 2\pi f_{\text{dip}}$. To keep a fixed K, we must take $A_{\text{dip}} \propto 1/f_{\text{dip}}$. This manner of phase modulation has been used previously to study multiphoton excitations in a single-color lattice [166].

Phasonic modulation may be achieved by translating only the secondary lattice:

$$\begin{aligned} &\delta_S(t) = A_{\text{phason}} \sin(2\pi f_{\text{phason}} t), \\ &\delta_P(t) = 0. \end{aligned} \tag{8.4}$$

where A_{phason} and f_{phason} are the driving amplitude and frequency of the phasonic drive. We similarly inversely scale A_{phason} and f_{phason} to enable a direct comparison to the dipolar drive.

Our spectroscopic protocol is as follows. We adiabatically load a BEC of ^{84}Sr into the ground band of the bichromatic lattice. A schematic of the experimental setup may

be found in Fig. 8.1. We then linearly ramp up the amplitude of the dipolar or phasonic modulation for 4 ms, and continue to modulate for 16 ms at constant amplitude. We then stop modulating and ramp down both lattices simultaneously at a rate which is adiabatic with respect to the energy gaps of the primary lattice to achieve band mapping onto free space momentum states [28]. This enables measurement of the fractional population of atoms no longer in the ground band of the primary lattice after modulation. We have performed such spectroscopy varying the drive amplitude, drive frequency, primary and secondary lattice depths, and modulation type (dipolar or phasonic).

8.3 Results

8.3.1 Phasonic spectroscopy

We first contrast dipolar driving to phasonic driving. We drive at comparable fixed dimensionless driving amplitudes, which are scaled by the depths of the lattices such that the ground band depletion fraction of the fundamental ground→2nd band resonance is the same for both drives. We carry out the experiment at variable primary lattice depth and modulation frequency, while holding the secondary lattice depth fixed at 1 $E_{R,S}$. Figure 8.2 shows this comparison, plotted in terms of f on the x-axis and primary lattice depth on the y-axis. In the dipolar case, we see excitations to higher bands which are consistent with the primary lattice band structure. Excitations to the 3rd band are visible but highly suppressed compared to the 2nd band resonance; we can explain this as being due to a selection rule based on the odd parity of the phase modulation.

In the phasonic case, we see numerous multiphoton transitions, in contrast to the phononic case. We can still see excitations of the fundamental resonances to the 2nd and 3rd bands with roughly equal strength. However, in addition to these 1st-order processes, we see higher-order processes driven much more efficiently. Fig. 8.2c shows the phasonic

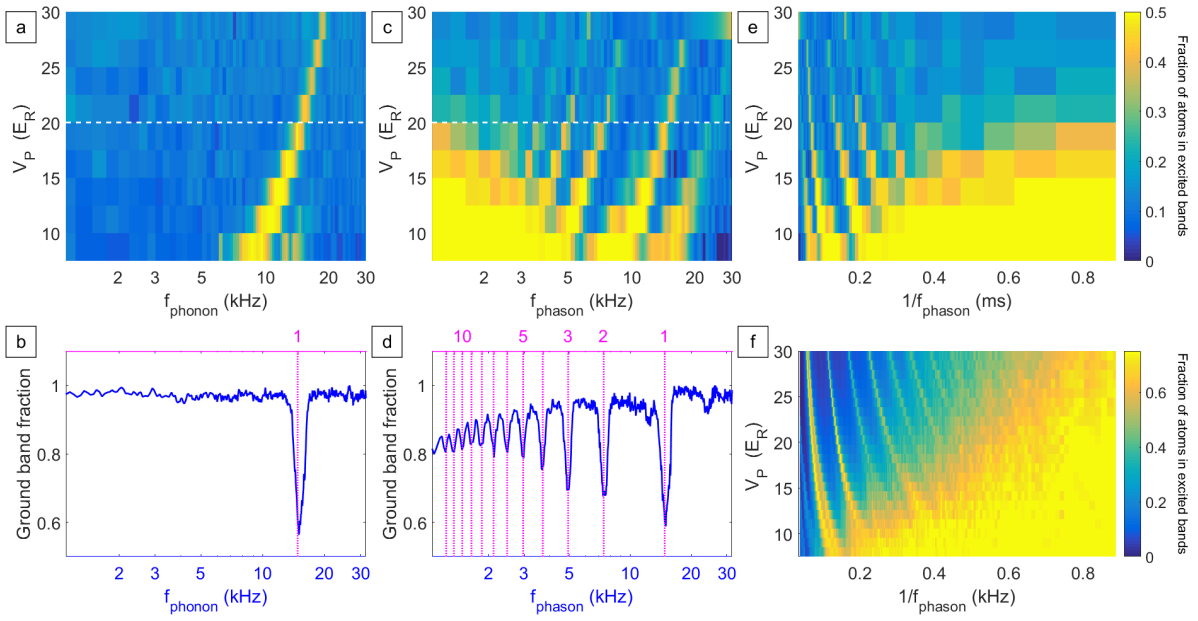

Figure 8.2: **a:** The fraction of atoms excited above the ground band by dipolar driving is plotted for various frequencies and primary lattice depths. **b:** High-resolution scan of **a** at 20 $E_{R,P}$ is taken to confirm that any higher-order excitations are negligible. The blue line shows data averaged over three repeats at each frequency. The magenta line is a guide to the eye showing the theoretical expected location of the fundamental ground-2nd band transition. **c:** The fraction of atoms excited above the ground band by phasonic driving is plotted for various frequencies and primary lattice depths. **d:** High-resolution scan of **c** at 20 $E_{R,P}$ is taken to confirm that any higher-order excitations are negligible. The blue line shows data averaged over three repeats at each frequency. The magenta line is a guide to the eye showing the theoretical expected location of the fundamental ground-2nd band transition as well as higher harmonics. **e:** Data from **c** plotted versus $1/f$ shows a broad absorption feature at large tunneling amplitudes and low frequencies. **f:** Simulation of phasonic spectroscopy done in collaboration with MPIPKS.

excitation spectrum for a 20 $E_{R,P}$ primary lattice and a 1 $E_{R,S}$ secondary lattice, holding the dimensionless drive amplitude constant. With a fine frequency scan, up to 12th-order multiphoton excitation processes to the 2nd band may be resolved. There is a second anomalous feature in both of these figures: the background depletion at low frequencies in Fig. 8.2d is consistent with what looks like a broad continuum of excitations at large tunneling amplitudes and low frequencies in Fig. 8.2e; by varying the dimensionful drive amplitude A_{phason}, we find that this feature is due to numerous overlapping high-order

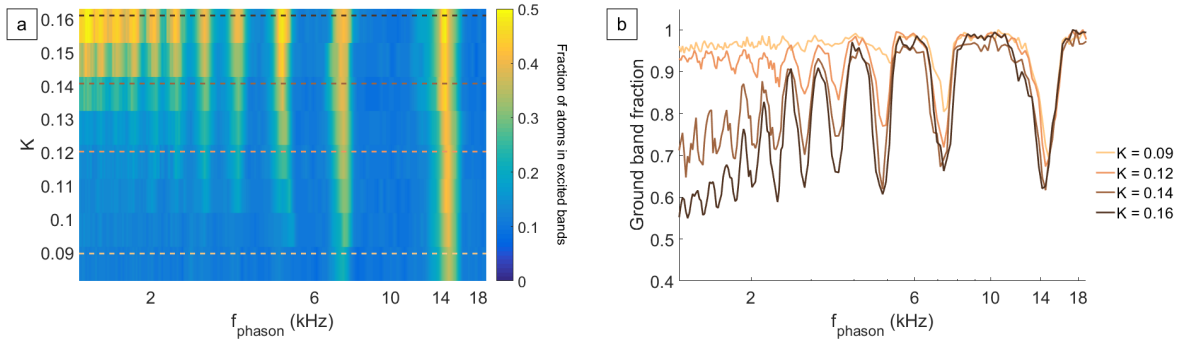

Figure 8.3: **a:** Higher harmonic amplitude dependence, showing onset of non-perturbative regime. Dotted lines indicate values of K for linecuts shown in **b**.

multiphoton transitions. In Fig. 8.2f, theoretical simulations based on time evolution of the Schrodinger equation show quantitative agreement with experimental results without adjustable parameters.

The increase in multiphoton resonance strength in the phasonic case is likely due to a combination of effects. At low frequencies, in order to keep the dimensionless driving amplitude constant, the real-space amplitude increases to around three lattice sites, which for a phasonic drive adds effective Fourier components. A second factor which is likely to influence higher-order processes is the extent to which band-coupling matrix elements are changed for phasonic driving compared to dipolar driving, since phase modulation of one lattice with respect to the other modifies the eigenenergies in the rest frame of the primary lattice in a way which does not conserve parity. It is possible that this drive does not obey any simple parity-based selection rules, allowing much higher-order excitation processes to occur.

We can probe further into the nature of these higher-order processes, as well as the low-frequency number depletion, by varying K. Fig. 8.3 shows the excitation spectrum for a 20 $E_{R,P}$ primary lattice and a 1 $E_{R,S}$ secondary lattice, varying the excitation frequency on the x-axis and K on the y-axis. We observe the appearance of many of the higher order resonances at some critical drive amplitude, which marks the onset of a

theoretically-predicted non-perturbative driving regime; the subharmonic strengths are suppressed as a function of K, but in a highly non-exponential way. We suspect that this non-perturbative driving onset is analogous to the appearance of the high harmonic generation plateau in ultrafast physics; we are currently working with theorists to figure out whether this is the case.

This is the first realization of phasonic spectroscopy in any context, and we observe new effects which are qualitatively different from the dipolar drive. This ability offers a new tool to study the electronic properties of quasicrystals.

8.3.2 Tuning quasiperiodicity

We can take full advantage of our ability to spectroscopically probe quasicrystals by changing the properties of the quasicrystal itself; the ability to start with an ordinary crystal and slowly turn on the secondary lattice offers a natural probe of the effects of quasiperiodicity. Tuning the period ratio and relative lattice depths, in conjunction with the ability to spectroscopically resolve small energy gaps, would enable a direct mapping of the multifractal Hofstadter butterfly spectrum. We can test the usefulness of lattice phase modulation techniques to directly measure the energy minigaps associated with the Hofstadter splitting. These minigaps are expected to support single-particle mobility edges (SPMEs), critical energies within bands below which states are extended and above which states are localized [29]. Experimental evidence has been found for SPMEs in a 1D quasiperiodic potential [30], though they have never been spectroscopically detected.

To probe the effect of emerging quasiperiodicity on an initially periodic structure, we perform dipolar modulation spectroscopy on a 10 $E_{R,P}$ primary lattice with fixed K, varying the depth of the secondary lattice. As shown in Fig. 8.4, we can clearly drive transitions between the ground and 2nd band, as well as some transitions between the ground and 3rd band. However, we also observe the emergence of minigaps which are

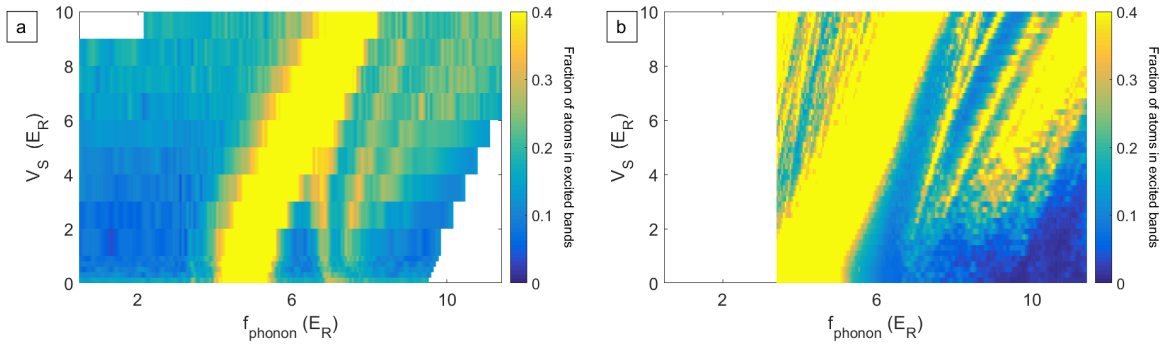

Figure 8.4: **a:** By starting with a pure 1064 nm lattice and increasing the depth of the 915 nm lattice, we directly observe the effects of bichromaticity on the energy spectrum, including minigaps which are hallmarks of constant-period-ratio slices through the Hofstadter spectrum. We see relatively good agreement with theoretical predictions based on time evolution of the Schrodinger equation (**b**), although there is one excitation we observe experimentally which is not reflected in the theory.

the spectral hallmark of quasiperiodicity.

An immediate future step would be tuning the period ratio of the bichromatic lattice from 915/1064 to something much more rational (798/1064, for example, which is expected to exhibit much larger gaps) and looking at the spectrum. In the future, we can consider tuning the wavelength ratio continuously to map out an experimentally-accessible slice of the Hofstadter spectrum.

8.4 Conclusion and outlook

The realization of phasonic spectroscopy in a tunable quantum quasicrystal opens several exciting directions for future work. Beyond tuning the period ratio to measure parts of the Hofstadter spectrum, it is possible to operate the bichromatic lattice in a regime in which certain bands are localized and others are delocalized [167]. This could allow us to study the effects of localization on heating processes, as well as excitations near the aforementioned SPMEs. It is also possible to expand this system to higher dimensions to study Anderson localization in many dimensions, as well as the fractional Mott insulator

at different fillings. Additionally, the 1D system presents various possibilities to study topological charge pumping. A recent proposal suggests Thouless pumping of bulk states possible using phasonic driving [113], and the Hofstadter spectrum supports edge states which may also be topologically pumped from one end of the system to the other.

We have realized a 1D quasiperiodic lattice and mapped its energy spectrum using the first demonstration of phasonic spectroscopy. We have showed that in contrast to dipolar driving, phasonic excitation can efficiently drive up to 12th-order multiphoton processes between bands. We have shown that in the low-frequency regime, these subharmonics become evident at a critical dimensionless drive amplitude, marking the onset of nonperturbative driving. We have used phase modulation to directly map the energy eigenstructure of a bichromatic lattice and resolved the emergence of minigaps as quasiperiodicity is gradually introduced, effectively mapping a slice of the Hofstadter butterfly spectrum and paving the way to extend that measurement to other period ratios.

Chapter 9

Future Work

In this chapter, I will briefly mention some groundwork we have laid in preparation for future experiments on the strontium machine. Future topics along the lines of strong-field quantum emulation or bichromatic lattice exploration can be found at the conclusions of Chapters 7 and 8, respectively.

9.1 Hunting for anyons: the Kitaev chain

One of the main directions we are planning to go in the next few years is hunting for experimental signatures of non-Abelian anyons. Anyons are a class of particle excitations which have different spin statistics than either fermions or bosons. They pick up a complex phase under particle exchange which could effectively give the particles a topologically-protected "memory" of how they have been exchanged with other particles; because of this, they are the building blocks for many proposed quantum computing architectures [168]. Despite many recent strides in our theoretical understanding of non-Abelian anyons, they have never been experimentally detected.

One possible way to observe them depends on experimental realization of the Kitaev chain [169]. The Hamiltonian for this model may be written in terms of fermionic creation

and annihilation operators:

$$H = \sum_{n=1}^{N} -t\Big(f_n^\dagger f_{n+1} + f_{n+1}^\dagger f_n\Big) + \Delta\Big(f_{n+1}^\dagger f_n^\dagger + f_n f_{n+1}\Big) - \mu_n\Big(f_n^\dagger f_n^\dagger - \frac{1}{2}\Big). \tag{9.1}$$

This Hamiltonian effectively describes a 1d tight-binding model of a p-wave superconductor. The edge states of this system are predicted to be Majorana zero-modes, a subclass of non-Abelian anyons.

The first Hamiltonian term includes hopping parameter t, and describes tunneling along the length of the chain. This is a property which is inherent to shallow optical lattices. The second term is a pairing term describing two-particle hopping either into or out of the chain, with associated energy Δ. The last term describes the chemical energy contribution to the energy.

Our proposed method of implementation involves a "duck lattice" realized by interfering 4 beams in 2 dimensions, each with a well-defined phase relative to the others. This geometry is shown in Fig. 9.1; the Kitaev chain is formed from the shallow potential sites, while a neighboring chain of deeper sites provides a "reservoir" of atoms. The phases of the beams need to be extremely well-controlled. We are currently using an extremely precise AOM drivers from Moglabs to achieve the necessary phase control, and are building various interferometer setups to test feedback. The chemical potential and hopping terms are easily realized in the Kitaev chains of this lattice. The pairing term translates to two atoms simultaneously hopping out of the Kitaev chain into the reservoir, or hopping into the Kitaev chain from the reservoir. This can be done dynamically via lattice modulation, or via an interaction blockade for bosons.

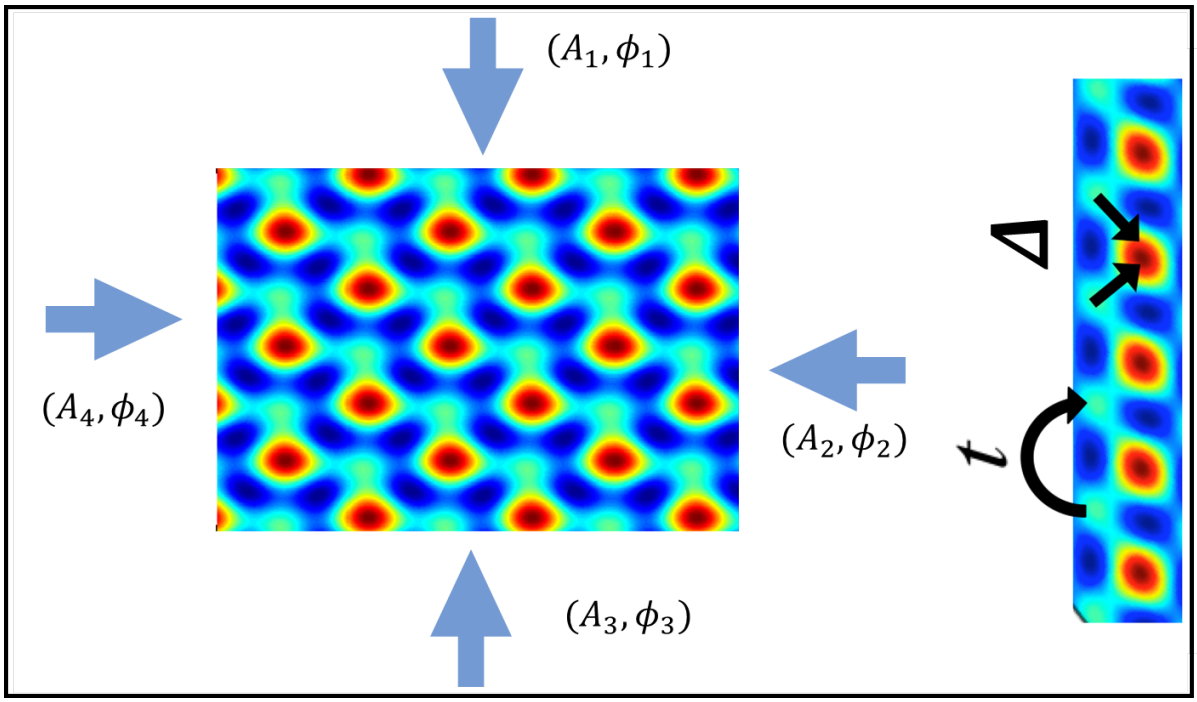

Figure 9.1: A 2d lattice potential consisting of zigzag chains is formed by interfering 4 beams with a well-defined phase relationship.

9.2 Quantum gas microscopy

Quantum gas microscopes have proven extremely valuable in the past decade. Since they allow probing atoms in lattices with single-site resolution, they have enabled the study of entanglement entropy and many-body localization [170, 171] and magnetic spin ordering [7, 8, 9] among many other interesting topics. We have designed a QGM for the strontium machine, are currently in the process of hydrogen-baking and constructing it. We are planning to transport the atoms from the main chamber to the science chamber using focus-tunable lenses from Optotune. We have already done a lot of calibration and testing for these lenses, and look forward to adding the science chamber onto the machine soon. The design and the objective lens are shown in Fig. 9.2.

A custom 0.8-NA objective lens was built by Special Optics to work at 461 nm and 689 nm at working distances of 1 mm air, 5 mm glass, and 4 mm vacuum. We plan to

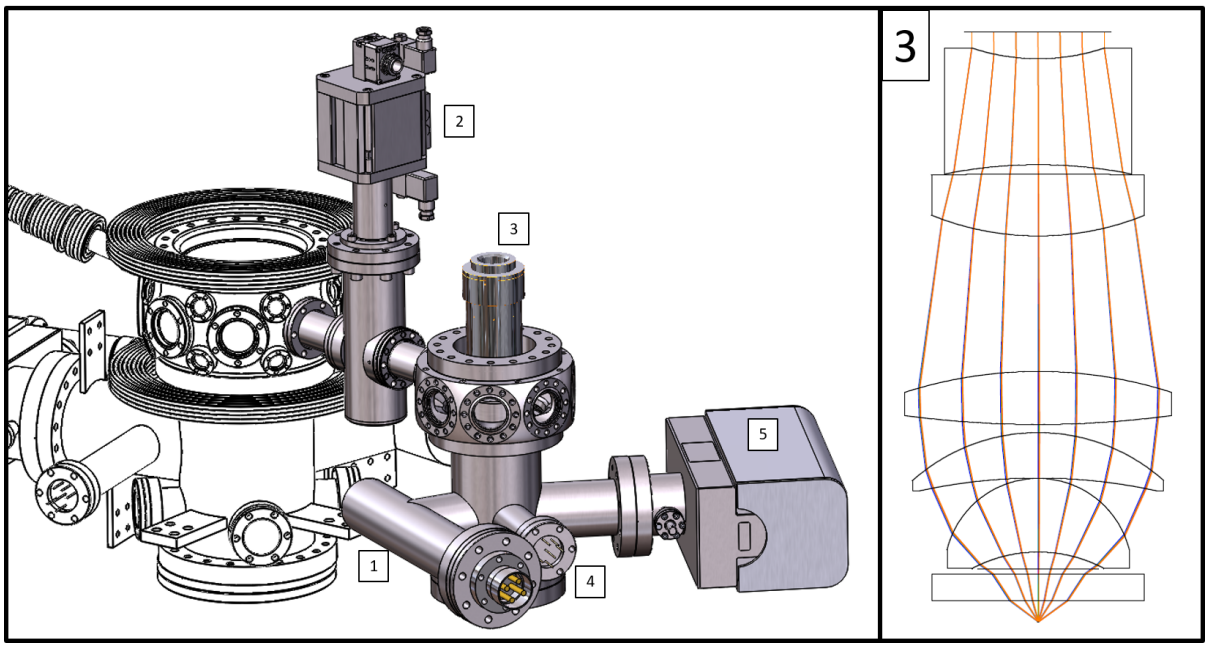

Figure 9.2: Solidworks mockup of a quantum gas microscope under construction for strontium. Figure shows (1) the titanium sublimation pump, (2) an all-metal gate valve which allows us to bake the science chamber separately from the main chamber, (3) the objective lens, (4) ion gauge, and (5) ion pump. The design for the 5-lens objective is shown to the right.

sideband-cool using the 689 nm transition, and preliminary calculations show that we should be able to scatter tens of photons per atom given reasonable background pressures. However, there is a chance these calculations are wrong. We would also like to try an imaging technique based on a bio-imaging process called STORM [172], in which only a few atoms are stochastically repumped from a dark state and then imaged at a time, such that their point-spread functions are much easier to fit. This process is repeated many times. If the atoms were trapped in the $^3P_2$ reservoir[1], one could imagine simply repumping with 403 nm light and imaging with 461 nm light. We have designed all of the science chamber viewports to have some wavelength flexibility in case one or more of these imaging options does not work.

[1] at low filling; at large filling, inelastic collisions in this state could be harmful

9.2.1 Novel cooling schemes: nuclear demagnetization

As discussed in Section 3.3.4, strontium could allow us to study the ground state of a system with SU(N) symmetry, but there are major hurdles to accomplishing this. If such a ground state could be realized, it still needs to be measured. The intercombination line provides a very nice tool to probe energies, but this may not be enough to clearly resolve any spin correlations we might hope to measure. It would be extremely nice to have single-site resolution as an additional measurement aid. The other big hurdle is how to achieve the temperatures necessary to see spin correlations; the Neel-order temperature is typically in the pK regime. To this end, we have a novel idea that we are hoping to test, which involves a combination of ^{87}Sr's large nuclear spin and adiabatic demagnetization refrigeration cooling (ADR), which has been demonstrated for electronic spins [173].

The basic idea of this scheme is to make use of the interplay between entropy in kinetic and spin degrees of freedom. A relatively cold spin-mixture can be placed in a gradient which separates the spins spatially. Once separated, the spins are cooled further (typically evaporatively), reducing their kinetic energy. The spins are then allowed to recombine: kinetic entropy will be converted into spin entropy, resulting in overall cooling.

The task of separating nuclear spins is not easy, but it has already been shown for ^{87}Sr at Innsbruck [21] using an optical Stern-Gerlach method: a red-detuned σ^- beam and a blue-detuned σ^+ beam near the 689 nm resonance are offset from the cloud and from each other in the z-direction, and a weak magnetic field is applied along the direction of beam propagation. In Fig. 9.3, we show the resulting potential and acceleration for each hyperfine state at a 16 G field; parameters can be found in the caption. For a demagnetization experiment, we would want to attempt some optical evaporation while maintaining the spin separation, so we also calculate the scattering rates for each spin.

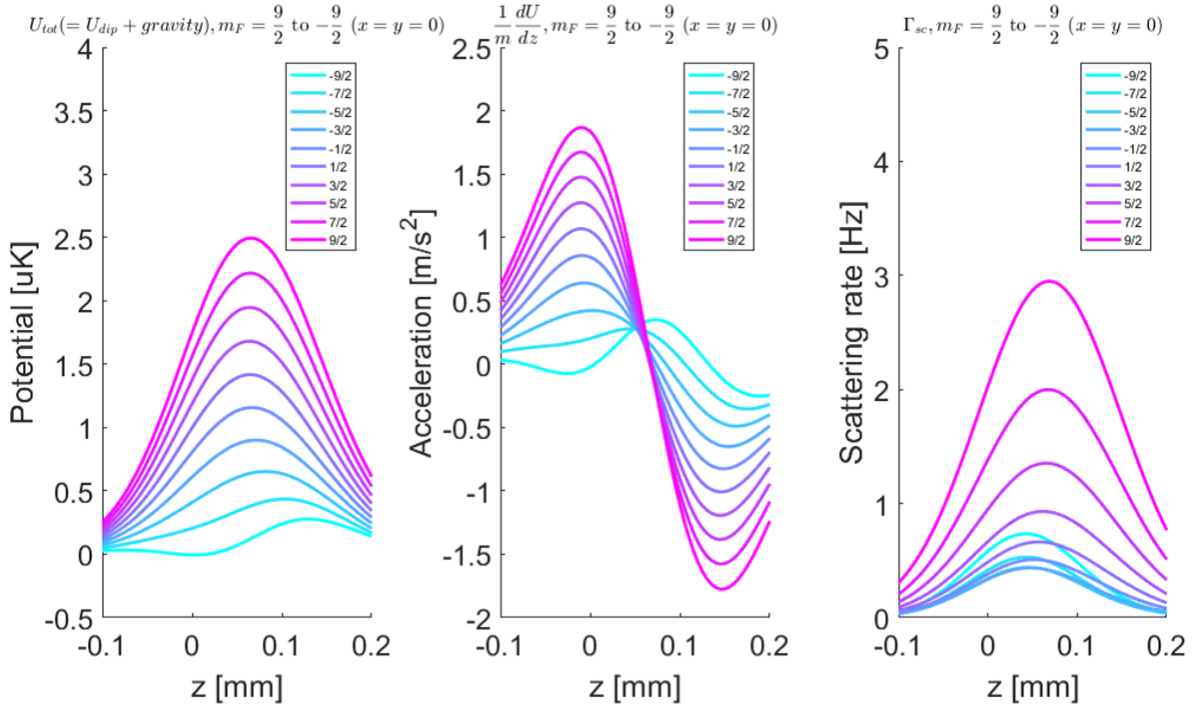

Figure 9.3: Potential, acceleration, and scattering rate for each hyperfine spin state from OSG beams (atoms are assumed to be at $z = 0$. Beams and 16 G B-field are pointed along the z-direction. OSG beam parameters for the red- and blue-detuned beams are $P_r = 0.5$ mW, $\omega_{0r} = 120$ μm, $Z_{0r} = 40$ μm, δ_r=-800 MHz, $P_b = 4$ mW, $\omega_{0b} = 160$ μm, $Z_{0b} = 70$ μm, and δ_b=+800 MHz

9.3 Additional thoughts and ideas

If the future directions of ultrafast physics and bichromatic lattices are trees and the ideas above are saplings, here are some twigs of other topics we have briefly discussed:

- Searching for the $\approx$ 515 nm magic wavelength in strontium using the tunable Ti:Sapph.
- Studies of the fractional Mott insulator once the Ti:Sapph tunable bichromatic lattice is set up.
- Creation of artificial gauge fields with fermions in "strained" (distorted/misaligned) optical lattices.

- Various ideas involving running lattices.
- Implementation of a Fibonacci lattice using two Ti:Sapph beams interfered at the appropriate angle.

I'm sure I'm missing many things; there's a vast unexplored world of really exciting physics here. I don't know- strontium's pretty cool.

> The Road goes ever on and on
> Out from the door where it began.
> Now far ahead the Road has gone,
> Let others follow it who can!

Appendix A

Notes on UHV Cleanliness and CF Assembly

Here is some (probably unsolicited) advice on UHV CF assembly. Everything usually goes fine, as long as you start from the assumption that vacuum cleanliness at UHV scales is voodoo magic and you should just take every precaution you can because otherwise troubleshooting will be difficult.

A.1 Cleaning

To keep your parts UHV-compatible, you will probably want to clean them thoroughly. We sonicated every part we possibly could (read: the smaller parts) according to the following procedure:

1. Figure out how to suspend your part in various solutions in the sonicator, making sure that the knife edges cannot accidentally come into contact with (thus be harmed by) the walls of the beaker of solution. If the parts are extremely small (like screws or microcapillaries), they may be placed in a plastic cup and then suspended in the solution.

2. Sonicate in a solution of 10 g Alconox detergent and 1 L of deionized water for 10 minutes.

3. Rinse in deionized water for 10 minutes.

4. Sonicate in standard lab-grade acetone (nothing fancy) for 10 minutes.

5. Sonicate in standard lab-grade isopropyl alcohol (IPA) for 10 minutes.

6. Carefully remove item from sonicator while wearing gloves. Place into aluminum foil and wrap until ready to assemble.

If you are using any kind of ceramic or other porous material, make sure that you bake the material properly after the sonication process. We use a little Black and Decker toaster oven in our lab for such cleaning purposes. If you are able to bake them under vacuum, that will certainly result in a better bake, but we have not found it necessary.

If you design any part which needs to exist in the vacuum, make sure that there are no places where pockets of air can get trapped. Such places can result in "virtual leaks" after the machine is baked, whereby tiny pockets of trapped gas at higher pressure can outgas over time.

A.2 CF Assembly

Here are some general precautions we took during all CF assembly:

- Nobody who recently had a haircut or shaved is allowed to come near assembly for at least a day/two showers.

- The space in which we are CF-assembling is usually enclosed by shower curtains (bought at a local hardware store) to protect against dust.

- We always wore gloves and hairnets. Occasionally, we would wear long catering-type plastic sleeves over our forearms. Those who grew facial hair often wore beard nets. We were liberal with glove changes.
- Any tool we brought into the enclosed space was typically wiped down with IPA and Kimwipes.
- If we saw a speck of dust on or near a knife edge, we typically tried to gently remove it with compressed air. If this did not work, we used the corner of an optics-grade cloth to gently brush at the speck to see if it could be removed. If it could not, we made a note of it for future leak-checking and moved on with some consternation.
- We try not to breathe into the chamber. We never spit into the chamber.

General assembly proceeds by placing a copper gasket between two knife edges, taking care not to scratch the edges. The copper can be quite forgiving, although after any amount of tightening of flanges over copper gaskets (even finger-tightening bolts), that gasket should not be reused. We always order from Duniway (due to good pricing, fast lead times, and easy-to-remember part numbers), and always buy platenuts (never scoff at something that torques itself!) and silver-plated 12-pt bolts, which makes undoing bolts much easier post-bake if ever necessary. If we have needed any special bolts which were not silver-plated, we bought lubricant to use during the tightening process, just in case. Bolts always should be tightened in a star pattern, using sharpie around the flange to keep track of the order of bolt tightening if necessary (this is particularly helpful for 6.00" CF flanges and larger). This ensures that the knife edges eat into the gasket evenly around the circumference of the flange to form a good seal.

If the bolts are accessible via a torque wrench, that is by far the safest way to go about tightening them, as overtightening can strip platenuts in the best case scenario, tapped holes on expensive parts in the worst case. It also allows you to incrementally

CF size	Bolt torque (in-lb)
1.33”	84
2.75”	144
4.50”+	180

Table A.1: CF nominal bolt torques

tighten each bolt in the star pattern up to the same torque. Required torque for various CF flange sizes is given in Table A.1. When we were young students and had to tighten bolts which torque wrenches could not access, we used other wrenches and pulled on them using a fish scale, using the wrench length and scale reading to estimate torque. We ruined several wrenches this way. Eventually, after tightening enough of them (some of which can be checked via torque wrench), the feeling “sinks into one’s bones” and the flanges can just be tightened by hand. It helps to have a long wrench, for the most ergonomic lever-arm.

Occasionally a connection will need to be redone, and the copper gasket can get stuck onto one of the knife-edges when they are pulled apart. At these times, if the gasket cannot be pulled off by hand, we have found a pair of vise-grip pliers indispensable to grabbing the gasket edges and carefully levering it off. 1.33” CF flanges are the absolute worst; if they need redoing, the gaskets almost always get stuck in our experience. Even the vise-grip will only get 50% of the stuck gaskets off. I intend to avoid this size flange at all cost in my future, but if ever I am forced to interact with one, I will insist on using silver-plated copper gaskets.

Nickel gaskets are extremely hard compared to copper, and thus are much less forgiving; if they get any scratches on them during assembly, we typically no longer trust them to hold vacuum. It helps a great deal to have a second pair of hands especially in this case, so that the gasket and knife edges can be guided together as cleanly as possible.

Once we fully tighten a CF flange, we typically do a “paper test” where we try to guide a piece of paper between the two mated flange surfaces. This is mostly a psychological

thing. To be honest, connected CF flanges that look great and well-mated may have a leak. Connected CF flanges which do not sit entirely parallel, or through which you can clearly see a sliver of gasket, could have a great seal. It's all nonsense, so you just have to do it to the best of your ability and see if it works.

Appendix B

Notes on Baking to UHV

When in the course of laboratory events it becomes necessary for a chamber to dissolve connections with the atmosphere and assume the ultra-high vacuum to which the Laws of Scientific Inquiry entitle it, a decent respect to the productivity of AMO science requires that lab members should bake the machine.

-Thomas Jefferson, probably

Water and other molecules at standard temperature and pressure tend to adsorb onto the walls of stainless steel; to achieve ultra-high vacuum, the steel needs to be baked out. During this process, the rates of desorption inside the chamber significantly increase, allowing much faster pumping to achieve lower pressures. If you are planning to bake, you will need some supplies, which include heating elements, ways to power heating elements, thermocouples (TCs) to monitor temperatures, and thermocouple readout, as well as thermally-insulating material. In this appendix, you will find descriptions of all of the materials and best practices we have gathered through eight bakes.[1] We do not hydrogen-bake our chamber prior to construction/water-baking, and we have achieved

[1] This number of bakes, in fairness, with equal probability could lead you to believe that we are equally either very bad or very good at baking.

satisfactory pressures; all of the discussion below pertains to water-baking methodology only.

B.1 Supplies

B.1.1 Heating elements and power

We use Omega Engineering Super-High Temperature Samox-insulated resistive heating tape (the STH line), in widths that vary from 1/2" to 1" and lengths that vary from 2' to 8', for the majority of our heating during bakes. We also use band heaters from Omega Heater (different company from Omega Engineering!) on viewport flanges and other flanges with large thermal mass, which may require more heat or attentiveness during the bake. The band heaters from Omega Heater come with basic hose clamps standard; we requested bayonet thermocouple adapters soldered onto them.

All of the heater electrical connections were either standard 120 V plugs or bare wire. For the latter, we soldered quick-connect terminals to the ends.

We use a large panel along with wall-mount variacs from McMaster-Carr to power our bakes. We have (12) 300 W variacs, (12) 600 W variacs, (8) 900 W variacs, and (2) 1200 W variacs. The leads on every mounted variac are soldered to the end of an extension cord which has been cut in two; the other bare end of the extension cord is soldered with quick-connect terminals. In this way, we can easily use these cords and regular extension cords to connect the heating elements to variacs over rather large distances across the lab.

B.1.2 Thermocouples and readout

We mainly use two types of surface-mount thermocouples from McMaster-Carr: Heavy duty stainless-steel-cabled bayonet TCs, and exposed-probe fiberglass-cabled TCs which

we affectionately refer to as "the dinky ones." Both have bare-wire leads. We plug them into readout boxes USB-TC from Measurement Computing. Each box can read out up to 8 TCs and work with any TC type (though we solely use J-type for bakes); we typically use somewhere around 6-7 boxes, thus up to 56 thermocouples for a bake of half of the machine (either the oven or the mainchamber). The USB-TC boxes are great because they come with Matlab drivers and libraries which work with only minimal configuration. We also bought one nice handheld TC reader for other locations.

We typically work Solidworks drawings into a Matlab GUI, which I wrote for the first few bakes and was improved upon by Cora Fujiwara in 2018. This GUI interfaces with all of the USB-TC boxes to update temperature readings once every couple of minutes, and incorporates a plot to see trends over time, whether there are any trouble spots which are colder or hotter than the mean temperature of the bake, etc. We were able to simply stream the desktop or teamview into the computer to monitor the bake from home, once we reached steady state.

B.1.3 Thermal insulation

The materials we typically use for bake insulation are copious amounts of aluminum foil, and some type of fiberglass insulation. We initially used McMaster-Carr high-temperature insulating sheets, but after finding a recommendation for Superwool blanket in Appendix B of the Stellmer thesis [21] and trying it out with our spectroscopy cells, we switched to that as our insulation of choice. It tends to be better at insulating, is friendlier to the environment, and is softer/nicer to work with and mold than fiberglass. While it is mildly less irritating to the skin, I still recommend heavy precautions to cover exposed skin when working with it, unless you wish to be covered in microcuts.[2]

[2]We typically wore full-length pants, labcoats, and gloves, with velcro or masking tape around the wrists to ensure no gaps between the latter two. We also wore face masks.

B.1.4 Other

In cases where we wanted to more carefully thermally protect certain regions of the table, we also used conformable Aerogel insulation to protect optics and lasers near the insulated chamber, and heat-reflecting insulation sheets to push away radiated heat from e.g. a mainchamber when an oven was being baked.

We used 3.5 Mil Kapton tape for any necessary adhesion.[3] We also buy flexible wire mesh to protect our viewports.

B.2 Thermal Considerations

There are some main thermal considerations to take into account when baking, some of which are absolute and some of which are relative. Many of our viewport AR coatings were rated to 200°C or 250°C, and the glass-to-metal seals on the viewports themselves ranged from 300°C-350°C ratings. The insulation on the wire we used for all of our slower and MOT coils was only rated to 160° C. However, the biggest worries were thermal gradients. While gradients across CF flanges have, in our experience, been quite robust, we still try to limit them to no larger than 20°C. Viewports present a unique problem because there is no good way to monitor the temperature of the glass, thermal conductivity over glass-metal seals is low, and the different expansion coefficients make them uniquely susceptible to large gradients. Much of our methodology evolution was focused on being careful about viewport monitoring and heating.

We typically run our regular UHV bakes at around 180°C for about 2 weeks, including ramp-up and cool-down. We find that with a target temperature of 180°C, our coldest spots are around 165°C (around areas with large thermal mass or near supports that draw heat to the optical table), and our hottest spots are around 200-210°C (areas around ion gauges, which run hot). Viewports are not allowed past around 190°C.

[3] If your tape is thinner, good luck getting it off the roll.

B.3 Methodology

B.3.1 Pre-bake

We first identify locations with large thermal mass (for example, gate valves, larger CF flanges, ion pump connections) and place band heaters in those areas, in case we need to provide a little bit of conductive heating to those places. We take care to label the band heater cords with their size and location on the machine, in case we need to connect them to variacs. If we are baking an oven and have band heaters around the metal reservoir, we just use those for the bake.

We place some fine wire mesh which has been properly cleaned and sonicated over each of the viewports, and attach them to the flanges with Kapton. This is to keep us from accidentally scratching any coatings with aluminum foil.

We make sure that only one of the supports on the chamber to be baked is firmly attached to the optical table. This is to account for thermal expansion, which is non-negligible over a machine that is roughly 8 feet long. We also place small sheet-metal shims between the supports and the optical table, which helps lower thermal conduction to the table and makes our bake more efficient.

We initially plan out locations for all thermocouples, keeping in mind areas like viewports (which may require more monitoring) and areas like the centers of nipples and tees (which require less), to maximize the amount of information we get. This allows us to start writing a GUI in parallel with other bake preparation. Bayonet TCs are assigned to sensitive areas (viewport CF flanges in particular) since they stay firmly in place during the bake. Dinky TCs are attached to locations on the machine with large amounts of Kapton tape, and then are firmly strain-relieved with nearby hose clamps. We plug all

of the thermocouples into the USB-TC boxes, plug the boxes into a computer that has been designated for the bake, and make sure they all work.

Once this is done, we wrap the entire machine in a few initial layers of aluminum foil, taking care to route all of the TC and heating element cords out of the foil in as few places as possible. This extends out to the bellows leading to our turbo pump, just to be safe about gradients across our valve. This foil, beyond providing layers of insulation, ensures that the majority of our heating will be convective rather than conductive. The only exception to the foil-wrapping procedure is the ion pumps, which have such a large mass that we need to heat them directly. We then wrap heating tape around the entire machine. We make sure to think about the locations of each tape in reference to what it will be heating, so that when we adjust the power sent to that tape, we are effectively specifying and heating one location on the machine. As we do this, we create a spreadsheet which keeps track of the heating tape size (e.g. its power requirement), its location on the machine, and any nearby thermocouples. This is a very useful spreadsheet during the bake. We also label the heating tape cord with its size and location, which is useful to connect the variacs once everything is insulated.

Setback: Our initial bake protocol involved heating all flanges, including viewport flanges, directly with band heaters. During that first bake, we also used only the dinky types of thermocouples, which were poorly attached with Kapton tape; several became disconnected during the course of the bake, and several others gave poor readings. A combination of these circumstances and a goal bake temperature of 200°C resulted in a bad bake, wherein the thermal gradient across one of the viewport glass-metal seals was too high and the vacuum broke. We did not make that mistake again. **Bake convectively**.

After the heating tapes are wound, we prepare packets of the Superwool surrounded by aluminum foil, and place these packets around the entire machine in at least one layer.

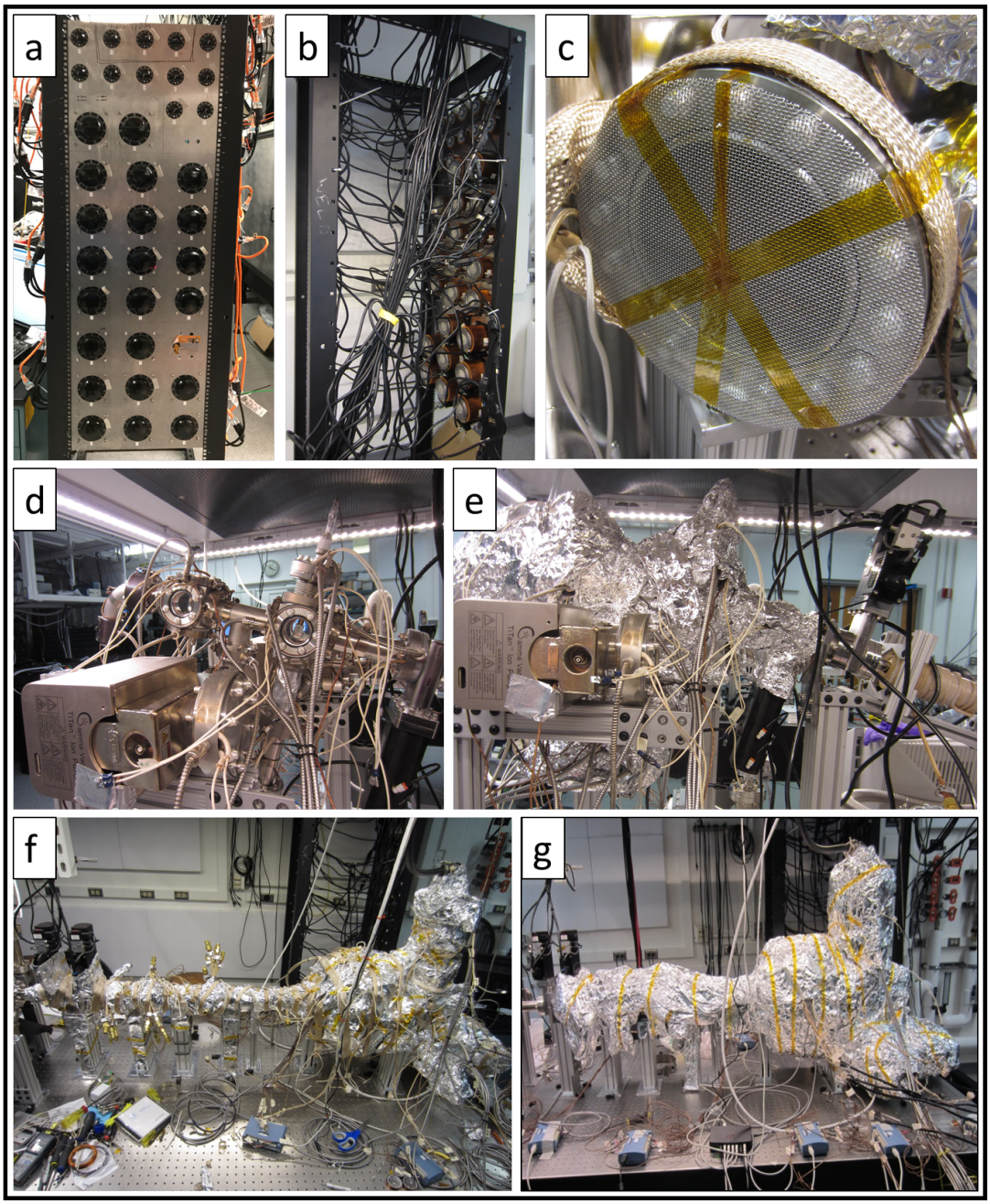

Figure B.1: **a,b:** The bake panel (front and back) with variacs and connections. **c:** Mesh protection over a viewport to keep us from accidentally scratching the coatings. **d:** Thermocouples and band heaters are attached directly to the machine (Sr oven bake pictured). **e:** Foil is wrapped around all but the ion pump. **f:** Heating tape is wrapped around the foil layer (Li main chamber bake pictured). **g:** The heating tape is covered with insulation and more foil. Thermocouple readout boxes are attached to thermocouples and control computer.

We go back and cover the packets with yet more aluminum foil until we are satisfied. We connect each of the heating tapes to a variac which will provide the appropriate amount of wattage.

If we can, we also attach a webcam to the computer to monitor our chamber pressures remotely.

B.3.2 The actual bake

We ramp up the variacs by a few percent at a time and let the temperatures stabilize. We then correct for any areas which are heating too slowly or quickly. This process iterates using human PIDs, or "grad-student-in-the-loop" technology, until we reach the desired temperatures of around 180°C.[4] We allow it to bake until we are happy with our turbo pressure (and RGA pressures, if we happen to be monitoring those), and towards the end of the bake degas of all of our ion gauges filaments, as long as our pressures are low enough. Our bakes have been at temperature for between 5 and 12 days, during which time we continue to actively monitor pressures and temperatures.

We then try to ramp down temperatures no faster than around 25°C/hour while turning on ion gauges and ion pumps, although we occasionally get impatient.

B.3.3 Post-bake

Our bakes have resulted in pressures around 10^{-9} Torr in our ovens, where we typically use elastomer-based valves and do not have Ti-sub pumps, and 10^{-11}-10^{-12} Torr in our mainchambers, where we typically care more about the quality of our pumps and are more careful during chamber assembly.

[4]This can be an arduous several-day process which you will likely share with others. It is important to find the right music to play during this time, and perhaps the right beers to drink, to encourage relaxation and group harmony.

Appendix C

Lab Infrastructure

This appendix discusses gruesome details, chronicles growing pains, and imparts a few small useful lessons learned while the lab has been built up.

C.1 Temperature, humidity, and seismic stability

Our lab is divided roughly into quadrants by four pneumatically-floated optical tables, three of which have "clouds" made of Unistrut and plywood hanging above them from the ceiling. The lithium laser table was bought at the inception of the lab and placed under one of the clouds, and to my knowledge there have been no problems. The strontium laser table was gifted to the lab from Prof. Dave Cannell, and dates back to the 1960s; while this table was floated soon after moving to the new lab space, the positioning of the pneumatic legs was poor, affecting the stability of the table to vibrations. One of the lasers on that table, a Toptica SHG-Pro 461 nm laser with a frequency-doubling cavity, was extremely susceptible to these vibrations, and we found that repositioning the legs was immensely helpful to the stability of the cavity lock.

The other two optical tables, the machine tables, rest under clouds which are both humidity- and temperature-controlled by an HVAC system, and enclosed by custom 80/20

enclosures. For many years, the setpoints and PID parameters on this system were not enough to combat the heat loads from machine operation, and we found that resulting variation of around 3°F would result in noticeable alignment and/or polarization shifts of our beams over the course of the day (for example, if we aligned our ODTs while the machine was "hot," we would need to wait for the enclosure to heat up to retrieve the same atom number). We took several steps to make our optics setups more robust, which are outlined in Appendix E, but we additionally put some effort into tuning setpoints and flowrates for the HVAC, which has made our recent experimental lives easier.

All of the visible laser systems (the 671 nm system, 461 nm system, and 689 nm system) are housed within small 80/20 and PVC custom enclosures to protect against dust; the 1064 nm system is housed similarly, using aluminum instead of PVC for safety. We also find that the covers for these enclosures generally help pointing stability.

C.2 Water system

In order to cool our magnets, electronics, and some lasers, we have a closed-loop water system in our lab which is separate from the building water. The biggest part of this system is a Neslabs III chiller (70 kW capacity), which contains a heat exchanger to cool our lab's closed-loop water system using the building chilled water supply, and a pump to circulate water at 50 psi. The chilled water is directed to a high-pressure booster pump (Flint and Walling PB1016S151), which provides us with the flow rates we need to effectively cool our magnets (our setpoint is around 100 psi). The chiller pump failed in November 2018; please see Appendix K for more information on the pump replacement and other chiller details. A schematic of water lines in the core is shown in Fig. C.1.

The high-pressure water lines in our lab are directed to water manifolds in the clouds above both machine tables, which break out cooling lines for each magnet. These manifolds also contain RTDs (Omega PR-20-2-100-3/16-2-E-T) and flow rate sensors (Malema

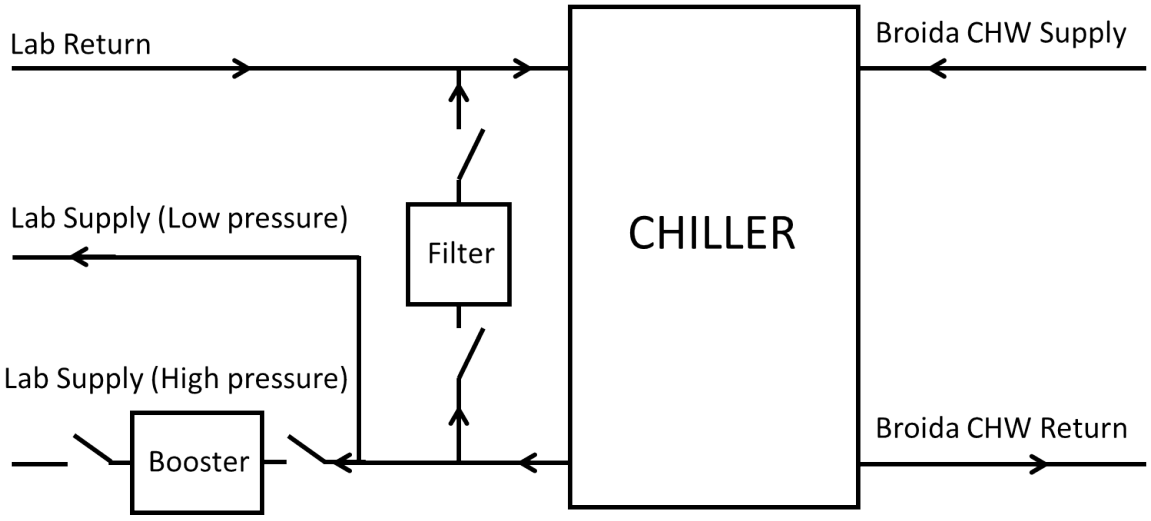

Figure C.1: An approximate diagram of water flow in the core. The low-pressure and high-pressure supply and return lines lead to breakout manifolds in the lab.

M-10000-S3051-00 and M-10000-S2031-00) to monitor temperatures and pressures for each line.

Setback: When our chiller does not have enough water in its reservoir, it shuts itself off. Back in June 2014, when we were running without any interlocks and very minimal water temperature monitors, this auto-shutoff occurred when we were running the booster pump, causing the input pressure to the booster to run extremely low. The booster subsequently overheated and broke. We installed water temperature monitors immediately afterwards. **Build interlocks early**.

In late 2016/early 2017, we found a large buildup of algae in the water system. We replaced the water in the chiller reservoir with a 10% solution by volume of isopropyl alcohol diluted with distilled water. This has worked fine for us so far; none of the materials in our pumps are rated lower than a "B" grade for 100% isopropyl alcohol. We also began shunting water away from the booster pump and through a cleaning filter at the end of every day, and directing it back at the start of every day, in the name of

keeping our water as clean as possible.

C.3 Control hardware and software

Both of our machines use the Atticus server and Cicero software platforms developed at MIT to control our experiments [153]. The server interfaces with a 10MHz Opal Kelly XEM3001 FPGA (connected with the control computer via USB) and 4 National Instruments output cards (32-channel digital cards, PCIe-6535, and 8-channel analog cards, PCI-6713) mounted in the control computer. On the lithium machine, a network clock is used to sync the cards as well as triggers for external circuits; on the strontium machines, the timebases are directly synced.

The logfiles generated by Cicero for each experimental run are associated with the camera images taken during that run using timestamps. All processing is accomplished in Matlab. For every set of data, the images are analyzed for basic useful information, and the resulting output is stored in a large Matlab struct called atomdata.mat; rather than reanalyzing the data every time we need to access it, we simply load the relevant atomdata file, and continue with any further analysis.

All of our data is saved directly onto our lab server, which is backed up onto box.com. Data backup is important.

C.4 Electronics

There are a few electronic architectures which we have developed in the lab over the past few years, which will be briefly detailed below.

C.4.1 AOM drivers

The most ubiquitous drivers (indeed, electronics) in lab are voltage controlled oscillator (VCO)-based AOM drivers, which were developed by an undergraduate researcher in 2013, and which we modify as necessary to give us the center frequencies, resolutions, and bandwidths we require for specific applications. Their stability tends to be limited by the thermal drift of VCOs and various passive elements in the circuitry, even after taking care to purchase low-thermal-coefficient coefficients. We work around slow drift by occasionally checking the outputs on a spectrum analyzer. The frequency at which we can either amplitude- or frequency-modulate the AOMs is actually limited by the 1 μs output resolution of Cicero. To overcome this problem on the lithium machine, Cora Fujiwara developed a DDS (direct digital synthesizer)-based driver using a Beaglebone platform, which allows modulation up to around 2 MHz; more on this architecture may be found in her thesis [47].

C.4.2 Beam shutters

We went through several iterations of home-built beam shutters using scavenged iPod hard drives. They had extremely fast ($\sim$ 10 μs) closing speeds, but the arms would "bounce" due to the undamped force of the shutter actuation, requiring more complicated Arduino-based pulse sequences to drive them. Additionally, that same actuation force required additional damping when mounting on the optical tables, as they would otherwise affect cavity locks. Zach Geiger eventually developed an inexpensive stepper-motor based design housed in a custom 3d-printed mount. These have a slower shutter speed of around 1 ms, but have been much more reliable and have the nice property of only requiring a TTL to open or close. We use them in all near-resonant beam paths.

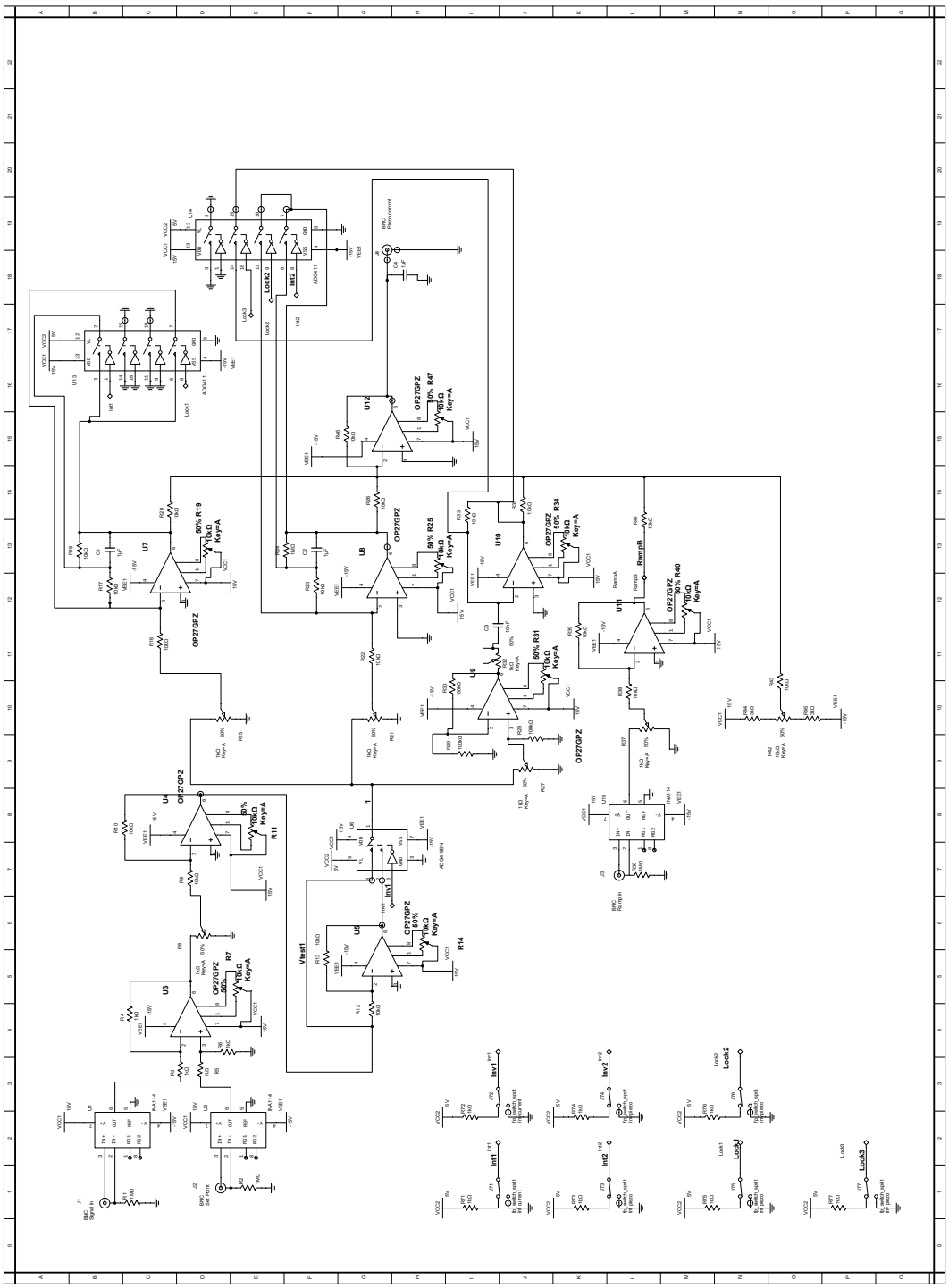

Figure C.2: Circuit diagram for lattice PIDs in strontium experiment. Design by Toshihiko Shimasaki.

C.4.3 PIDs

We use homebuilt PIDs to stabilize all of our atom-trapping beams. We went through several iterations of PIDs; the original designs only allowed us to follow setpoints up to around 2 kHz before we began to see significant distortions and gain problems. We still use these designs to stabilize our optical dipole traps during cooling, but for all other stabilization we use a circuit designed by our postdoc Toshihiko Shimasaki, which follows setpoints nicely up to 10 kHz and only results in phase delays up to 40 kHz. This design was based off of one used in the DeMille group at Yale, which in turn was developed from a design used at Innsbruck; the schematic may be found in Fig. C.2.

C.5 Magnet winding

For all of our large magnets, we decided to use square-profile hollow copper wire, both to ease wire-stacking during the winding process and to make water-cooling possible. We settled on alloy 101 OD 0.1875" wire with a wall thickness of 0.032", custom from Small Tube Products; Small Tube Products directly shipped to S&W Wire Co, which insulated the wire with Daglass (fiberglass) insulation rated to 180°C (we never baked the wire above 160°C, just to be safe). Throughout the winding process, we used thermally-conducting electrically-insulating Duralco NM25 epoxy; the resulting effective thickness of each wound layer of wire was 0.2". We were careful not to mix too much epoxy at one time, as we found that large batches could not be properly mixed and thus bonded the wire poorly. We also outgassed each batch of epoxy, once mixed, in a small vacuum chamber for ten minutes.

We constructed a custom jig out of 80/20 hardware (Fig. C.3A), and took special precautions to make sure there was tension on the thick wire at all times, such that our wire spacing in both radial and axial dimensions remained constant. While winding a given layer, we made sure there was enough radial tension on the wire by levering the spool

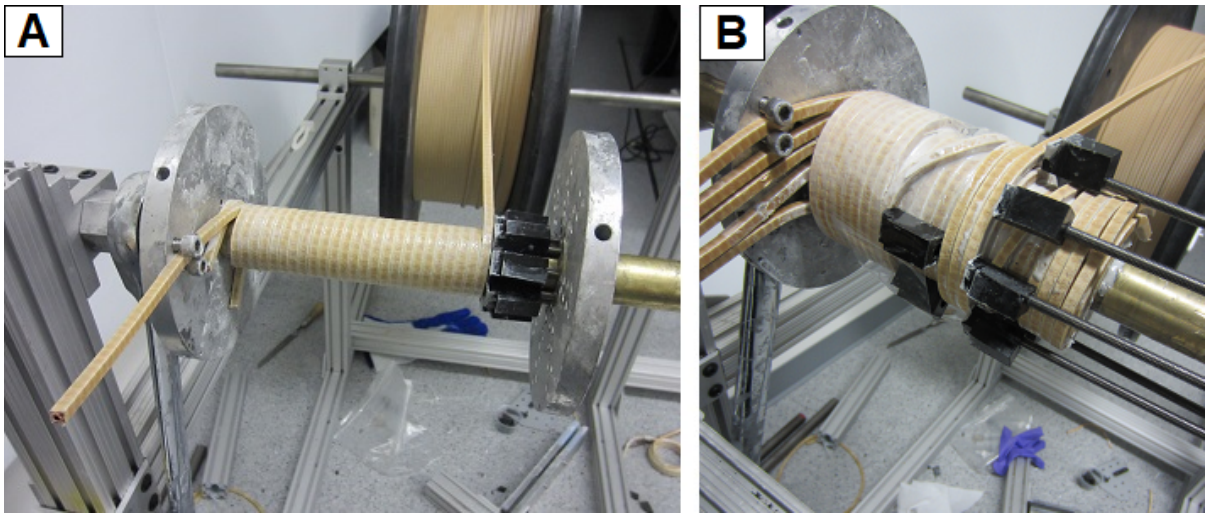

Figure C.3: The winding rig and various spacers are shown during the process of winding a slower solenoid.

in the opposite direction from which the solenoid was being wound (e.g, if we torqued the solenoid axle in $\hat{z}$ to wind the magnet, the spool would be simultaneously torqued heavily in $-\hat{z}$). We machined a custom jig which supported long screws at different radii, and used them, along with plastic spacers, to exert axial force on every layer of the solenoid such that tension would not be lost while that solenoid layer dried. We also used spacers to create gaps in the solenoid layers where needed (Fig. C.3B). Since a large amount of force needed to be exerted both on the solenoid axle and the wire spool during the winding process and epoxy needed to be applied to the wire progressively, winding was typically a 3-person job.

C.6 Interconnects for water-cooled electronics

The square shape of the wire meant that we had to somehow engineer a sound connection to round Swage-Lok PVC connectors. The process was eventually developed largely by one of our intrepid undergraduate students, and involved fitting a length of copper tubing onto the stripped square wire and connecting them by flowing large amounts of solder

into the gaps with a blowtorch. Swage connectors could then be fit onto the copper tubing and used to interface with PVC connections. More details on this process may be found in Ruwan Senaratne's thesis [22].

Appendix D

Strontium Polarizability Calculations

The concept of polarizability, the metric of how much an atom responds to an AC electric field of a certain magnitude and frequency, is central to understanding light shifts and, by extension, trapping potentials. In the contexts of atomic clocks, where one wishes to measure a transition frequency with extremely high precision, it is highly desirable to trap atoms such that the transition frequency is unaffected. Unfortunately, the vast majority of trapping frequencies will shift ground and excited states by different amounts because the states will have different polarizabilities. Not only will the transition frequency be shifted, but it will also be generally broadened due to inhomogeneity of trapping intensities. However, for some transitions, there exists a trapping frequency at which the ground state and excited state have the same polarizability, and transitions are thus unaffected by the trapping potential. This is called the magic wavelength.

The definition of polarizability is deceptively simple. In addition to dependence on the electric field frequency and magnitude, it can also depend on the polarization of the field; any polarizability which is only dependent on the external electric field is usually referred to as scalar polarizability. There are also higher-order polarizabilities which are dependent on the total angular momentum of the state to first and second order; these are usually called the vector and tensor polarizabilities.

Even scalar polarizabilities are extremely difficult to calculate. Recall from Section 2.2.4 that this quantity depends on the square of dipole matrix element between the ground and excited state. However, for atoms heavier than helium, it becomes exponentially more difficult to determine those states exactly. Atoms are strongly-correlated quantum systems, and no tractable exact theory exists, even of their static properties. Several theorists, such as Marianna Safronova, have dedicated significant effort to *ab-initio* calculations to determine various contributions to the polarizability of certain atomic transitions. Experimentalists at JILA, among other places, have spent many years measuring these polarizabilities with extremely high precision for strontium optical clocks [174]. While theorists can help experimentalists predict approximate magic wavelengths, which is critical when deciding what lasers to buy, magic wavelengths are usually only precisely found and characterized via direct experimental measurement.

In this appendix, I detail some calculations done in collaboration with Alexandre Cooper-Roy at Caltech, following the calculation method detailed in the Boyd thesis [175]. There are alternative calculation methods [176], but this one happens to work well for many of the values found in literature. The references used for the calculations may be found in Tables D.1, D.2,and D.3.

D.1 Calculations

The general form of the scalar polarizability α for a ground state g in a trapping potential with frequency ω_L is

$$\alpha_g(\omega_L) = 2e^2 \sum_k \frac{\hbar\omega_{gk}|\langle\varphi_k|\mathbf{d}|\varphi_g\rangle|^2}{\hbar^2(\omega_{gk}^2 - \omega_L^2)} \tag{D.1}$$

where the sum is taken over all excited states k with corresponding transition frequencies ω_{gk}, and $\mathbf{d}$ is the dipole operator. This may be rewritten in terms of the transition rates

A_{gk} for each transition from state g

$$\alpha_g(\omega_L) = 6\pi\epsilon_0 c^3 \sum_k \frac{A_{gk}}{\omega_{gk}^2(\omega_{gk}^2 - \omega_L^2)}, \tag{D.2}$$

so all we need to know are measured transition rates for all transitions from the ground state to every excited state (at least where the data is available), and the corresponding transition frequencies ω_{gk} (again, where data are available).

Literature commonly provides the total transition rate A_T from an excited state (e.g., the lifetime of the excited state), which accounts for all possible states to which it can decay. We need to calculate the probability of falling into a particular ground state g. This requires knowing the branching ratio β, which may be calculated based on the quantum numbers of the ground and excited states:

$$\beta_{gk} = \frac{(2J_g+1)\begin{Bmatrix} J_g & J_k & 1 \\ L_k & L_g & S \end{Bmatrix}^2}{\sum_{J=|L_g-S|}^{|L_g+S|}(2J+1)\begin{Bmatrix} J & J_k & 1 \\ L_k & L_g & S \end{Bmatrix}^2} \sum_{m_k}^{J_k}(2J_k+1)\begin{pmatrix} J_g & 1 & J_k \\ m_g & p & -m_k \end{pmatrix}^2, \tag{D.3}$$

where matrices denoted by {} are Wigner 6-j symbols and by () are Wigner 3-j symbols. p refers to the polarization of light: -1, 0, 1 correspond to σ^-, π, σ^+. We can then write

$$A_{gk} = A_T \times \beta_{gk} \times \zeta(\omega_{gk}), \tag{D.4}$$

where ζ is an energy correction term also commonly found in literature.

Various sources provide energies instead of frequencies, determine A_{gk} instead of providing A_T, etc; we can also directly add known polarizability corrections to the final calculation of α_g; for example, [176] provides core corrections for $^1S_0$ and $^3P_0$ which are taken into account in the calculation.

The resulting calculations are shown in Fig. D.1 for absolute polarizability, an example of typical AC Stark Shifts, and zooms-in on the magic wavelengths for the clock transition as well as linearly- and circularly-polarized $^3P_1$ transitions. Note that determinations for

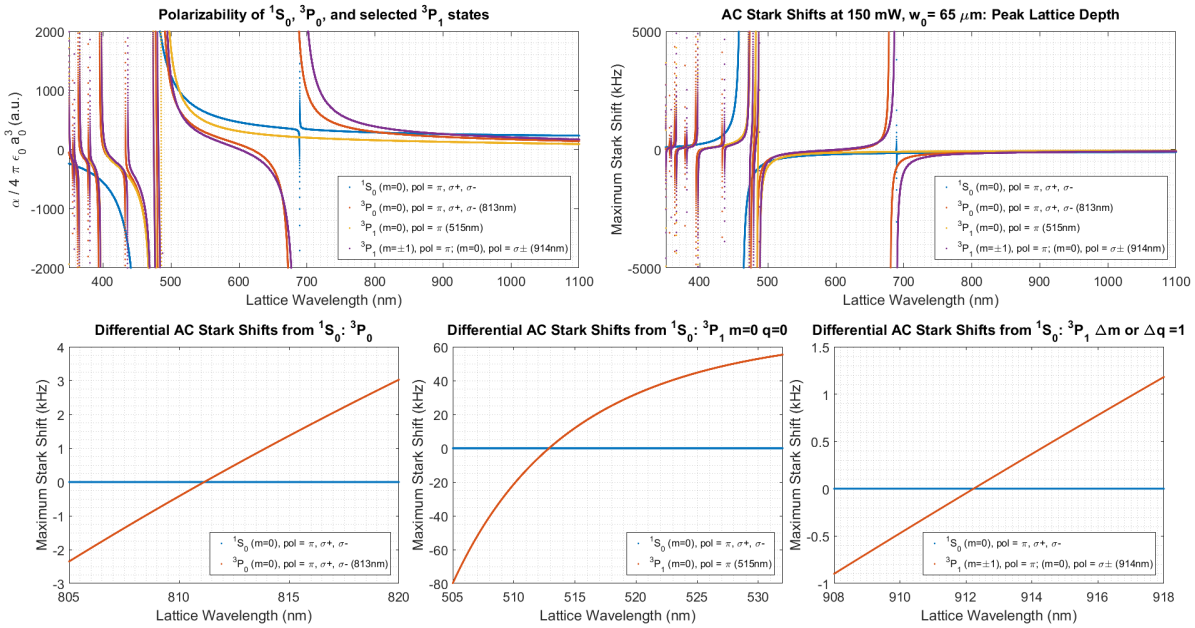

Figure D.1: Calculated strontium polarizability for $^1S_0$, $^3P_0$, and selected $^3P_1$ states.

the $^1S_0 \rightarrow^3 P_0$ and $^1S_0 \rightarrow^3 P_1(\Delta m = 0, p = 1)$ magic wavelengths greatly differ from the experimentally-determined values of 813.4 nm and 915 nm [177] [175]. The exact magic wavelength for $^1S_0 \rightarrow^3 P_1(\Delta m = 0, p = 0)$ is unknown but starting to come into use in strontium optical tweezer experiments [178, 179].

D.2 References

The numbers listed here are not necessarily the ones given in the references listed, but have been calculated based on the given quantities. They have also been rounded. Transitions are grouped into tables by ground state g, which may be found in the captions.

For the ground state, there are no energy corrections ζ, nor branching ratios β since there is no state to decay into; A_{gk} values are typically available in the literature.

k	ω_{gk}	A_{gk}	Ref.

$5s5p^3P_1$	2.732	0.0469	[180]
$5s5p^1P_1$	4.0872	190.0057	[181]
$5s6p^3P_1$	6.425	1.87	[182]
$4d5p^1P_1$	7.029	0.15	[182]
$5s7p^1P_1$	7.331	5.34	[182]
$5s8p^1P_1$	7.758	16.85	[182]
$5s9p^1P_1$	8.001	18.34	[182]
$5s10p^1P_1$	8.164	11.50	[182]
$5s11p^1P_1$	8.279	6.65	[182]
$5s12p^1P_1$	8.357	3.724	[183]
$5s13p^1P_1$	8.415	2.356	[183]
$5s14p^1P_1$	8.458	1.574	[183]
$5s15p^1P_1$	8.491	1.166	[183]
$5s16p^1P_1$	8.516	0.850	[183]
$5s17p^1P_1$	8.535	0.644	[183]
$5s18p^1P_1$	8.551	0.504	[183]
$5s19p^1P_1$	8.564	4.246	[183]
$5s20p^1P_1$	8.574	0.321	[183]
$5s21p^1P_1$	8.583	0.256	[183]
$5s22p^1P_1$	8.590	0.207	[183]
$5s23p^1P_1$	8.596	0.175	[183]
$5s24p^1P_1$	8.602	0.143	[183]
$5s25p^1P_1$	8.606	0.124	[183]
$5s26p^1P_1$	8.610	0.101	[183]
$5s27p^1P_1$	8.614	0.083	[184]

$5s28p\,^1P_1$	8.617	0.0763	[184]
$5s29p\,^1P_1$	8.619	0.0722	[184]
$5s30p\,^1P_1$	8.622	0.0550	[184]
$5s31p\,^1P_1$	8.624	0.0503	[184]
$5s32p\,^1P_1$	8.626	0.0466	[184]
$5s33p\,^1P_1$	8.628	0.0418	[184]
$5s34p\,^1P_1$	8.629	0.0315	[184]
$5s35p\,^1P_1$	8.631	0.0284	[184]
$5s36p\,^1P_1$	8.632	0.0213	[184]
$5s37p\,^1P_1$	8.633	0.0155	[184]
$5s38p\,^1P_1$	8.634	0.0128	[184]
$5s39p\,^1P_1$	8.635	0.0120	[184]
$5s40p\,^1P_1$	8.636	0.0090	[184]
$5s41p\,^1P_1$	8.637	0.0079	[184]
$5s42p\,^1P_1$	8.638	0.0070	[184]
$5s43p\,^1P_1$	8.639	0.0060	[184]
$5s44p\,^1P_1$	8.639	0.0054	[184]

Table D.1: Strontium polarizability data for ground state $^1S_0$

k	ω_{gk}	A_T	ζ	Ref.
$5s6s\,^3S_1$	2.773	84.996	1.0828	[185]
$5s7s\,^3S_1$	4.353	11.998	1.0517	[185]
$5s8s\,^3S_1$	4.981	8.2162	1.0450	[185]
$5s9s\,^3S_1$	5.299	4.5336	1.0422	[185]
$5s10s\,^3S_1$	5.483	2.7671	1.0408	[185]
$5p^2\ ^3P_1$	3.9712	120	1.0373	[185]
$5s4d\,^3D_1$	0.7236	0.4123	1.2660	[185]
$5s5d\,^3D_1$	3.8972	60.999	1.0544	[185]
$5s6d\,^3D_1$	4.7785	24.620	1.0457	[185]
$5s7d\,^3D_1$	5.1889	14.199	1.0424	[185]
$5s8d\,^3D_1$	5.4153	8.5097	1.0407	[185]
$5s9d\,^3D_1$	5.5549	5.5108	1.0400	[185]

Table D.2: Strontium polarizability data for ground state $^3P_0$

k	ω_{gk}	A_T	ζ	Ref.
$5s6s\,^3S_1$	2.739	84.9995	1.0421	[185, 186]
$5s7s\,^3S_1$	4.329	12.0012	1.0264	[185, 186]
$5s8s\,^3S_1$	4.947	8.2199	1.0230	[185]
$5s9s\,^3S_1$	5.265	4.5311	1.0216	[185]
$5s10s\,^3S_1$	5.448	2.7714	1.0208	[185]
$5p^2\ ^3P_1$	3.937	120.00	1.0099	[185, 186]
$5p^2\ ^3P_2$	3.889	120.00	1.0503	[185, 186]
$5s4d\,^3D_1$	0.6884	0.4117	1.0901	[185]
$5s5d\,^3D_1$	3.863	60.9999	1.0261	[185, 186]
$5s6d\,^3D_1$	4.745	24.6195	1.0228	[185]
$5s7d\,^3D_1$	5.155	14.2007	1.0213	[185]
$5s8d\,^3D_1$	5.380	8.5103	1.0206	[185]
$5s9d\,^3D_1$	5.520	5.5090	1.0203	[185]
$5s4d\,^3D_2$	0.6997	0.4124	1.1444	[185]
$5s5d\,^3D_2$	3.866	60.9996	1.0284	[185, 186]
$5s6d\,^3D_2$	4.746	24.6199	1.0234	[185]
$5s7d\,^3D_2$	5.156	14.1997	1.0219	[185]
$5s8d\,^3D_2$	5.381	8.5106	1.0210	[185]
$5s9d\,^3D_2$	5.520	5.5095	1.0203	[185]

Table D.3: Strontium polarizability data for ground state $^3P_1$

Appendix E

Trap and Lattice Stability

Around the time we started to work on lattice experiments, we noticed some small mechanical and optical instabilities which soon became untenable, as drifting alignment and power changed our lattice depth by more than a few percent. Briefly listed here are various steps we eventually took which helped the overall stability of lattice experiments specifically, and the overall machine operation generally.

E.1 Mechanical

E.1.1 Breadboard supports/fortification

Since our strontium breadboards sit around 15" above the optical table, there is a greater chance for vibrational instability. When a collimated beam was placed on one of the side breadboards and imaged around 3 feet away on the other side breadboard using a beam profiles, we saw drift of the beam center on the order of ± 10 μm. To fix this issue, we put two clamping feet on each breadboard support to attach to the optical table, and tightened then down as much as was physically possible. We attached 6" 45° supports between each support and the breadboard in at least 1 dimension (2 dimensions if space

allowed). We also affixed metal plates to the bottoms of the breadboards to attach each side breadboard to the back breadboard. These fixes reduced the beam center drift in the same measurement to ± 2 μm.

We also bought a sack of lead shot to fill the hollow 80/20 supports, but we are waiting for a true rainy day scenario (a main chamber rebake, or something with similarly grave implications) to implement this.

E.1.2 Steel mirror mounts

We have found that the thermal drift from aluminum mirror mounts can result in large changes in alignment and coupling efficiency over time. To fix this, in cases where alignment was important for machine stability, we switched out certain mirror mounts for steel mounts. At really crucial places, we used double-sprung steel mounts for maximal stability.

E.1.3 Lids on optics

Our machines are contained in enclosures underneath clouds which include HVAC systems for temperature and humidity control. There are vents which should produce laminar flow inside the enclosure. In addition to this, there are also air currents produced by thermal gradients in the enclosure, especially where magnet wires dissipate heat near the chamber. We have found it critical to erect makeshift "enclosures" for the breadboard optics using 1/2" posts and custom-bent sheet metal (we do this ourselves in the machine shop); without them, the beam positions at the atoms are liable to drift on the order of around 10 μm.

E.2 Optical

E.2.1 Angle-polished fibers

One of the dangers with fiber-coupled lattice beams is that light inevitably will hit the front surface of the fiber, whether that light is from a retroreflection or a separate counterpropagating beam. This can actually make lattice alignment much easier, since recoupling light into the fiber provides a nice constraint on how well the two beams are overlapped. However, if any of that retroreflected light (which propagates normal to the fiber face) reflects from the fiber facet, it can generate a third beam almost parallel to the lattice which can interfere to change the lattice depth (in theory, this beam can retroreflect many times). Since the path length for this third beam is very long, its phase is accordingly more susceptible to any thermal drifts of optical components. The maximum amount by which it can change the depth of the lattice goes as intensity to the 4th power, which means that even very weak beams reflected from the fiber face can produce significant changes in the lattice depth. The effect is even more pronounced if the lattice is being phase-modulated, as is the case in our experiment.

The amount of light which is reflected from the fiber face can be significantly suppressed by using angle-polished fibers, such that any reflections are deflected by an angle of around 16°. We were not aware for a long time that the fibers we initially used were flat-polished (we had ordered APC fibers), and debugging and fixing this issue led to much more stable lattice depths.

E.2.2 Dichroics

In our lattice experiments, we use short-pass dichroic mirrors to separate the lattice beams from imaging beams. If any lattice light is transmitted through the dichroic rather than reflected, it could potentially retroreflect off of optics in the imaging beam

path and cause unwanted interference with the other lattice beams. Most dichroics have a preferred polarization for which the extinction ratio is increased by a factor of order $\sim$10. Changing our lattice beam polarizations to the dichroic-preferred one also led to more stable lattice depths.

E.2.3 Cleanup cubes

Dissipated power in the 1064 nm isolators, as well as overall dissipated heat in the enclosures, increases the temperatures inside both the machine enclosure and the 1064 nm enclosure. One of the biggest resultant thermal effects we see on our optics is drift in polarization, particularly for the high-power 1064 nm laser. We use zero-order waveplates wherever possible, but we see drift nonetheless, usually observed in the context of drifting powers in various beams post-polarizing beam splitters. The drift also comes from small changes in 45° mirrors, which scramble any non-linear polarization. We added so-called "cleanup cubes," which are just polarizing beam splitter cubes, at many locations in the optical setup but most critically near the polarization-dependent light pickoffs for our PIDs, which guarantee that our light remains linearly polarized until/unless we need it to be otherwise. Adding these cubes increased the lifetime by our ODTs by a factor of a little less than two. Additionally, it helped fix drift in our evaporation endpoints throughout the course of the day.

Appendix F

Imaging System and Alignment Tricks

This appendix contains a brief list of some tricks we have found useful to align a 4f absorption imaging system and lattice beams. It also includes pictures of the strontium red MOT 1 taken along every imaging axis currently set up, with labels to point out the directions of gravity and the oven on the image.

F.1 Imaging and alignment tricks

When setting up any kind of beam which will have a small waist at the atomic plane (like an ODT), it is useful to have an imaging axis along the same axis to help with alignment. We use $4f$ telescope systems on either side of our chamber: one on the ingoing side to expand the imaging beam to fill the camera sensor (lenses 1 and 2), and one on the outgoing side to magnify the image of our atoms (lenses 3 and 4). In each telescope, at least one lens (often the one closer to the chamber) is mounted on a precision stage, such that we can be sure of our beam focusing and our image magnification.

We typically set up the imaging beam and the ODT at the same time, using the following methodology. Lens 1 is of relatively little importance, as only the imaging light hits it. Lens 2, the focusing lens, is typically an achromat doublet; we have found this

necessary on the strontium machine due to large chromatic aberrations from 461 nm to 1064 nm. We place this lens such that the imaging beam is roughly collimated, and set up a very rough telescope with lenses 3 and 4 after the chamber. We then take an image of the cloud along that axis with an irised-down imaging beam. We use the iris pinhole and the image on the camera to roughly align the ODT. We use a perpendicular axis to image atoms trapped in the ODT for different trapped hold times to observe their motion, and use this to walk lens 2 such that the focus is in approximately the right place. We move lens 1 to collimate the imaging beam through the chamber.

After the chamber, lenses 3 and 4 are achromat doublets. Lens 3, the objective lens is placed to collimate the ODT beam out to as far as we can, which is usually 2-3 m (we check this using a beam profiler). Lens 4 is placed around $f_3 + f_4$ away from lens 3, and a camera is set f_4 from lens 4. We walk lens 4 and the camera to focus images of the atoms onto the camera (Babinet's principle states that the lack of a point source behaves like a point source); this is usually done using an ODT which has some component normal to the axis being set up. Once these lenses are well-focused, the ODT can be aligned (at low power) to the location of the atomic image on the camera. Looking at the waist of the ODT on the camera (which should be an image plane of the atoms) should allow fine walking of lens 2 to minimize spot size.

If knowing the magnification of the imaging axis to a relatively high precision is important, especially if using a heavier atom, it can be useful to fit the acceleration of an atomic cloud time-of-light fall, which can be compared to gravity.

F.1.1 Setting up a lens

In the pursuit of minimizing astigmatism and coma as much as possible, we have found it important to set the flat surface of plano-convex lenses as normally as possible to the direction of light propagation. By iterating between an iris/pinhole immediately after

the lens and a pinhole at some distance from the lens, affixed by a lens tube, we can ensure this. We have also found it useful to keep the flat surface of the lenses towards the middle of a telescope, in accordance with the Abbe sine criterion.

F.2 Imaging axes on the strontium machine

A full list of the specifications for each of our imaging axes may be found in Table 5.7. In Fig. F.1 are raw OD images of a red MOT 1 taken along each axis, with the direction of gravity and approximate direction of the oven indicated.[1] Note that the directions marked on the Andor assume that the beams all travel orthogonally to each other. The lattice and ODT are measured to be orthogonal to within 0.5°, so those axes have been used to calibrate the direction of the slower axis. Every other beam is referenced to the slower axis.

[1] I am 100% sure of the directions indicated for the Andor, Lattice, and Tight Trap axes; I am 85% sure of the directions indicated for the ODT and XODT.

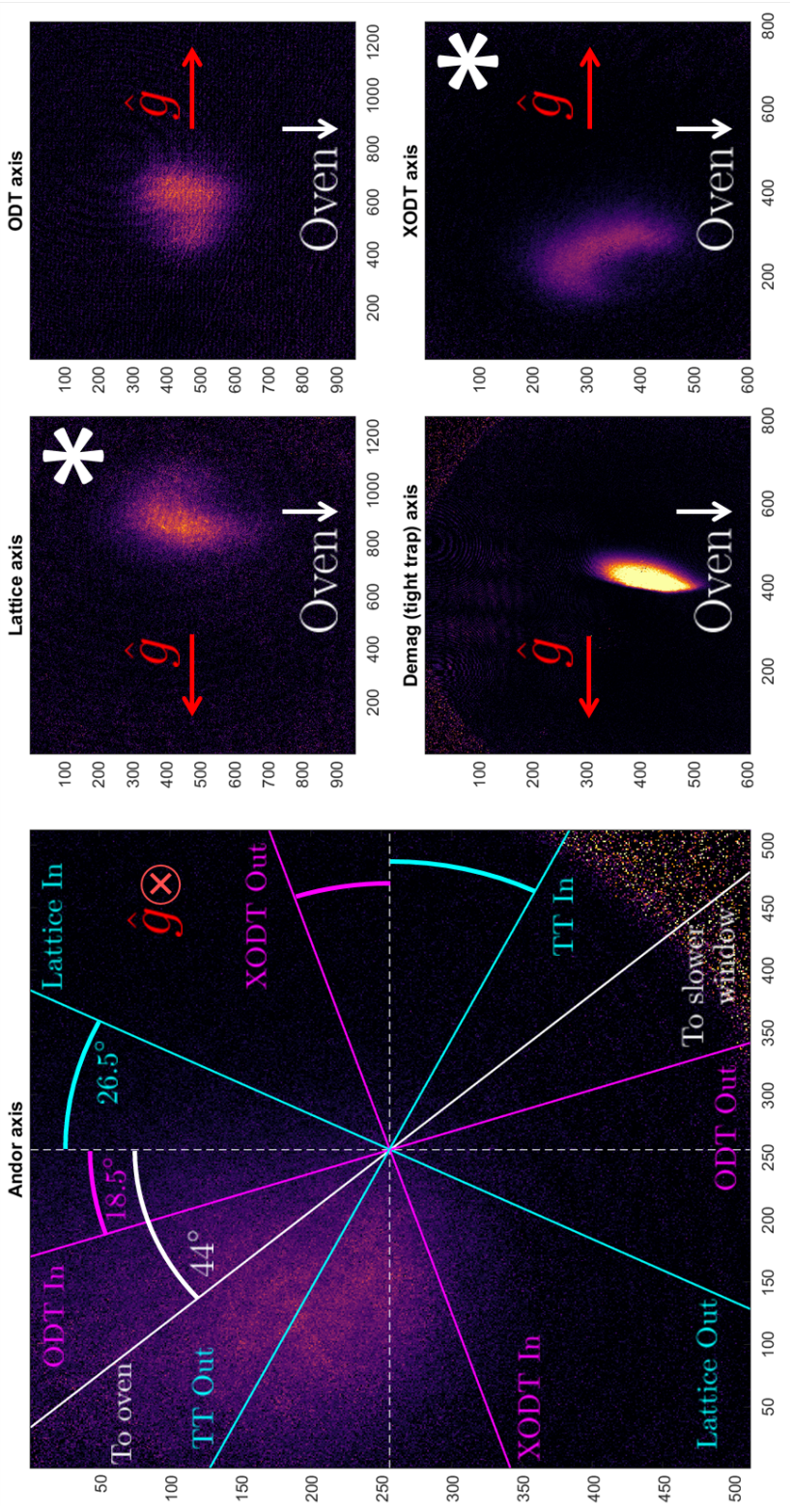

Figure F.1: This figure shows OD images of an RM1 along each imaging axis. Note that the "tight trap in" direction marks the camera side of the chamber for that imaging axis, while the "out" directions correspond to the camera positions for the other axes. The images marked with an asterisk indicate that the image is flipped horizontally over the gravity axis compared to real space. This happens because they have an odd number of mirrors in the beam path.

Appendix G

Mainchamber Drawings

In this appendix, you will find technical drawings for the following parts:

- Lithium main chamber (5 pages)
- Lithium bucket windows (2 pages)
- Lithium breadboards (4 pages)
- Strontium main chamber (4 pages)
- Strontium breadboards (4 pages).

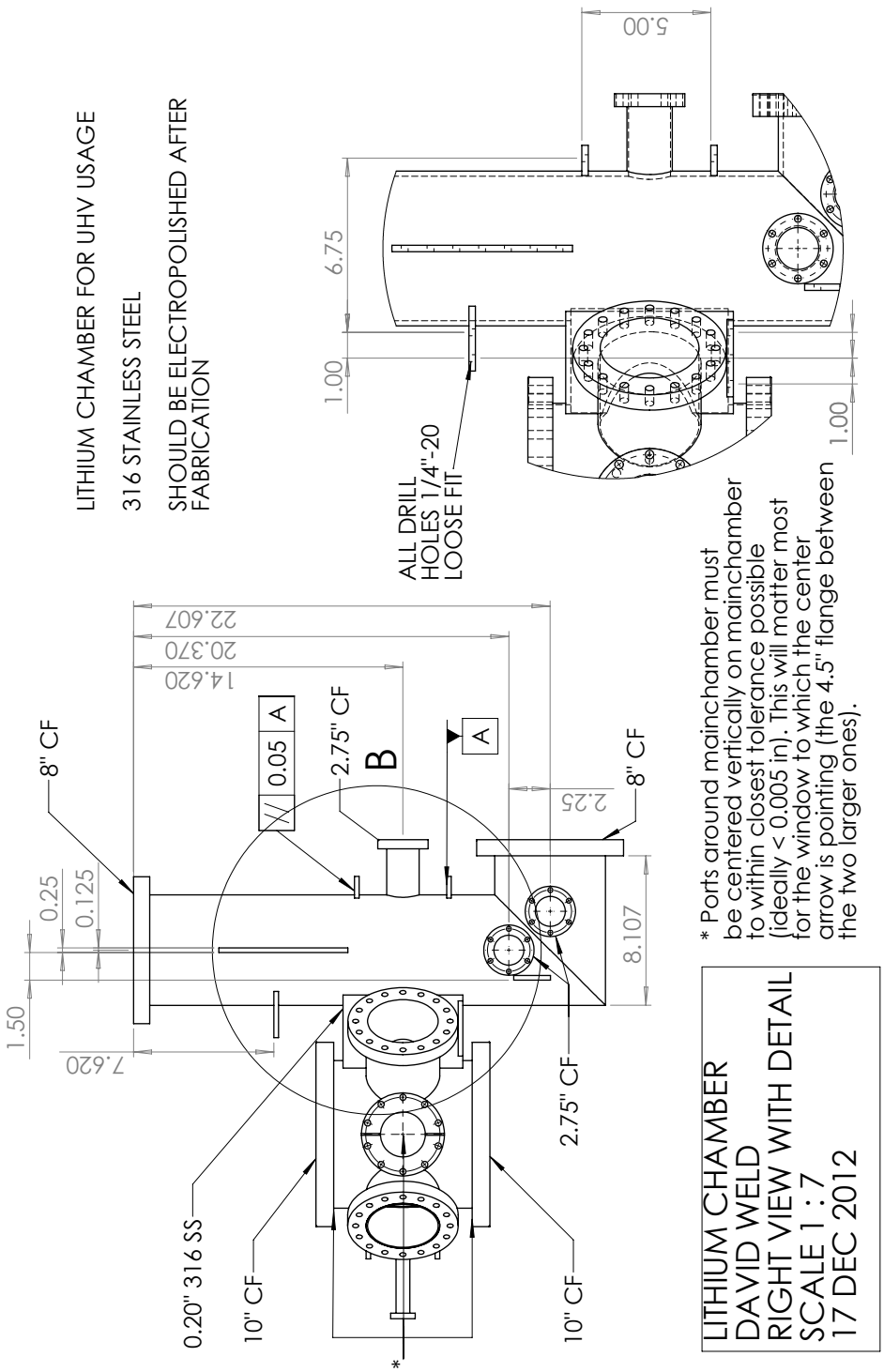

Figure G.1: Lithium main chamber page 1

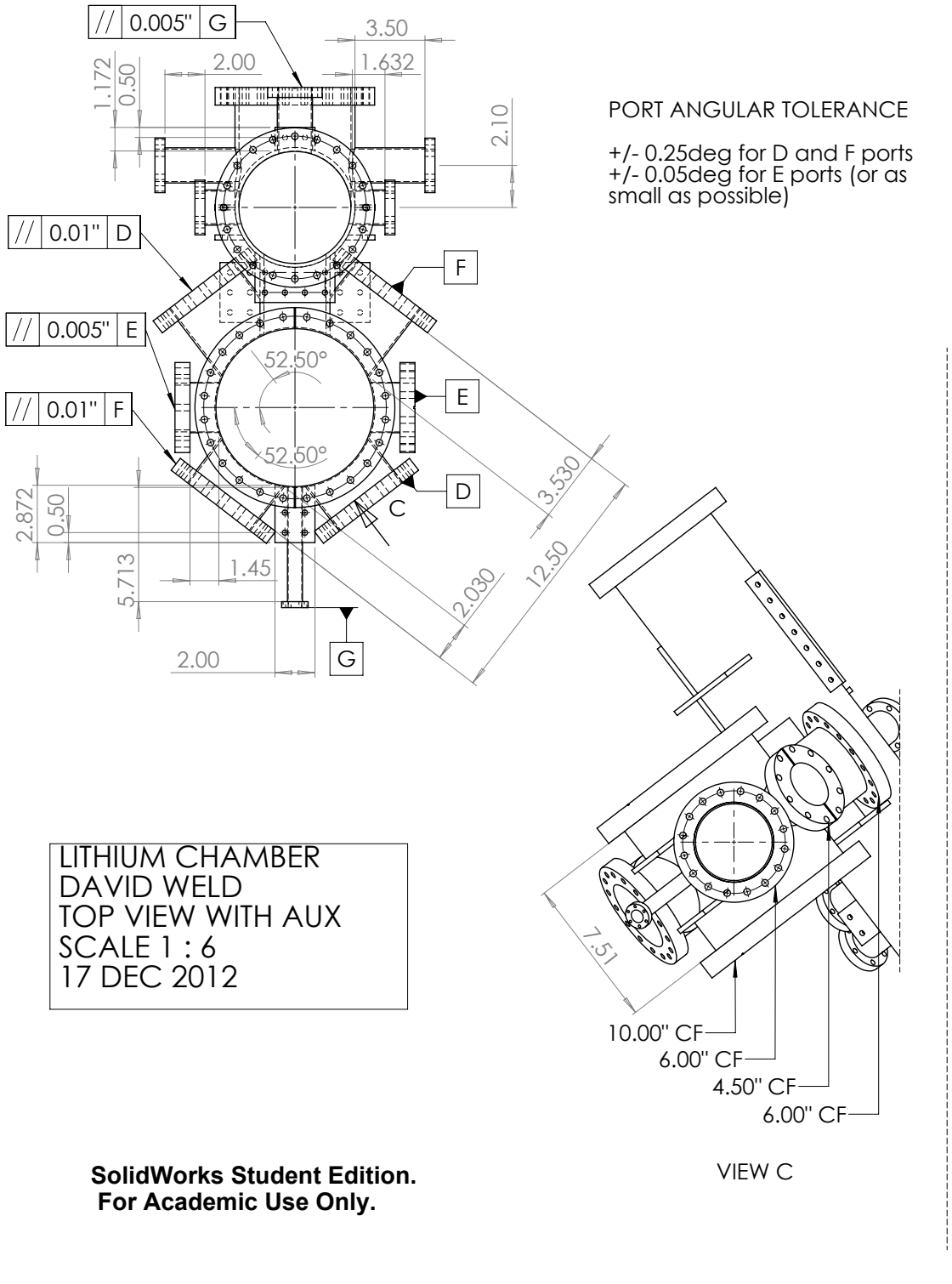

Figure G.2: Lithium main chamber page 2

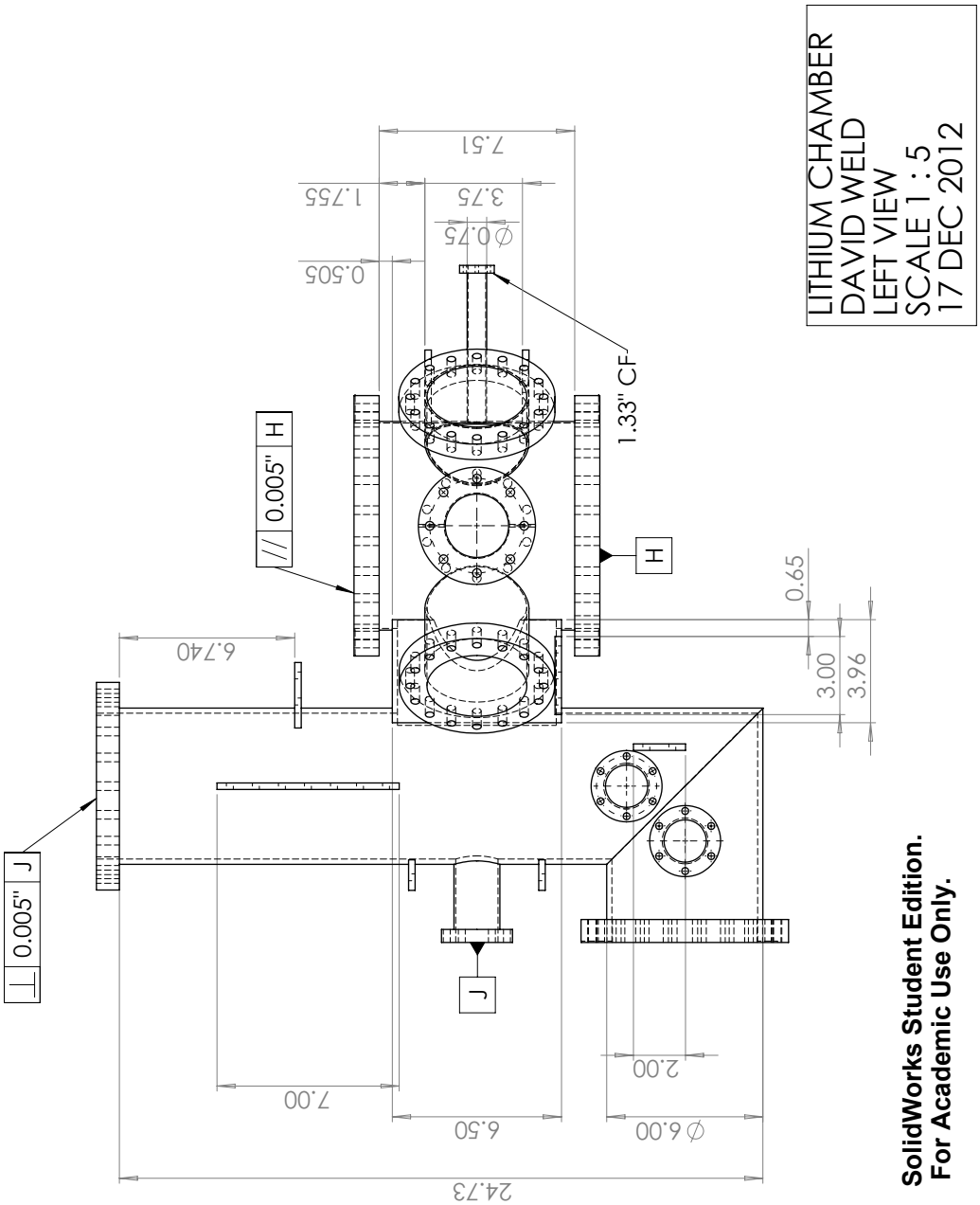

Figure G.3: Lithium main chamber page 3

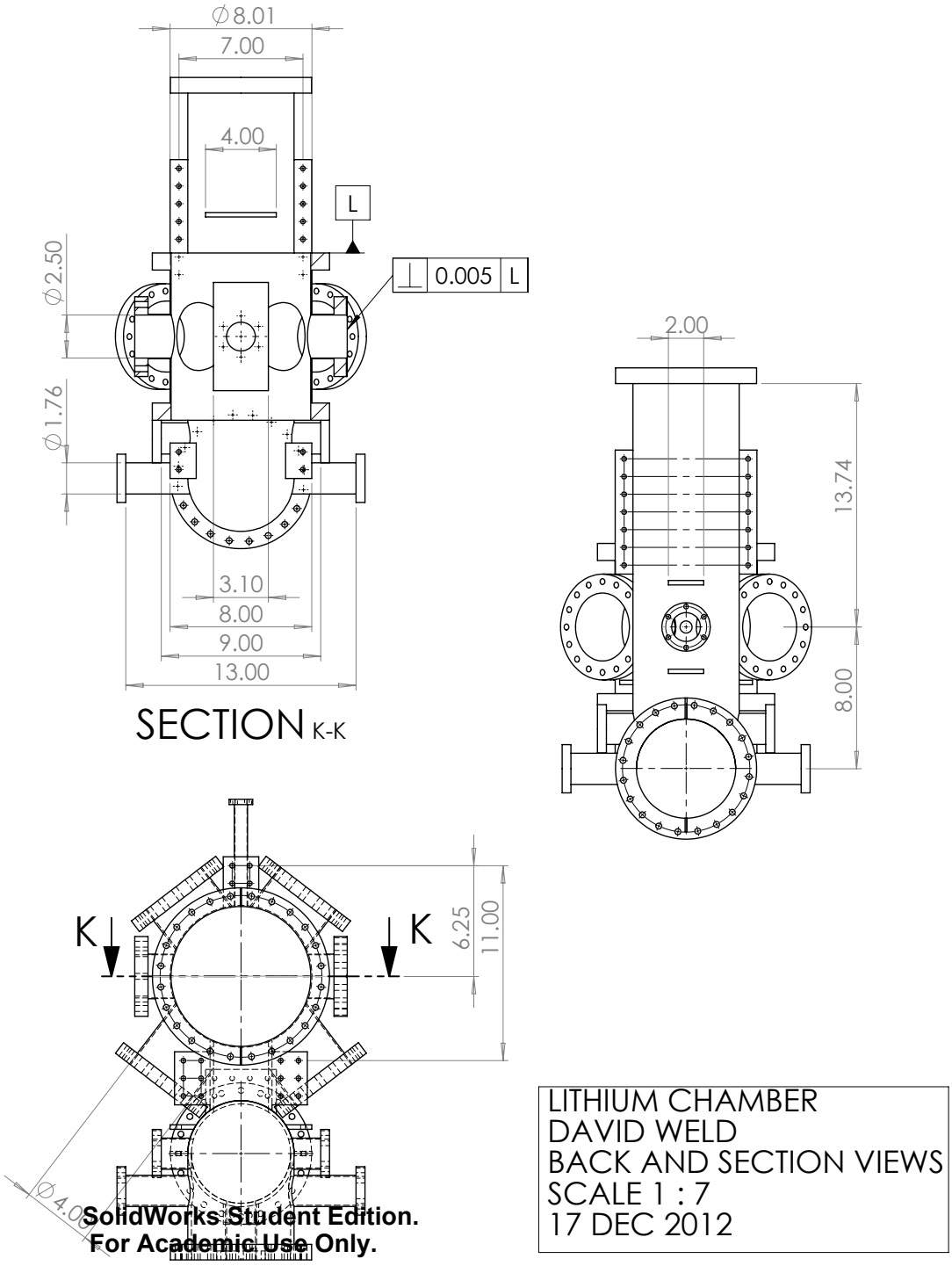

Figure G.4: Lithium main chamber page 4

Figure G.5: Lithium main chamber page 5

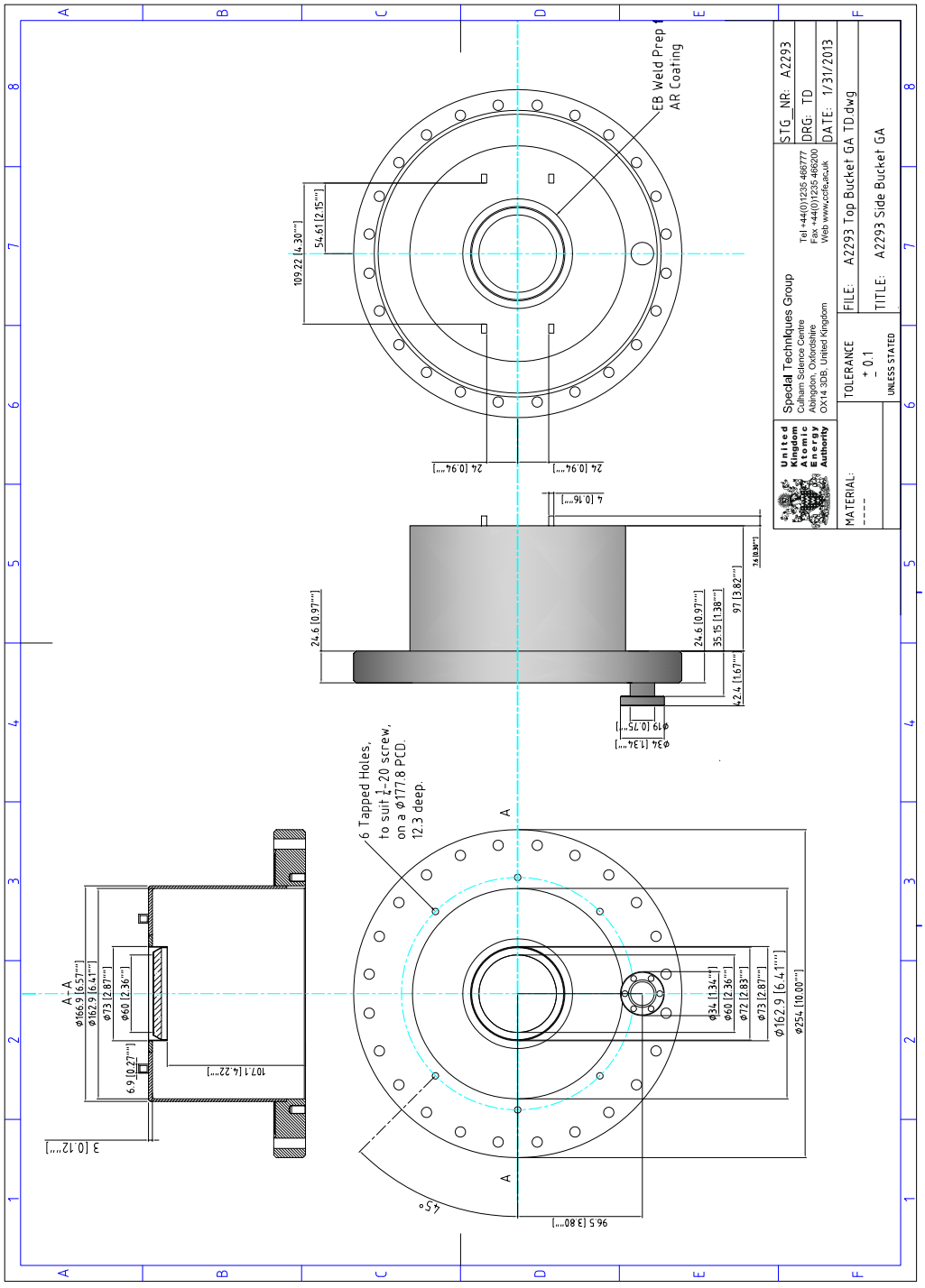

Figure G.6: Lithium top bucket technical drawing

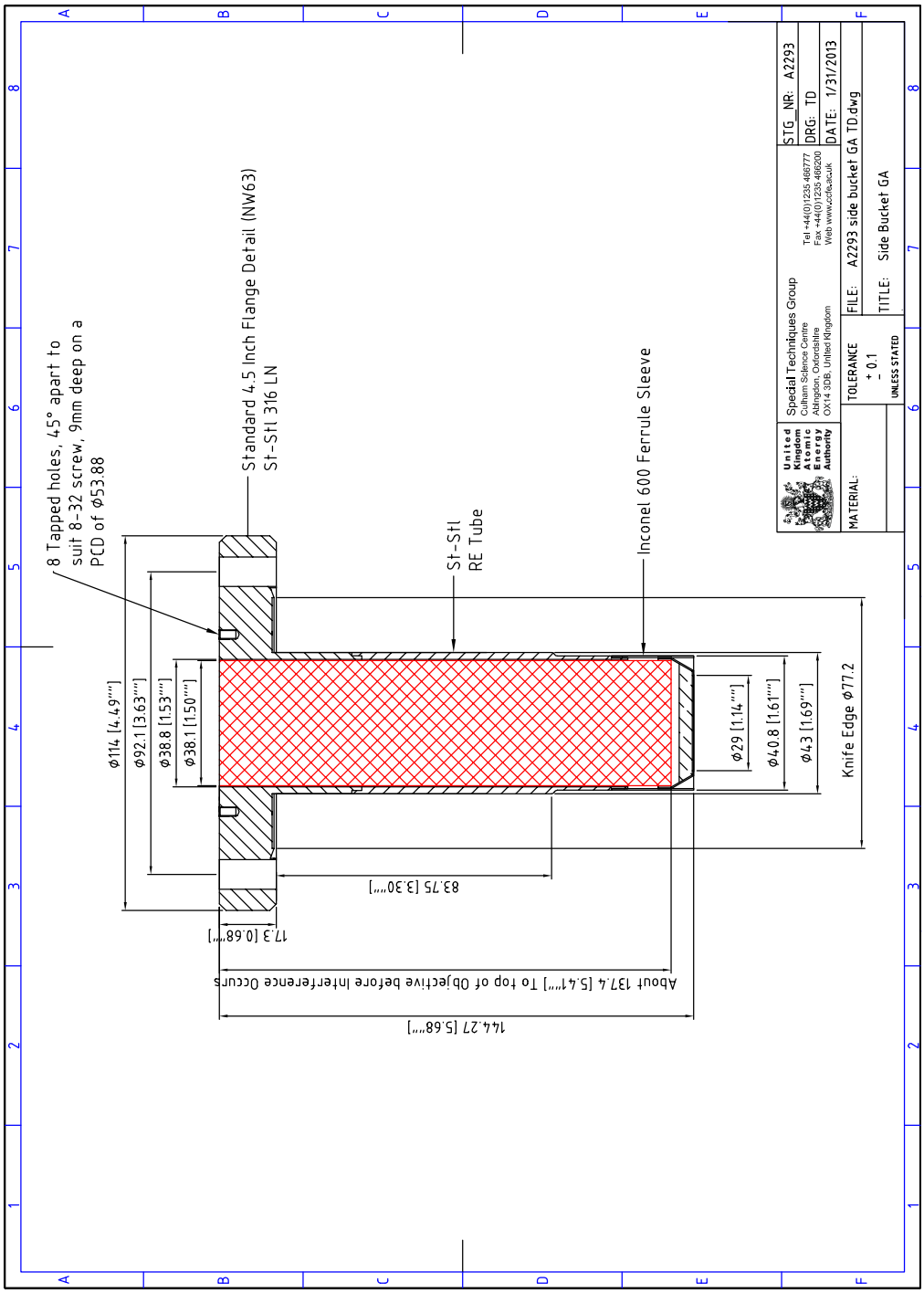

Figure G.7: Lithium side bucket technical drawing

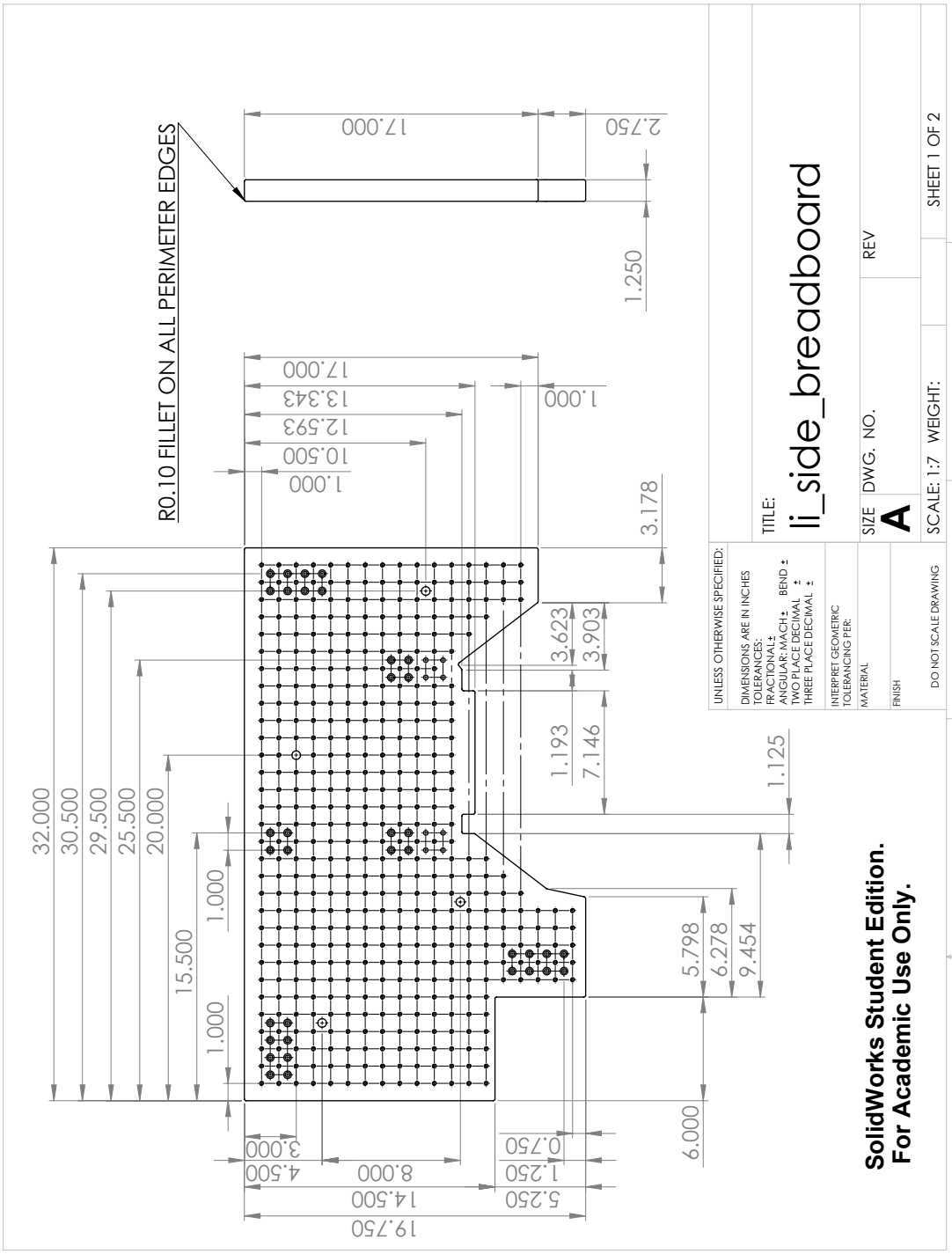

Figure G.8: Lithium side breadboard 1 technical drawing

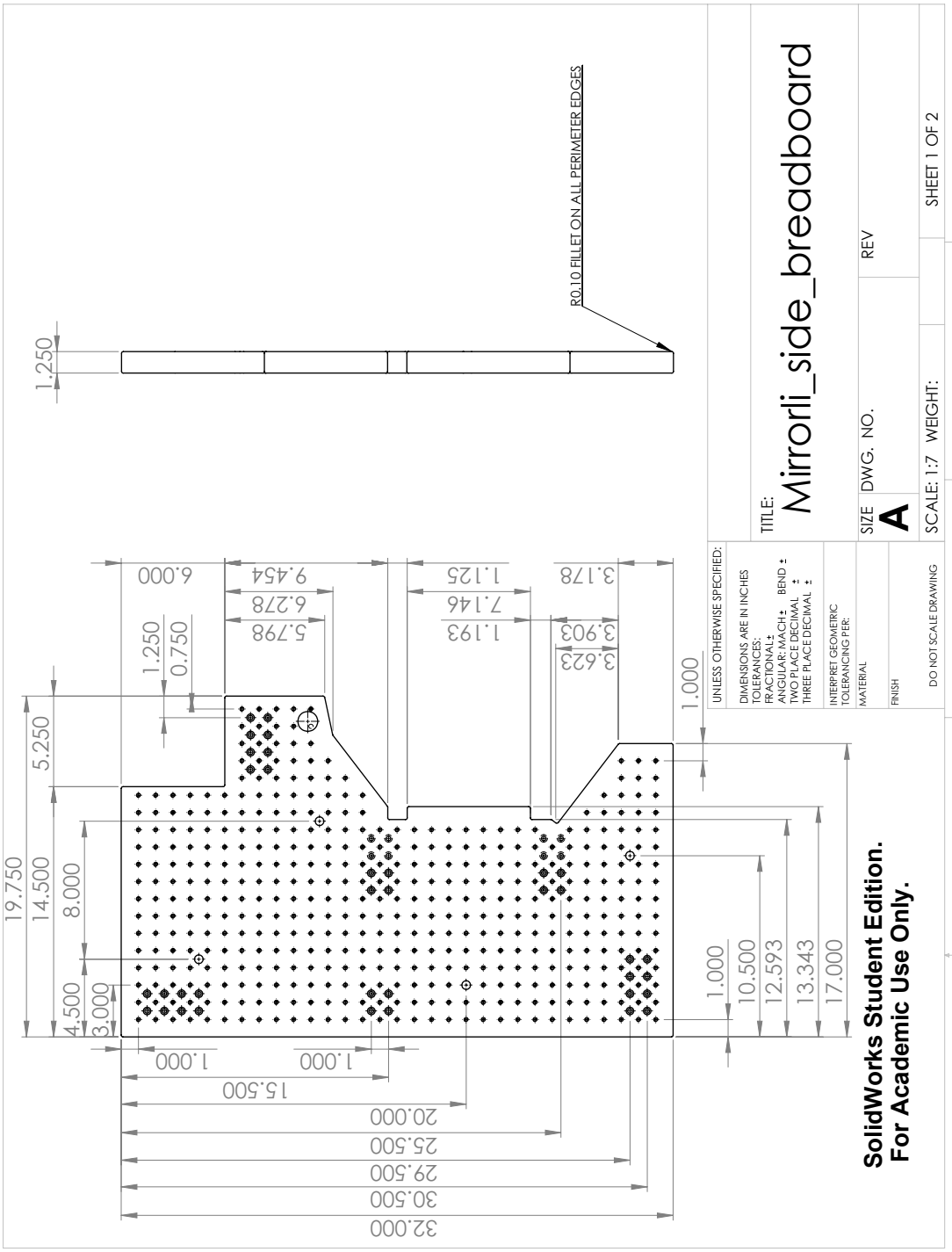

Figure G.9: Lithium side breadboard 2 technical drawing

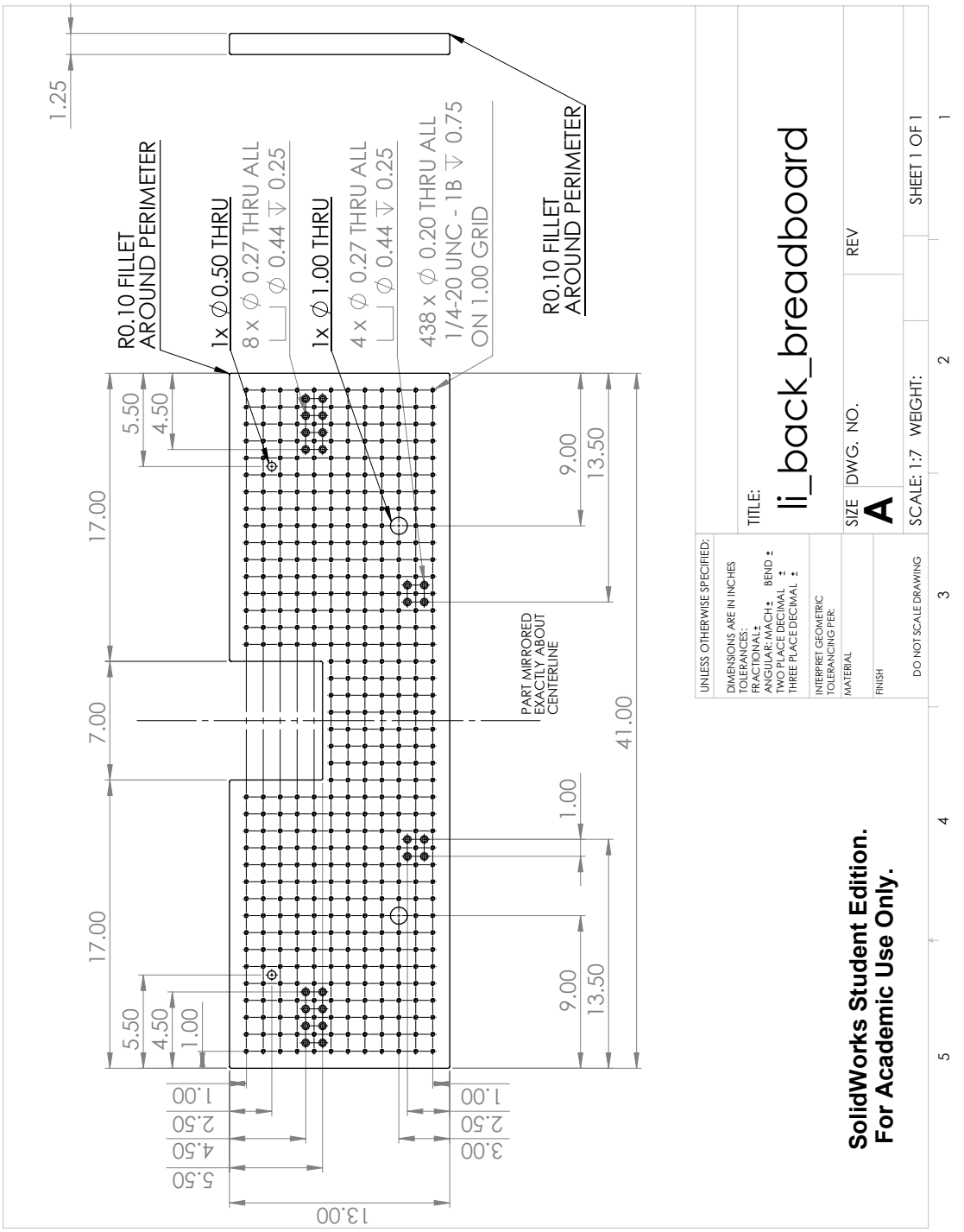

Figure G.10: Lithium back breadboard technical drawing

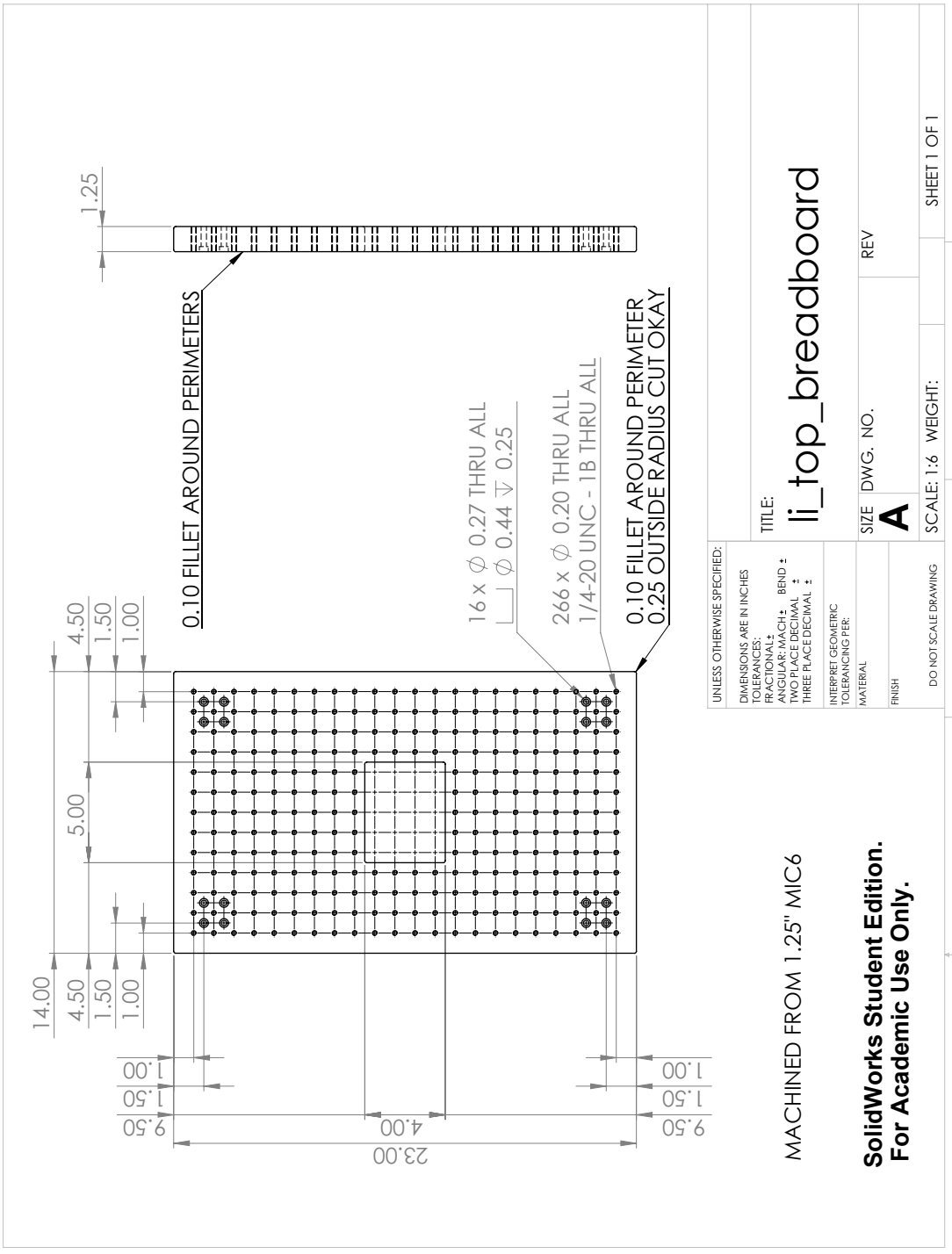

Figure G.11: Lithium top breadboard technical drawing

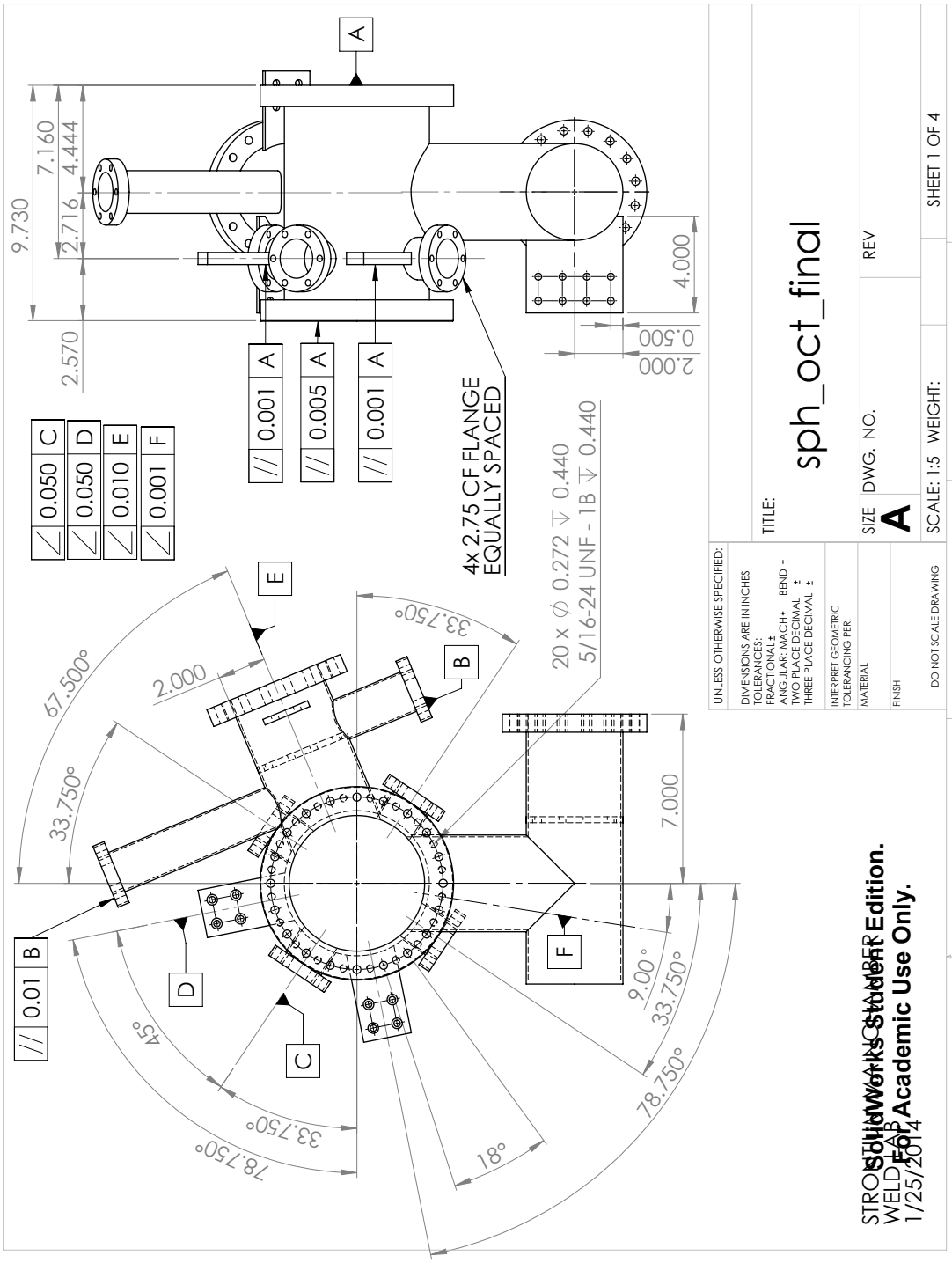

Figure G.12: Strontium main chamber page 1

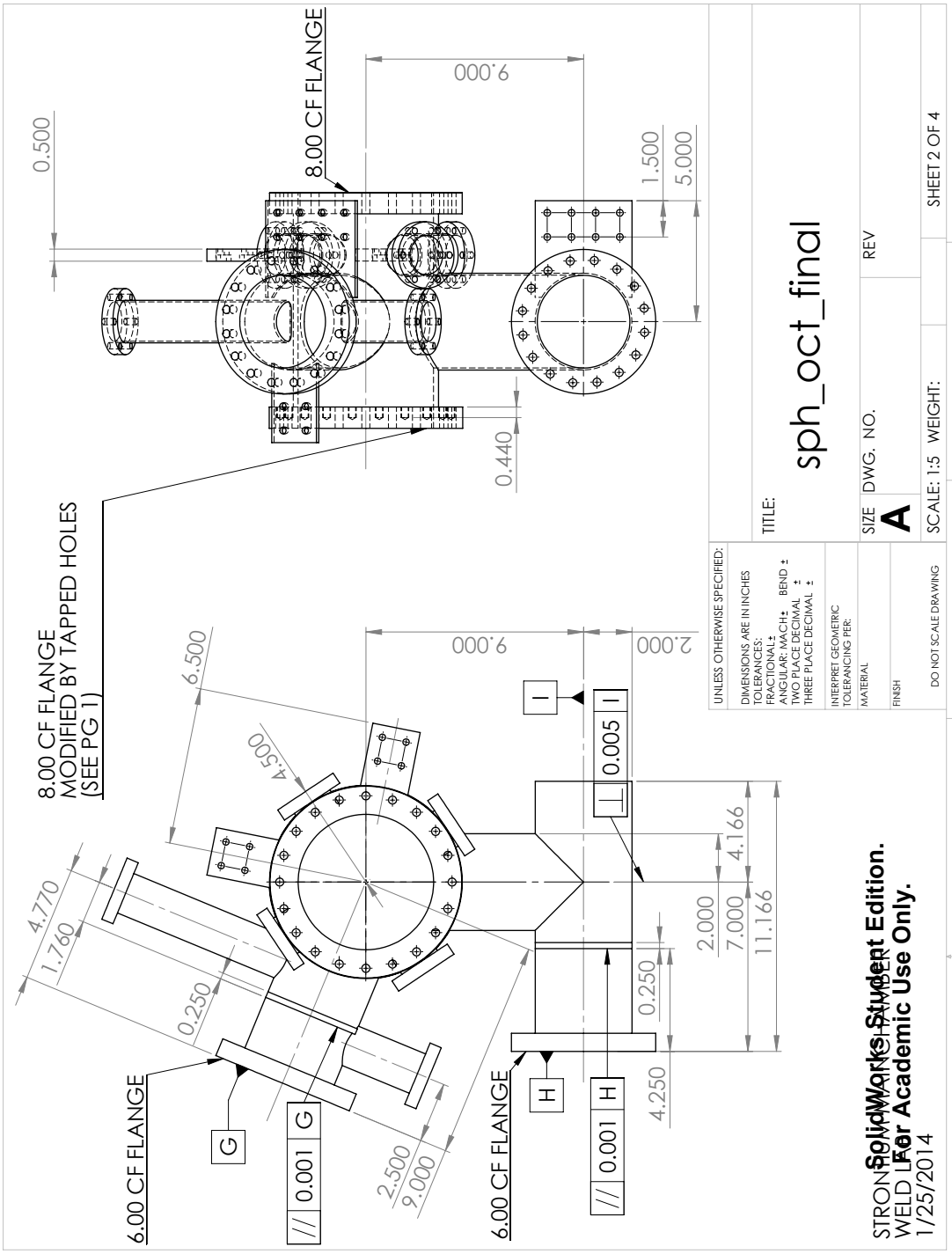

Figure G.13: Strontium main chamber page 2

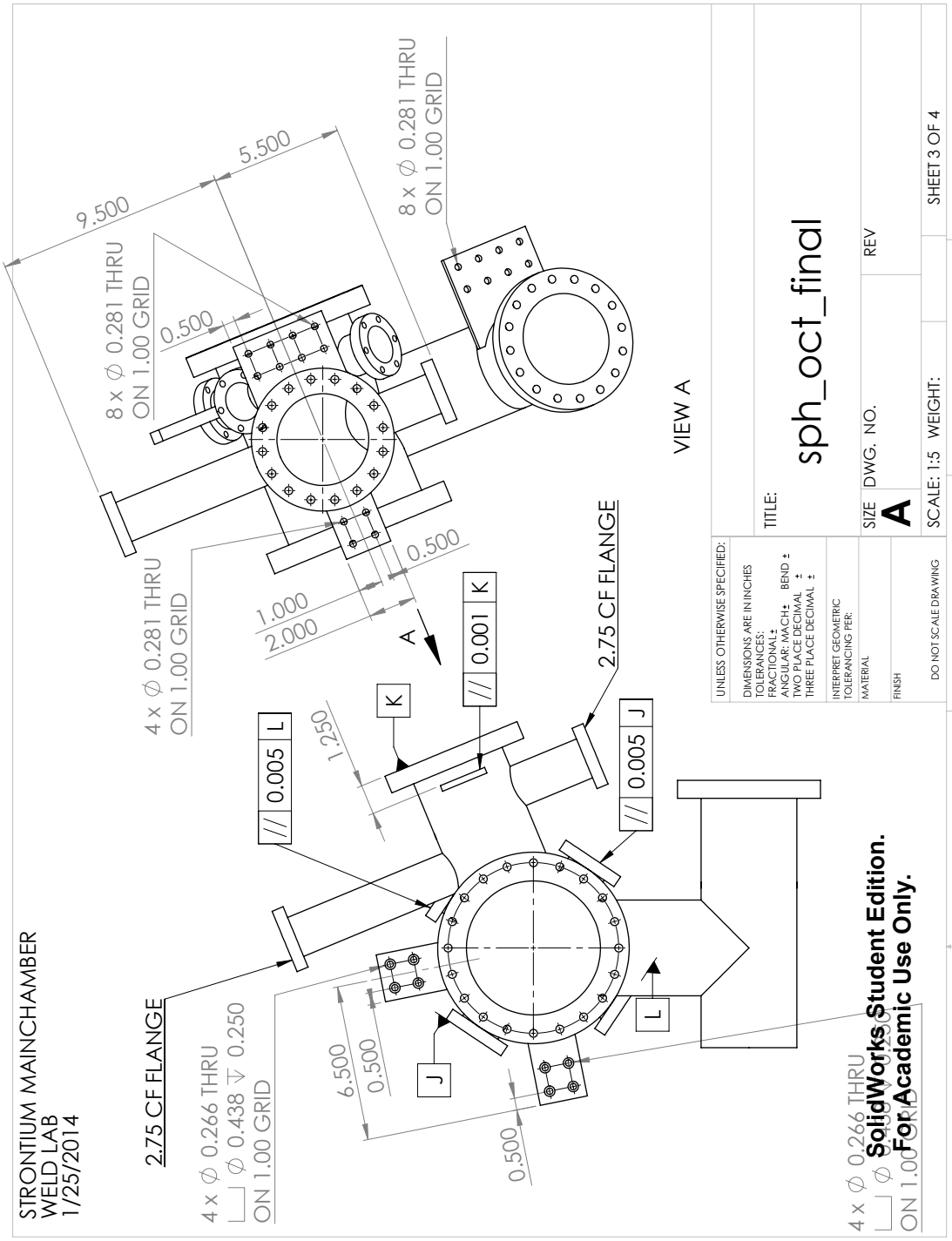

Figure G.14: Strontium main chamber page 3

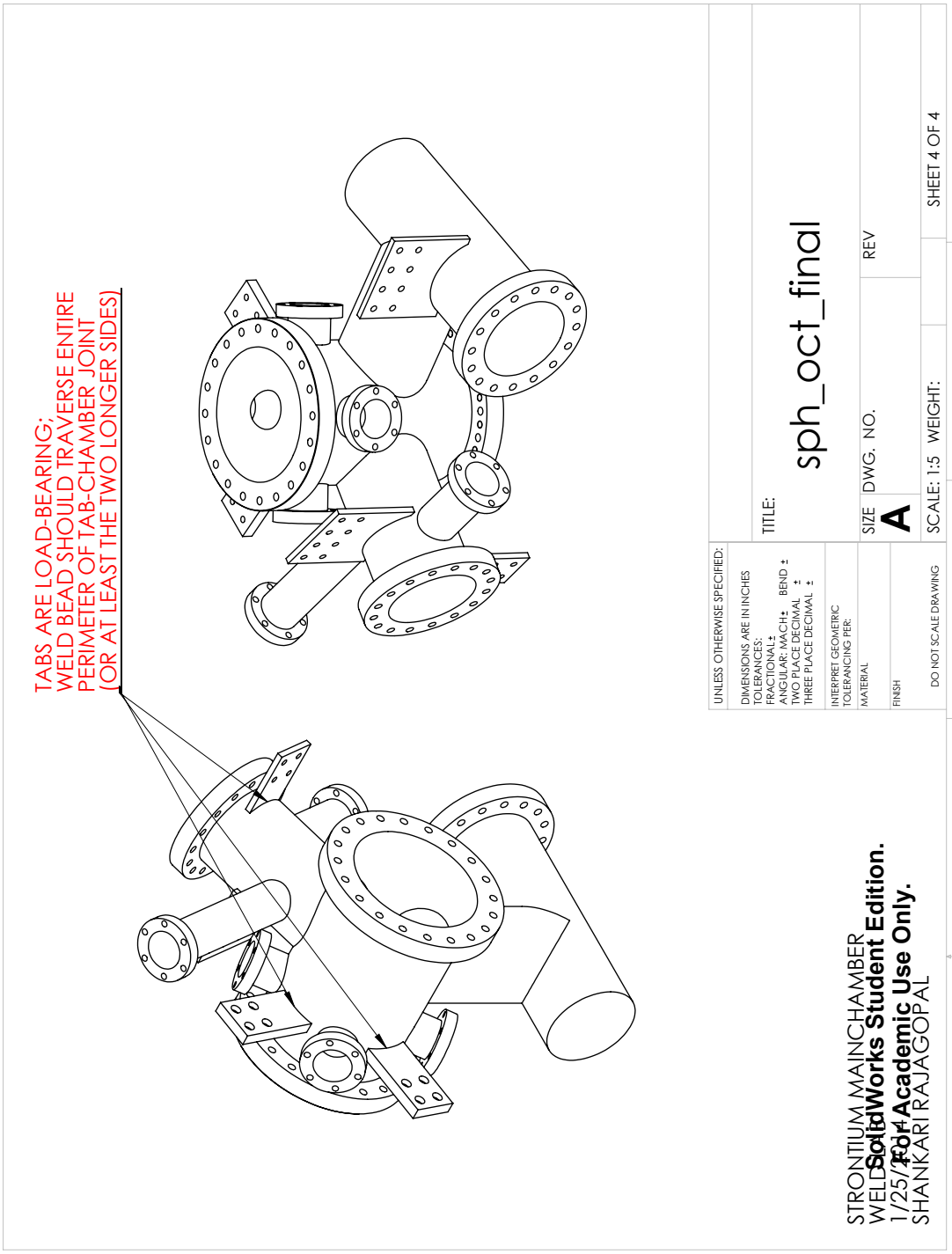

Figure G.15: Strontium main chamber page 4

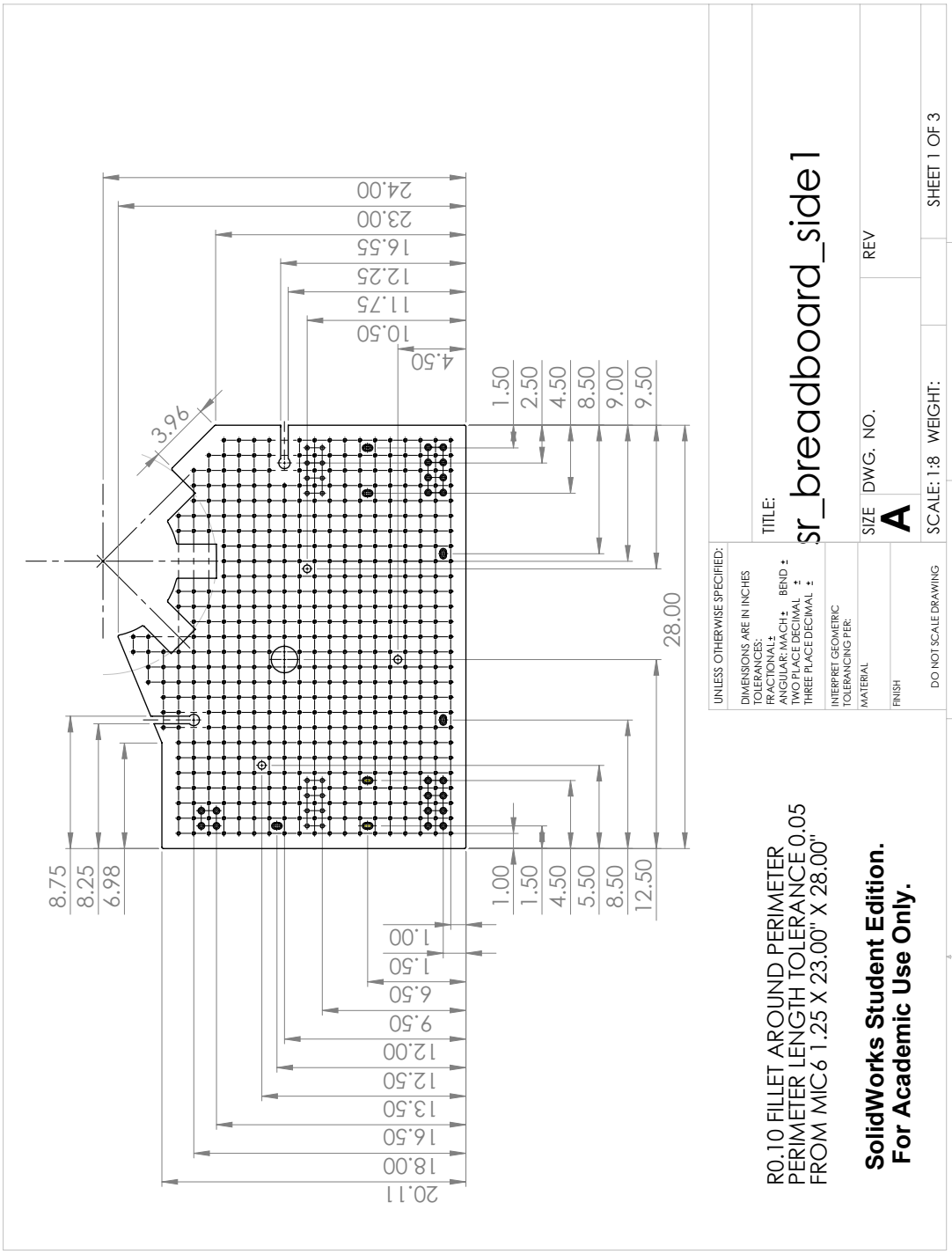

Figure G.16: Strontium side breadboard 1 technical drawing

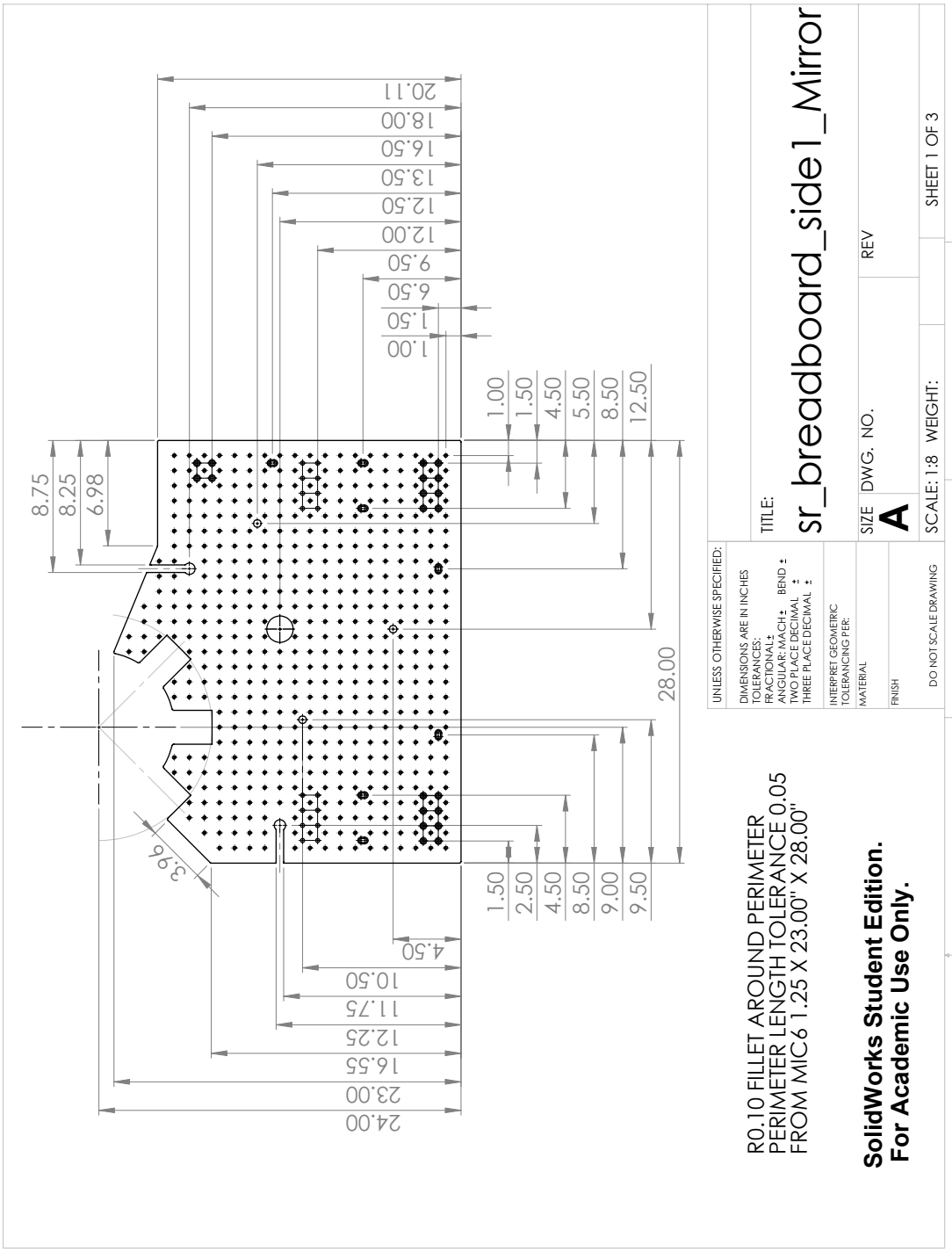

Figure G.17: Strontium side breadboard 2 technical drawing

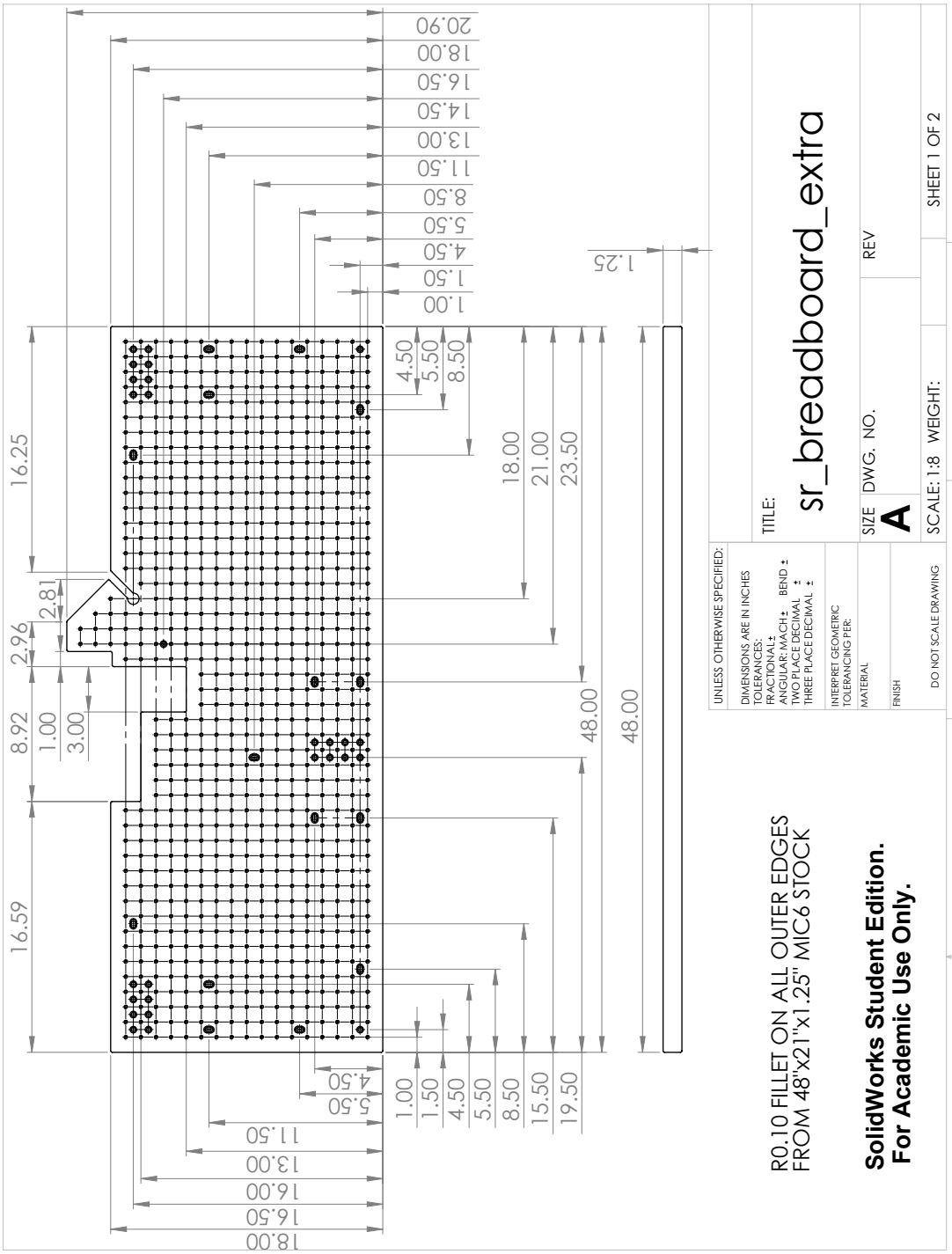

Figure G.18: Strontium back breadboard technical drawing

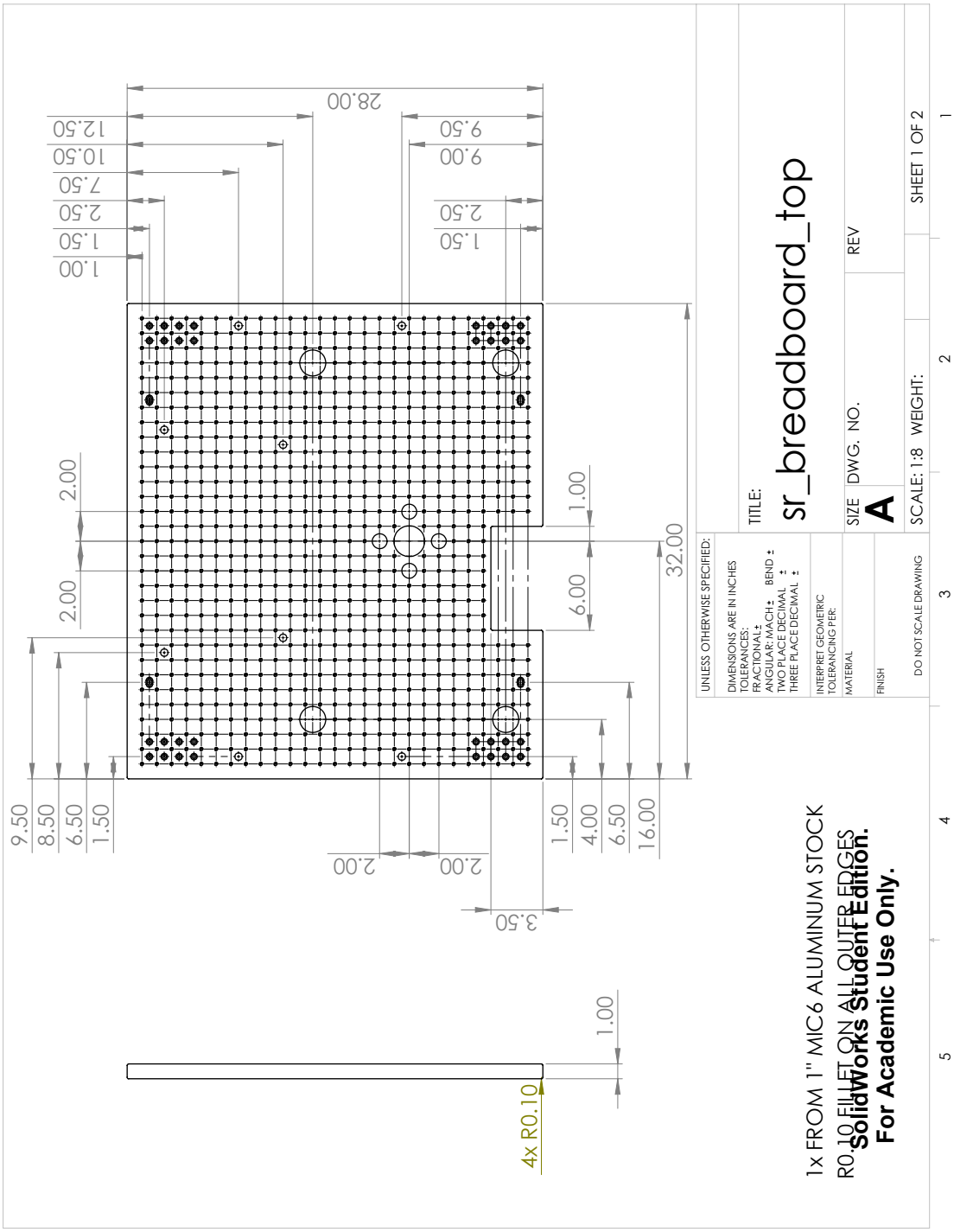

Figure G.19: Strontium top breadboard technical drawing

Appendix H

Viewport AR Curves

In this appendix, you will find theoretical AR curves provided by various companies for the following:

- Lithium main chamber side viewports (coated by Lesker).
- Lithium bucket windows (coated by UKAEA).
- Strontium main chamber side viewports (coated by Optical Filter Source (OFS)).
- Strontium QGM side viewports (coated by OFS, purchased but need to order 2 replacement 2.75" CF viewports).
- Strontium QGM bucket windows (curves from OFS, not yet purchased).
- Strontium QGM bucket windows at low incident angles from the normal (curves from OFS, not yet purchased).
- Strontium QGM bucket windows at high incident angles from the normal, since we have been considering 1064 nm shallow-angle reflection for transport and loading (curves from OFS, not yet purchased).

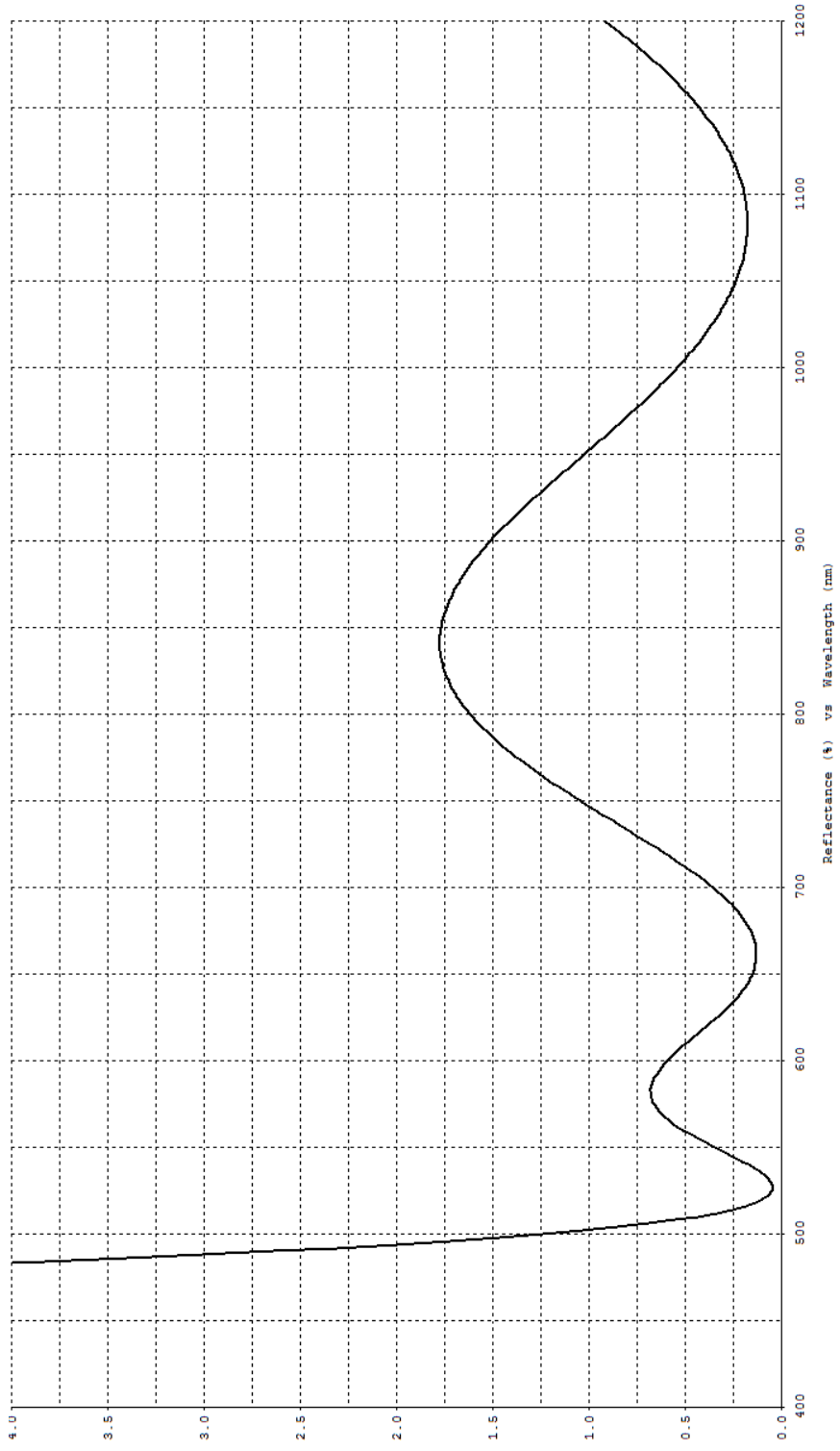

Figure H.1: AR curves for Lesker side windows on lithium main chamber. Reflects the coatings we received rather than those we ordered.

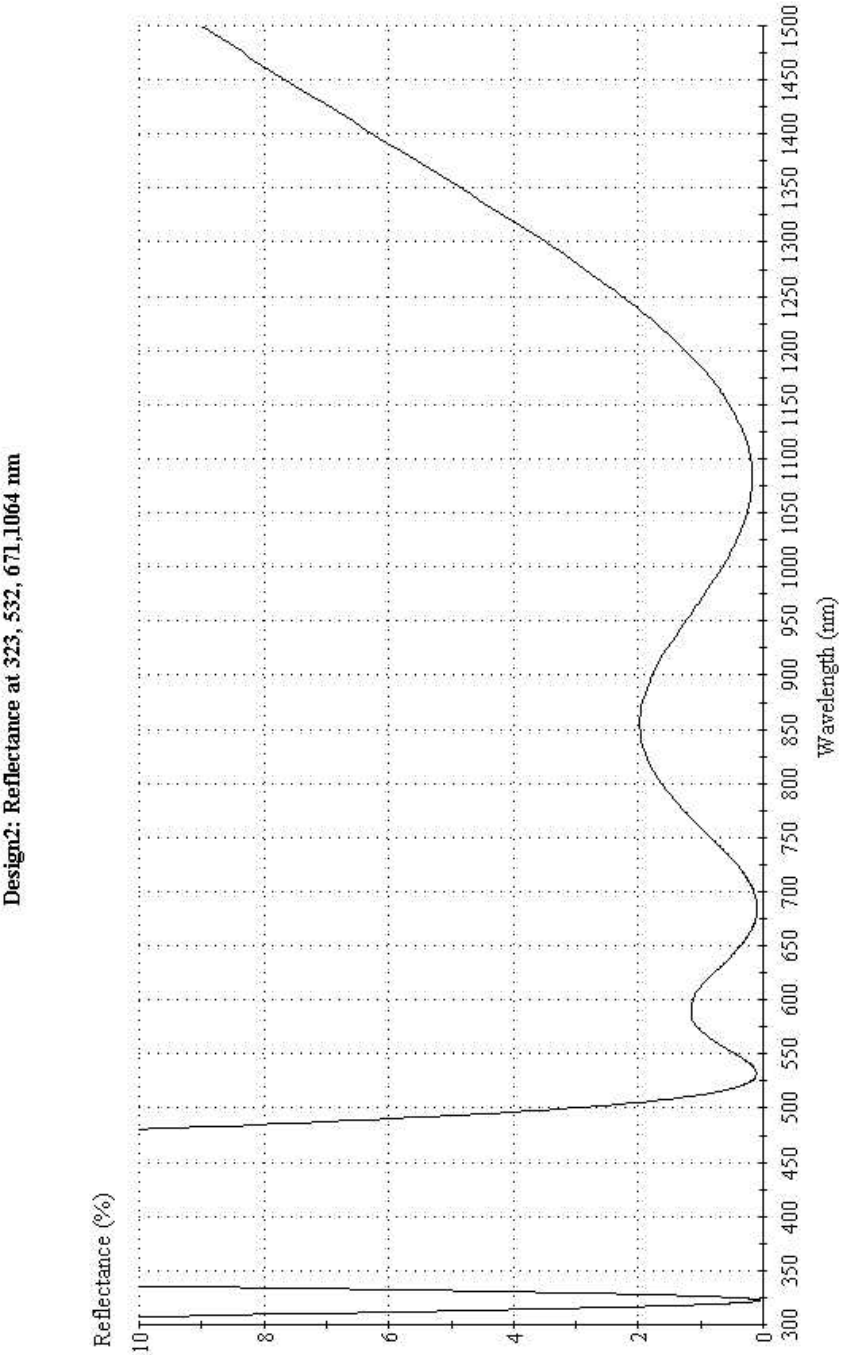

Figure H.2: AR curves for UKAEA bucket windows on lithium main chamber.

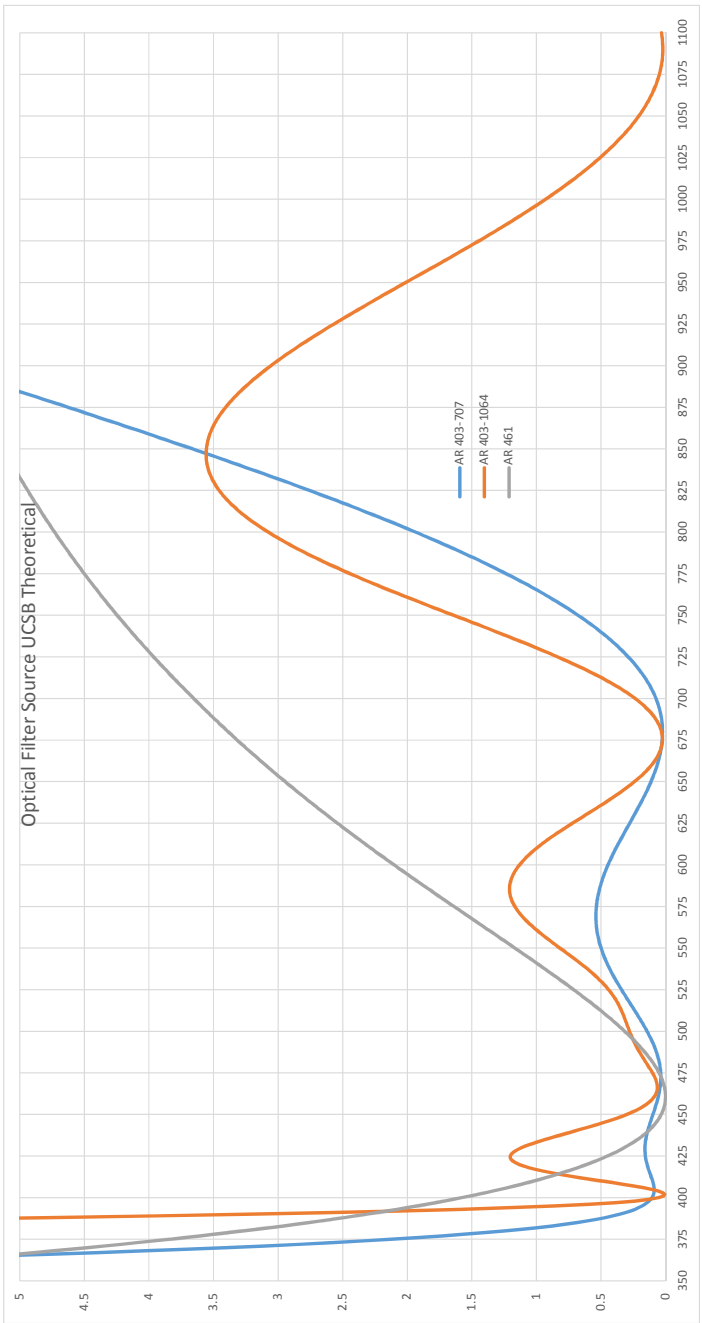

Figure H.3: AR curves for OFS coatings on strontium main chamber. We ordered the orange option.

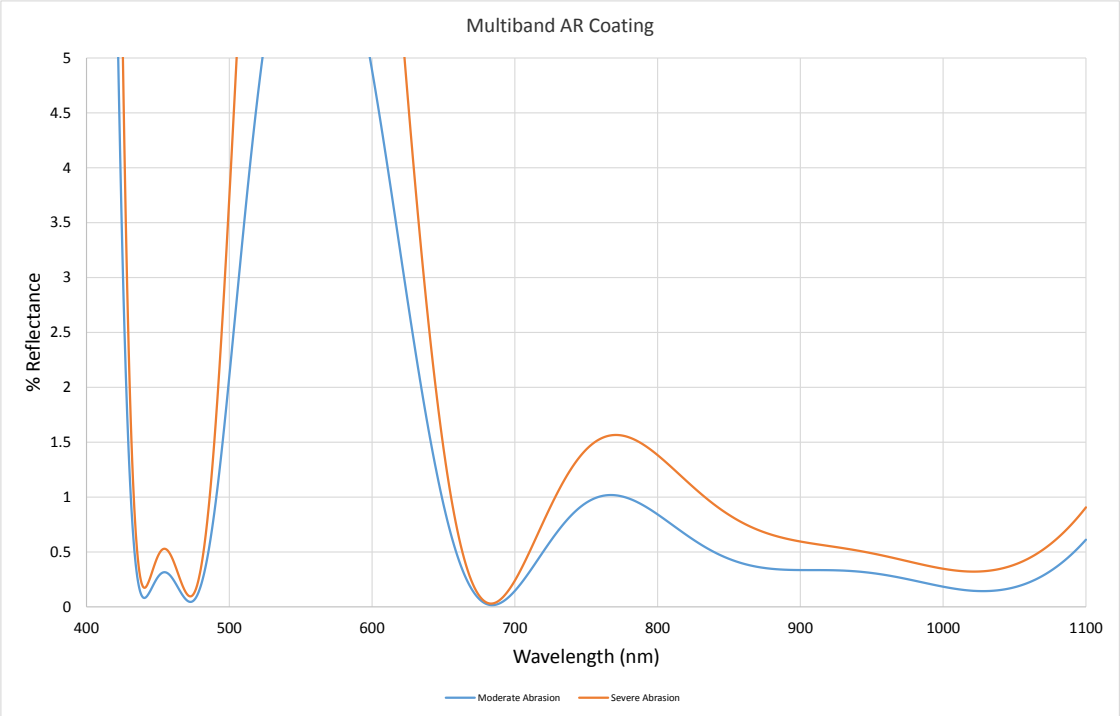

Figure H.4: AR curves for OFS coatings for strontium QGM side viewports. These were ordered, but two were stolen for a rebuild of the strontium oven transverse cooling section and have not been replaced. We ordered the orange (severe abrasion-resistant) version.

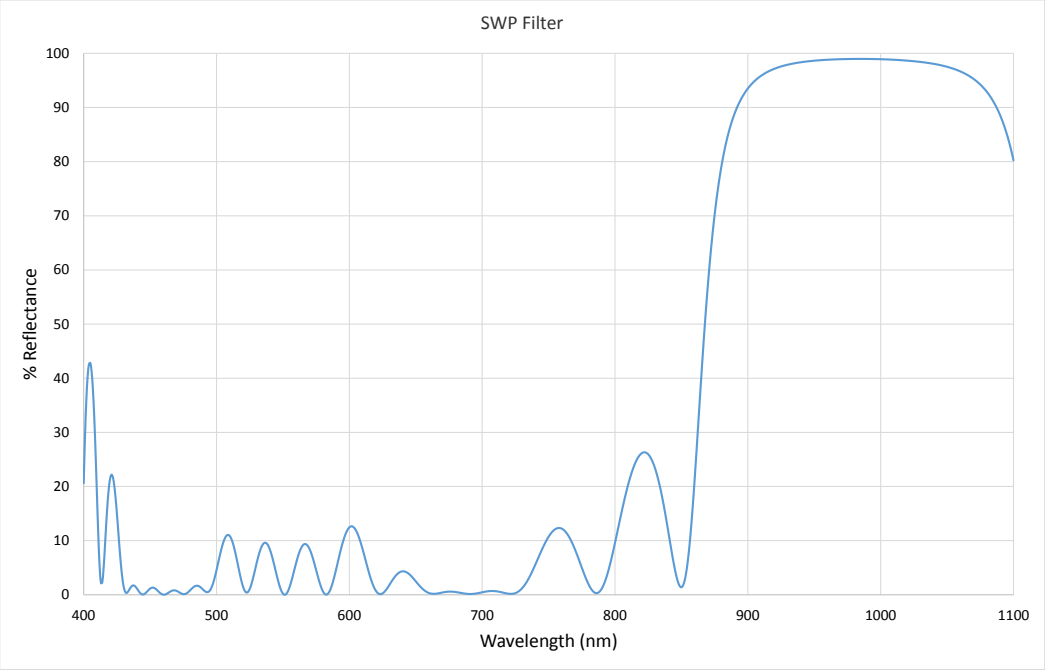

Figure H.5: AR curves for OFS coatings for strontium QGM bucket windows. These have not yet been ordered.

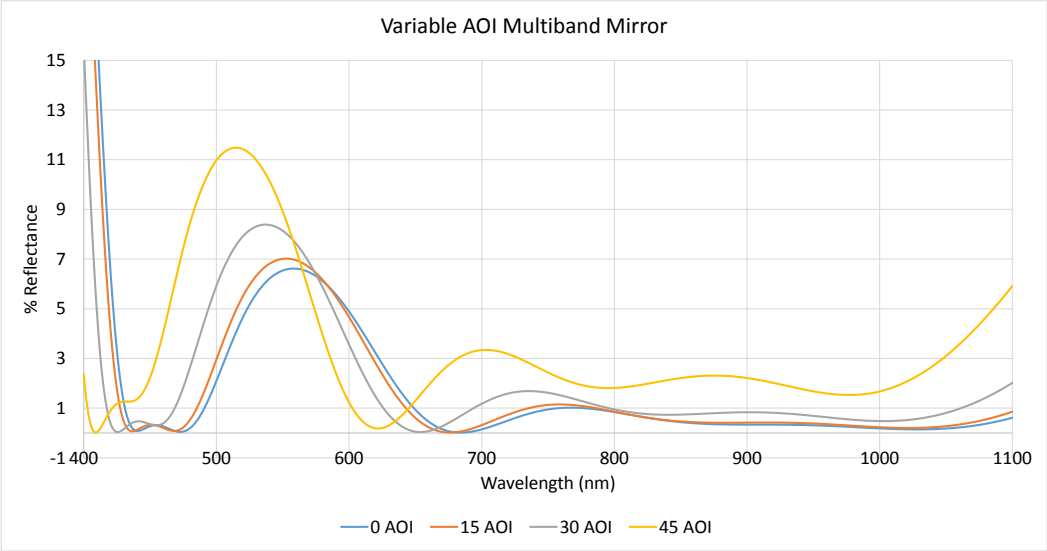

Figure H.6: AR curves for OFS coatings for strontium QGM bucket windows at various low angles from the normal (0 degrees).

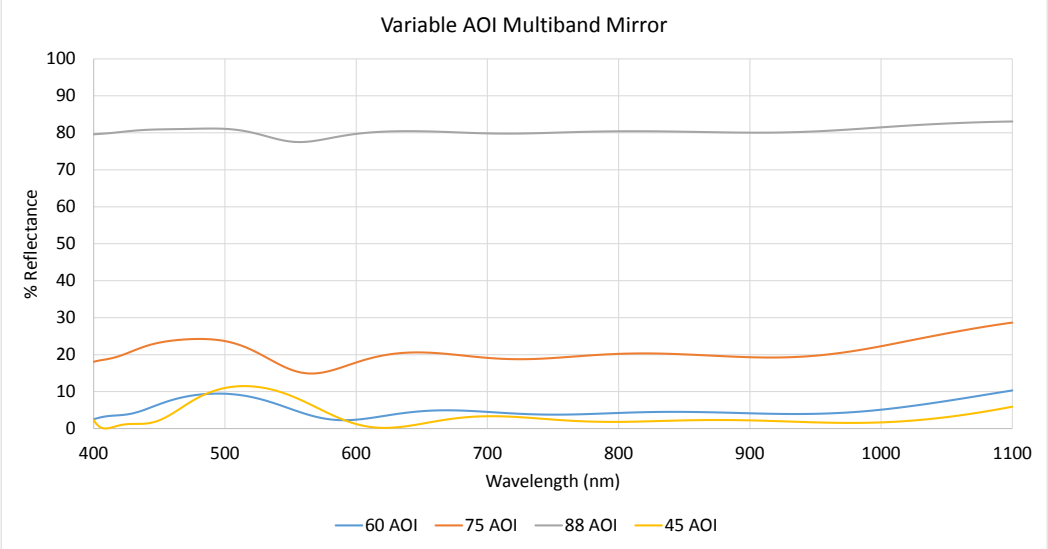

Figure H.7: AR curves for OFS coatings for strontium QGM bucket windows at various high angles from the normal (0 degrees). These curves predict s-polarization values; p-polarization can vary from 0 to 15% from these.

Appendix I

Other Custom Part Drawings

In this appendix, you will find technical drawings for several custom-designed parts that we use on the strontium machine:

- Viewport caps for MOT cagemounted optics (2 pages)
- MOT coil supports (2 pages)
- Jig for the Andor camera front face (1 page)
- Imaging jig to connect our vertical objective lens to the top breadboard via a 1" cagemount system (1 page)
- The current 689 nm spectroscopy cell design, as well as an improved one for the next iteration (2 pages)
- Supports for the strontium oven and slower (5 pages)
- Feet to interface between 80/20 supports and the optical table (4 pages).

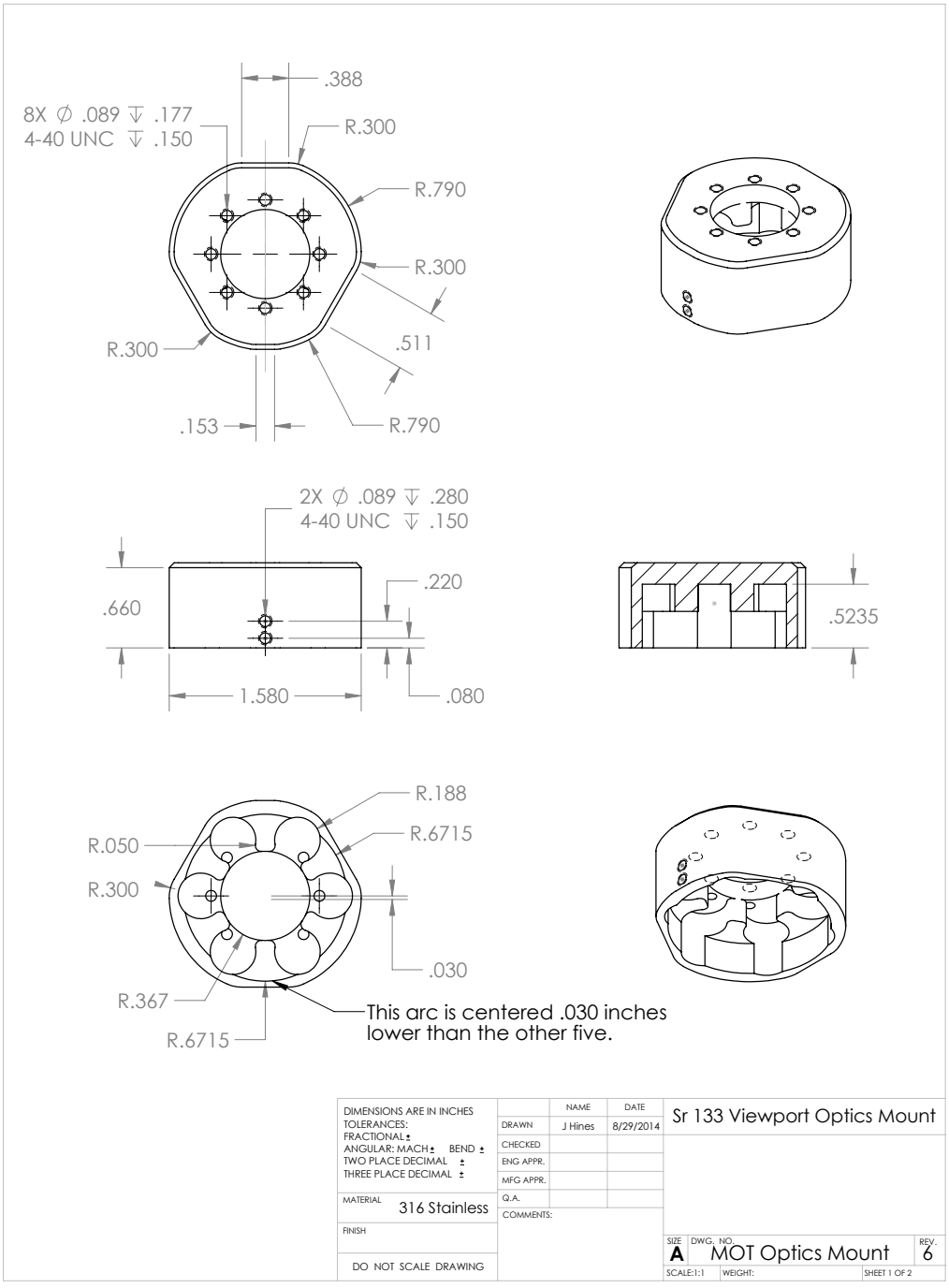

Figure I.1: Strontium cage-mounted MOT cap

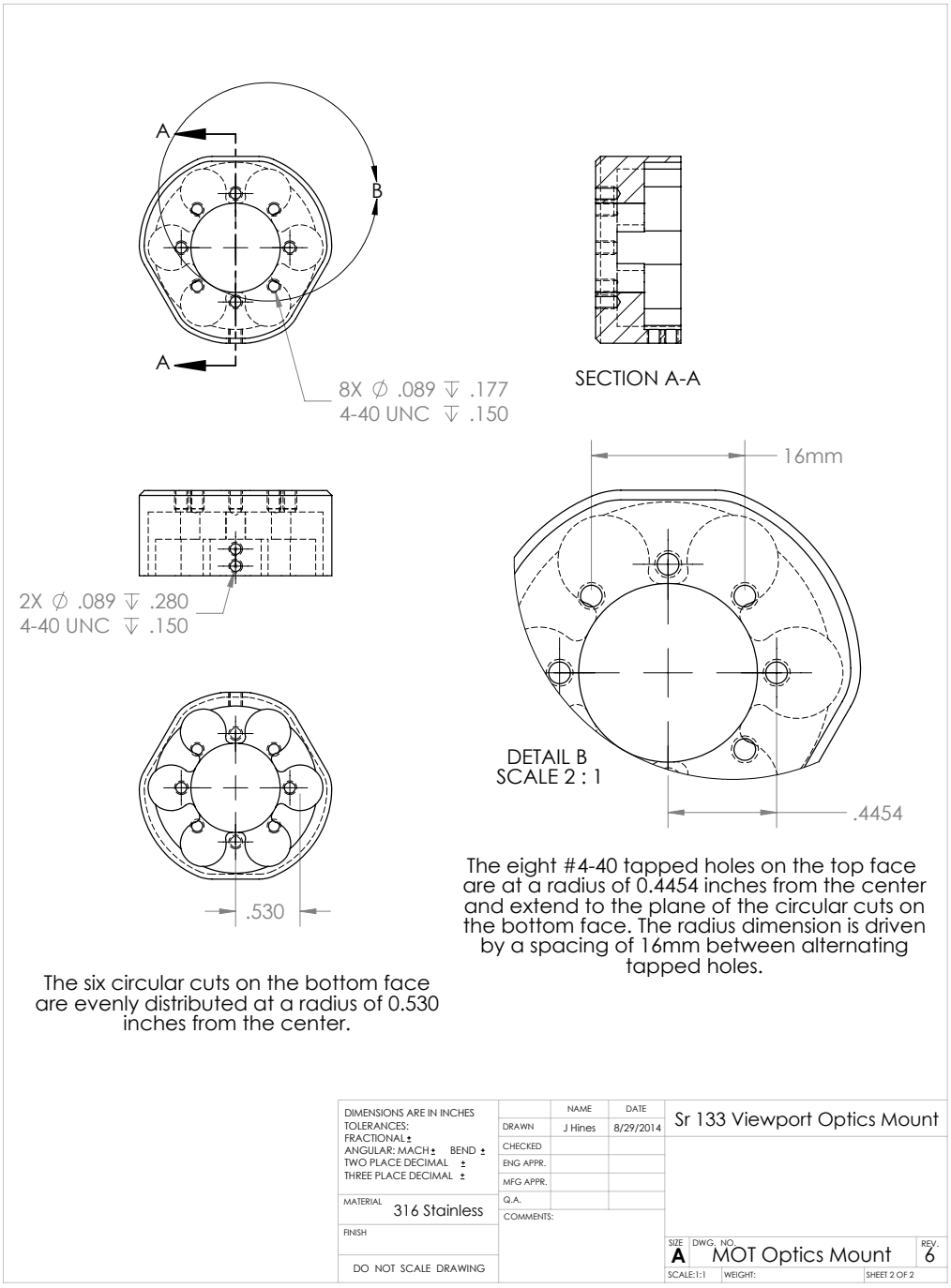

Figure I.2: Strontium cage-mounted MOT cap

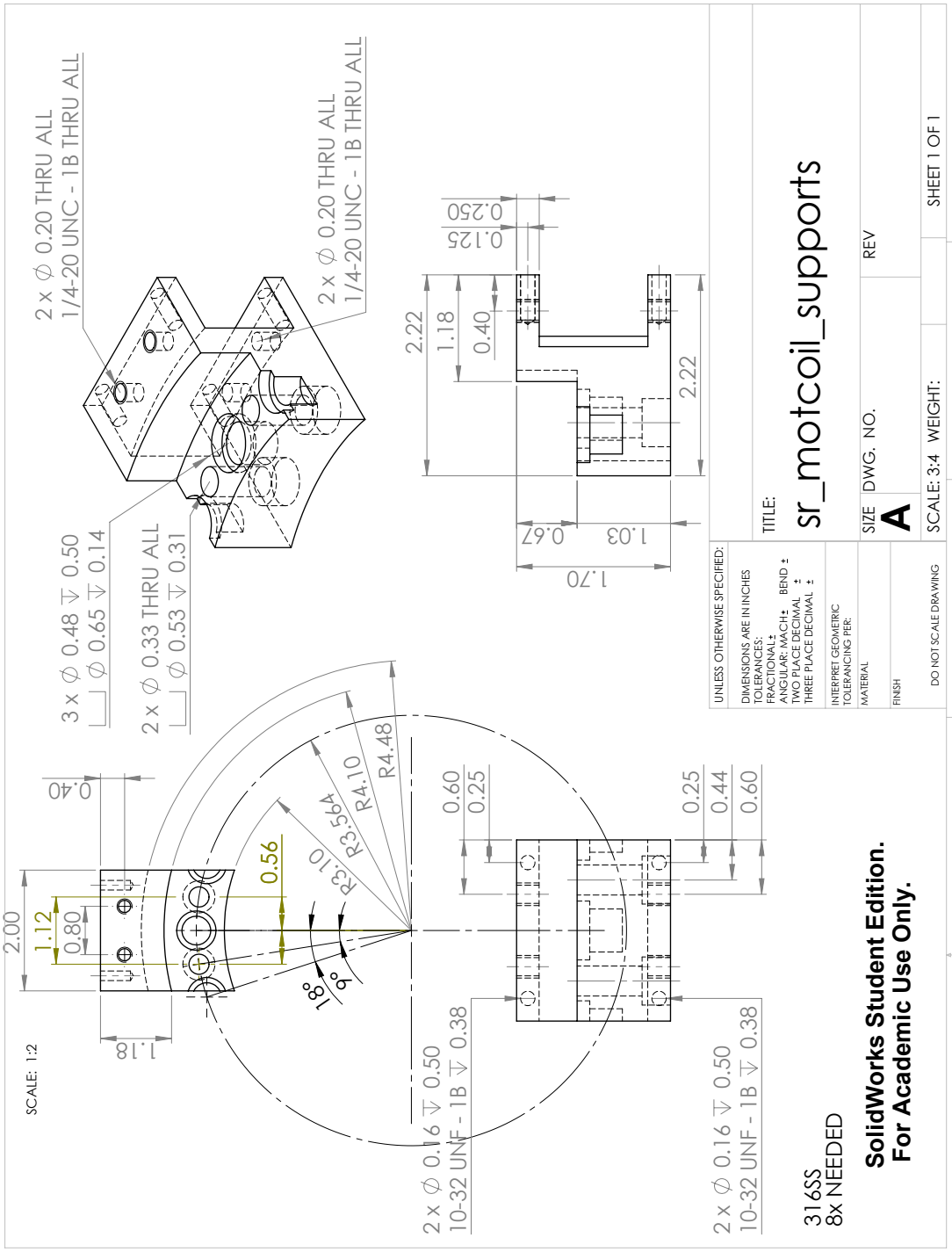

Figure I.3: Strontium MOT coil inner support

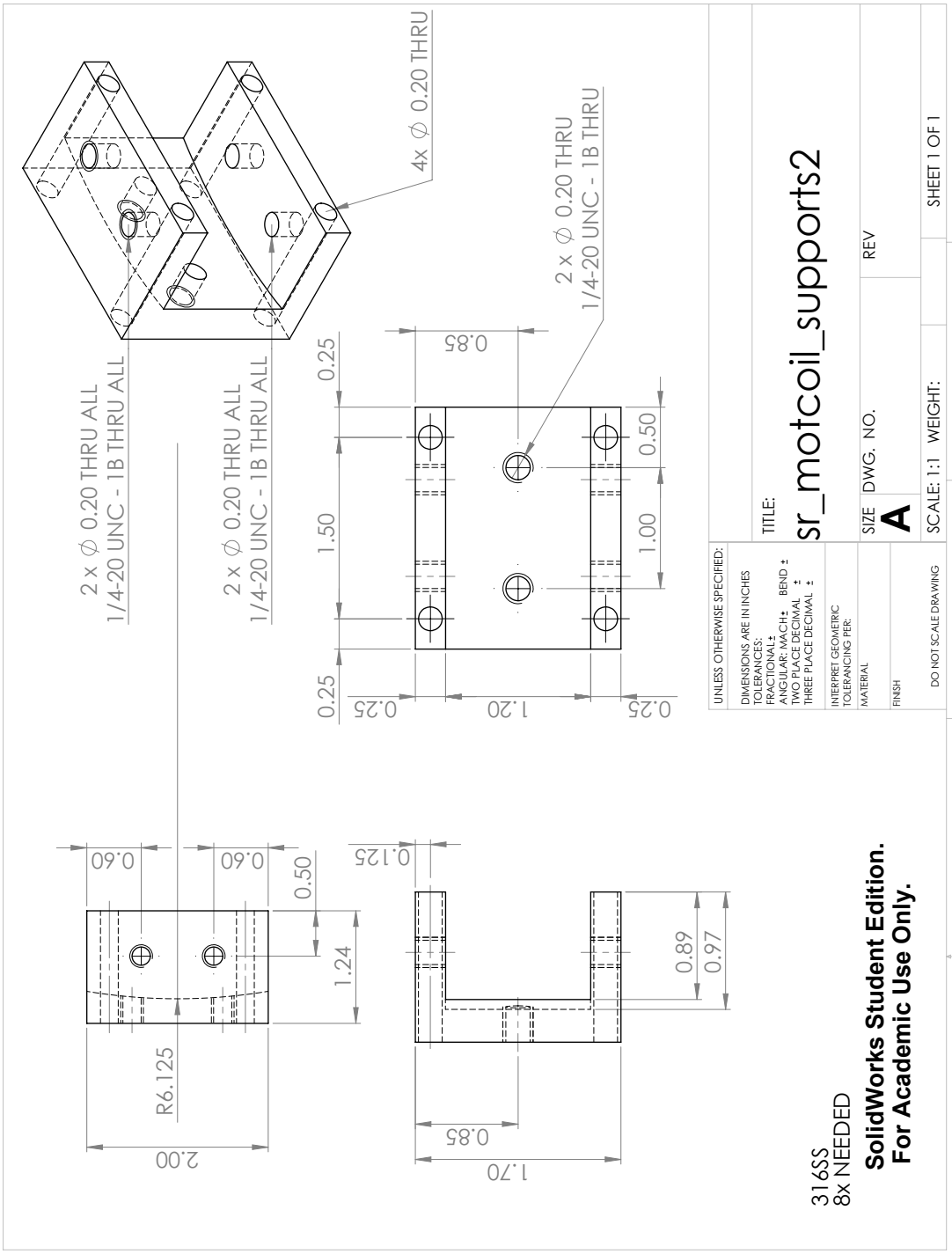

Figure I.4: Strontium MOT coil outer support

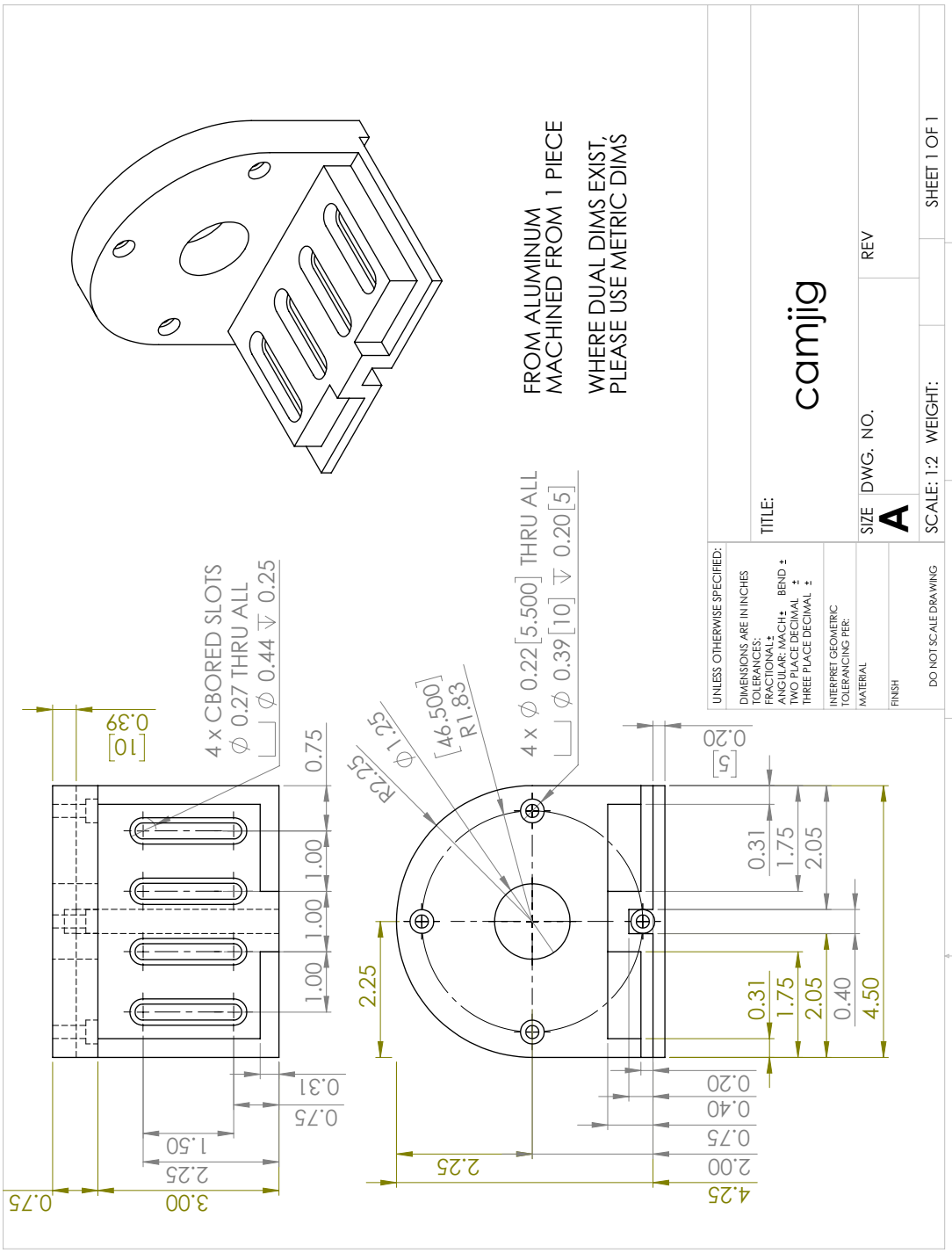

Figure I.5: Andor camera jig for breadboard

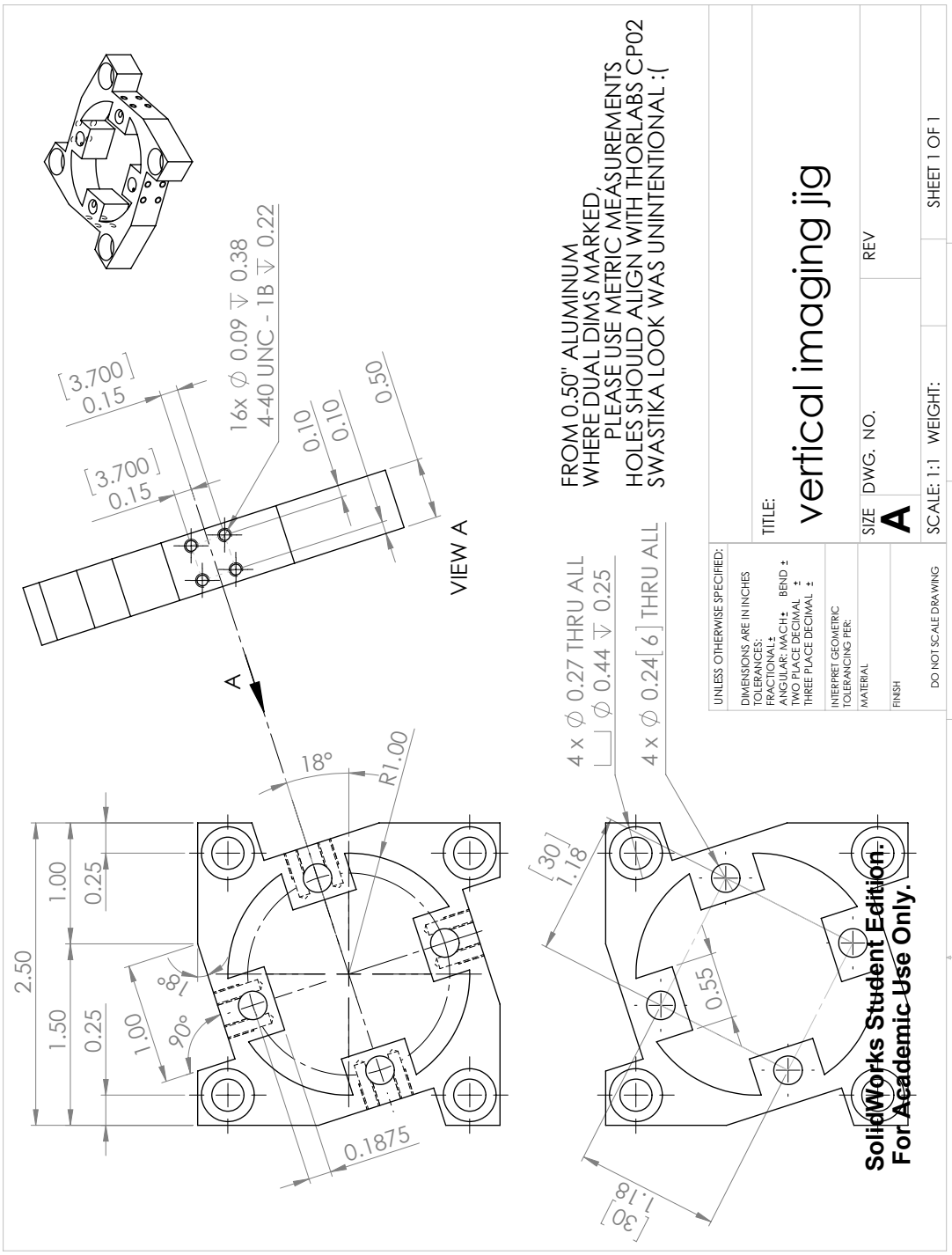

Figure I.6: Strontium imaging jig: breadboard to 1" cage mount system

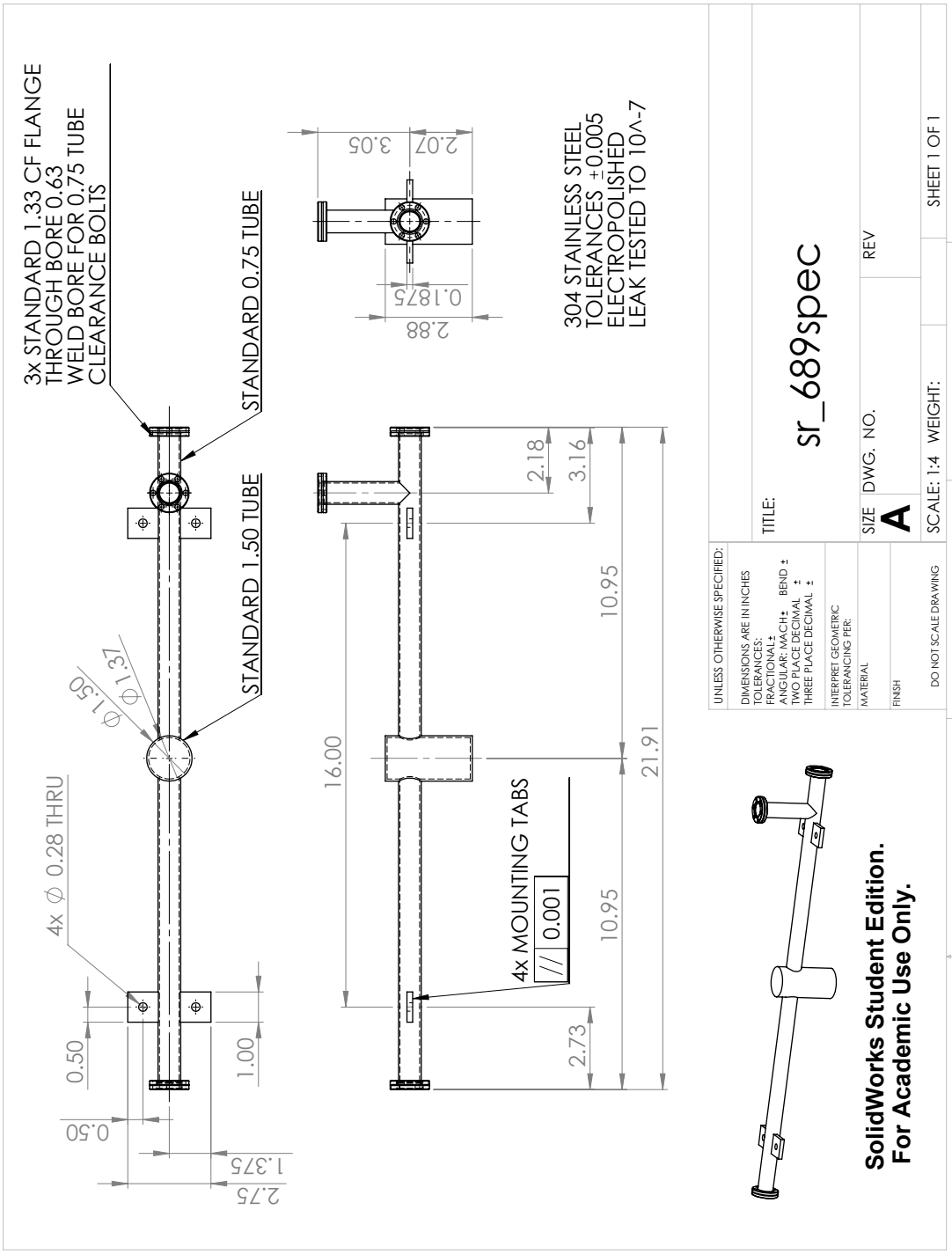

Figure I.7: Drawings for the cell currently in use on the machine.

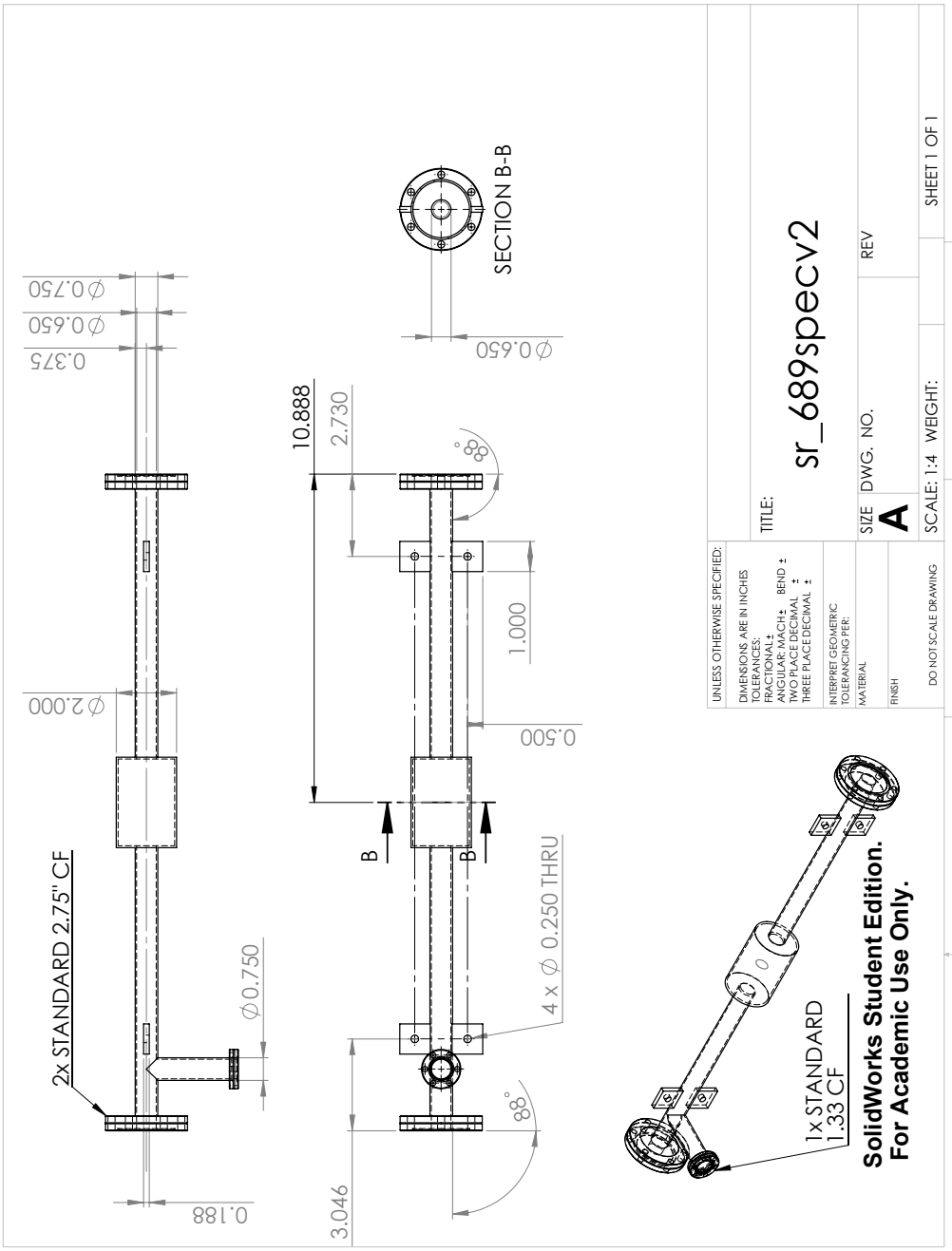

Figure I.8: Updated drawings for an improved cell (not yet made). Barrel should help minimize effects of mass migration; slightly angled viewports should help minimize noise on the signal from backreflection interference; larger viewport size should allow larger usable diameter for light.

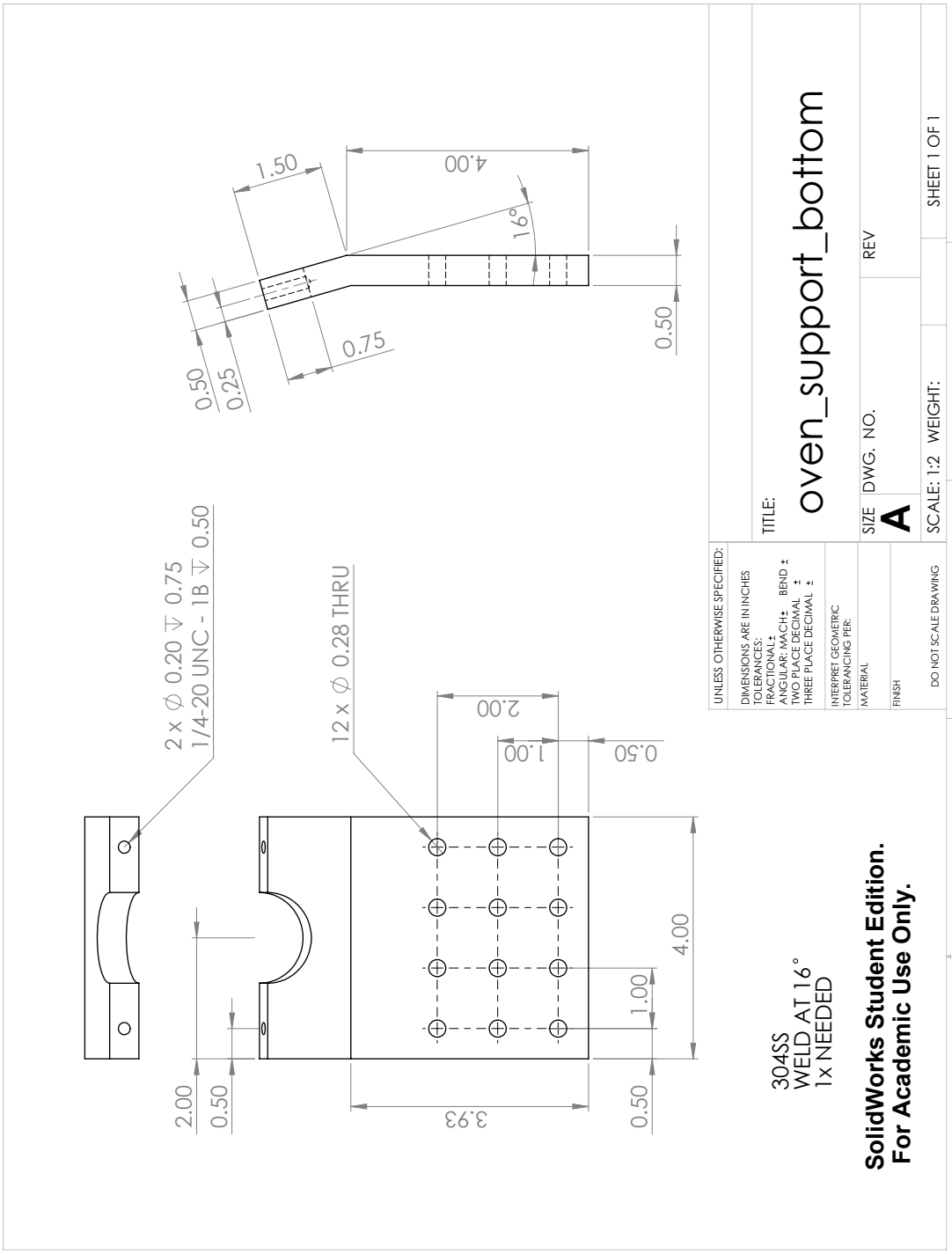

Figure I.9: Strontium oven bottom support

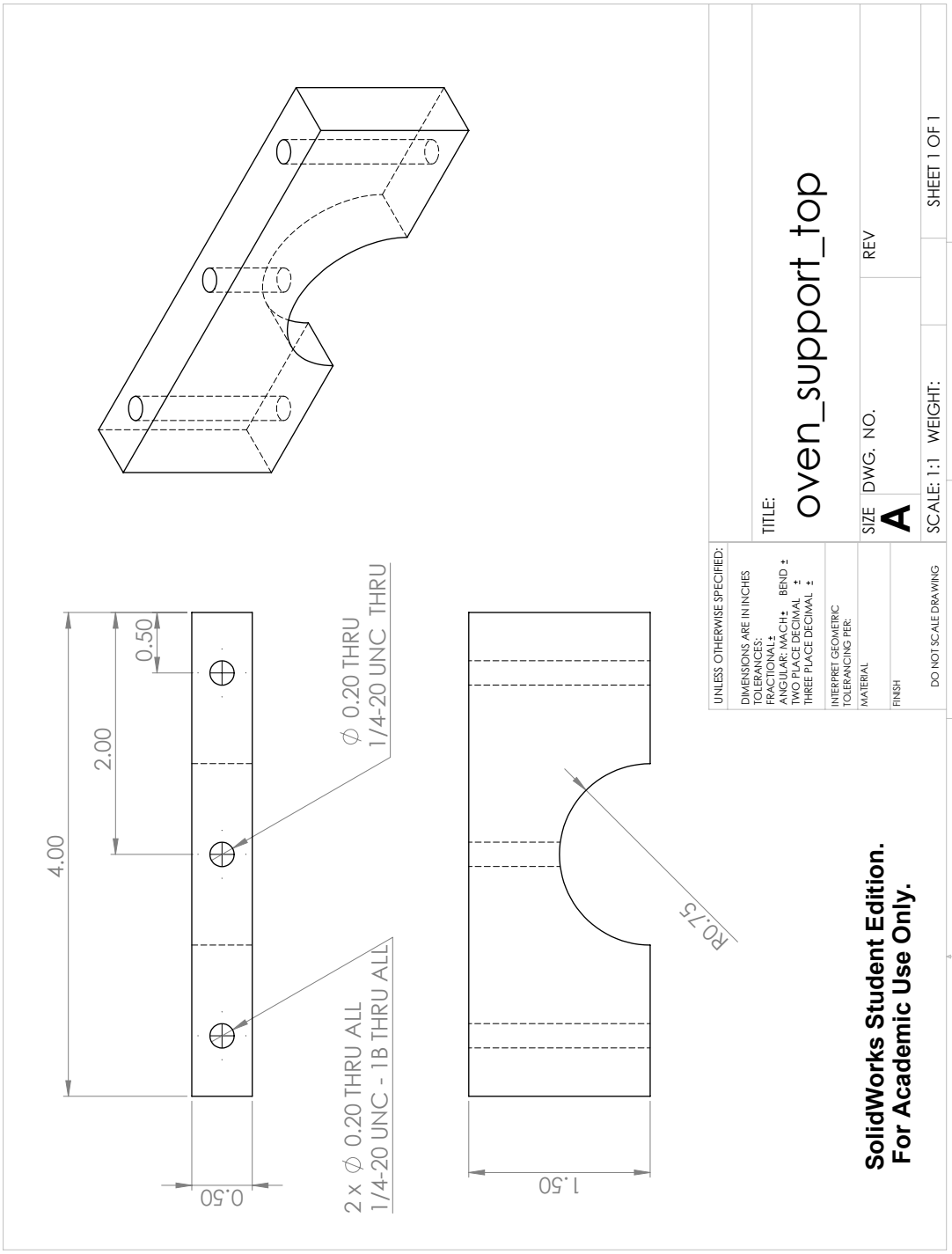

Figure I.10: Strontium oven top support

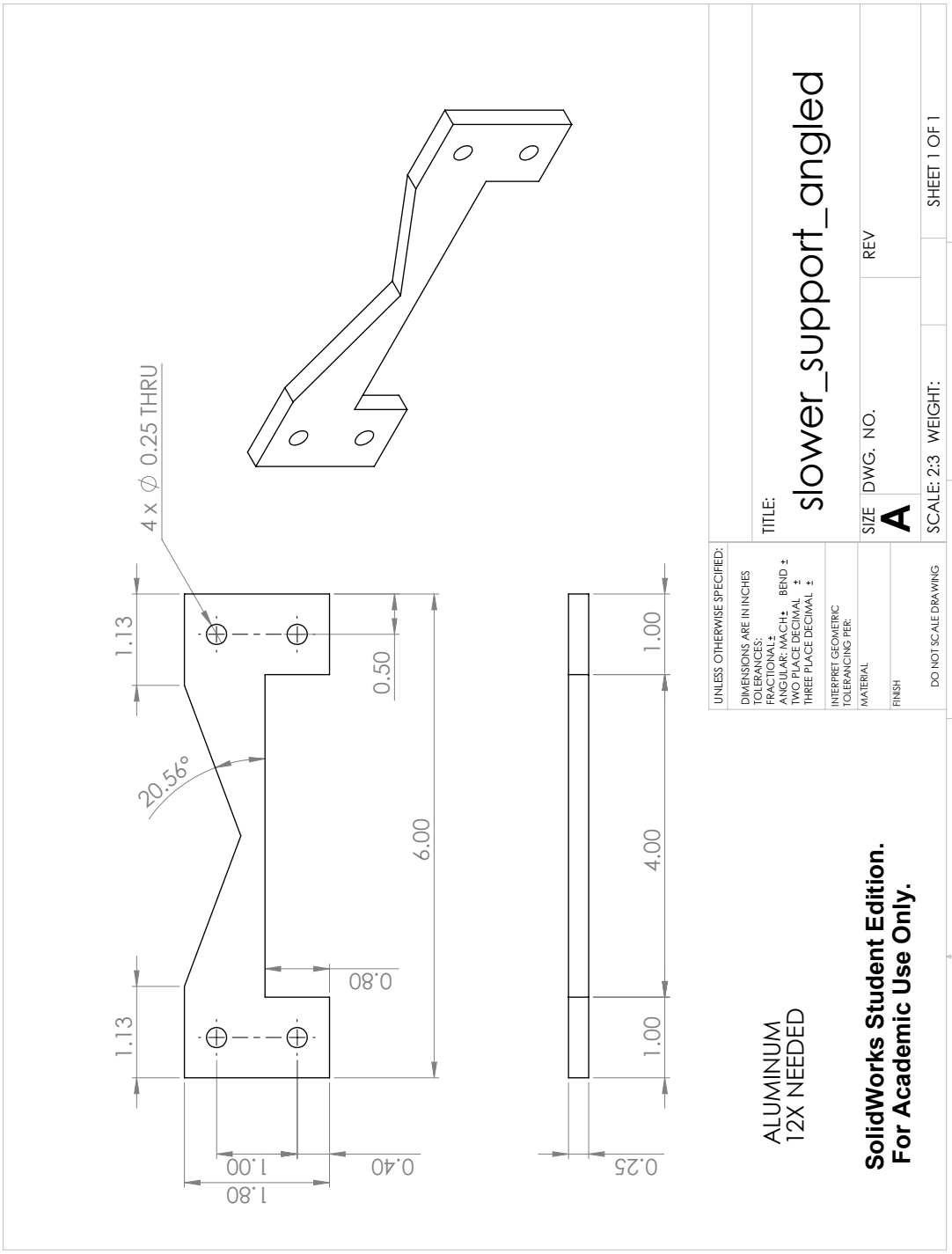

Figure I.11: Strontium slower middle support

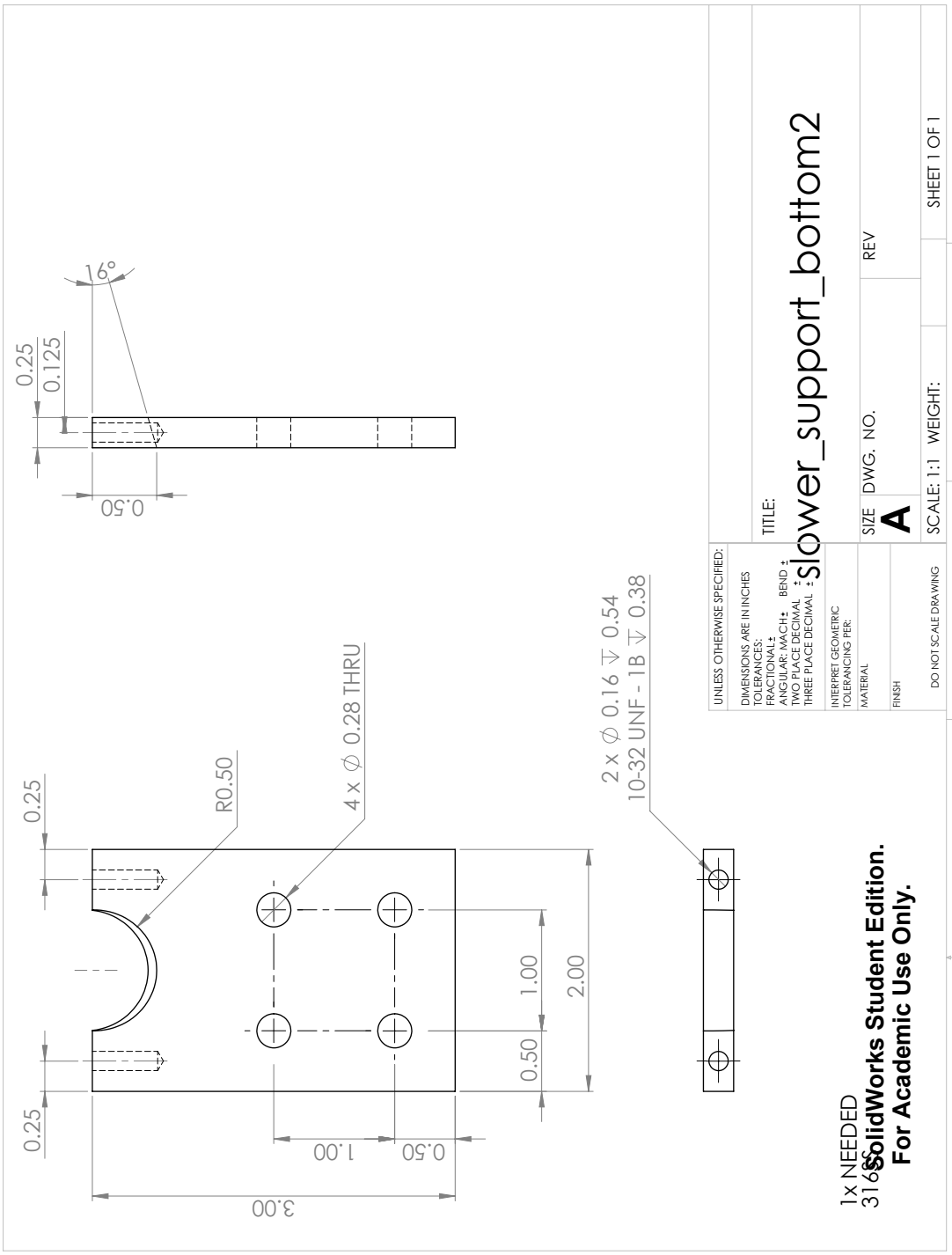

Figure I.12: Strontium slower miniMOT bottom support

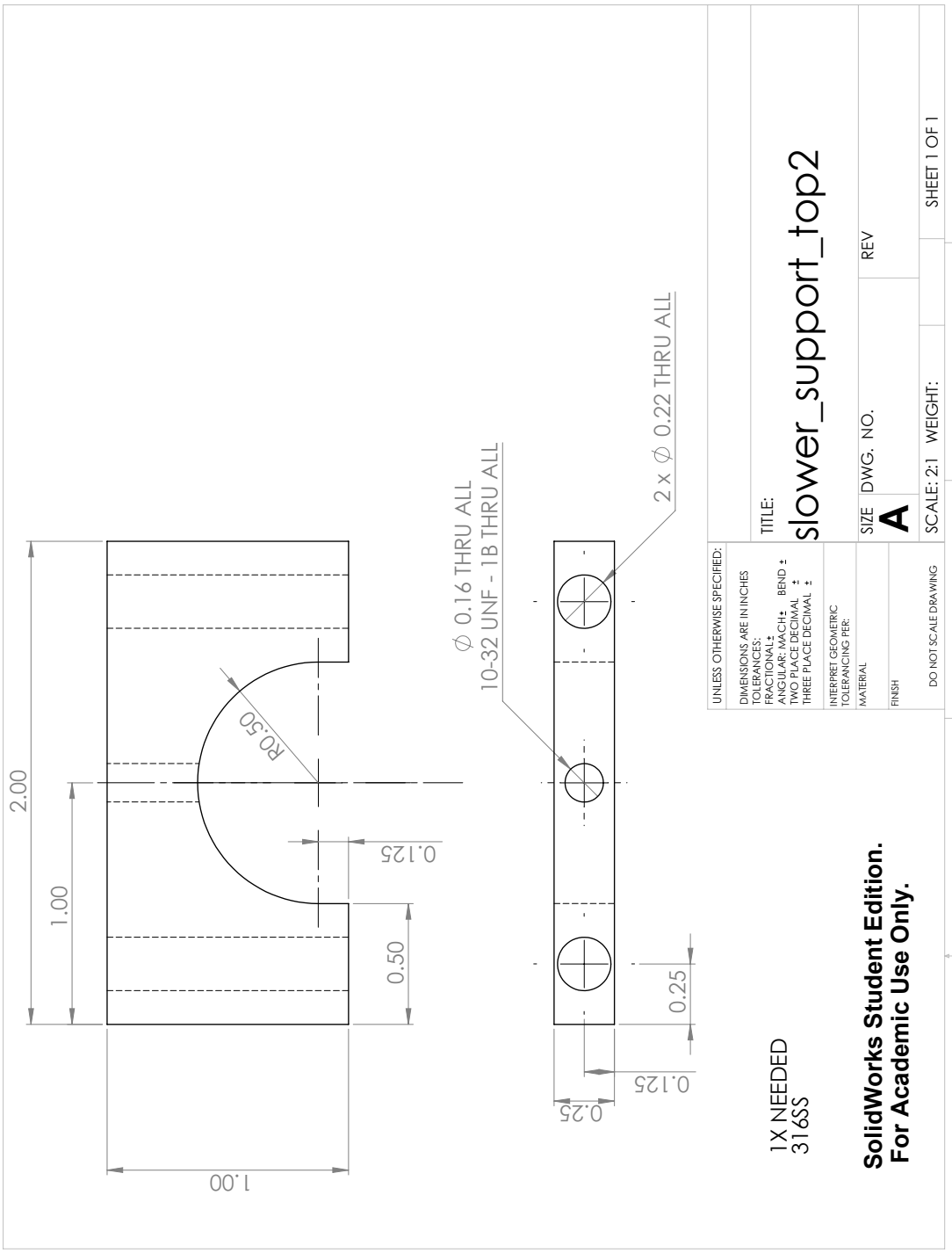

Figure I.13: Strontium slower miniMOT top support

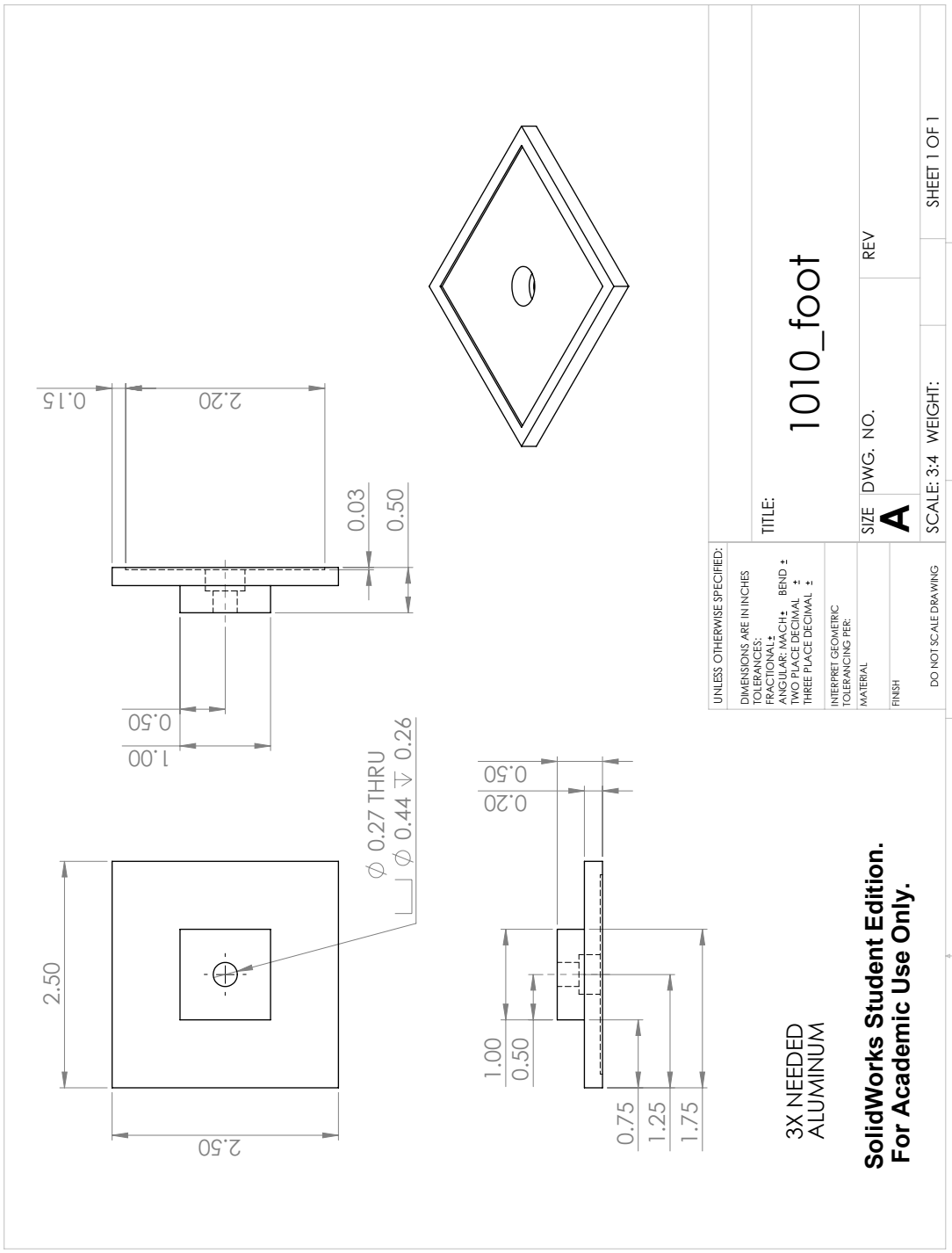

Figure I.14: 1010 foot for 80/20 support

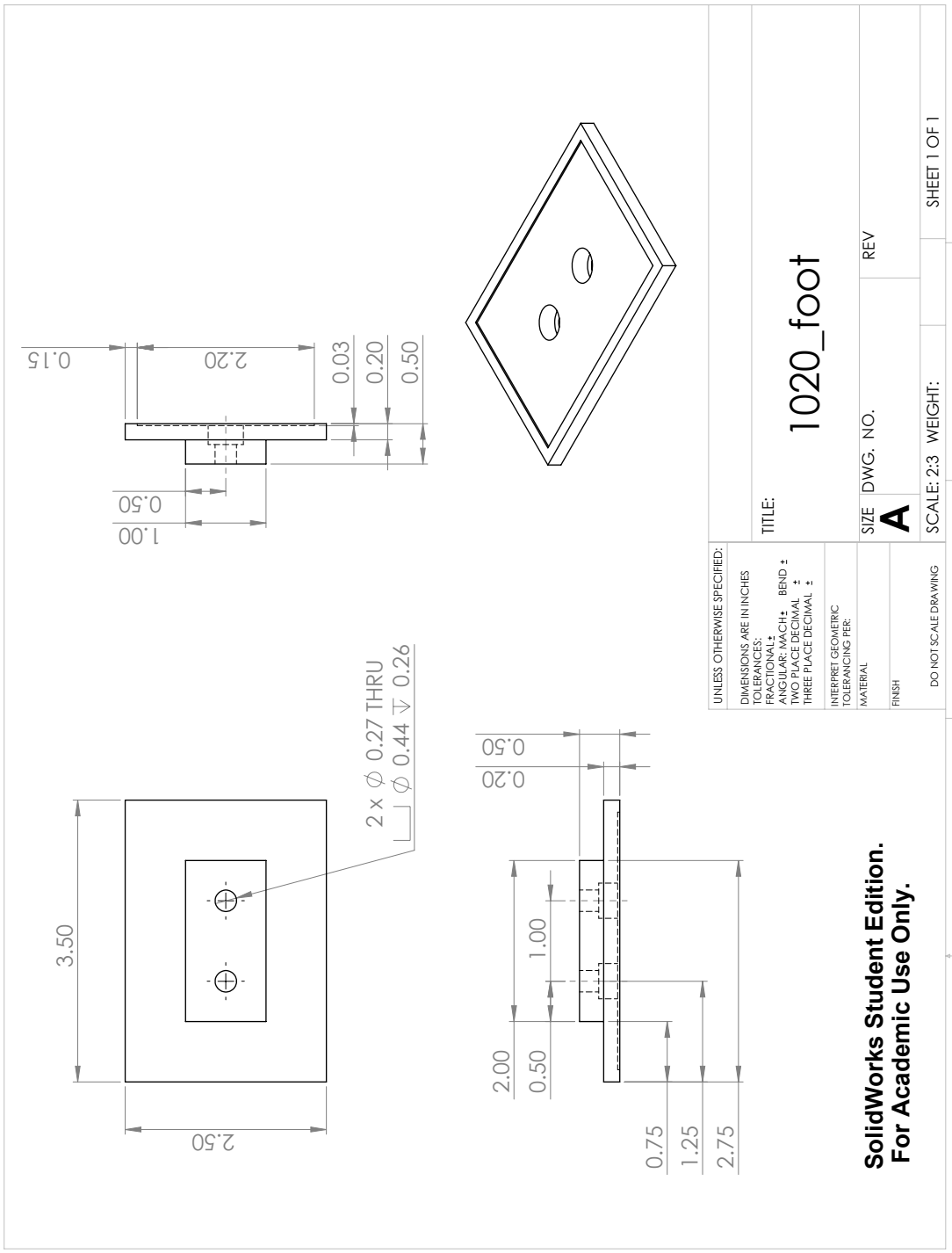

Figure I.15: 1020 foot for 80/20 support

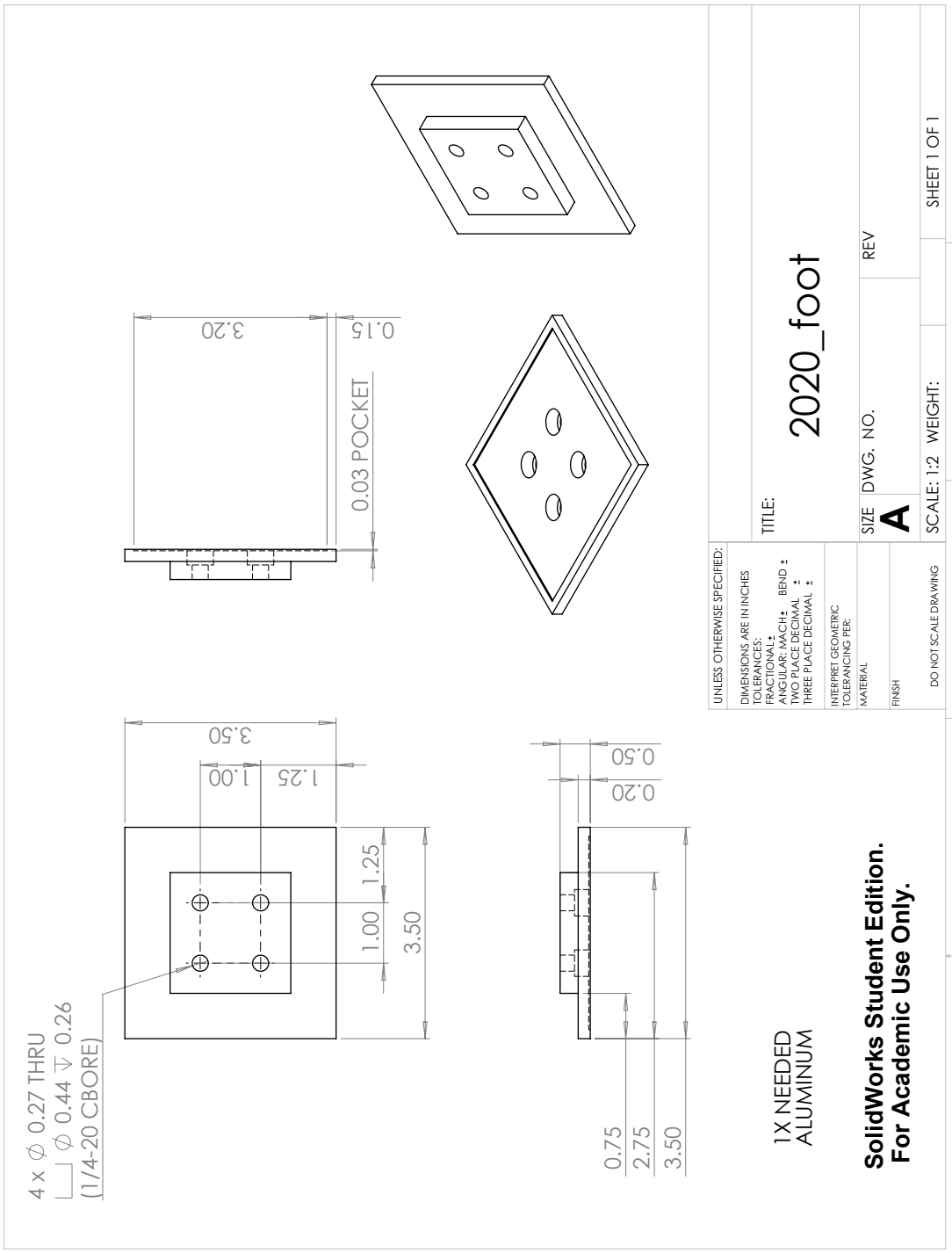

Figure I.16: 2020 foot for 80/20 support

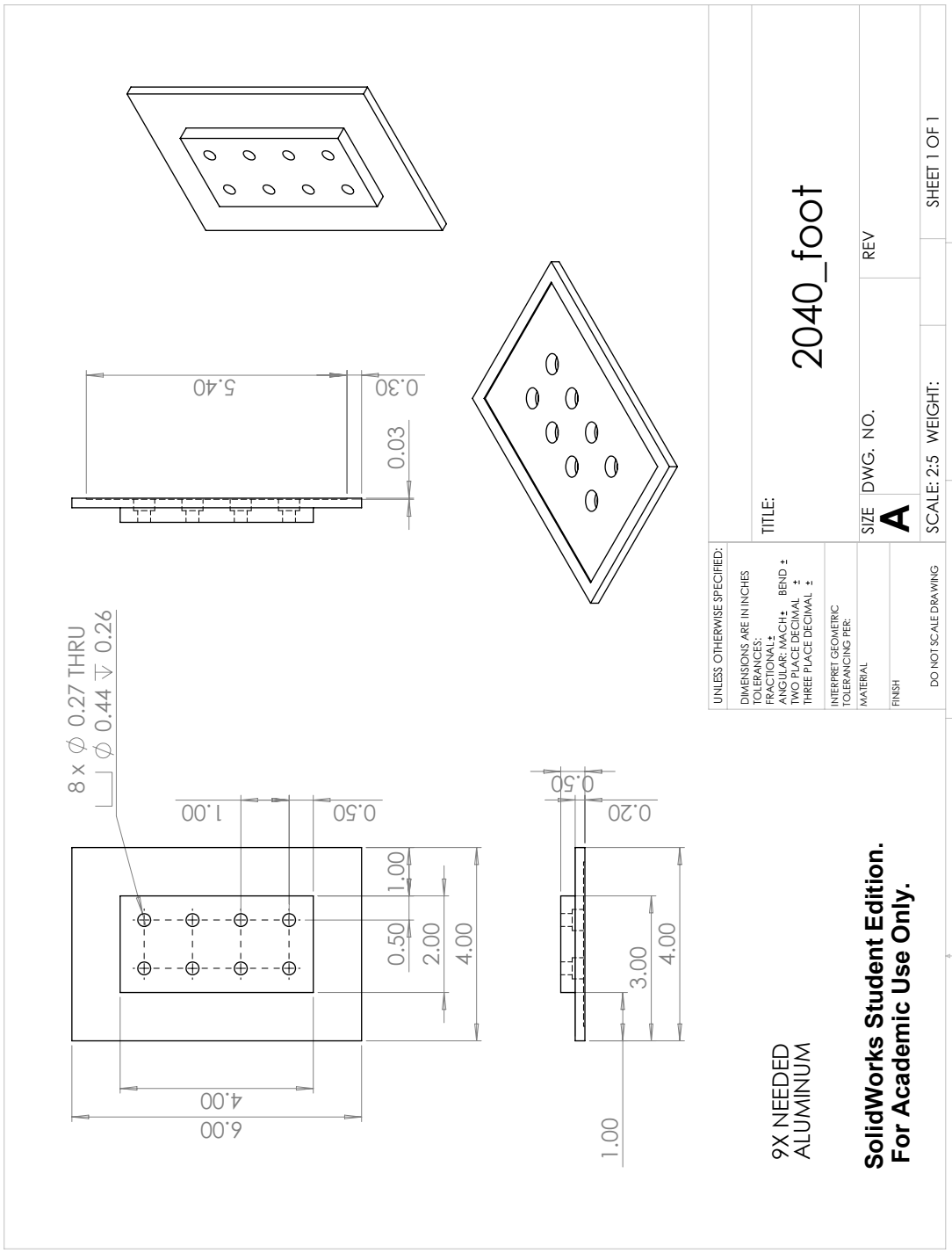

Figure I.17: 2040 foot for 80/20 support

Appendix J

Notes on Pacific Laser Equipment Waveplate Rotators

The strontium machine uses waveplate rotators to redirect power from ODTs to lattices and back. These were designed and made by Pacific Laser Equipment (PLE). They are programmed with software macros via Hyperterminal, and 2π radians corresponds to 3240 discrete rotation positions. Descriptions of macros 1, 2, and 3 can be found in Section J.1. If the currently programmed macros 1 and 2 differ slightly from those below, don't worry about changing them. If the rotator controller box ever loses power, you will need to run the startup sequence in Section J.2. If you are curious what various commands are, Section J.3 provides explanations as well as input syntax if not described elsewhere.

J.1 Macros

- Our zero macros are unnecessary and have been erased. If they are not erased on startup, they can mess up calibration of the starting position of the waveplates. Our one macros have been reprogrammed and set to recalibrate at an arbitrary

position of 600. Their programming is as follows, for x = 1 or 2 is the channel address:

  - xDM1: LN,ST,MN,MR500,MR-10000,WA1000,DH,LF,MA600

- Our two macros have been set as a "warmup". These should just force the rotators to turn back and forth over and over until they warm up enough to run their full range of motion (one should see the numbers on the tracking output approach 1000 and -1000.

  - xDM2: (MA1000, WA300, MA-1000,WA300)RP99

- The three macros have been set to the following:

  - xDM3 = ST,RN,AL1234,FD43,SV90000,SA500,SQ900, SC300, SR25, UD, RR1234
  - We have manually set SR25 to SR50. This refers to the percentage of power being dumped into the rotators when they are idle; we are hoping the increase keeps them warmer. If we ever power on again, we should set this manually via 1sr50 ⟨ enter ⟩ 2sr50 ⟨ enter ⟩.

- xDM7 = RAxxxx. Executes motion on digital low TTL to absolute position xxxx (may be xxx depending on value needed- do not need buffer zeroes).

- xDM8 = RAxxxx. Executes motion on digital high TTL to absolute position xxxx (may be xxx depending on value needed- do not need buffer zeroes).

J.2 Startup Procedure

- Open Hyperterm and make sure connection is established

- If recently power cycled, type 1em0 ⟨enter⟩ and 2em0 ⟨enter⟩ to erase macros 0.

- Turn reporting on by typing 1RN ⟨enter⟩ and 2RN ⟨enter⟩. This will allow the rotators to report back to the hyperterm so you can see what is going on.

- Check macros 1, 2, and 3 by typing 'xTMy' for x channel and y macro. If they do not match the macros above, reinput macros 1,2,and 3 for each of the two channels, taking care to replace SR25 with SR50 in macro 3. NB: If the numbers following RP or WA for either channel's Macro 2 are slightly different from those above, it's ok. Those just set wait times and repeat numbers.

- Run macro 1 for both channels by typing 1CM1 ⟨enter⟩ 2CM1 ⟨enter⟩. This will calibrate the positions of both rotators and should stop at position 600 for both.

- Run macro 2 for both channels by typing 1CM2 ⟨enter⟩ 2CM2 ⟨enter⟩. This will warm up the rotators. Let this run until both output tracking positions that appear to swing up to 1000 and down to -1000.

  - **Troubleshoot:** If the rotators appear to be stagnant (give them a couple of minutes to start moving), it means there is not enough torque to start the driving even after some time. In this case, type 1ab and 2ab as many times as it takes for the drivers to stop running and stop outputting anything (there might be some gibberish output). Then type 1sv5000 ⟨ enter ⟩ 2sv5000 ⟨ enter ⟩. This will decrease the rotating velocity and increase torque until rotation begins. Once they have warmed up a bit, increase velocity again via 1sv90000 ⟨ enter ⟩ 2sv90000 ⟨ enter ⟩.

- Once rotators warm up, check the status of xDM7 and xDM8- they should reflect the positions you want at low and high levels. Test high and low levels via digital TTL. At any point, you can make the rotators tell you exactly where they are via xTP, for channel x. This is 100% reliable in our experience.

- **Troubleshoot:** If, at any point, you forget to type a channel number, it will start throwing gibberish at you. If this happens, type 1ab ⟨ enter ⟩ 2ab ⟨ enter ⟩ as many times as necessary.

J.3 Commands key

None of these are caps sensitive. **None of these should ever be used directly from the hyperterm command without a channel number preceding.** If part of a macro definition, said macro definition should have a channel number, but nothing after the equals sign should.

- LN- Lineswitch on. If this is on, the rotator will stop at position 0 regardless of which direction it approaches from, and regardless of which position it was headed to.
- LF- Lineswitch off. See LN.
- ST- Stop. Tells rotator to stop what it's doing.
- MN- Turns motor on.
- MR- Move relative. Will only start when previous command is finished. Number refers to positions to move- positive is clockwise, negative counterclockwise. 2π radians corresponds to 3240 spaces.
- MA- Move absolute. Will only start when previous command is finished. Number refers to position to move to- see MR for more.
- RA- Remote absolute. Like MA, but will start as soon as command is received.
- WA- Wait. Number refers to number of milliseconds to wait.

- DH- Define home. Sets current position to 0.
- RP- Repeat all preceding commands which were in parentheses. Number after refers to number of times commands will repeat.
- RN- Reporting on. Will make rotators output tracking information.
- RF- Reporting off. See RN.
- AL1234- Allows administrative access.
- FD43- Sabin told me what this did but I tuned out because it was boring and irrelevant.
- SV- Set velocity. Lower velocity is more torque. Number is some absolute value.
- GV- Get velocity. Returns velocity value.
- SA- I have forgotten. There are a lot of these. It influences available torque.
- GA- Get A, whatever that is.
- SQ- refers to how much power is utilized when not idle. Number is a percentage times ten of the total available power.
- GQ- Get Q value.
- SC- Set current. Number is in mA. Currently set at current limit.
- GC- Get current value.
- SR- Set resting. Number is percentage of total power available that gets dumped into rotators when idle.
- GR- Get resting power percentage.

- UD- Update. Writes all changes from RAM onto device EEPROM.
- RR1234- Reboots device.
- CMy- tells channel to execute macro y.
- DMy- must be followed by an equals sign and then a definition. Defines macro y.
- TMy- Outputs the currently programmed definition of macro y.
- TP- Tells current tracked position of the channel.

Appendix K

Notes on Chiller Revival

In November of 2018, our chiller developed a large internal leak which did not allow for operation anymore. This appendix details a few notes on the fixes, and what we learned in the process.

We found out that there was an issue because we continuously needed to refill the chiller once every two hours. We found a leak at the bottom which we measured to be around 30 mL/min, which was roughly consistent with the refills. We opened up the chiller and found evidence of some corrosion on the internal pump, roughly underneath the location of its internal mechanical seal. We ordered replacement parts for the internal seal (0118 and 0232) from Halsted and Hoggan, local distributors for Price Pump. In the meantime, we began to open the pump for replacement. Once we extricated the pump electrically and mechanically from the chiller, we found it difficult to remove anything past the impeller; in particular, the mechanical seal stayed stuck to the shaft. UCSB's head water guy, Brandon, came out to lend us his puller (a Pronto J4234B) to pry off the seals.

We ended up finding that the mechanical seal was, in fact the source of the ticking. The mechanical seal consists of a ceramic teflon-coated seat, which sits stationary in the gasket. There is then a carbon ring which rotates with the shaft and slides on the surface

of the ceramic. Then there is a spring to provide tension, and the seat head, which sits against the impeller. The impeller screws onto the end of the shaft. Here's what we think could have happened, but there's not really any one culprit which we can say is a smoking gun:

1. Some awful incident a long time ago (possibly the incident where the old booster melted) caused some small amount of damage to the ceramic part of the seal, which may be thermally sensitive? That's what Brandon seemed to think, at least.

2. That small seal issue started letting water into the other side of the pump.

3. The water on the other side of the pump began to corrode the shaft (Fig. K.1a), to the point where there was a very large amount of buildup on it. This corrosion was the reason the seal spring and head were so stuck. We especially noticed lots of buildup where the ceramic ring sits on the shaft, and quite a bit of wear on the inside of that ring.

4. We also noticed that the carbon ring, which is supposed to rotate against the ceramic surface, was shattered in multiple places (Fig. K.1b)- though it's not clear which part of this happened before or after our wrenching the part off of the seal.

In the instruction manual, the reassembly instructions state very clearly that the pump shaft needs to be thoroughly cleaned, with no evidence of grooving, pitting, or fretting. It says to polish with extra-fine emery cloth, and if the shaft is grooved, fretted, or worn, replace the entire motor. We acquired emery cloth to attempt to sand down the shaft corrosion, but were unsuccessful. We decided to replace the pump (from Halsted and Hoggan: PN HP75BN-550-06111-100-36-1D6).

When the new pump arrived, we noticed it had a different motor from the old pump (new: JL1309A, old:3807BA), which meant that the wiring was different. The wiring diagrams were all in the manuals, though, and we figured it out. Once the pump was

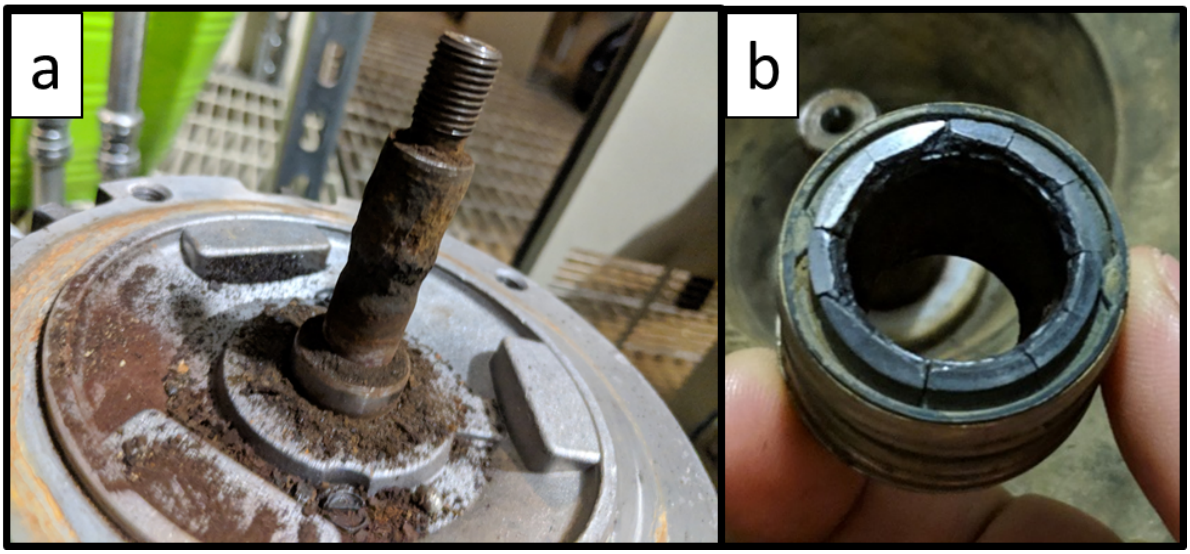

Figure K.1: **(a)** shows the extent of the corrosion on the pump shaft. **(b)** shows the damage on the carbon ring, part of the mechanical seal that failed and caused the leak.

replaced mechanically and electrically, some hose clamps and tubing were purchased from Home Depot so we could test the pump. Unfortunately, it did not turn on. We spent some time trying to debug the internal electrical connections, as it is a very old model that nobody seems to have wiring diagrams for. We thought we may have blown a fuse, but couldn't find internal fuses.

We finally called Trillium (the local distributor for Thermo-Scientific, the chiller brand) and talked to Danial, who put us in touch with Marvin, the head engineer. Marvin is great and was nice enough to Facetime with us to help us debug. From talking to him and wire-tracing, we figured out that we don't have any internal fuses, and established the wiring diagram for the most relevant wires (Fig. K.2). Once we checked the DC voltage (across the purple wires), we realized that the voltage was derated by some proportionality constant which was consistent with the two possible input voltage settings: 208 V vs 240 V. This setting is set by a switch external to the wiring panel rather close to the pump, which means we could have inadvertently flipped it. Once it was reset to 208 V, the chiller worked again.

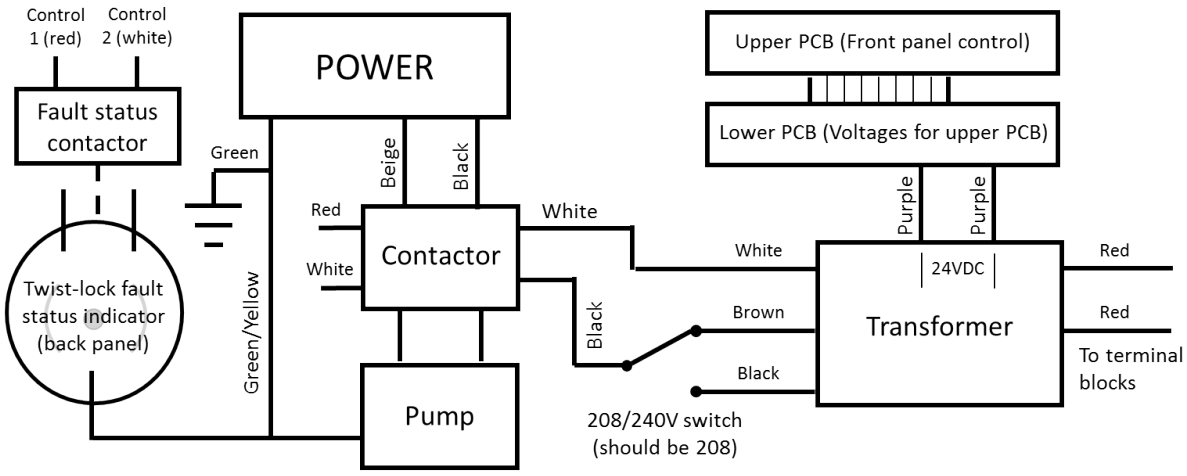

Figure K.2: This schematic is not meant to help the reader understand the electrical workings of the chiller, but if that is your goal, this should help you trace the wires, at least until the terminal blocks. Those were difficult enough to access that we basically gave up trying to make sense of them.

We got Tony from UCSB maintenance to help us make connections back to the building's water system; much of the Teflon on the brass connectors was extremely worn. The connections were redone using KeyTite, a liquid lubricant and sealant which he heavily recommended over Teflon. If we ever wanted to replace the torn-off insulation from those seals to prevent condensation, he recommended cork insulation.

We bought a Midget Twist-Lock connector for the interlock on the back of the chiller, and ran wires from the core to the lab. When connected, those lines will be closed if the chiller is operational, and open if it turns itself off. These will be connected to an interlock in the lab.

A final note for future Weld Lab members: there is a weldlabupdates thread called "Chiller's dead, long live the chiller" which contains all of the hyperlinks, manuals, diagrams, photos, and more detail about this process. I hope you never have to refer to it, but it exists.

Appendix L

"Better Know a Strontium Machine"

The fightin' Strontium!

This appendix is intended for a new student on the strontium machine to use as a quick reference guide to what things are and where they are in the lab, and includes a small section on machine start-up. It will likely become outdated very quickly and serve as a reminder of the state of the machine circa 2019.

L.1 Strontium machine turn-on procedure

1. **Start heating up the oven**, ensuring that the nozzle is always hotter than the cup. This takes a while, as the nozzle is more poorly insulated. Continue turning up in stages until the cup is 600°C, the nozzle 650°C; this can happen in parallel with turning up various other things and checking/tweaking up laser powers if necessary. Once the heater thermocouples read the correct temperatures, it will take some extra time for the oven to reach thermal equilibrium; use the MOT fluorescence to decide when that has happened.

2. **Turn the 461 nm laser on** to let the 922 nm master equilibrate.

3. **Connect the 689 nm spec cell variacs**, which are color-coded (will take around an hour to heat enough to lock to), and **turn on the 461 nm spec cell heater** (will take around 15 min to heat enough to lock to).

4. **Turn on the 403 nm laser, 689 nm master and TAs, and lock the 461 nm cavity**. Make sure there has not been a brownout; if there has been, turn on the TECs for all Arroyo controllers.

5. **Turn the key on the 1064 nm amplifier** to enable it. Check that the panel says "Remote Control."

6. **Turn on the 915 nm laser** and TA if you will be using it.

7. **Check that your water monitor has not crashed.** It is unsafe to run the machine without a working water monitor.

8. **Open the water shunt and flip the valves** in the core to close the filter path and open the booster pump path. Check that the chiller pressure is nominal.

9. If you are turning on the magnets, **turn on the booster pump switch**. Check that the high pressure gauge reads 100 psi; if not, adjust the shunt valve until it does. Check that the water monitors read around 19°C.

10. **Turn on the magnets**. The steady-state water monitor temperatures should not rise above 33°C if all is well. Happy machine-running!

L.2 Images

Figure L.1: **1:** AOM RF amplifiers for ODT and XODT. **2:** NKT AdjustiK seed. **3:** NKT BoostiK amplifier. **4:** MiniMOT analog controller. **5:** MiniMOT power supply. **6:** Voltage summing amplifier for piezo driver. **7:** AA Systems A303 piezo driver. **8:** Band heater controllers for oven. **9:** Tarth (control computer for water monitors, 1064 nm seed, 1064 nm amplifier). **10:** RTDs and flowmeters for water manifold.

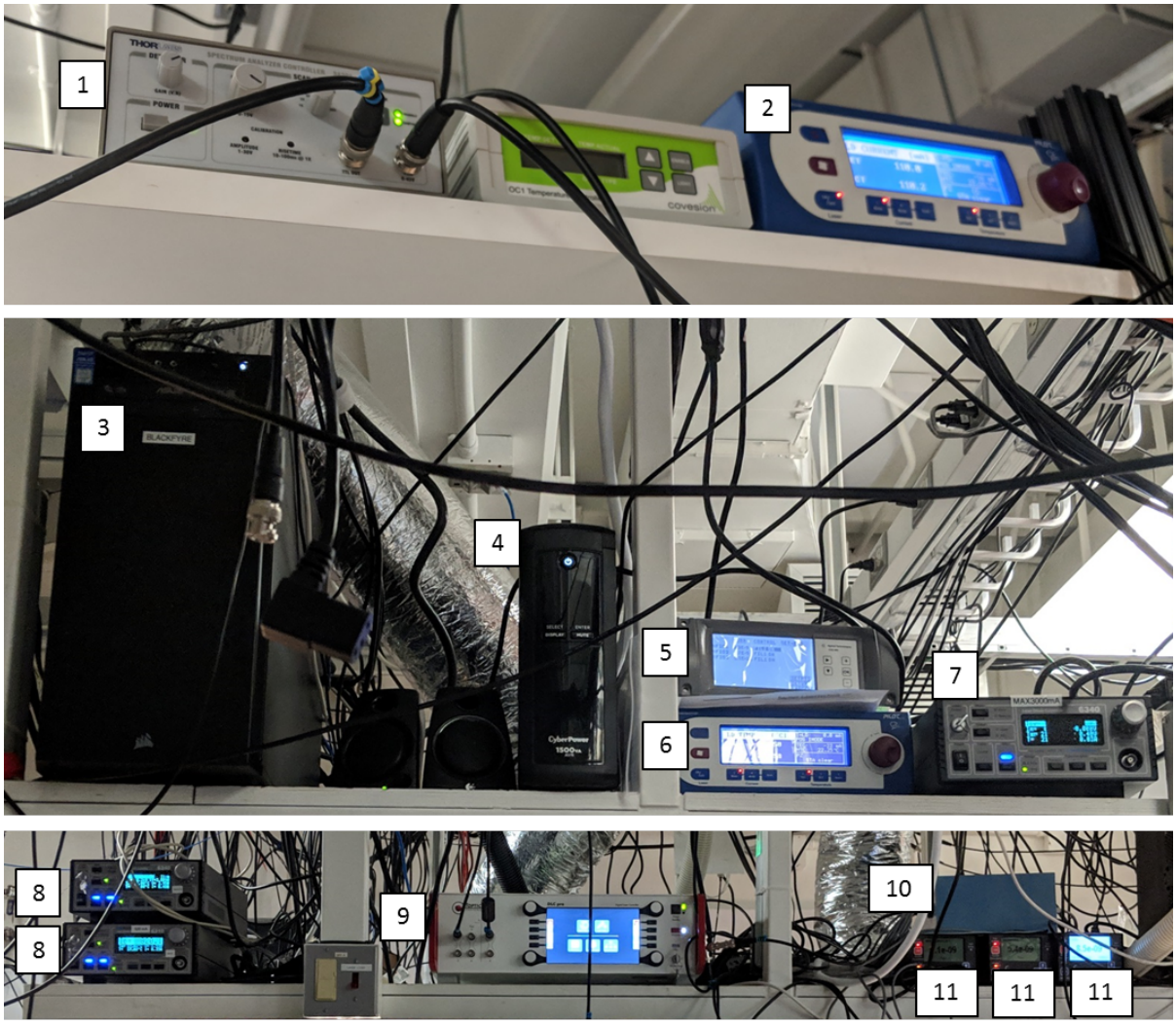

Figure L.2: **1:** Thorlabs Fabry-Perot cavity driver. **2:** 403 nm Sacher laser controller. **3:** Blackfyre (control computer for waveplate rotators, picomotors, and general analysis). **4:** One of many UPSs to protect the machine against power outages. **5:** Ion gauge controller. **6:** 915 nm Sacher laser controller. **7:** 915 nm TA controller. **8:** 689 nm controllers for TAs. **9:** Toptica DLCPro controller for 689 nm master laser. **10:** Picomotor controller box for tight trap alignment. **11:** Ion pump controllers.

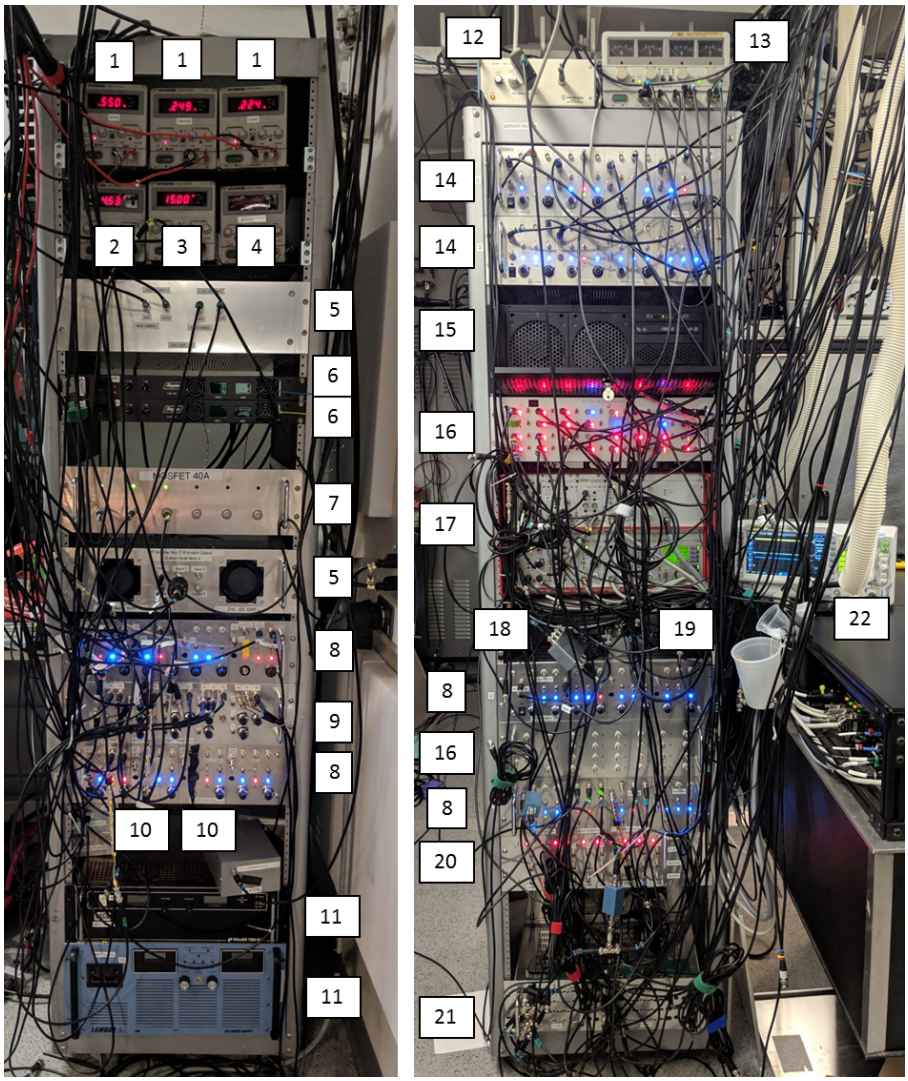

Figure L.3: **1:** Shim current supplies. **2:** Slower current MOSFET control. **3:** Power for miniMOT analog controller. **4:** Atomic beam shutter power supply. **5:** RF amplifiers for 1064 nm AOMs. **6:** Zeeman slower power supplies. **7:** MOSFETs. **8:** Homebuilt AOM driver boxes (precision, 4 drivers/box). **9:** PIDs (old design; used for ODT, XODT, tight trap). **10:** Analog controls for MOT power supplies. **11:** MOT power supplies. **12:** IntraAction driver for spectroscopy double-pass AOM. **13:** Power supplies for analog switch and sample-and-hold circuits. **14:** Homebuilt AOM driver boxes (non-precision, 4 drivers/box). **15:** Arryn (control computer for 461 nm software, 403 nm software, 689 nm software, Atticus, and Cicero; main experimental control computer, contains NI cards.) **16:** Digital breakout boxes (analog breakouts are on other side of this rack). **17:** Toptica control modules for SHG-Pro 461 nm laser. **18:** Analog switch circuit. **19:** Sample-and-hold circuit. **20:** Old shutter Arduino control box; outdated. **21:** PID (new design; used for 689 nm MOT power and all lattice beams). **22:** Scope to monitor 461 nm cavity photodiode and scan signals.

Figure L.4: **1:** Rivers monitor. **2:** Tarth monitor. **3:** Rivers (control computer for 403 nm digital lock to cavity signal, scope traces from Kapitza-Dirac diffraction). **4:** Monitor for lattice PIDs. **5:** Monitor for ODT/XODT PIDs. **6:** Monitor for MOT currents, 689 nm MOT PID. **7:** MOT fluorescence camera monitor. **8:** Arryn monitors. **9:** Blackfyre monitors. **Left:** “What about that shadowy place?” “That’s beyond our borders. You must never go there.”

Appendix M

Lullaby for a 461 Laser

Keeping the 461 nm laser[1] running requires some TLC. Here is a list of things that need to be done to ensure its upkeep, roughly in order of decreasing frequency.

For cavity alignment, cavity cleaning, and overall power drops, I offer a disclaimer that **before following the steps detailed below, you should call Toptica support- they are incredibly helpful and will be able to confirm problems and provide guidance**, and anyway I can't guarantee that I haven't misremembered or forgotten something here.

M.1 TA recoupling

At least once a week, we find that the coupling of the master seed to the internal TA has drifted. The few times we have checked the actual TA IR output, the drift has corresponded to a 940-950 mW output rather than the usual 1.05-1.10 W. We are typically still able to lock the cavity to a mode, but the blue output falls by 10-20 mW.

We usually just look at the blue power on a power meter and recouple the TA using the external access holes and a couple of M2.5 drivers. The majority of the power can

[1] I like to think of it as Obi-Wan (Alec, obviously, not Ewan) to the lithium 671 nm's Darth Vader.

usually be retrieved by changing the vertical adjustment of the first mirror, and the rest can usually be retrieved via horizontal adjustment of the same. We will occasionally do a full two-mirror walk to make sure we haven't inadvertently wandered into a bad corner of phase space, but it's not necessary on a weekly basis.

M.2 Desiccant packet switching

Unfortunately, water has a strong absorption line at 922 nm, which means that the circulating power in the cavity attenuates if the humidity is high. We need to switch out the desiccant fairly regularly; the longest we have gone with the same packets is around 4 months, but if it is rainy outside, we may have to switch it out several times in a week. We put two packets in the cavity each time; fitting the desiccant lid back on without interfering with the o-ring seal becomes tight, but it's worth it for the longer lifetime. The packets are kept in a vacuum-tight jar with silicone desiccant and indicators; they may be reused several times provided they are baked prior to each use. After several bakes, the plastic seals on the packets begins to deteriorate. Toptica is usually very nice about sending us replacements as needed. The easiest way to tell that the desiccant needs switching is that the cavity lock will start to fail at the edge of a 1 V scan around the resonance.

After the desiccant is switched, it can be nice to reset the cavity lock PID parameters (if the power still drops out after multiple desiccant-switch attempts, the gain on the PID may need to be increased slightly and the parameters reset). The parameters for a good DC lock typically do not work for a scan, so they should be set while the Digilock is scanning the master at our typical scan speeds ($\sim$11 Hz). The gain on that lock should not be increased beyond around 6; nominal values are 3 to 4, and we try not to take it above 5. We typically set I such that the power just barely does not drop out at the edges of the scan; too much higher and we start to see ringing. The P and D parameters

are set by looking at the noise on the cavity photodiode signal.

M.3 Frequency mode

We have not had to manually touch the grating in 5 years. We occasionally monitor the master on a cavity (using the aux port), but we have never seen it go multimode. The laser is rarely ever mode-hoppy. If it becomes so, a piezo offset/current walk on the controller modules has always allowed us to recover.

M.4 Cavity realignment

Cavity alignment should typically not require redoing unless one of the PZTs needs replacement, which it did in early 2016; measurement across PZT1 read only 240 ohms. Luckily, PZT2 still worked, and we were able to operate during the replacement leadtime by adjusting the PID parameters. Once the replacement arrived, we were able to follow Toptica's instructions for replacement and then realign the cavity. NB: If the PZT stack does need replacement, check that the o-ring between the new replacement assembly and cavity housing is in place.

In the event that the cavity requires realignment, the following steps should be followed. The mirrors are referred to in the order in which the light hits them in the bowtie cavity: RM1, RM2 (attached to the PZT assembly), RM3, and RM4 (see Fig.M.1). Each has 3 adjustment screws, but using the 2 decoupled ones will suffice; be careful that you're not accidentally trying to loosen the full mirror assembly. You will need to be a little bit careful accessing some of the vertical adjustment screws, as an L-driver can easily interfere with the beam. An IR viewer is very helpful. You'll need an M2 driver for crystal movement, (2) M1.5 drivers for the cavity adjustment, and an M2.5 driver for the second incoupling mirror, all of which are stored in a cup near the laser. If they are

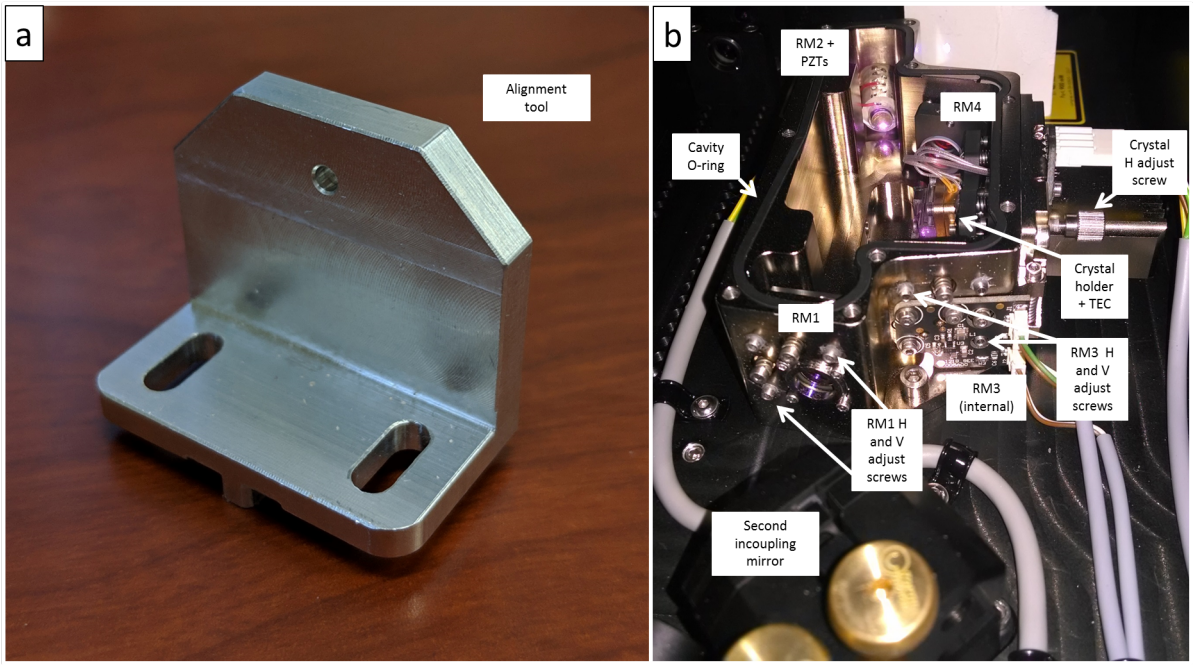

Figure M.1: **(a)** shows the alignment tool if the cavity ever needs to be removed for a gross realignment of the incoupling beam path. **(b)** shows the cavity, with some features of interest marked.

not there, yell at people until they are, and make sure they are never moved.

1. In the event that the two incoupling mirrors are grossly misaligned, and in this case only, the cavity may be removed from the laser housing. Toptica provided us with an alignment tool which may be placed in a groove in the laser housing and slid along the correct incoupling line to correctly align those two mirrors. The target on the tool is quite small, so the alignment can be adjusted quite precisely by placing an optics cleaning sheet in the IR beam path to locate the center of the beam (this should be done at low TA current). Once the cavity is replaced, the beams should be hitting the center of RM1 and RM3 (RM2 is not adjustable).

2. RM3 should be adjusted to send the light through the center of the doubling crystal such that it hits the center of RM4. The two faces of the crystal should be perpendicular to the beam.

3. Adjust RM4 such that the reflected IR light hits RM1 and overlaps with the incoming beam.

4. Adjust RM1 such that the reflected IR light hits RM2 and overlaps with the incoming beam. At this point, you should start to see cavity modes on the cavity photodiode when scanning the piezo, and some small amount of blue light escaping the cavity, and the cavity lid can be closed and the TA current increased. Make sure nothing interferes with the o-ring seal on the cavity, as it is important for both humidity and dust control.

5. RM3 is the mirror which controls the angle of the outgoing 461 nm light, and it is imperative that that light hit the center of the downstream lens and prism pair. If this is not the case, walk the second incoupling mirror and RM3 to get the light to propagate through the crystal and through the optics after the cavity; the second incoupling mirror should not require too much movement.

6. Walk RM4 and RM1 to maximize the size of the main cavity mode. The active area of the photodiode is not large, so depending on the characteristics of the cavity, the absolute signal size may change slightly. It is also not a good metric for the absolute 461 nm power out of the cavity. It should be used as a metric for the quality of the mode matching, and the relative size of the main cavity mode should be at least 10 times larger than the next largest mode.

7. The vertical crystal alignment is quite robust and mostly decoupled from other adjustments; it can be quickly walked to maximize the 461 nm power exiting the laser housing.

8. Looking at the 461 nm power out of the laser housing, slightly walk the horizontal crystal alignment and the horizontal RM4 alignment to improve phase-matching, then walk RM4 and RM1 to maximize the cavity mode, and then do a small walk

of the incoupling mirrors. Iterating this step should restore the total power. The laser housing lid should then be closed.

M.5 Cavity cleaning

The cavity lid and laser housing lid should almost always be closed to minimize dust/particulates. However, if dirty cavity mirrors are suspected as a source of cavity badness, they can be cleaned. The last time this happened, it manifested as an inability to extinguish higher-order cavity modes when adjusting the alignment. If this becomes necessary, acquire cotton swabs and use the very-high-quality acetone which is in the flammables cabinet. Align the ring cavity to maximize the main mode as well as possible. Check the blue power.

1. Block the IR light.
2. Remove the cavity cover and carefully swipe a mirror once, cleanly, with acetone using the cotton swab.
3. Wait a few seconds for any extra acetone to evaporate, and then close the cavity cover.
4. Unblock the IR light and check the blue power out of the cavity.
5. If the power is the same, try a different mirror. If the power is less than where you started, follow steps 1-4 until the power is retrived. If the power is increased, clean the same mirror again and iterate until power no longer increases.

After the mirrors are cleaned, the cavity mode size and the phase matching may need to be reoptimized.

M.6 Overall power drops

Some groups have had issues with power damage on their crystals. The recommended solution for this is to translate the crystal (1 full turn of all 3 adjustment screws at a time) so that the light hits a different spot. However, doing so has never fixed any of the issues we've had, and we have never seen any sign of power damage so far.

The overall power has dropped from around 600 mW when we first bought the laser in 2012 to 380 mW in 2014 (both measured using a thermal head, which is important); it has remained constant since then. Some amount of that may be caused by slight mode mismatches between the TA outcoupling mode and the cavity mode, and could be due to slight drift in the TA outcoupling lens. Adjustments to this lens are extremely sensitive, so I have been loathe to touch it when someone from Toptica has not been present. However, it may become necessary if the power drops too much further. At that point, I'd call Toptica support to see what they recommend. I cannot possibly recommend them highly enough.

Bibliography

[1] M. H. Anderson, J. R. Ensher, M. R. Matthews, C. E. Wieman, and E. A. Cornell. Observation of bose-einstein condensation in a dilute atomic vapor. Science, 269(5221):198–201, 1995.

[2] K. B. Davis, M. O. Mewes, M. R. Andrews, N. J. van Druten, D. S. Durfee, D. M. Kurn, and W. Ketterle. Bose-einstein condensation in a gas of sodium atoms. Phys. Rev. Lett., 75:3969–3973, Nov 1995.

[3] B. DeMarco and D. S. Jin. Onset of fermi degeneracy in a trapped atomic gas. Science, 285(5434):1703–1706, 1999.

[4] Quantum phase transition from a superfluid to a mott insulator in a gas of ultracold atoms. Nature, 415(6867):39–44, 2002.

[5] Maxime Ben Dahan, Ekkehard Peik, Jakob Reichel, Yvan Castin, and Christophe Salomon. Bloch oscillations of atoms in an optical potential. Phys. Rev. Lett., 76:4508–4511, Jun 1996.

[6] Giacomo Roati, Chiara D'Errico, Leonardo Fallani, Marco Fattori, Chiara Fort, Matteo Zaccanti, Giovanni Modugno, Michele Modugno, and Massimo Inguscio. Anderson localization of a non-interacting bose-einstein condensate. Nature, 453:895 EP –, Jun 2008.

[7] Maxwell F. Parsons, Anton Mazurenko, Christie S. Chiu, Geoffrey Ji, Daniel Greif, and Markus Greiner. Site-resolved measurement of the spin-correlation function in the fermi-hubbard model. Science, 353(6305):1253–1256, 2016.

[8] Guillaume Salomon, Joannis Koepsell, Jayadev Vijayan, Timon A. Hilker, Jacopo Nespolo, Lode Pollet, Immanuel Bloch, and Christian Gross. Direct observation of incommensurate magnetism in hubbard chains. Nature, 565(7737):56–60, 2019.

[9] Peter T. Brown, Debayan Mitra, Elmer Guardado-Sanchez, Peter Schauß, Stanimir S. Kondov, Ehsan Khatami, Thereza Paiva, Nandini Trivedi, David A. Huse,

and Waseem S. Bakr. Spin-imbalance in a 2d fermi-hubbard system. Science, 357(6358):1385–1388, 2017.

[10] Russell A. Hart, Pedro M. Duarte, Tsung-Lin Yang, Xinxing Liu, Thereza Paiva, Ehsan Khatami, Richard T. Scalettar, Nandini Trivedi, David A. Huse, and Randall G. Hulet. Observation of antiferromagnetic correlations in the hubbard model with ultracold atoms. Nature, 519:211 EP –, Feb 2015.

[11] Daniel Greif, Thomas Uehlinger, Gregor Jotzu, Leticia Tarruell, and Tilman Esslinger. Short-range quantum magnetism of ultracold fermions in an optical lattice. Science, 340(6138):1307–1310, 2013.

[12] C.A. Regal and D.S. Jin. Experimental realization of the bcs-bec crossover with a fermi gas of atoms. volume 54 of Advances In Atomic, Molecular, and Optical Physics, pages 1 – 79. Academic Press, 2007.

[13] K.-K. Ni, S. Ospelkaus, D. Wang, G. Quéméner, B. Neyenhuis, M. H. G. de Miranda, J. L. Bohn, J. Ye, and D. S. Jin. Dipolar collisions of polar molecules in the quantum regime. Nature, 464:1324 EP –, Apr 2010.

[14] Christopher Foot. Atomic Physics. Oxford University Press, New York, first edition, 2005.

[15] H. Smith C. J.Pethick. Bose-Einstein Condensation in Dilute Gases. Cambridge University Press, New York, second edition, 2008.

[16] David Guery-Odelin Claude Cohen-Tannoudji. Advances in atomic physics: an overview. World Scientific Publishing, Singapore, first edition, 2011.

[17] Wolfgang Ketterle. In Atomic and Optical Physics I—MIT Course No. 8.421. Cambridge MA, Spring 2012. MIT OpenCourseWare.

[18] Zachary Geiger. An Apparatus for Dynamical Quantum Emulation Using Ultracold Lithium. PhD thesis, University of California, Santa Barbara, 2017.

[19] Kevin Singh. Floquet Engineering with Ultracold Lithium in Optical Lattices. PhD thesis, University of California, Santa Barbara, 2019.

[20] Florian Schreck. Mixtures of Ultracold Gases: Fermi Sea and Bose-Einstein Condensate of Lithium Isotopes. PhD thesis, University of Paris, 2002.

[21] Simon Stellmer. Degenerate quantum gases of strontium. PhD thesis, University of Innsbruck, 2013.

[22] Ruwan Senaratne. Quantum Simulation of Strongly-Driven Systems Using Ultracold Lithium and Strontium. PhD thesis, University of California, Santa Barbara, 2018.

[23] Kevin E. Strecker, Guthrie B. Partridge, Andrew G. Truscott, and Randall G. Hulet. Formation and propagation of matter-wave soliton trains. Nature, 417(6885):150–153, 2002.

[24] Andrew T. Grier, Igor Ferrier-Barbut, Benno S. Rem, Marion Delehaye, Lev Khaykovich, Frédéric Chevy, and Christophe Salomon. Λ-enhanced sub-doppler cooling of lithium atoms in D_1 gray molasses. Phys. Rev. A, 87:063411, Jun 2013.

[25] P. Hamilton, G. Kim, T. Joshi, B. Mukherjee, D. Tiarks, and H. Müller. Sisyphus Cooling of Lithium. ArXiv e-prints, August 2013.

[26] R. Grimm, M. Weidemueller, and Y. Ovchinnikov. Optical dipole traps for neutral atoms. ArXiv e-prints, Feb 1999.

[27] R. Walters, G. Cotugno, T. H. Johnson, S. R. Clark, and D. Jaksch. Ab initio derivation of hubbard models for cold atoms in optical lattices. Phys. Rev. A, 87:043613, Apr 2013.

[28] D. McKay, M. White, and B. DeMarco. Lattice thermodynamics for ultracold atoms. Phys. Rev. A, 79:063605, Jun 2009.

[29] Xiao Li, Xiaopeng Li, and S. Das Sarma. Mobility edges in one-dimensional bichromatic incommensurate potentials. Phys. Rev. B, 96:085119, Aug 2017.

[30] Henrik P. Lüschen, Sebastian Scherg, Thomas Kohlert, Michael Schreiber, Pranjal Bordia, Xiao Li, S. Das Sarma, and Immanuel Bloch. Single-particle mobility edge in a one-dimensional quasiperiodic optical lattice. Phys. Rev. Lett., 120:160404, Apr 2018.

[31] Michael E. Gehm. Preparation of an optically-trapped degenerate Fermi gas of ^{6}Li: Finding the route to degeneracy. PhD thesis, Duke University, 2003.

[32] National Center for Biotechnology Information. Pubchem database. lithium-7, cid=11564465. Available at https://pubchem.ncbi.nlm.nih.gov/compound/11564465 (2019/03/20).

[33] W. Scherf, O. Khait, H. Jäger, and L. Windholz. Re-measurement of the transition frequencies, fine structure splitting and isotope shift of the resonance lines of lithium, sodium and potassium. Zeitschrift für Physik D Atoms, Molecules and Clusters, 36(1):31–33, Mar 1996.

[34] W. I. McAlexander, E. R. I. Abraham, and R. G. Hulet. Radiative lifetime of the $2p$ state of lithium. Phys. Rev. A, 54:R5–R8, Jul 1996.

[35] Craig J. Sansonetti, C. E. Simien, J. D. Gillaspy, Joseph N. Tan, Samuel M. Brewer, Roger C. Brown, Saijun Wu, and J. V. Porto. Absolute transition frequencies and

quantum interference in a frequency comb based measurement of the ^{6,7}Li d lines. Phys. Rev. Lett., 107:023001, Jul 2011.

[36] E. Arimondo, M. Inguscio, and P. Violino. Experimental determinations of the hyperfine structure in the alkali atoms. Rev. Mod. Phys., 49:31–75, Jan 1977.

[37] E. R. I. Abraham, W. I. McAlexander, C. A. Sackett, and Randall G. Hulet. Spectroscopic determination of the s-wave scattering length of lithium. Phys. Rev. Lett., 74:1315–1318, Feb 1995.

[38] Hulet group. private communication.

[39] S. E. Pollack, D. Dries, M. Junker, Y. P. Chen, T. A. Corcovilos, and R. G. Hulet. Extreme tunability of interactions in a ^{7}Li bose-einstein condensate. Phys. Rev. Lett., 102:090402, Mar 2009.

[40] William I. McAlexander. Collisional interactions in an ultracold lithium gas. PhD thesis, Rice University, 2000.

[41] Paul S. Julienne and Jeremy M. Hutson. Contrasting the wide feshbach resonances in ^{6}Li and ^{7}Li. Phys. Rev. A, 89:052715, May 2014.

[42] Kevin E. Strecker. Tunable Interaction in Quantum Degenerate Lithium. PhD thesis, Rice University, 2004.

[43] NIST. Atomic data for strontium. Available at https://physics.nist.gov/PhysRefData/Handbook/Tables/strontiumtable1.htm (2019/03/22).

[44] J. E. Sansonetti and G. Nave. Wavelengths, transition probabilities, and energy levels for the spectrum of neutral strontium (sri). Journal of Physical and Chemical Reference Data, 39(3):033103, 2010.

[45] Simon Stellmer and Florian Schreck. Reservoir spectroscopy of $5s5p\ ^3p_2$–$5snd\ ^3D_{1,2,3}$ transitions in strontium. Phys. Rev. A, 90:022512, Aug 2014.

[46] S. Blatt, T. L. Nicholson, B. J. Bloom, J. R. Williams, J. W. Thomsen, P. S. Julienne, and J. Ye. Measurement of optical feshbach resonances in an ideal gas. Phys. Rev. Lett., 107:073202, Aug 2011.

[47] Cora J. Fujiwara. Dissertation. To be published June 2019, 2019.

[48] NIST. Chemistry webbook, srd 69: lithium. Available at https://webbook.nist.gov/cgi/cbook.cgi?ID=C7439932&Mask=4&Type=ANTOINE&Plot=on (2019/03/10).

[49] Ruwan Senaratne, Shankari V. Rajagopal, Zachary A. Geiger, Kurt M. Fujiwara, Vyacheslav Lebedev, and David M. Weld. Effusive atomic oven nozzle design using an aligned microcapillary array. Review of Scientific Instruments, 86(2):023105, 2015.

[50] Claudiu Stan. Experiments with Interacting Bose and Fermi Gases. PhD thesis, Massachusetts Institute of Technology, 2005.

[51] D.B. Montgomery. Solenoid magnet design: the magnetic and mechanical aspects of resistive and superconducting systems. Solenoid magnet design. Wiley-Interscience, 1969.

[52] Matthew Squires. High repetition rate Bose-Einstein condensate production in a compact, transportable vacuum system. PhD thesis, University of Colorado, Boulder, 2008.

[53] MIT BEC 5 Group,. private communication.

[54] Hao-Ze Chen, Xing-Can Yao, Yu-Ping Wu, Xiang-Pei Liu, Xiao-Qiong Wang, Yu-Ao Chen, and Jian-Wei Pan. Narrow-linewidth cooling of ^{6}li atoms using the 2s-3p transition. Applied Physics B, 122(11):281, Nov 2016.

[55] C. B. Alcock, V. P. Itkin, and M. K. Horrigan. Vapour pressure equations for the metallic elements: 298âĂŞ2500k. Canadian Metallurgical Quarterly, 23(3):309–313, 1984.

[56] W.E. Forsythe. In Smithsonian Physical Tables (9th Revised Edition), chapter Table 363. Evaporation of Metals. Knovel, 1954; 2003.

[57] M. ASANO and K. KUBO. Vapor pressure of strontium below 660Âřk. Journal of Nuclear Science and Technology, 15(10):765–767, 1978.

[58] A.J.H. Boerboom, H.W. Reyn, and J. Kistemaker. Heat of sublimation and vapour pressure of strontium. Physica, 30(1):254 – 257, 1964.

[59] G De Maria and V Piacente. Vapor pressures of calcium and strontium by transpiration method. The Journal of Chemical Thermodynamics, 6(1):1 – 7, 1974.

[60] YU. A. PRISELKOV and A.N.NESMEYANOV. Doklady Akad. Nauk SSSR, 95(1207), 1954.

[61] Matthew A Norcia, Julia R K Cline, John P Bartolotta, Murray J Holland, and James K Thompson. Narrow-line laser cooling by adiabatic transfer. New Journal of Physics, 20(2):023021, feb 2018.

[62] John P. Bartolotta, Matthew A. Norcia, Julia R. K. Cline, James K. Thompson, and Murray J. Holland. Laser cooling by sawtooth-wave adiabatic passage. Phys. Rev. A, 98:023404, Aug 2018.

[63] Yenny Natali Martinez de Escobar. Bose-Einstein Condensation of ^{84}Sr. PhD thesis, Rice University, 2007.

[64] Shankari V. Rajagopal, Kurt M. Fujiwara, Ruwan Senaratne, Kevin Singh, Zachary A. Geiger, and David M. Weld. Quantum emulation of extreme non-equilibrium phenomena with trapped atoms. Annalen der Physik, 529(8):1700008, 2017.

[65] Immanuel Bloch, Jean Dalibard, and Wilhelm Zwerger. Many-body physics with ultracold gases. Rev. Mod. Phys., 80(3):885, 2008.

[66] Maciej Lewenstein, Anna Sanpera, Veronica Ahufinger, Bogdan Damski, Aditi Sen, and Ujjwal Sen. Ultracold atomic gases in optical lattices: mimicking condensed matter physics and beyond. Adv. Phys., 56(2):243–379, 2007.

[67] Immanuel Bloch, Jean Dalibard, and Sylvain Nascimbene. Quantum simulations with ultracold quantum gases. Nat Phys, 8(4):267–276, 04 2012.

[68] Simon Sala, Johann Förster, and Alejandro Saenz. Ultracold-atom quantum simulator for attosecond science. Phys. Rev. A, 95:011403, Jan 2017.

[69] Stephan Arlinghaus and Martin Holthaus. Driven optical lattices as strong-field simulators. Phys. Rev. A, 81:063612, Jun 2010.

[70] Dirk-Sören Lühmann, Christof Weitenberg, and Klaus Sengstock. Emulating molecular orbitals and electronic dynamics with ultracold atoms. Phys. Rev. X, 5:031016, Aug 2015.

[71] Anatoli Polkovnikov, Krishnendu Sengupta, Alessandro Silva, and Mukund Vengalattore. *Colloquium*: Nonequilibrium dynamics of closed interacting quantum systems. Rev. Mod. Phys., 83:863–883, Aug 2011.

[72] Ferenc Krausz and Misha Ivanov. Attosecond physics. Rev. Mod. Phys., 81:163–234, Feb 2009.

[73] P. B. Corkum and Ferenc Krausz. Attosecond science. Nat Phys, 3(6):381–387, 06 2007.

[74] P. B. Corkum. Plasma perspective on strong field multiphoton ionization. Phys. Rev. Lett., 71:1994–1997, Sep 1993.

[75] M. Greiner, O. Mandel, T. Esslinger, T. W. Hänsch, and I. Bloch. Quantum phase transition from a superfluid to a mott insulator in a gas of ultracold atoms. Nature, 415:39–44, 2002.

[76] Jonathan Simon, Waseem S. Bakr, Ruichao Ma, M. Eric Tai, Philipp M. Preiss, and Markus Greiner. Quantum simulation of antiferromagnetic spin chains in an optical lattice. Nature, 472(7343):307–312, 04 2011.

[77] Markus Greiner, Olaf Mandel, Theodor W. Hansch, and Immanuel Bloch. Collapse and revival of the matter wave field of a Bose-Einstein condensate. Nature, 419(6902):51–54, 09 2002.

[78] H. Lignier, C. Sias, D. Ciampini, Y. Singh, A. Zenesini, O. Morsch, and E. Arimondo. Dynamical control of matter-wave tunneling in periodic potentials. Phys. Rev. Lett., 99(22):220403, Nov 2007.

[79] Toshiya Kinoshita, Trevor Wenger, and David S. Weiss. A quantum Newton's cradle. Nature, 440(7086):900–903, 04 2006.

[80] S. Hofferberth, I. Lesanovsky, B. Fischer, T. Schumm, J. Schmiedmayer, et al. Non-equilibrium coherence dynamics in one-dimensional bose gases. Nature, 449(7160):324–327, 09 2007.

[81] S. R. Wilkinson, C. F. Bharucha, K. W. Madison, Qian Niu, and M. G. Raizen. Observation of atomic wannier-stark ladders in an accelerating optical potential. Phys. Rev. Lett., 76:4512–4515, Jun 1996.

[82] Steven R. Wilkinson, Cyrus F. Bharucha, Martin C. Fischer, Kirk W. Madison, Patrick R. Morrow, Qian Niu, Bala Sundaram, and Mark G. Raizen. Experimental evidence for non-exponential decay in quantum tunnelling. Nature, 387(6633):575–577, 06 1997.

[83] D B Milosevic, G G Paulus, D Bauer, and W Becker. Above-threshold ionization by few-cycle pulses. Journal of Physics B: Atomic, Molecular and Optical Physics, 39(14):R203, 2006.

[84] T. Nubbemeyer, K. Gorling, A. Saenz, U. Eichmann, and W. Sandner. Strong-field tunneling without ionization. Phys. Rev. Lett., 101:233001, Dec 2008.

[85] Dror Shafir, Hadas Soifer, Barry D. Bruner, Michal Dagan, Yann Mairesse, Serguei Patchkovskii, Misha Yu. Ivanov, Olga Smirnova, and Nirit Dudovich. Resolving the time when an electron exits a tunnelling barrier. Nature, 485(7398):343–346, 05 2012.

[86] Adrian N. Pfeiffer, Claudio Cirelli, Mathias Smolarski, Darko Dimitrovski, Mahmoud Abu-samha, Lars Bojer Madsen, and Ursula Keller. Attoclock reveals natural coordinates of the laser-induced tunnelling current flow in atoms. Nat Phys, 8(1):76–80, 01 2012.

[87] M. Uiberacker, Th. Uphues, M. Schultze, A. J. Verhoef, V. Yakovlev, M. F. Kling, J. Rauschenberger, N. M. Kabachnik, H. Schroder, M. Lezius, K. L. Kompa, H. G. Muller, M. J. J. Vrakking, S. Hendel, U. Kleineberg, U. Heinzmann, M. Drescher, and F. Krausz. Attosecond real-time observation of electron tunnelling in atoms. Nature, 446(7136):627–632, 04 2007.

[88] M. Pont and M. Gavrila. Stabilization of atomic hydrogen in superintense, high-frequency laser fields of circular polarization. Phys. Rev. Lett., 65:2362–2365, Nov 1990.

[89] Shambhu Ghimire, Anthony D. DiChiara, Emily Sistrunk, Pierre Agostini, Louis F. DiMauro, and David A. Reis. Observation of high-order harmonic generation in a bulk crystal. Nat Phys, 7(2):138–141, 02 2011.

[90] A. P. Chikkatur, A. Görlitz, D. M. Stamper-Kurn, S. Inouye, S. Gupta, and W. Ketterle. Suppression and enhancement of impurity scattering in a bose-einstein condensate. Phys. Rev. Lett., 85:483–486, Jul 2000.

[91] B. Olmos, D. Yu, Y. Singh, F. Schreck, K. Bongs, and I. Lesanovsky. Long-range interacting many-body systems with alkaline-earth-metal atoms. Phys. Rev. Lett., 110:143602, Apr 2013.

[92] Mizuki Oku, Yu Hou, Xi Xing, Beth Reed, Hong Xu, Chao Chang, Cheuk-Yiu Ng, Kiyoshi Nishizawa, Keijiro Ohshimo, and Toshinori Suzuki. 3s rydberg and cationic states of pyrazine studied by photoelectron spectroscopy. The Journal of Physical Chemistry A, 112(11):2293–2310, 2008.

[93] P. M. Paul, E. S. Toma, P. Breger, G. Mullot, F. Augé, Ph. Balcou, H. G. Muller, and P. Agostini. Observation of a train of attosecond pulses from high harmonic generation. Science, 292(5522):1689–1692, 2001.

[94] Y. Mairesse, A. de Bohan, L. J. Frasinski, H. Merdji, L. C. Dinu, P. Monchicourt, P. Breger, M. Kovačev, R. Taïeb, B. Carré, H. G. Muller, P. Agostini, and P. Salières. Attosecond synchronization of high-harmonic soft x-rays. Science, 302(5650):1540–1543, 2003.

[95] Gerardo G. Naumis and F.J. Lopez-Rodriguez. The electronic spectrum of a quasiperiodic potential: From the Hofstadter butterfly to the Fibonacci chain. Physica B: Condensed Matter, 403(10-11):1755 – 1762, 2008.

[96] Patricia A. Thiel and Jean Marie Dubois. Quasicrystals: Electrons in a strange sea. Nature, 406(6796):570–573, 08 2000.

[97] P. Moras, W. Theis, L. Ferrari, S. Gardonio, J. Fujii, K. Horn, and C. Carbone. Quasicrystalline electronic states of a one-dimensionally modulated Ag film. Phys. Rev. Lett., 96:156401, Apr 2006.

[98] E. Y. Vedmedenko, U. Grimm, and R. Wiesendanger. Noncollinear magnetic order in quasicrystals. Phys. Rev. Lett., 93:076407, Aug 2004.

[99] Yaacov E. Kraus, Yoav Lahini, Zohar Ringel, Mor Verbin, and Oded Zilberberg. Topological states and adiabatic pumping in quasicrystals. Phys. Rev. Lett., 109:106402, Sep 2012.

[100] Feng Mei, Shi-Liang Zhu, Zhi-Ming Zhang, C. H. Oh, and N. Goldman. Simulating Z_2 topological insulators with cold atoms in a one-dimensional optical lattice. Phys. Rev. A, 85:013638, Jan 2012.

[101] Kevin A. Madsen, Emil J. Bergholtz, and Piet W. Brouwer. Topological equivalence of crystal and quasicrystal band structures. Phys. Rev. B, 88:125118, Sep 2013.

[102] Alan I. Goldman, Tai Kong, Andreas Kreyssig, Anton Jesche, Mehmet Ramazanoglu, Kevin W. Dennis, Sergey L. Bud'ko, and Paul C. Canfield. A family of binary magnetic icosahedral quasicrystals based on rare earths and cadmium. Nature Materials, 12(8):714–718, 08 2013.

[103] Li-Jun Lang, Xiaoming Cai, and Shu Chen. Edge states and topological phases in one-dimensional optical superlattices. Phys. Rev. Lett., 108:220401, May 2012.

[104] Marc de Boissieu. Phonons, phasons and atomic dynamics in quasicrystals. Chem. Soc. Rev., 41:6778–6786, 2012.

[105] Per Bak. Symmetry, stability, and elastic properties of icosahedral incommensurate crystals. Phys. Rev. B, 32:5764–5772, Nov 1985.

[106] Joshua E. S. Socolar, T. C. Lubensky, and Paul J. Steinhardt. Phonons, phasons, and dislocations in quasicrystals. Phys. Rev. B, 34:3345–3360, Sep 1986.

[107] C. Janot, L. Loreto, and R. Farinato. Special defects in quasicrystals. Physica Status Solidi B, 222(1):121–132, 2000.

[108] K. Singh, K. Saha, S. A. Parameswaran, and D. M. Weld. Fibonacci optical lattices for tunable quantum quasicrystals. Phys. Rev. A, 92:063426, Dec 2015.

[109] Giacomo Roati, Chiara D'Errico, Leonardo Fallani, Marco Fattori, Chiara Fort, Matteo Zaccanti, Giovanni Modugno, Michele Modugno, and Massimo Inguscio. Anderson localization of a non-interacting Bose-Einstein condensate. Nature, 453(7197):895–898, 06 2008.

[110] Michael Schreiber, Sean S. Hodgman, Pranjal Bordia, Henrik P. Lüschen, Mark H. Fischer, Ronen Vosk, Ehud Altman, Ulrich Schneider, and Immanuel Bloch. Observation of many-body localization of interacting fermions in a quasirandom optical lattice. Science, 349(6250):842–845, 2015.

[111] Yaacov E. Kraus and Oded Zilberberg. Topological equivalence between the fibonacci quasicrystal and the harper model. Phys. Rev. Lett., 109:116404, Sep 2012.

[112] Mor Verbin, Oded Zilberberg, Yoav Lahini, Yaacov E. Kraus, and Yaron Silberberg. Topological pumping over a photonic fibonacci quasicrystal. Phys. Rev. B, 91:064201, Feb 2015.

[113] Netanel H. Lindner, Erez Berg, and Mark S. Rudner. Universal chiral quasisteady states in periodically driven many-body systems. Phys. Rev. X, 7:011018, Feb 2017.

[114] Ruwan Senaratne, Shankari V. Rajagopal, Toshihiko Shimasaki, Peter E. Dotti, Kurt M. Fujiwara, Kevin Singh, Zachary A. Geiger, and David M. Weld. Quantum simulation of ultrafast dynamics using trapped ultracold atoms. Nature Communications, 9(1):2065, 2018.

[115] R. Dum, A. Sanpera, K.-A. Suominen, M. Brewczyk, M. Kuś, K. Rzaz̨ewski, and M. Lewenstein. Wave packet dynamics with bose-einstein condensates. Phys. Rev. Lett., 80:3899–3902, May 1998.

[116] D.-S. Lühmann, C. Weitenberg, and K. Sengstock. A quantum simulator for molecules: Imaging molecular orbitals and electronic dynamics with ultracold atoms. ArXiv e-prints, March 2015.

[117] Shankari V. Rajagopal, Kurt M. Fujiwara, Ruwan Senaratne, Kevin Singh, Zachary A. Geiger, and David M. Weld. Quantum emulation of extreme non-equilibrium phenomena with trapped atoms. Annalen der Physik, 529(8):1700008, 2017.

[118] Christian Gross and Immanuel Bloch. Quantum simulations with ultracold atoms in optical lattices. Science, 357(6355):995–1001, 2017.

[119] Russell A. Hart, Pedro M. Duarte, Tsung-Lin Yang, Xinxing Liu, Thereza Paiva, Ehsan Khatami, Richard T. Scalettar, Nandini Trivedi, David A. Huse, and Randall G. Hulet. Observation of antiferromagnetic correlations in the hubbard model with ultracold atoms. Nature, 519(7542):211–214, 03 2015.

[120] Maxime Ben Dahan, Ekkehard Peik, Jakob Reichel, Yvan Castin, and Christophe Salomon. Bloch oscillations of atoms in an optical potential. Phys. Rev. Lett., 76(24):4508–4511, Jun 1996.

[121] Th. Fennel, K.-H. Meiwes-Broer, J. Tiggesbäumker, P.-G. Reinhard, P. M. Dinh, and E. Suraud. Laser-driven nonlinear cluster dynamics. Rev. Mod. Phys., 82:1793–1842, Jun 2010.

[122] L V Keldysh. IONIZATION IN THE FIELD OF A STRONG ELECTROMAGNETIC WAVE. J. Exp. Theor. Phys., 47:1945–1957, 1964.

[123] F H M Faisal. Multiphoton transitions. iv. bound-free transition integrals in compact forms. J. Phys. B: At. Mol. Phys., 6(3):553, 1973.

[124] Howard R. Reiss. Gauges for intense-field electrodynamics. Phys. Rev. A, 22:770–772, Aug 1980.

[125] M. Lewenstein, Ph. Balcou, M. Yu. Ivanov, Anne L'Huillier, and P. B. Corkum. Theory of high-harmonic generation by low-frequency laser fields. Phys. Rev. A, 49:2117–2132, Mar 1994.

[126] D. S. Jin, J. R. Ensher, M. R. Matthews, C. E. Wieman, and E. A. Cornell. Collective excitations of a bose-einstein condensate in a dilute gas. Phys. Rev. Lett., 77:420–423, Jul 1996.

[127] M.-O. Mewes, M. R. Andrews, N. J. van Druten, D. M. Kurn, D. S. Durfee, C. G. Townsend, and W. Ketterle. Collective excitations of a bose-einstein condensate in a magnetic trap. Phys. Rev. Lett., 77:988–991, Aug 1996.

[128] C. Fort, M. Prevedelli, F. Minardi, F. S. Cataliotti, L. Ricci, G. M. Tino, and M. Inguscio. Collective excitations of a 87 rb bose condensate in the thomas-fermi regime. EPL (Europhysics Letters), 49(1):8, 2000.

[129] S. Stringari. Collective excitations of a trapped bose-condensed gas. Phys. Rev. Lett., 77:2360–2363, Sep 1996.

[130] P. Öhberg, E. L. Surkov, I. Tittonen, S. Stenholm, M. Wilkens, and G. V. Shlyapnikov. Low-energy elementary excitations of a trapped bose-condensed gas. Phys. Rev. A, 56:R3346–R3349, Nov 1997.

[131] András Csordás and Robert Graham. Collective excitations in bose-einstein condensates in triaxially anisotropic parabolic traps. Phys. Rev. A, 59:1477–1487, Feb 1999.

[132] B. D. Esry. Hartree-fock theory for bose-einstein condensates and the inclusion of correlation effects. Phys. Rev. A, 55:1147–1159, Feb 1997.

[133] R. Walsworth and L. You. Selective creation of quasiparticles in trapped bose condensates. Phys. Rev. A, 56:555–559, Jul 1997.

[134] Nobuyuki Takei, Christian Sommer, Claudiu Genes, Guido Pupillo, Haruka Goto, Kuniaki Koyasu, Hisashi Chiba, Matthias Weidemüller, and Kenji Ohmori. Direct observation of ultrafast many-body electron dynamics in an ultracold rydberg gas. Nature Communications, 7:13449 EP –, 11 2016.

[135] Simon Stellmer, Meng Khoon Tey, Bo Huang, Rudolf Grimm, and Florian Schreck. Bose-Einstein condensation of strontium. Phys. Rev. Lett., 103(20):200401, Nov 2009.

[136] David R. Yarkony. Conical intersections:âĂŽäâ the new conventional wisdom. J. Phys. Chem. A, 105(26):6277–6293, 2001.

[137] M. Hentschel, R. Kienberger, Ch. Spielmann, G. A. Reider, N. Milosevic, T. Brabec, P. Corkum, U. Heinzmann, M. Drescher, and F. Krausz. Attosecond metrology. Nature (London), 414(6863):509–513, 2001.

[138] J. Itatani, F. Quéré, G. L. Yudin, M. Yu. Ivanov, F. Krausz, and P. B. Corkum. Attosecond streak camera. Phys. Rev. Lett., 88:173903, Apr 2002.

[139] Ferenc Krausz and Misha Ivanov. Attosecond physics. Rev. Mod. Phys., 81:163–234, Feb 2009.

[140] S. L. Chin and N. R. Isenor. Multiphoton ionization in atomic gases with depletion of neutral atoms. Canadian Journal of Physics, 48(12):1445–1447, 1970.

[141] G Mainfray and C Manus. No Title. In S L Chin and P Lambropoulos, editors, Multiphoton ionization of Atoms, pages 7–34. Academic Press, Toronto, 1984.

[142] A. l'Huillier, L. A. Lompre, G. Mainfray, and C. Manus. Multiply charged ions induced by multiphoton absorption in rare gases at 0.53 μm. Phys. Rev. A, 27:2503–2512, May 1983.

[143] A. Baltuška, Th. Udem, M. Uiberacker, M. Hentschel, E. Goulielmakis, Ch. Gohle, R. Holzwarth, V. S. Yakovlev, A. Scrinzi, T. W. Hänsch, and F. Krausz. Attosecond control of electronic processes by intense light fields. Nature (London), 421(6923):611–615, feb 2003.

[144] Liang-You Peng and Anthony F Starace. Attosecond pulse carrier-envelope phase effects on ionized electron momentum and energy distributions. Phys. Rev. A, 76:043401, 2007.

[145] M F Kling, J Rauschenberger, A J Verhoef, E Hasoví, T Uphues, D B Mil Seví C, H G Muller, and M J J Vrakking. Imaging of carrier-envelope phase effects in above-threshold ionization with intense few-cycle laser fields. New J. Phys., 10(10):25024–25024, 2008.

[146] Michael Krüger, Markus Schenk, and Peter Hommelhoff. Attosecond control of electrons emitted from a nanoscale metal tip. Nature (London), 475:78–81, 2011.

[147] M F Kling, Ch Siedschlag, A J Verhoef, J I Khan, M Schultze, Th Uphues, Y Ni, M Uiberacker, M Drescher, F Krausz, and M J J Vrakking. Control of electron localization in molecular dissociation. Science, 312(5771):246–8, apr 2006.

[148] T Rathje, A M Sayler, S Zeng, P Wustelt, H Figger, B D Esry, and G G Paulus. Coherent Control at Its Most Fundamental: Carrier-Envelope-Phase-Dependent Electron Localization in Photodissociation of a H Ã¿ 2 Molecular Ion Beam Target. Phys. Rev. Lett., 111:093002, 2013.

[149] J. M. Ngoko Djiokap, S. X. Hu, L. B. Madsen, N. L. Manakov, A. V. Meremianin, and Anthony F. Starace. Electron vortices in photoionization by circularly polarized attosecond pulses. Phys. Rev. Lett., 115:113004, Sep 2015.

[150] M. Isinger, R. J. Squibb, D. Busto, S. Zhong, A. Harth, D. Kroon, S. Nandi, C. L. Arnold, M. Miranda, J. M. Dahlström, E. Lindroth, R. Feifel, M. Gisselbrecht, and A. L'Huillier. Photoionization in the time and frequency domain. Science, 358(6365):893–896, 2017.

[151] F. Serwane, G. Zürn, T. Lompe, T. B. Ottenstein, A. N. Wenz, and S. Jochim. Deterministic preparation of a tunable few-fermion system. Science, 332(6027):336–338, 2011.

[152] N T Zinner and A S Jensen. Comparing and contrasting nuclei and cold atomic gases. Journal of Physics G: Nuclear and Particle Physics, 40(5):053101, 2013.

[153] Aviv Keshet and Wolfgang Ketterle. A distributed, graphical user interface based, computer control system for atomic physics experiments. Rev. Sci. Instrum., 84(1):015105, 2013.

[154] S. V. Rajagopal, T Shimasaki, P Dotti, R Senaratne, and D. M. Weld. Phasonic spectroscopy of tunable quantum quasicrystals. In preparation, 2018.

[155] A I Goldman and M Widom. Quasicrystal structure and properties. Annual Review of Physical Chemistry, 42(1):685–729, 1991.

[156] Yaacov E. Kraus and Oded Zilberberg. Topological equivalence between the fibonacci quasicrystal and the harper model. Phys. Rev. Lett., 109:116404, Sep 2012.

[157] Mor Verbin, Oded Zilberberg, Yaacov E. Kraus, Yoav Lahini, and Yaron Silberberg. Observation of topological phase transitions in photonic quasicrystals. Phys. Rev. Lett., 110:076403, Feb 2013.

[158] J. E. Lye, L. Fallani, C. Fort, V. Guarrera, M. Modugno, D. S. Wiersma, and M. Inguscio. Effect of interactions on the localization of a bose-einstein condensate in a quasiperiodic lattice. Phys. Rev. A, 75:061603, Jun 2007.

[159] M. Schreiber, S. S. Hodgman, P. Bordia, H. P. Lüschen, M. H. Fischer, R. Vosk, E. Altman, U. Schneider, and I. Bloch. Observation of many-body localization of interacting fermions in a quasi-random optical lattice. arXiv:1501.05661, January 2015.

[160] L. Guidoni, C. Triché, P. Verkerk, and G. Grynberg. Quasiperiodic optical lattices. Phys. Rev. Lett., 79:3363–3366, Nov 1997.

[161] L. Guidoni, B. Dépret, A. di Stefano, and P. Verkerk. Atomic diffusion in an optical quasicrystal with five-fold symmetry. Phys. Rev. A, 60:R4233–R4236, Dec 1999.

[162] Bryce Gadway, Jeremy Reeves, Ludwig Krinner, and Dominik Schneble. Evidence for a quantum-to-classical transition in a pair of coupled quantum rotors. Phys. Rev. Lett., 110:190401, May 2013.

[163] Konrad Viebahn, Matteo Sbroscia, Edward Carter, Jr-Chiun Yu, and Ulrich Schneider. Matter-wave diffraction from a quasicrystalline optical lattice. Phys. Rev. Lett., 122:110404, Mar 2019.

[164] Justus A. Kromer, Michael Schmiedeberg, Johannes Roth, and Holger Stark. What phasons look like: Particle trajectories in a quasicrystalline potential. Phys. Rev. Lett., 108:218301, May 2012.

[165] M. Widom. Discussion of phasons in quasicrystals and their dynamics. Philosophical Magazine, 88(13-15):2339–2350, 2008.

[166] M. Weinberg, C. Ölschläger, C. Sträter, S. Prelle, A. Eckardt, K. Sengstock, and J. Simonet. Multiphoton interband excitations of quantum gases in driven optical lattices. Phys. Rev. A, 92:043621, Oct 2015.

[167] S. Aubry and G. André. Analyticity breaking and Anderson localization in incommensurate lattices. Ann. Isr. Phys. Soc., 3:133, 1980.

[168] Chetan Nayak, Steven H. Simon, Ady Stern, Michael Freedman, and Sankar Das Sarma. Non-abelian anyons and topological quantum computation. Rev. Mod. Phys., 80:1083–1159, Sep 2008.

[169] Alexei Kitaev. Anyons in an exactly solved model and beyond. Annals of Physics, 321(1):2 – 111, 2006. January Special Issue.

[170] Rajibul Islam, Ruichao Ma, Philipp M. Preiss, M. Eric Tai, Alexander Lukin, Matthew Rispoli, and Markus Greiner. Measuring entanglement entropy in a quantum many-body system. Nature, 528:77 EP –, Dec 2015. Article.

[171] Christian Gross and Immanuel Bloch. Quantum simulations with ultracold atoms in optical lattices. Science, 357(6355):995–1001, 2017.

[172] Michael J. Rust, Mark Bates, and Xiaowei Zhuang. Sub-diffraction-limit imaging by stochastic optical reconstruction microscopy (storm). Nature Methods, 3:793 EP –, Aug 2006.

[173] David M. Weld, Patrick Medley, Hirokazu Miyake, David Hucul, David E. Pritchard, and Wolfgang Ketterle. Spin gradient thermometry for ultracold atoms in optical lattices. Phys. Rev. Lett., 103:245301, Dec 2009.

[174] S. L. Campbell, R. B. Hutson, G. E. Marti, A. Goban, N. Darkwah Oppong, R. L. McNally, L. Sonderhouse, J. M. Robinson, W. Zhang, B. J. Bloom, and J. Ye. A fermi-degenerate three-dimensional optical lattice clock. Science, 358(6359):90–94, 2017.

[175] Martin M. Boyd. High Precision Spectroscopy of Strontium in an Optical Lattice: Towards a New Frequency Standard for Frequency and Time. PhD thesis, University of Colorado, Boulder, 2007.

[176] M. S. Safronova, S. G. Porsev, U. I. Safronova, M. G. Kozlov, and Charles W. Clark. Blackbody-radiation shift in the sr optical atomic clock. Phys. Rev. A, 87:012509, Jan 2013.

[177] Tetsuya Ido and Hidetoshi Katori. Recoil-free spectroscopy of neutral sr atoms in the lamb-dicke regime. Phys. Rev. Lett., 91:053001, Jul 2003.

[178] Alexandre Cooper, Jacob P. Covey, Ivaylo S. Madjarov, Sergey G. Porsev, Marianna S. Safronova, and Manuel Endres. Alkaline-earth atoms in optical tweezers. Phys. Rev. X, 8:041055, Dec 2018.

[179] M. A. Norcia, A. W. Young, and A. M. Kaufman. Microscopic control and detection of ultracold strontium in optical-tweezer arrays. Phys. Rev. X, 8:041054, Dec 2018.

[180] R. Drozdowski, M. Ignaciuk, J. Kwela, and J. Heldt. Radiative lifetimes of the lowest 3p1 metastable states of ca and sr. Zeitschrift für Physik D Atoms, Molecules and Clusters, 41(2):125–131, Jun 1997.

[181] Masami Yasuda, Tetsuo Kishimoto, Masao Takamoto, and Hidetoshi Katori. Photoassociation spectroscopy of ^{88}Sr: Reconstruction of the wave function near the last node. Phys. Rev. A, 73:011403, Jan 2006.

[182] W H Parkinson, E M Reeves, and F S Tomkins. Neutral calcium, strontium and barium: determination of f values of the principal series by the hook method. Journal of Physics B: Atomic and Molecular Physics, 9(2):157–165, feb 1976.

[183] W R S Garton, J P Connerade, M A Baig, J Hormes, and B Alexa. Measurement of oscillator strengths in the ultraviolet by magneto-optical rotation. Journal of Physics B: Atomic and Molecular Physics, 16(3):389–397, feb 1983.

[184] J P Connerade, W A Farooq, H Ma, M Nawaz, and N Shen. Atomic f-value measurements of high rydberg members by pulsed laser-based magneto-optical spectroscopy. Journal of Physics B: Atomic, Molecular and Optical Physics, 25(7):1405–1426, apr 1992.

[185] Xiaoji Zhou, Xia Xu, Xuzong Chen, and Jingbiao Chen. Magic wavelengths for terahertz clock transitions. Phys. Rev. A, 81:012115, Jan 2010.

[186] Gustavo García and José Campos. Transition probabilities for triplet levels of sr(i). Journal of Quantitative Spectroscopy and Radiative Transfer, 39(6):477 – 483, 1988.